Dynamics of solar Coronal Mass Ejections: forces that impact their propagation

A thesis
Submitted in partial fulfillment of the requirements
Of the degree of
Doctor of Philosophy

By

Nishtha Sachdeva
20123214



INDIAN INSTITUTE OF SCIENCE EDUCATION AND RESEARCH
PUNE

January, 2018

Certificate

Certified that the work incorporated in the thesis entitled "*Dynamics of solar Coronal Mass Ejections: forces that impact their propagation*", submitted by *Nishtha Sachdeva* was carried out by the candidate, under my supervision. The work presented here or any part of it has not been included in any other thesis submitted previously for the award of any degree or diploma from any other University or institution.

Date **Dr. Prasad Subramanian**

Declaration

I declare that this written submission represents my ideas in my own words and where others' ideas have been included, I have adequately cited and referenced the original sources. I also declare that I have adhered to all principles of academic honesty and integrity and have not misrepresented or fabricated or falsified any idea/data/fact/source in my submission. I understand that violation of the above will be cause for disciplinary action by the Institute and can also evoke penal action from the sources which have thus not been properly cited or from whom proper permission has not been taken when needed.

Date **Nishtha Sachdeva**

Roll No.- 20123214

For
Ma & Papa

Acknowledgements

These past few years have been a continuous learning process, not just scientifically but also on the personal front and I am deeply thankful to all the people who were a part of this journey.

Foremost, I express my sincere gratitude to my thesis advisor, Dr. Prasad Subramanian for his guidance, support and motivation. Much of this work is a result of his encouragement and enthusiasm. He has taught me not just science but to always be positive and inquisitive. Thank you is a small word for all the gratitude I hold for you for being empathetic and supportive during trying times.

I thank IISER Pune for my PhD fellowship and research facilities. I am grateful to IISER academic staff and the Dept. of Physics academic staff for making our lives a little easier. I also thank IISER administration, library, security and house-keeping for their services.

I appreciate the valuable suggestions and feedback from Dr. Durgesh Tripathi and Dr. Bhas Bapat, members of my Research Advisory Committee. Their inputs have helped in improving this study considerably.

I am deeply indebted to my collaborator, Dr. Angelos Vourlidas at JHU APL for his constant cooperation and guidance at every stage of this research work. I also thank Dr. Robin Colaninno for helping me through our first project together. I am grateful to Dr. Volker Bothmer for the invaluable learning experience through many discussions over coffee during the German winter. I thank him for his mentorship and hospitality during my visit to Göttingen, Germany. A big thankyou to all the members of his group who helped me during my stay and made it memorable. I acknowledge the support from Erasmus-Mundus NAMASTE scholarship for this opportunity.

The solar physics group at IISER is a great bunch to be a part of and share science with. I thank Arun, Madhusudan and Sasikumar, who have been extremely supportive seniors. Tomin for many wonderful stories we've shared. Mayur and Debesh for all the discussions, academic and non-academic.

I have met some of the most amazing people here at IISER who have

given me countless memories to be cherished always. Shishir, thank you for being there and putting up with me. You inspire me to live free, and I try, Always. Reja and Sanku for being extraordinary friends. Jyoti, Rohit, Gunjan, Harshini, Aman and Rabindranath for being an important part of this incredible time in my life.

Special mention to the constants in my life, my friends, Swamita, Prachi, Kritika and Jaya who make me happy by being there always.

I am grateful to my guardians in Pune for being so caring and helpful.

Finally, I thank my parents who are reflected in all that I am, and my sister. My father, who left too early and would have been supremely proud of me, like he always was, of any and every achievement of mine. My mother, whose constant love and unwavering support keeps me going forward. Ma, your strength inspires me everyday. I dedicate this work to both of you.

Abstract

The Sun occasionally ejects parts of its outer atmosphere into the interplanetary medium. These massive, large-scale eruptions from its corona are called coronal mass ejections (CMEs). As CMEs propagate, they evolve and expand, often driving interplanetary shocks and accelerating energetic particles. Earth-directed CMEs can cause extreme geo-magnetic storms leading to significant disruptions in satellite operations, space-bound technologies, and near-Earth space weather. It is therefore becoming increasingly important to understand the Sun-Earth dynamics of CMEs in order to develop reliable tools for predicting their arrival speed and time at the Earth.

It is generally assumed that Lorentz forces dominate the early stages of CME propagation and solar wind aerodynamic drag takes over later on. However, the precise distance range where one force dominates over the other is not well known.

In this study, we investigate the Sun-Earth dynamics of a set of 38 well-observed CMEs using data from the *Solar Terrestrial Relations Observatory* (STEREO), the *Solar and Heliospheric Observatory* (SOHO) missions and the *WIND* instrument. We seek to quantify the relative contributions of Lorentz force and aerodynamic drag on their propagation. The CMEs are 3D reconstructed using a geometrical fitting technique called the Graduated Cylindrical Shell (GCS) model to derive observed CME parameters. The fitting procedure provides the height-time profile, radius, and width of the CMEs which are used to derive other parameters, such as mass and cross-sectional area. These observed and derived parameters are used in the models for the forces acting on CMEs. Using a microphysical prescription of the drag coefficient (and not an empirical value), we find that solar wind aerodynamic drag adequately accounts for the dynamics of the fastest CMEs (initial velocity$>$ 900 km s^{-1}) from as low as 3.5 $R_\odot$ (Sachdeva et al., 2015). For relatively slower CMEs, however, we find that when the drag-based model is initiated below the distances ranging from 12 to 50 $R_\odot$, the observed CME trajectories cannot be accounted for. This suggests that aerodynamic drag force dominates the dynamics of slower CMEs only above these heights. This is at variance with the general perception that the solar wind drag influence

is significant just above a few solar radii. We also find that for slower CMEs, the drag "does not do much", i.e. the CMEs evolve very little above these heights.

To investigate CME dynamics below the heights where aerodynamic drag dominates, we consider the Torus Instability model for the driving Lorentz force (Kliem and Török, 2006). Using observational inputs to the model, we find that the Lorentz force increases from equilibrium and peaks between 1.65–2.45 $R_\odot$ for all CMEs, following which it decreases gradually. We do not find a clear distinction between the peak positions for slow and fast CMEs. We find that for fast CMEs, Lorentz forces become negligible in comparison to aerodynamic drag as early as 3.5–4 $R_\odot$. For slow CMEs, however, they become negligible only by 12–50 $R_\odot$. This justifies the success of the drag-only model for fast CMEs. In case of slow CMEs, the Lorentz force is only slightly smaller than the drag force even beyond 12–50 $R_\odot$. In other words, the difference between the two forces is more pronounced for fast CMEs than for slow ones. For these slow events, our results suggest that some of the magnetic flux carried by CMEs might be expended in expansion or heating. These dissipation effects might be important in describing the propagation of slower CMEs (Sachdeva et al., 2017). To the best of our knowledge, this is the first systematic study in this regard using a diverse CME sample.

A physical understanding of the forces that affect CME propagation and how they compare with each other at various heliocentric distances is an important ingredient in building tools for describing and predicting CME trajectories.

List of Publications

1. CME propagation – where does aerodynamic drag "take over"?
   Sachdeva, N., Subramanian, P., Colaninno, R., Vourlidas, A. 2015, The Astropysical Journal, 809, 158

2. CME dynamics using STEREO and LASCO observations: The relative importance of Lorentz Forces and Solar wind drag.
   Sachdeva, N., Subramanian, P., Vourlidas, A., Bothmer, V. 2017, Solar Physics, 292, 118

Contents

Certificate i

Declaration iii

Acknowledgements i

Abstract iii

List of Publications v

List of figures xiv

List of tables xv

1 Introduction **1**

1.1 The Sun 1

1.1.1 Introduction 1

1.1.2 Properties 3

1.1.3 Solar structure 4

1.1.4 Plasma β-parameter 5

1.2 Coronal Mass Ejections 7

1.2.1 Introduction 7

1.2.2 History of CME observations 8

1.2.3 Properties of CMEs 13

1.2.4 CME onset, initiation and propagation 15

1.3 Sun-Earth connection - Space Weather 19

1.3.1 Solar wind and space weather 21

1.3.2 Coronal mass ejections and space weather 22
1.3.3 Space weather forecasting 23
1.4 Motivation and Thesis organization 23

2 CME Selection and Geometrical fitting **27**
2.1 Introduction 27
2.2 Instruments and Observations 28
2.3 Selection Criteria 30
2.4 Fitting Technique 33
2.4.1 Graduated Cylindrical Shell (GCS) Model 33

3 CME dynamics and propagation **41**
3.1 Introduction 41
3.2 Forces acting on CMEs 42
3.2.1 Lorentz driving force 42
3.2.2 Aerodynamic drag force 43
3.3 Force Equation 45
3.4 Solar wind Drag Model 46
3.4.1 Drag Coefficient C_D 46
3.4.2 CME Cross-sectional Area 48
3.4.3 Models for Solar wind parameters 48
3.4.4 Calculation of CME Mass 49
3.4.5 Solving for V_{cme} 51
3.5 The TI Lorentz Force Model 52
3.5.1 CME current 52
3.5.2 Calculating the CME current I 53
3.5.3 Lorentz force profile 54

4 Results and Discussion **59**

4.1 Introduction . . . 59

4.2 Sample Description . . . 60

4.3 Part 1 - Aerodynamic Drag . . . 61

4.3.1 Fast CMEs . . . 62

4.3.2 Slow CMEs . . . 62

4.4 Part 2 - Lorentz Force . . . 66

4.4.1 Lorentz force vs aerodynamic drag . . . 70

5 Future Work **95**

5.1 Expansion of CME sample . . . 95

5.2 Proxies for the initial acceleration phase of CMEs . . . 96

5.3 Plasma Heating . . . 97

5.4 1D $\rightarrow$ 3D force Equation . . . 97

5.5 Solving a full force equation . . . 97

6 Appendix **99**

6.1 CME Virtual Mass . . . 99

6.2 The TI Lorentz Force Model . . . 100

6.2.1 Net Lorentz force . . . 100

6.2.2 CME current at equilibrium (I_{eq}) . . . 101

6.2.3 CME current I . . . 101

6.2.4 Final Lorentz force expression . . . 102

6.2.5 Decay Index n . . . 103

6.3 Equivalence of two Lorentz force models . . . 104

6.4 GCS fittings for all CMEs . . . 107

Bibliography . . . 159

Publications in international refereed journals . . . 159

List of Figures

1.1 Butterfly diagram of sunspots 2

1.2 Magnetic activity of the Sun over one solar cycle 3

1.3 Structure of the Sun 5

1.4 Electron density and temperature profile of the Sun 6

1.5 Plasma-β in the solar atmosphere for 100 G and 2500 G. . . . 7

1.6 First observation of a CME 8

1.7 SOHO LASCO observation of a CME on February 27, 2000 . . 10

1.8 Location of STEREO spacecraft on December 31, 2006, 2010, 2014 and 2017 at 00:00 UT 11

1.9 STEREO images of a CME event on September 28, 2012 . . . 12

1.10 Timeline of the history of CMEs 13

1.11 Classic three-part CME structure and Halo CME. 14

1.12 CME and Sunspot number overlap 15

1.13 Tether-cutting mechanism 17

1.14 Breakout model 17

1.15 Model current loop depicting toroidal forces 18

1.16 Phases of CME acceleration 19

1.17 Aurora visible in Alaska, USA on October 16-17, 2003. 20

1.18 Space weather effects 21

1.19 Interaction between solar wind and Earth's magnetosphere . . 22

2.1 Simultaneous observation of a CME in LASCO C2 and STEREO COR2 A/B and positions of STEREO A/B. 31

2.2 Schematic for GCS model 36

2.3 GUI interface for GCS fitting technique. 37

3.1 Lorentz force profile 54

3.2 Individual $J \times B$ terms in Lorentz force equation 55

4.1 Plot of observed initial height (h_0) for all CMEs. 60

4.2 Flowchart for drag force analysis method 64

4.3 Drag initiation height ($\widetilde{h}_0$) for all CMEs. 65

4.4 Plot of Lorentz force parameters (I and B_{ext}) at equilibrium . 68

4.5 Plot of Lorentz force magnitude and peak position. 69

4.6 Plot of the Fall % *versus* v_0 and $\widetilde{h}_0$ 70

4.7 Plot of decay index n for all CMEs. 70

4.8 Plot of F_{diff}% for all CMEs. 72

4.9 Height-time and Force profiles for CMEs 1 and 2 76

4.10 Height-time and Force profiles for CMEs 3 and 4 77

4.11 Height-time and Force profiles for CMEs 5 and 6 78

4.12 Height-time and Force profiles for CMEs 7 and 8 79

4.13 Height-time and Force profiles for CMEs 9 and 10 80

4.14 Height-time and Force profiles for CMEs 11 and 12 81

4.15 Height-time and Force profiles for CMEs 13 and 14 82

4.16 Height-time and Force profiles for CMEs 15 and 16 83

4.17 Height-time and Force profiles for CMEs 17 and 18 84

4.18 Height-time and Force profiles for CMEs 19 and 20 85

4.19 Height-time and Force profiles for CMEs 21 and 22 86

4.20 Height-time and Force profiles for CMEs 23 and 24 87

4.21 Height-time and Force profiles for CMEs 25 and 26 88
4.22 Height-time and Force profiles for CMEs 27 and 28 89
4.23 Height-time and Force profiles for CMEs 29 and 30 90
4.24 Height-time and Force profiles for CMEs 31 and 32 91
4.25 Height-time and Force profiles for CMEs 33 and 34 92
4.26 Height-time and Force profiles for CMEs 35 and 36 93
4.27 Height-time and Force profiles for CMEs 37 and 38 94

6.1 Current profile using Kliem and Török (2006) prescription . . 105
6.2 Current profile using Chen (1996) prescription 107
6.3 GCS fit for CME 1 at 17:54 108
6.4 GCS fit for CME 2 at 11:24 109
6.5 GCS fit for CME 3 at 06:54 110
6.6 GCS fit for CME 4 at 18:54 111
6.7 GCS fit for CME 5 at 05:39 112
6.8 GCS fit for CME 6 at 11:54 113
6.9 GCS fit for CME 7 at 10:24 114
6.10 GCS fit for CME 8 at 06:39 115
6.11 GCS fit for CME 9 at 03:39 116
6.12 GCS fit for CME 10 at 08:53 117
6.13 GCS fit for CME 11 at 15:39 118
6.14 GCS fit for CME 12 at 02:54 119
6.15 GCS fit for CME 13 at 09:54 120
6.16 GCS fit for CME 14 at 04:24 121
6.17 GCS fit for CME 15 at 02:24 122
6.18 GCS fit for CME 16 at 04:39 123
6.19 GCS fit for CME 17 at 02:24 124

6.20 GCS fit for CME 18 at 11:24 . . . 125
6.21 GCS fit for CME 19 at 13:54 . . . 126
6.22 GCS fit for CME 20 at 13:39 . . . 127
6.23 GCS fit for CME 21 at 15:54 . . . 128
6.24 GCS fit for CME 22 at 04:24 . . . 129
6.25 GCS fit for CME 23 at 18:39 . . . 130
6.26 GCS fit for CME 24 at 18:24 . . . 131
6.27 GCS fit for CME 25 at 17:24 . . . 132
6.28 GCS fit for CME 26 at 14:39 . . . 133
6.29 GCS fit for CME 27 at 17:39 . . . 134
6.30 GCS fit for CME 28 at 00:54 . . . 135
6.31 GCS fit for CME 29 at 05:54 . . . 136
6.32 GCS fit for CME 30 at 18:54 . . . 137
6.33 GCS fit for CME 31 at 16:54 . . . 138
6.34 GCS fit for CME 32 at 15:24 . . . 139
6.35 GCS fit for CME 33 at 07:39 . . . 140
6.36 GCS fit for CME 34 at 08:24 . . . 141
6.37 GCS fit for CME 35 at 02:39 . . . 142
6.38 GCS fit for CME 36 at 22:54 . . . 143
6.39 GCS fit for CME 37 at 00:39 . . . 144
6.40 GCS fit for CME 38 at 08:24 . . . 145

List of Tables

2.1 Observational details of CMEs in the sample 38

2.2 GCS fitted parameters for all CMEs at first observed height . 39

3.1 Solar wind parameters, CME mass and decay index 57

4.1 Results of aerodynamic drag analysis 74

4.2 Results of Lorentz force analysis 75

6.1 GCS fitting parameters for each CME as corresponding to Figures 6.3-6.40 146

Chapter 1

Introduction

This chapter introduces some overall properties of the Sun, coronal mass ejections (CMEs) and space weather. We begin with an introduction to the properties of the Sun, its structure and atmosphere. Historical and observational details of CMEs are discussed, describing the instruments used to observe the Sun and solar transients. We describe the properties of CMEs along with details regarding their onset and propagation. We also discuss the space weather and how the Sun-Earth connection is influenced by CMEs. We finally detail the organization of the rest of the thesis.

1.1 The Sun

1.1.1 Introduction

About 4.6 billion years ago, the most extraordinary "ordinary" star of our solar system was born. The Sun is the source of sustenance of life on Earth and plays a prominent role in art, religion, and science in human history. While ancient astronomers recorded the movement and features on the Sun by observing with the naked eye, it was only in the 17^{th} century, with the invention of the telescope, that systematic records of sunspot observations were made. Since then we have come a long way in understanding, observing and explaining the structure, evolution, and properties of the Sun and its related phenomena.

The sunspot cycle was discovered by Samuel Heinrich Schwabe who found that the number of sunspots varied over a regular period. This was further confirmed by a Swiss astronomer Rudolf Wolf (in 1852) who established this

period of variation as $\sim$ 11 years. In 1908, George E. Hale measured the magnetic field in sunspots for the first time. During a cycle of 11 years, the active, magnetic regions migrate from high latitudes to lower latitudes near the equator which is seen in the famous Butterfly diagram of sunspot positions (Figure 1.1). The magnetic polarity of the global solar magnetic field reverses over the course of a cycle, with the magnetic activity varying with the number of sunspots. With observations beginning from 1755, we are currently (in 2017-2018) in the solar cycle 24 which began in December 2008 and reached its maximum in 2014. Figure 1.2 shows the eleven years of magnetic activity (in extreme UV wavelengths) on the Sun during solar cycle 23, starting with a quiet period during the minimum in 1996 to increased activity, followed by a decrease till 2006.

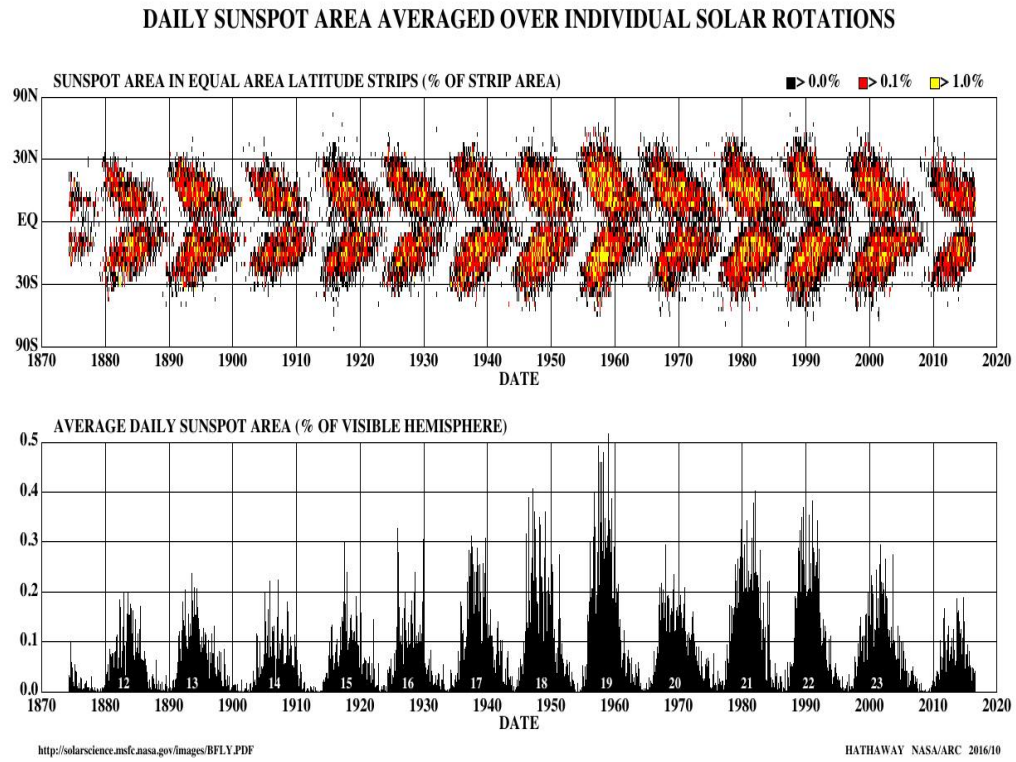


Figure 1.1: The butterfly diagram showing the positions of the sunspots for each rotation of the sun since May 1874. It can be seen that the spot bands first form at mid-latitudes, widen, and then move towards the equator as each cycle progresses. *Image credit- NASA MSFC (https://solarscience.msfc.nasa.gov/).*

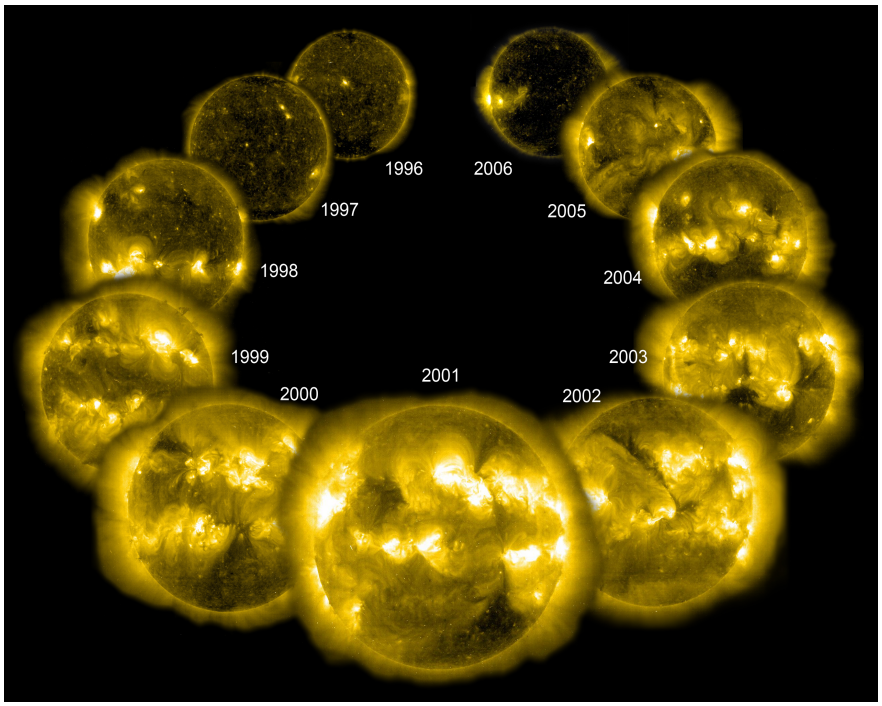


Figure 1.2: Full disk images of the corona in 284 Å wavelength of extreme UV light of the the solar cycle 23 (1996 - 2006) showing the variation of magnetic activity on the Sun.*Image credit- SOHO EIT.*

1.1.2 Properties

The nearest star and center of our solar system, the Sun is a main sequence star of spectral type G2V. Below we list a few characteristic properties of this star:

1. **Radius** - The Sun has a equatorial radius of $(6.96 \pm 0.001) \times 10^5$ km which is about 109 times the radius of the Earth.

2. **Distance** - The Sun-Earth distance is 1 astronomical unit (AU) which is equal to 1.496×10^8 km or 215 times the solar radii ($R_\odot$).

3. **Mass** - The total mass of the Sun is $(1.98 \pm 0.0003) \times 10^{30}$ kg with a volume of 1.4×10^{27} cubic meters. It is large enough to fit about 1.3 million Earths.

4. **Luminosity and composition** - Solar luminosity, $L_\odot = (3.844 \pm 0.010 \times 10^{26})$ Watt. The Sun is composed primarily of hydrogen and helium and only about 2% of heavier elements like oxygen, carbon and iron.

1.1.3 Solar structure

Like other stars, the Sun is a massive ball of ionized gas held together by its gravitational pull leading to immense pressure and temperature conditions. The structure of the Sun can be conceptually divided into six regions: the solar interior which includes the core, the radiative zone, and the convective zone, and the solar atmosphere which includes the photosphere, the chromosphere and the corona (Figure 1.3).

1. **Solar Interior**

   The central region of the Sun, called the core has a temperature of about 1.5×10^7 K and pressure which exceeds 2.5×10^{11} atm. These conditions sustain the thermonuclear fusion processes which produce large amounts of energy in the core of the Sun. It extends up to 0.25 $R_\odot$. Beyond the core, up to 0.7 $R_\odot$ lies the radiative zone with temperatures of about 2×10^6 K. The energy produced in the solar core is transferred via radiation through this region. Since the density in this region is high ($2 \times 10^4 - 2 \times 10^2\, kg\, m^{-2}$) and the mean free path of photons is very small ($\sim 9 \times 10^{-2}$ cm), it takes over 170,000 years for the photons to travel from the core to the top of the radiative zone.

   The core and the radiative zone rotate as a solid body (rigid rotation) whereas the convective zone rotates differentially. The layer between the radiative zone and the convective zone is called the tachocline. Due to the difference in the rotation rates, the tachocline is subjected to shear flows which are thought to be the source of generating the magnetic fields and powering the solar dynamo. The convective zone extends from 0.7 $R_\odot$ up to the solar surface. Plasma heated at the tachocline expands and rises up creating convective currents in this zone. This material cools as it reaches the surface, which decreases the density and it sinks to the base of the convective zone. As this cycle continues, the solar surface or the photosphere gets a granular appearance. The magnetic loops generated in the core twist and wind-up due to the differential rotation of the convective zone. This causes the magnetic pressure to increase and the loops become buoyant, rising up through the solar surface and creating sunspots on the solar disk. These sunspots are visible as dark regions on the surface and always appear in pairs of opposite magnetic polarity.

2. **Solar Atmosphere**

   The lowest layer of the solar atmosphere is the visible surface of the Sun called the photosphere. It is about 500 km in thickness with a temperature of $\sim$ 5000 K and particle density of $10^{23}\, m^{-3}$. The Sun becomes opaque to visible light below the photosphere *i.e.* all light escapes freely above the photosphere. The layers of the solar atmosphere

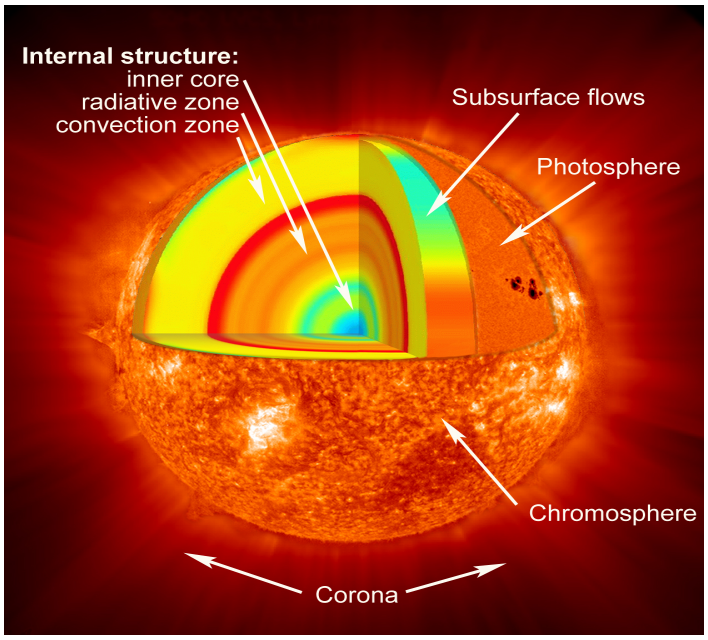


Figure 1.3: Image depicting different layers of the Sun. Solar Interior comprising of the hot core, radiative zone and the convective zone. Photosphere forms the solar surface followed by the chromosphere and the solar corona. *Image credit- NASA (https://www.nasa.gov).*

above the photosphere are visible only during a solar eclipse. In the chromosphere, the temperature falls up to ~ 4500 K, before it increases to about 20000 K. This layer extends to about 2000 km above the photosphere with density $\sim 10^{16}\, m^{-3}$. Above the chromosphere lies a thin layer ($\sim$ 200 km) called the transition region, where the temperature increases from 20000 K to about 10^6 K. Despite decades of research, it is not yet clear how the corona gets heated to such high temperatures. The solar corona, at 2500 km from the photosphere has proton densities in the range $10^{14}\, m^{-3}$ to $< 10^{12}\, m^{-3}$ for heights $> 1\mathrm{R}_\odot$ (Aschwanden, 2005). The average temperature in the corona ranges from $1 - 2 \times 10^6$ to $8 - 20 \times 10^6$ K in the hottest regions (Figure 1.4). The solar corona is visible during eclipses due to Thomson scattering of the photospheric light by the highly ionized coronal plasma.

1.1.4 Plasma β-parameter

The magnetic fields on the solar surface are not homogeneous. Sunspots can have field strengths of about 2000-3000 G, while active regions on the surface have average photospheric fields of 100-300 G. On the other hand, the quiet Sun generally has an average field of 0.1-0.5 G. Ratio of the thermal plasma pressure (p_{th}) to the magnetic pressure (p_{mag}) is

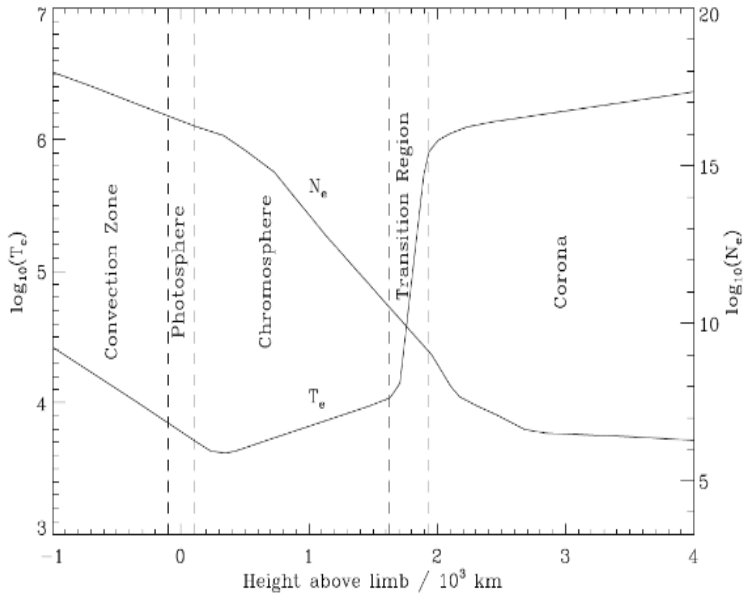


Figure 1.4: A 1D model for electron density ($N_e(cm^{-3})$ and temperature ($T_e(K)$) profile through different layers of the Sun) from Gabriel and Mason (1982).

given by the plasma-β parameter.

$$\beta = \frac{p_{th}}{p_{mag}} = \frac{nk_BT}{B^2/8\pi} \tag{1.1}$$

where, n is the number density, k_B is the Boltzmann constant, T is the temperature and B is the magnetic field strength. Plasma-$\beta < 1$ indicates that the region is magnetically dominated. Most parts of the solar corona have $\beta < 1$; however, it increases above 1 in the outer corona. Gas pressure dominates ($\beta > 1$) in the photosphere and the chromosphere as well (Figure 1.5).

The solar corona is also the source of a continuous stream of particles in all directions called the solar wind. Due to the high temperature in the corona, particles have enough kinetic energy to escape the gravity of the Sun with speeds of about $\sim 300 - 400$ km s^{-1}. The solar wind plasma carries with it the embedded solar magnetic field which forms the interplanetary magnetic field (IMF). The magnetic activity of the Sun manifests itself in the form of active regions, flares and solar transients including solar wind and coronal mass ejections. These govern the space weather and affect the Sun-Earth climate.

The next section discusses a specific kind of large-scale solar transients, called coronal mass ejections that primarily drive the space weather and affect the near-Earth environment.

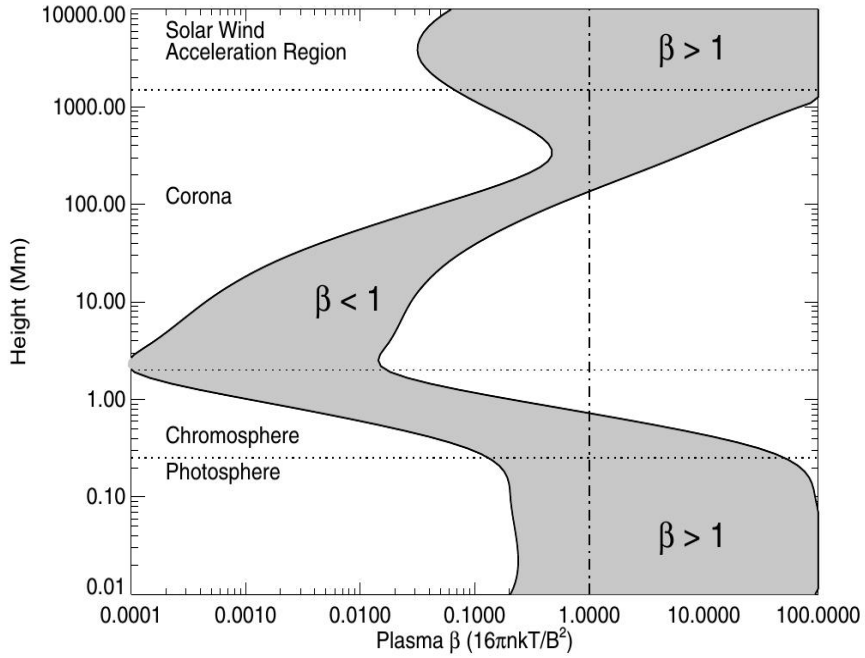


Figure 1.5: Plasma-β in the solar atmosphere for two assumed field strengths-100 G and 2500 G. Magnetic pressure dominates over the gas pressure in the inner corona (< 0.2 $R_\odot$). *Image adapted from Aschwanden (2005).*

1.2 Coronal Mass Ejections

1.2.1 Introduction

In 1841, a telegraph system in Exter was affected by strong magnetic fluctuations causing a train delay of about 16 minutes. This is the first documented account of manifestation of a solar magnetic activity which was reported by the Nature Journal (1871). Throughout history many such instances have been recorded, most famous being the Carrington event of 1859, when a CME was believed to have impacted the Earth's magnetosphere causing one of the biggest solar storms in history. Many such accounts of geo-magnetic storms exist. However, coronal mass ejections (CMEs), were discovered, only in 1971 (Hansen et al., 1971; Tousey, 1973). Figure 1.6 shows one of the earliest drawings of the 1860 solar eclipse that shows a CME identified later by Jack Eddy.

Coronal mass ejections (CMEs) are massive and energetic expulsions of coronal plasma and magnetic fields into the interplanetary (IP) medium. CMEs may erupt from any region of the solar corona, but are often mostly associated with the lower latitudes, especially during the solar minimum. CMEs can have speeds ranging from a few hundred to a few thousand kilo-

meters per second with mass of the order of 10^{15} gms. CMEs often create shocks in the interplanetary medium as they propagate which causes particle acceleration and bursts of radio emission. They sometimes impact the Earth's magnetosphere; when they do, they can cause geomagnetic storms which disrupt space-based technologies, navigation, telecommunications and pose a threat to the safety of airline carriers and astronauts. Due to their direct impact on space weather as well as their indirect affect on humankind, CMEs are a widely studied solar phenomena. CME observations using space-based instruments began in the twentieth century and continues with major upgradations in observing technology and quality of data.

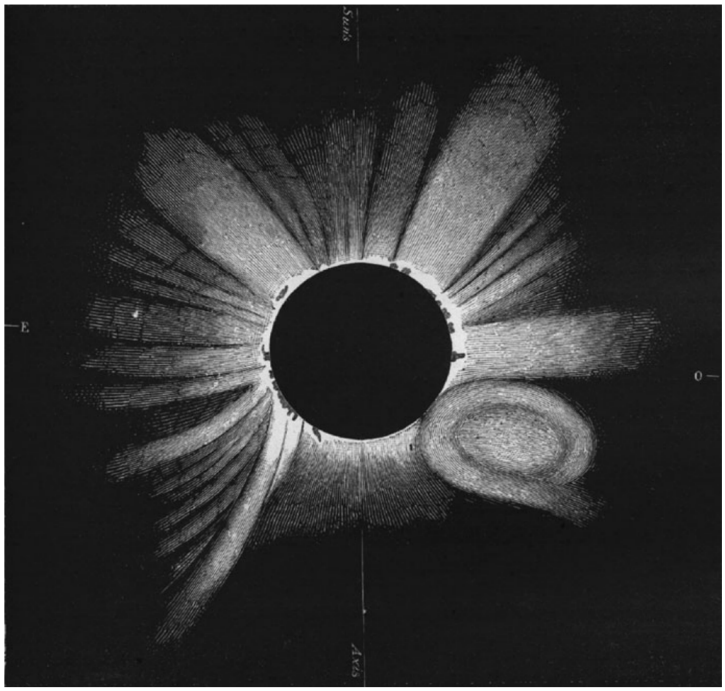


Figure 1.6: First observation of a coronal mass ejection. Drawing of the 1860 solar eclipse. *Image taken from Howard (2011).*

1.2.2 History of CME observations

1. **Remote Sensing**

   White light emissions from the solar corona arise from photospheric radiation which is Thomson-scattered by free electrons. An enhanced brightness indicates an enhanced coronal column density along the line of sight. Based on this principle, CMEs are imaged in white-light using coronagraphs that observe the Sun by creating an artificial eclipse, blocking the solar disk and imaging the solar corona. The first observations of CMEs using space coronagraphs were made by the seventh *Orbiting Solar Observatory* (OSO-7, 1971) in early 1970's (Tousey,

1973). It observed a total of 20 CMEs before it re-entered the Earth's atmosphere. Improved quality and longer observational periods were achieved by the *Apollo Telescope Mount* (ATM) coronagraph on board *Skylab* (MacQueen et al., 1974) which observed about 77 transients between May 1973 and February 1974, which were all recognized as CMEs. The term coronal mass ejections first appeared in Gosling et al. (1976) based on *Skylab* observations. The *Solwind* (1979) coronagraph on board the *Air Force satellite P78-1* (Michels et al., 1980) and the *Coronagraph/Polarimeter* (CP) on board the *Solar Maximum Mission* (SMM, 1980) satellite (MacQueen et al., 1980) continued observations into the 1980's. Among the most significant discoveries of these coronagraphs was the first Earth-directed CME (observed in November 1976) by Russ Howard and co-workers (Howard et al., 1982). The *Solwind* and SMM coronagraphs detected over 2000 CMEs providing data for the first statistical analysis for studying the CME structure, mass, angular extension and location (Howard et al., 1985).

By 1992, Kahler (1992) demonstrated through a detailed review of CME and flare observations, metric radio bursts, IP shocks, magnetic fields and solar energetic particles and their geomagnetic effects that CMEs (not flares) were the major drivers of heliospheric and geomagnetic phenomena. Regardless, a large portion of the solar community was convinced that solar flares were the primary drivers of space weather. This came to be known as the "Solar Flare Myth" as described by Gosling (1993), who confirmed the source of IP shocks and storm to be CMEs and not solar flares. Towards the end of 1995, however, more clarity was achieved following the launch of the *Solar and Heliospheric Observatory* (SOHO) (Brueckner et al., 1995) which provided more conclusive CME data using the *Large Angle and Spectrometric Coronagraph* (LASCO). LASCO consists of three coronagraphs that observe the solar corona in white-light from 1.1 – 30 $R_{\odot}$. Data from LASCO was used to identify "Halo CMEs" for the first time and construct larger statistical CME databases (*e.g., http://lasco-www.nrl.navy.mil/cmelist.html* and *http://cdaw.gsfc.nasa.gov/CME_list*). So far LASCO has detected 10^4 CMEs (Yashiro et al., 2004). The unparalleled quality and resolution of data from SOHO has made it a cornerstone for solar observations (Example - Figure 1.7).

In 2003, the *Solar Mass Ejection Imager* (SMEI), a heliospheric imager on board the *Coriolis* spacecraft was launched to observe the outer corona in white light (Eyles et al., 2003). SMEI observed about 400 transients during 8.5 years of its life (Webb et al., 2006). The first white light heliospheric imagers (HI) were launched onboard the twin *Helios* (1974,1976) spacecraft (Richter et al., 1982; Jackson, 1985). The zodiacal light polarimeters observed 0.3–1 AU with a limited field of view, providing only partial images of interplanetary counterparts of CMEs

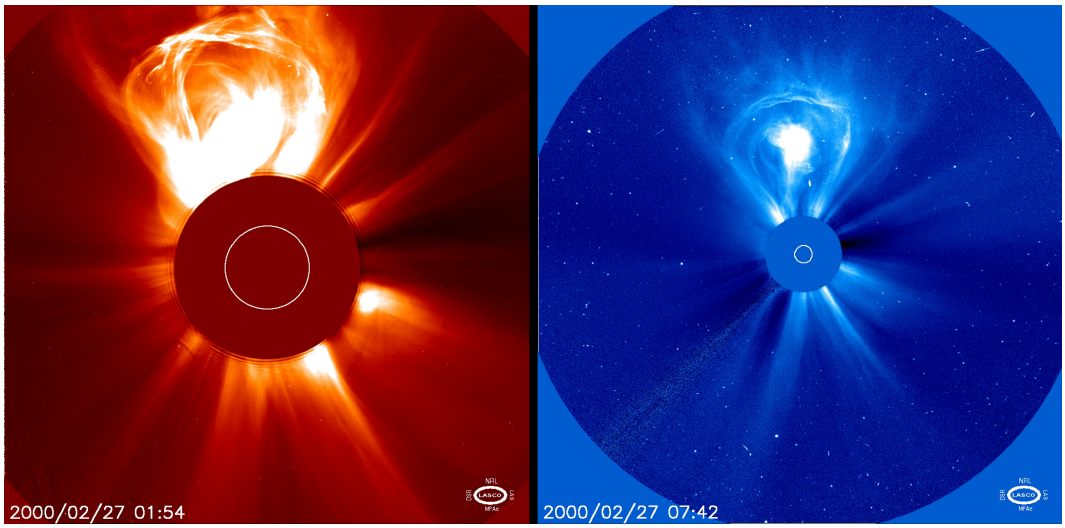


Figure 1.7: A coronal mass ejection on February 27, 2000 taken by SOHO LASCO C2 (left) and C3 (right) coronagraphs. *Image credit: https://sohowww.nascom.nasa.gov/*

(called ICMEs) in white light. The launch of the twin *Solar Terrestrial Relations Observatory* (STEREO) spacecrafts in 2006 (Howard et al., 2008) heralded a new approach to solar observations. The *Sun Earth Connection Coronal and Heliospheric Investigation* (SECCHI) mission on board STEREO consists of coronagraphs (COR1, COR2) and heliospheric imagers (HI1, HI2). The STEREO mission consists of two spacecrafts, STEREO Ahead (A) and STEREO Behind (B), one moving slightly faster than the other in the ecliptic plane in opposite directions. The coronagraphs and heliospheric imagers provide white light observations of CMEs covering a field of view from 1.4–318 $R_{\odot}$. Figure 1.8 depicts the location of the STEREO A and B spacecrafts on December 31 in different years (2006. 2010, 2014 and 2017). Figure 1.9 shows the COR2 A and B observations of a CME on September 28, 2012.

White light CME observations have been accompanied by observations of the solar disk at coronal wavelengths with the SOHO *Extreme Ultraviolet Imaging Telescope* (EIT), SOHO *Coronal Diagnostic Spectrometer* (CDS) imagers, STEREO *Extreme-Ultra Violet Imager* (EUVI) and instruments onboard *Yohkoh* (1991-2001) and *Transition Region And Coronal Explorer* (TRACE, 1998) spacecraft (Zhang et al., 2001). The *Reuven Ramaty High Energy Solar Spectroscopic Imager* (RHESSI, 2002) and *Hinode* spacecraft (2006) include hard and soft X-ray imagers to investigate solar responses to CME launches. In 2010, the *Atmospheric Imaging Assembly* (AIA) onboard the *Solar Dynamics Observatory* (SDO) was launched in a geosynchronous orbit which includes white light, ultra-violet and extreme ultra-violet imagers providing a

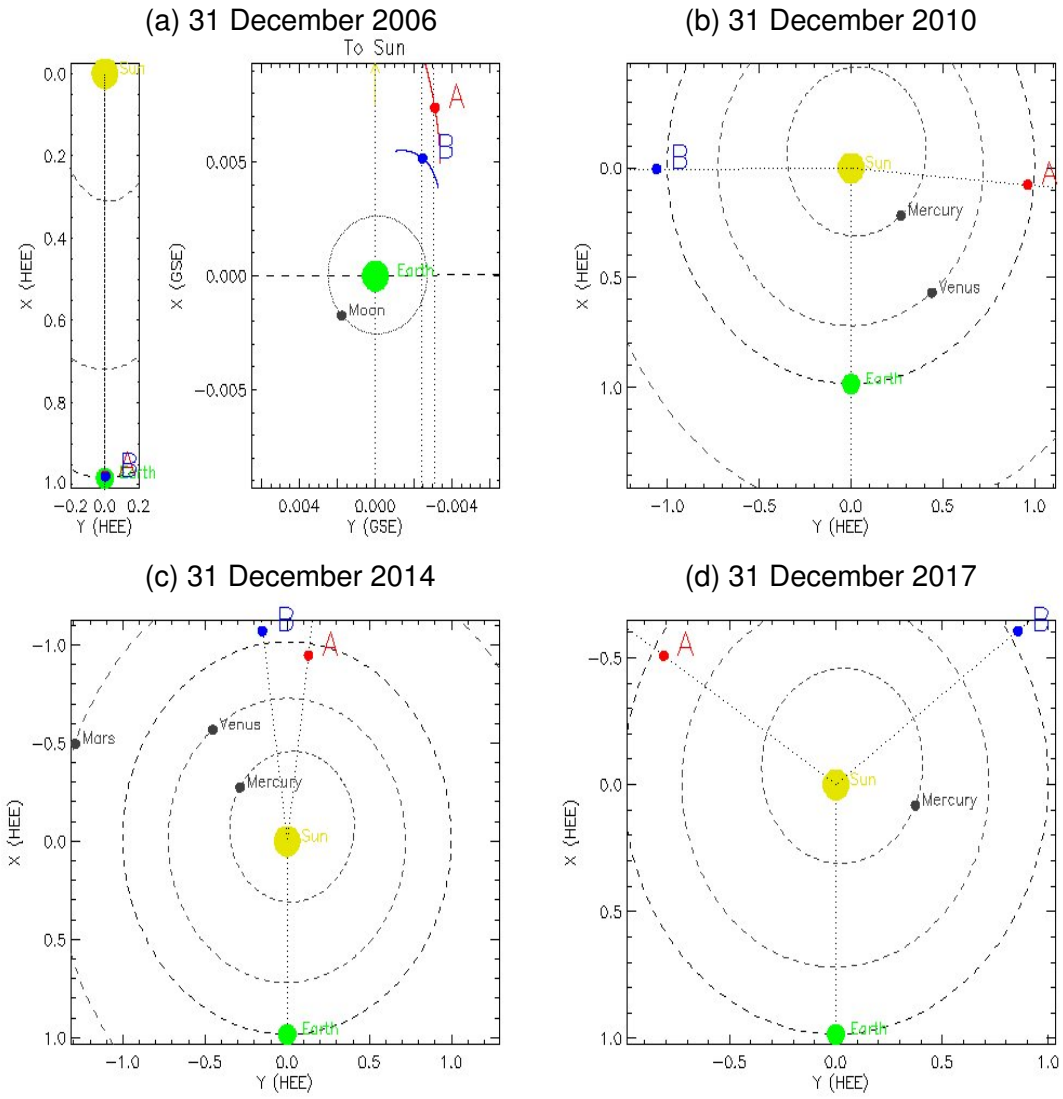


Figure 1.8: Location of STEREO Spacecrafts A and B on December 31, (a) 2006, (b) 2010, (c) 2014 and (d) 2017 at 00:00 UT. The color scheme is as follows: Red circle- STEREO-A , Blue circle- STEREO-B, Green circle- Earth, Yellow circle-Sun. The two STEREO spacecrafts separate by around 22.5° from the Earth every year. *Image credit: STEREO orbit tool https://stereo-ssc.nascom.nasa.gov/where.shtml.*

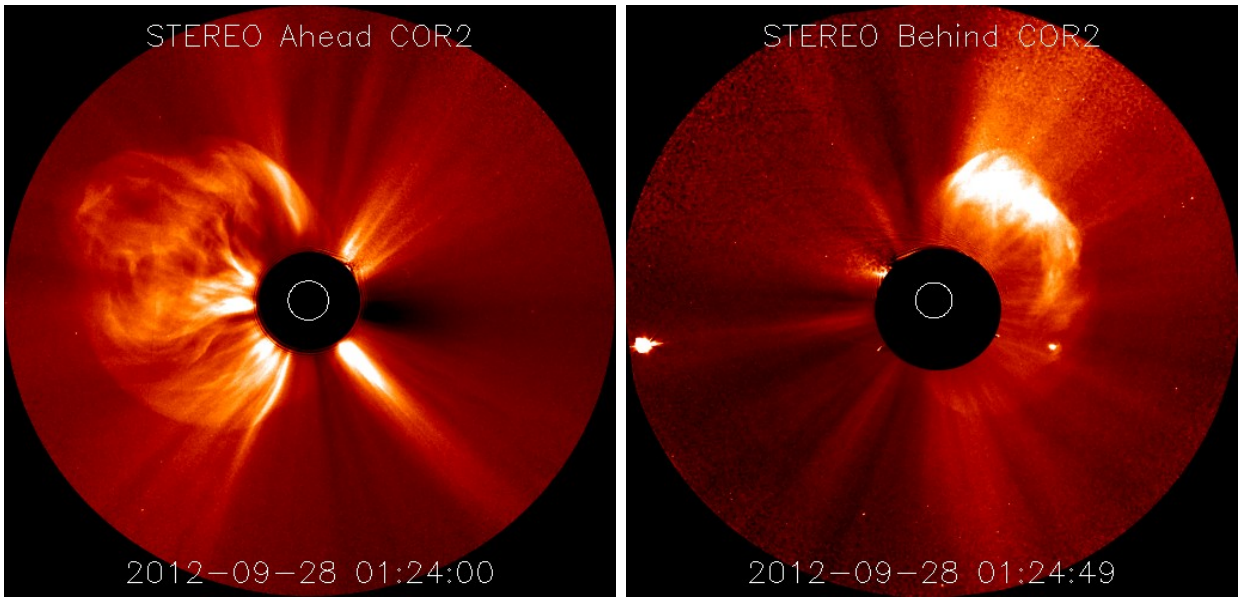


Figure 1.9: Images of a Halo CME on September 28, 2012 from STEREO COR2 A (Ahead) and COR2 B (Behind) coronagraphs. *Image credit: https://stereo-ssc.nascom.nasa.gov/*

wealth of solar observations over multiple wavelengths. The *Solar Orbiter* (2019) and *Parker Solar Probe* (2018) are future missions for heliospheric observations.

2. **Interplanetary Scintillation**

   Before coronagraphs observed the interplanetary counterparts of coronal mass ejections (ICMEs) at large distances from the Sun (> 50 $R_\odot$), other methods such as interplanetary scintillation (IPS) (Hewish et al., 1964; Houminer and Hewish, 1974; Manoharan, 2006, 2010) were used for this purpose. IPS is the variation in the radio signal from distant sources due to density perturbations in the interplanetary medium. These distortions in radio sources at meter wavelengths are used to monitor the solar wind and density fluctuations in the medium to track ICMEs traveling between the Sun and the Earth. However, IPS observations need to be improved to efficiently differentiate between density perturbations due to ICMEs and corotating interaction regions (CIRs). CIRs are mergers of fast and slow streams causing density enhancements.

3. **In-situ observations**

   Apart from remote sensing observations, *in-situ* measurements of plasma parameters from spacecrafts at 1 AU and beyond provide supporting observations. Examples include *Ulysses*, launched in 1990, *WIND* (1994) and the *Advanced Composition Explorer* (ACE, 1997). The

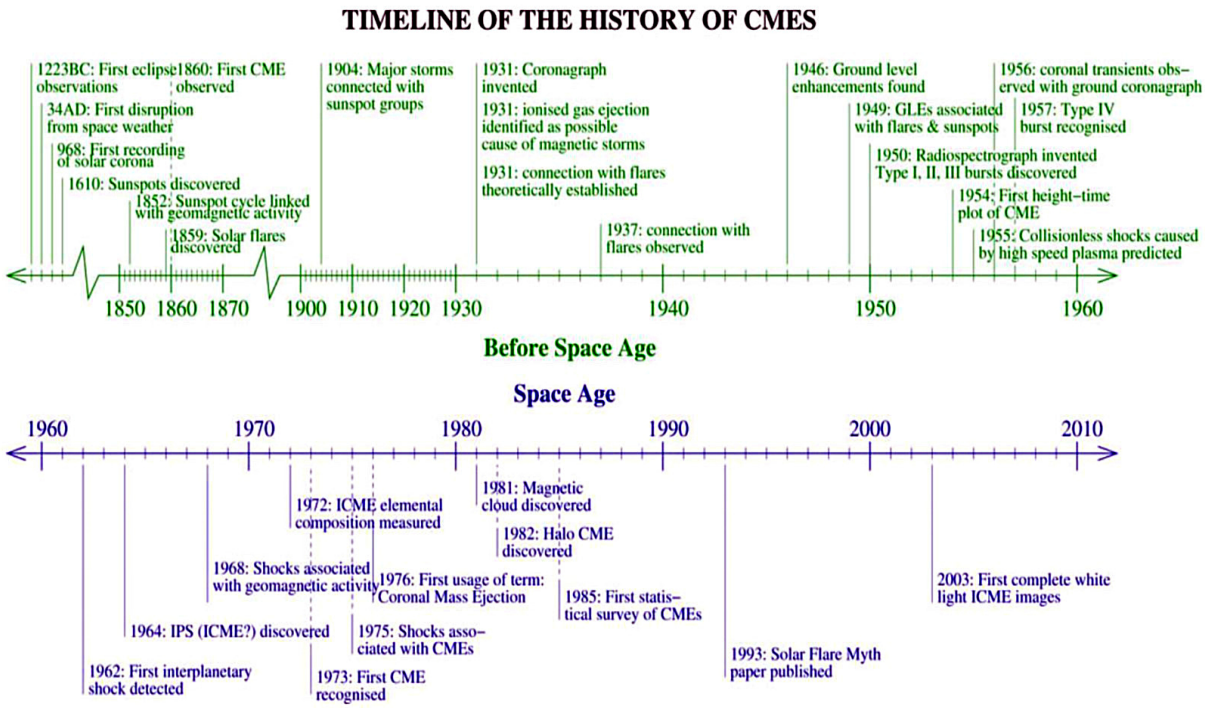


Figure 1.10: Timeline of the history of significant events related to CMEs before (green) and during (blue) the space age. *Image credit:* Howard (2011)

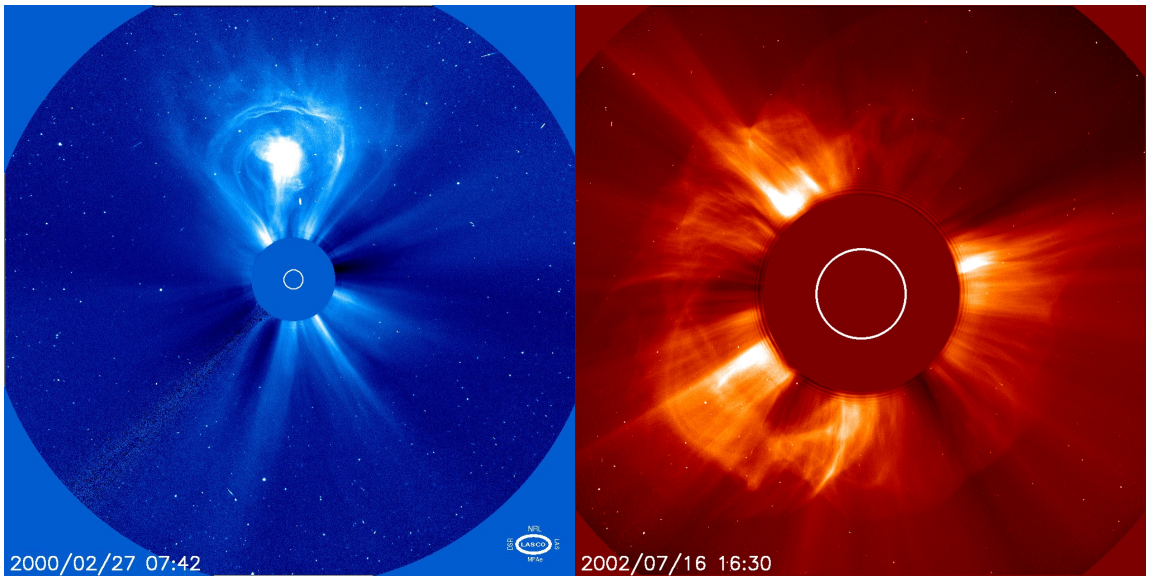
WIND and *ACE* spacecrafts have sophisticated instrumentation for continuous monitoring of solar, interplanetary and magnetospheric activity.

1.2.3 Properties of CMEs

1. **Morphology**

   Images from coronagraph observations have shown that CMEs come in a variety of shapes and sizes. However, the classical morphology is the "three-part" CME structure - a bright central core, followed by a dark cavity enveloped by a frontal loop (*e.g.* Low, 1996; Hundhausen, 1999; Cremades and Bothmer, 2004) (Figure 1.11 a). This is usually interpreted as compressed plasma ahead of a flux rope followed by a cavity surrounded by a bright filament/prominence. It needs to be pointed out that not all CMEs have the classic three-part structure; many CMEs can have complex or distorted geometries. The line of sight along which CMEs are viewed plays a major role in determining the observed CME geometry.

2. **Size and Location**



(a) CME morphology (b) Halo CME

Figure 1.11: Panel (a) shows a CME on February 27, 2012 imaged by LASCO C2 coronagraph showing the three-part morphology-bright frontal loop, dark cavity and a central core. Panel (b) shows a Halo CME on July 16, 2002 observed by the SOHO/LASCO C2 coronagraph. *Image credit: https://stereo-ssc.nascom.nasa.gov/.*

CMEs can appear as narrow jets, as well as wide eruptions. Owing to the viewing perspective in the plane of the sky, SOHO LASCO categorizes CMEs with angular widths ≈360° as " Halo " CMEs and widths $> 120°$ as "Partial Halos" (Yashiro et al., 2004). Halo CMEs can in fact also be CMEs with only tens of degrees of angular width propagating along the Sun-Earth line either towards or away from the Earth. These CMEs usually span the entire occulting disks as they expand (Chen, 2011) (Figure 1.11 b). During the solar minimum, CMEs typically erupt from regions near the solar equator while they occur over a wider range of latitudes near the solar maximum (St. Cyr et al., 2000).

3. **Occurrence rate**

   The number of CMEs erupting has a direct correlation with solar activity. There may be about 4-5 CME events per day during the solar maximum and ≈ 1 event in a day near the solar minimum (Yashiro et al., 2004). Figure 1.12 shows the variation in the daily occurrences of CMEs with the sunspot number from 1997 to 2017.

4. **Mass and Energy**

   LASCO observations have shown that the average mass and energy of CMEs is of the order of 10^{15} gms and 10^{30} ergs respectively. Vourlidas et al. (2010) suggest that CME masses may be underestimated by a

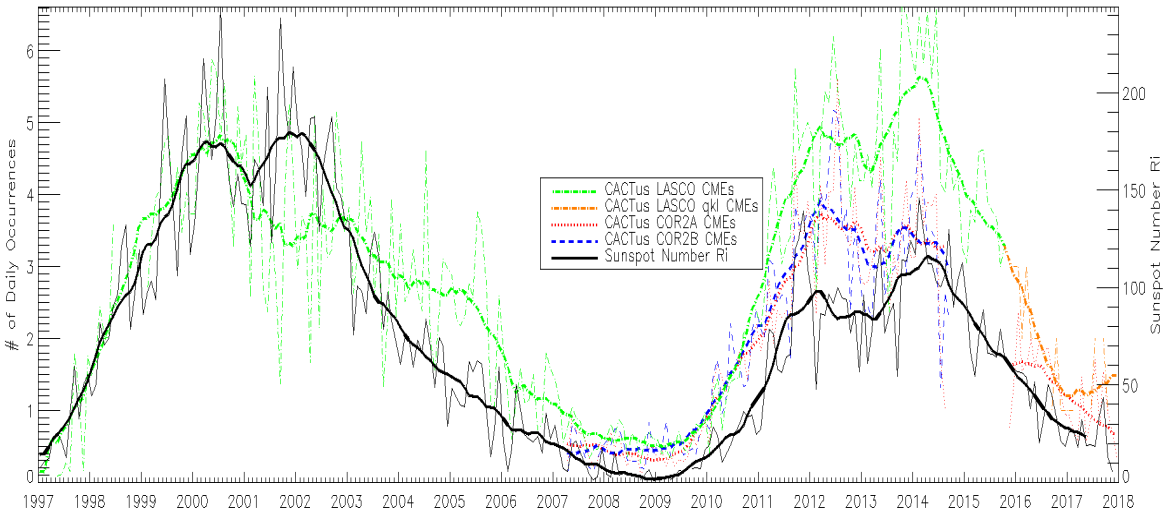


Figure 1.12: Overlap of number of daily occurrences of CMEs with the Sunspot number using the CACTUS catalog. *Image Courtesy: http://sidc.oma.be/cactus/.*

factor of two and CME kinetic energies by a factor of 8 due to effects of projection. They note that the CME mass increases as a function of height and saturates beyond 10 $R_\odot$.

5. **CME velocity**

   The radial propagation velocity of a CME is the speed of the frontal loop projected in the plane of the sky. It can vary from $\sim$ 20 km s^{-1} to $>$ 2500 km s^{-1} . However, efforts are made to correct for projection effects, so as to determine the actual CME speed.

1.2.4 CME onset, initiation and propagation

1. **CME onset**

   It is generally accepted that CMEs are initiated in the corona *i.e.* they are a coronal phenomenon and the energy required to launch these massive structures with speeds of hundreds of kilometers per second comes from this region. Since the corona has low plasma-β, gas pressure alone is not enough to drive these eruptions; CMEs are predominantly magnetically dominated and the energy required to accelerate them is provided by the coronal magnetic fields.

   For a CME to erupt from its state of equilibrium in the low corona, the onset mechanisms must include some instability which disturbs this equilibrium, leading to eruption of the magnetic structure. Due to lack of observational evidence for such mechanisms of CME onset and acceleration in the low corona, the solar physics community relies heavily

on physics-based theoretical models. Most of these initiation models assume that the currents that build up in the solar corona continuously evolve until they can no longer be stable and lead to an eruption. The stored magnetic free energy that drives CMEs can manifest in different forms, like an expanding massive CME (in most cases) as well as erupting filaments. The release of energy can also accelerate energetic particles and cause electromagnetic radiation emission in the form of a flare. Multi-wavelength observations of these phenomenon associated with CMEs in the early stages of their eruption provide clues for understanding the eruption processes (*e.g.* Chen, 2011). These include, flares, prominences, coronal dimming, coronal and shock waves (Webb and Howard, 2012).

2. **Initiation models**

   Mechanisms that facilitate CME initiation may be broadly divided into two classes: those that rely on magnetic reconnection and those that do not require reconnection. Magnetic reconnection can be broadly described as the restructuring of magnetic field lines to release the magnetic stresses that build up due to emerging flux and differential rotation (Aschwanden, 2005).

   To account for the amount of energy required over a short period of time, models like the tether-cutting (Figure 1.13) or flux cancellation mechanism (Sturrock, 1989; Moore et al., 2001) and magnetic breakout model (Antiochos et al., 1999; Lynch et al., 2008) (Figure 1.14) have been invoked. In the tether-cutting model, the overlying field does not reconnect; it only expands and reconnection occurs beneath the overlying field. In the breakout model, the flux or field lines that reconnect are a part of the central flux and the overlying magnetic field.

   Models that do not appeal to magnetic reconnection include flux injection (Chen, 1996), kink instability (Török and Kliem, 2003) and torus instability (Kliem and Török, 2006). Based on the toroidal forces experienced by a curved current-carrying loop, Chen (1989) derived the $J \times B$ Lorentz force acting on a section of a torus. They assume that a flux-rope CME initially at equilibrium, erupts as a result of poloidal flux being injected into it. Figure 1.15 shows the conditions for the flux-injection model where the 'p' and 't' indicate the poloidal and toroidal components respectively. These $J \times B$ forces drive the CMEs in the major radial direction (Chen, 1989, 1996). Forces acting on a CME due to the toroidal field and the average thermal pressure increase the CME radius, while the forces due to the ambient pressure and the poloidal field act in the opposing direction. Action of these competing forces causes the CMEs to radially expand as well. The pressure balance between the CME and the surrounding medium causes them CMEs to expand at a rate inversely proportional to the speed of the solar wind

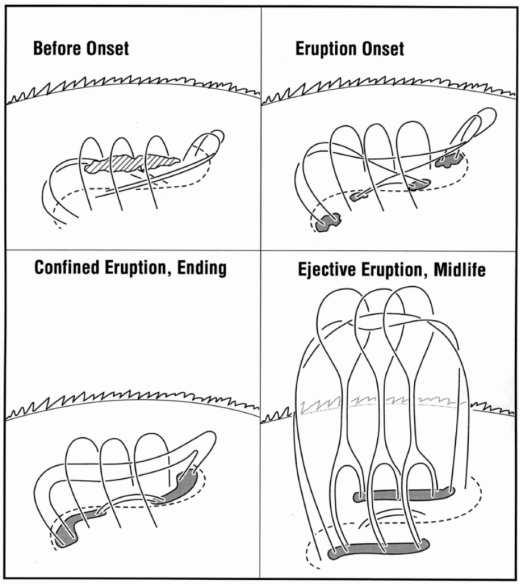


Figure 1.13: Tether-cutting mechanism adapted from Moore et al. (2001). The overlying field restrains the sheared core field followed by reconnection which triggers the rise of the core stretching the overlying field.

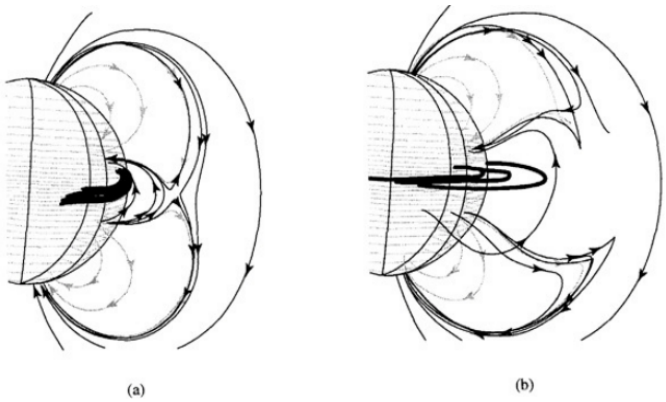


Figure 1.14: Breakout model with reconnection above the central flux system. Thick lines indicate the core field that evolve resulting in final eruption. Adapted from Antiochos et al. (1999).

(Wang and Sheeley, 1990). This is termed super-radial expansion.

The kink instability model considers continuous shearing of the footpoints of the magnetic flux ropes creating twists, which creates an instability leading to an eruption that releases the tension (Hood and Priest, 1981). Kliem and Török (2006) describe the torus instability model for CME eruption by considering the expansion of a current carrying ring held down by an external overlying field. The ring is unstable to expansion if the external field decays sufficiently fast.

3. **Propagation models**

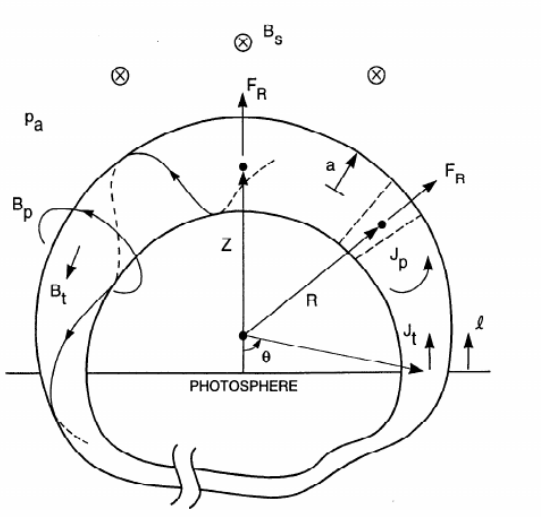


Figure 1.15: Conditions for the flux injection model Chen (1989, 1996). F_R is the Lorentz force in the radial direction, J and B indicate current density and magnetic field respectively. Subscript p corresponds to poloidal and t corresponds to toroidal components.

CMEs are generally thought to accelerate rapidly in the low corona following which they propagate into the interplanetary medium. Figure 1.16 shows the speed-time profile of an event on June 11, 1998 along with the soft X-ray flux profile of an associated flare. Three phases of CME acceleration and flare intensity evolution are demarcated in the Figure (Zhang et al., 2001). The evolution of CMEs can be attributed to aerodynamic drag and shocks. Interaction of CMEs with the ambient solar wind results in an aerodynamic drag force which can be either accelerating or decelerating. The solar wind is a continuous flow of streaming particles from the Sun into the heliosphere. As the solar wind expands through the interplanetary medium, it drags the solar magnetic field with it which corotates with the Sun (Parker, 1965). This ambient medium formed by the solar wind interacts via momentum coupling with the propagating CMEs, causing fast CMEs to slow down and slower ones to speed up. This represents an attempt to equilibrate the CME speeds with the speed of the solar wind. The solar wind drag-force model based on this principle has had considerable success in describing the observed propagation of CMEs (*e.g.* Cargill, 2004; Vršnak et al., 2010; Subramanian et al., 2012; Sachdeva et al., 2015).

The shock-based models regard ICMEs as a shock wave moving through the ambient solar wind *i.e.* the ICME is considered as a perturbation in the surrounding medium. Some of the models describing this approach are outlined in Dryer and Smart (1984) and Smith and Dryer (1990). Some models like ENLIL (Odstrčil and Pizzo, 1999) treat the CME as a separate ejecta that propagates in the background solar wind. CMEs

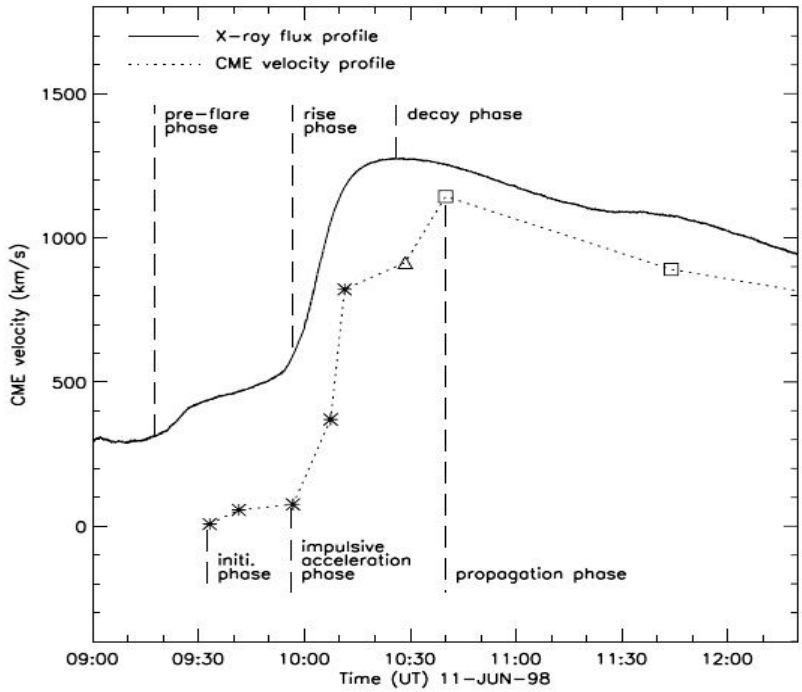


Figure 1.16: Speed-time profile of a CME on June 11, 1998 along with the soft-X ray flux profile of an associated flare. Three phases of CME acceleration and flare intensity evolution are demarcated in the figure. *Image adapted from Zhang et al. (2001).*

are considered to be dense structures with no intrinsic magnetic field in this model. These propagation models are used to effectively and accurately predict the observed CME dynamics and their arrival time and speed at the Earth.

The following section describes the cause-effect relationship in terms of how CMEs and other solar phenomena affect space weather.

1.3 Sun-Earth connection - Space Weather

Many phenomena related to the Sun can directly and/or indirectly influence space-borne technology and the near-Earth space environment. The first observations of Sun-Earth connection were made by Edmund Halley in 1716. He suggested that particles moving along the Earth's magnetic field lines caused auroras (Figure 1.17). By the mid-nineteenth century, geomagnetic disturbances were connected to solar processes and long term observations showed that their occurrences were correlated with the 11-year variability of the solar cycle.

Space weather refers to conditions on the Sun and the solar wind, magnetosphere, ionosphere and thermosphere that can influence the performance and reliability of space-borne and ground-based technological systems and can affect human life and health (definition by U.S. National Space Weather Plan). The affects of solar activity include (but are not limited to) disruption in satellite operations, communications, navigation, radiation hazards to astronauts and airline passengers, failure of power supply grids, leading to societal as well as economic losses. Figure 1.18 shows the various ways in which solar activity affects the Earth.

The main forms of solar energy output that determine the conditions for space weather include - fast and slow solar wind streams, co-rotating interaction regions (CIRs), flares, coronal mass ejections and their interplanetary counterparts and solar energetic particles. Solar phenomena leading to large perturbations in the coupled magnetosphere-ionosphere system of the Earth are called geoeffective (Pulkkinen, 2007). Flares release flashes of photons that can heat up the terrestrial atmosphere causing satellites to drop to lower orbits. During major solar storms, particles are accelerated to near-relativistic energies, endangering astronauts traveling through the interplanetary space. Coronal mass ejections drive shocks and solar energetic particles causing geomagnetic storms.



Figure 1.17: Aurora visible in Alaska, USA during October 16-17, 2003 as a result of the famous Halloween solar storm. *Image courtesy-Ulrike Haug.*

Owing to their tremendous impacts, forecasting space weather effects is a major challenge. The accuracy of prediction of CME arrival and its impact on the Earth's magnetosphere is still quite poor, although much effort has

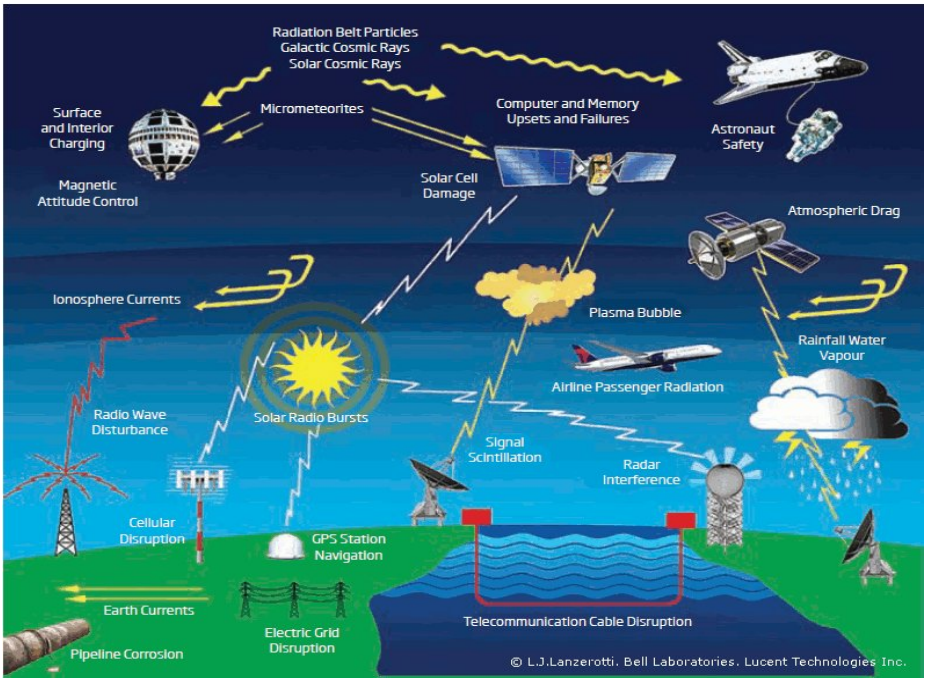


Figure 1.18: This image shows the various ways in which solar disturbances and associated phenomena affect the technology and life on Earth. *Image courtesy-Bell Laboratories.*

been made to understand the underlying physics in order to develop better warning tools. Space weather storms can be divided into three classes based on their size (Bothmer and Daglis, 2007):
1) M-region storms- comprising of fast solar wind stream and CIRs,
2) CMEs - smaller in size but greater in intensity, and
3) Auroral electrojets - smallest in size, greatest in intensity, creating rapid fluctuations of magnetic fields at the ground level.

1.3.1 Solar wind and space weather

Besides electromagnetic radiation, the Sun emits a flow of charged particles and embedded magnetic fields from the solar corona into the interplanetary space. This continuous stream of plasma is called the solar wind, which travels with speeds of a few hundred km s^{-1}. This supersonic solar wind impinges on the Earth's magnetosphere inducing currents and creating fluctuations in the Earth's magnetic fields. Magnetic reconnection between the northward pointing magnetospheric fields and the southward or B_z component of the interplanetary magnetic field (IMF) carried by the solar wind allows the charged particles to enter the magnetosphere (Schwenn, 2006). As the solar wind flow is diverted around the Earth's magnetosphere, the dynamic pressure of the solar wind and the IMF compresses the Earth's

magnetic fields on the Sun-facing side and stretches the fields to extend as far out as the night side (Figure 1.19). The solar wind interacts with the

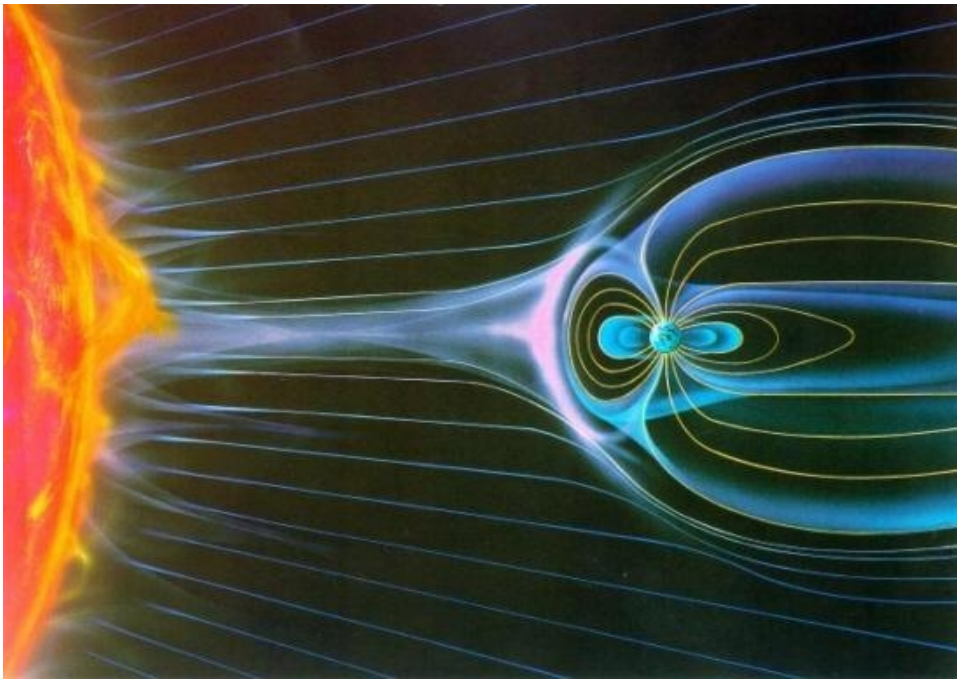


Figure 1.19: Artist impression of the impact of solar wind on the Earth's magnetosphere. Solar wind compresses the day side and stretches the magnetic fields on the night side of the Earth. *Image courtesy - NASA.*

terrestrial magnetic field by forming a standing bow shock that slows, deflects and heats the plasma. The Earth's magnetosphere acts both as a shield against the solar wind and as a net that gathers solar wind momentum flux and stirs the magnetospheric plasma. Electromagnetic radiation from the Sun that reaches the Earth much faster than the solar wind flow also affects the Earth's environment. It increases solar irradiance which causes heating of the upper atmosphere, affecting the drag experienced by low-Earth-orbiting satellites. In the outer magnetosphere, solar energetic particles pose a danger for the satellite systems and instrumentation (Baker, 2000).

1.3.2 Coronal mass ejections and space weather

Coronal mass ejections (CMEs) rapidly develop into large-scale structures expanding to sizes greater than that of the Sun itself. When Earth-directed, these eruptions of plasma and magnetic fields can cause intense geomagnetic storms. Fast CMEs can drive interplanetary shocks that interact with the Earth's bow-shock, transferring energy to the magnetosphere and compressing the dayside magnetopause. These compression effects travel towards the

tailward side at the solar wind speed, causing strong auroral activity observable almost instantaneously all around the auroral oval (Zhou and Tsurutani, 2001). CMEs can also accelerate solar energetic particles (SEPs) that can penetrate the skins of space-borne probes and damage technical systems. The SEP fluxes from flares and CMEs can increase radiation levels endangering the lives of astronauts as well as enhance ionization and excitations in the Earth's middle atmospheric polar caps causing ozone depletion (Jackman et al., 2005).

One of the most famous examples of a geo-effective solar event is the Halloween storm of 2003 during solar cycle 23. A series of solar flares and CMEs between mid-October to early November 2003 hit the Earth's magnetosphere affecting the satellite systems, causing power outages in Sweden and auroras as far south as Texas. There was a temporary failure of the SOHO satellite and damages caused to the *Advanced Composition Explorer* (ACE) spacecraft as well.

1.3.3 Space weather forecasting

The damaging effects of solar phenomena necessitates an accurate warning and predictive tool to determine the space weather affects, prevent disruptions in technical systems and ensure the safety of airlines and astronauts. Space weather research needs studies to quantitatively predict the magnetospheric and ionospheric conditions based on measurements of the solar wind and interplanetary magnetic field. The aim is to understand the physics of solar processes so that primary predictions can be made using early solar observations (*e.g.* Chen, 2011; Manchester et al., 2017). Advances in observational capacity of heliospheric missions as well as scientific efforts in developing both theoretical and numerical models are bringing us closer to building a dependable framework for forecasting the arrival and affects of solar transients on the Earth.

1.4 Motivation and Thesis organization

Based on the discussions in the previous sections highlighting the importance of space weather affects and their prediction, it is crucial to develop a thorough understanding of the evolution and propagation dynamics of CMEs. Since CMEs are major drives of the near-Earth space weather, physics behind their dynamics is important for improved advance warning tools which are vital in this era of technological dependence. With this goal, we select a set of well-observed CMEs using STEREO and SOHO coronagraph observations and derive physical parameters for each event (Chapter 2). We

investigate the forces that affect CME propagation using physics-based models for Lorentz force and solar wind aerodynamic drag force (Chapter 3). We quantify the heliocentric distances at which each of these forces dominate the CME dynamics and how they compare with each other in magnitude (Chapter 4).

Below is a brief summary of all the chapters:

1. **Chapter 2 : CME Selection and Geometrical fitting**
   This chapter describes the data sample used for this study. Observations from SOHO and STEREO missions in the rising phase of solar cycle 24 (2010 onwards) are used to identify CMEs based on detailed selection criteria outlined in this chapter. A geometrical fitting technique (Graduated Cylindrical Shell model) is used to fit the selected CMEs to derive physical parameters (positional and structural). We provide details of the fitting technique and the CME sample of 38 events selected for this work along with their GCS parameters.

2. **Chapter 3 : CME dynamics and propagation**
   This chapter discusses the forces that affect CME dynamics as they erupt from the solar corona and propagate into the interplanetary space. We focus on Lorentz forces that drive CMEs and aerodynamic drag due to the ambient solar wind. Various approaches to these forces along with the specific models that we use in this study are described in this chapter in the form of a force equation. Details of the models for individual forces (Lorentz force and solar wind drag), parameters involved in the force prescription and their calculations using observational data derived by GCS fitting are also described. It outlines the analysis method for the two forces which is applied on all the CMEs in our sample to estimate the height beyond which aerodynamic drag force begins to dominate CME propagation, to determine the Lorentz force profile and compare the magnitude of the two forces at different heliocentric distances.

3. **Chapter 4 : Results and Discussions**
   This chapter describes in detail the results of the force analysis for all the CMEs in the sample. Using the solar wind drag analysis, we determine the range of heights beyond which the aerodynamic force becomes dominant for both slow and fast CMEs. The Lorentz force profiles for all the events are shown in this chapter and compared to the solar wind drag force magnitude. Results for all events are tabulated and discussed in detail in this chapter.

4. **Chapter 5 : Future Work**
   Based on our findings described in the previous chapter, suggestions

for future analysis that can be done using a larger data set are listed in this Chapter.

5. **Chapter 6 : Appendix**
   The Appendix describes some supplementary material including models for virtual mass calculation and a simplified version for the Lorentz force model used for calculations. We also show a comparative treatment and equivalence of two different models for Lorentz forces: the one used in this work (torus instability model) and another based on poloidal flux injection. This chapter also shows the remote sensing data and the GCS fitting at a single time stamp for all CMEs.

Chapter 2

CME Selection and Geometrical fitting

Using LASCO and STEREO coronagraph data, we identify 38 CMEs based on criteria described in this chapter. The white-light coronagraph images of these CMEs are fitted using a geometrical flux-rope model. The Graduated Cylindrical Shell (GCS) model is used to reconstruct the 3D geometry of each CME to obtain their physical parameters. We describe the detailed criteria for selecting the CME events, the geometrical fitting procedure and list the observed parameters for each CME.

2.1 Introduction

With the launch of the *Solar and Heliospheric Observatory* (SOHO; Domingo et al., 1995) in 1996 and the *Solar Terrestrial Relations Observatory* (STEREO; Kaiser et al., 2008) in 2006, it has been possible to observe the solar atmosphere and the Sun – Earth system continuously. Data compiled from these missions has been used to analyze the dynamics of solar coronal mass ejections (CMEs) in this study during the rising phase of solar cycle 24 (which began in 2008). The copious amount of data from these instruments requires a systematic and efficient procedure for shortlisting events for useful and conclusive analysis. Data for the selected CMEs are acquired from Instrument Resource data archives available online for both LASCO and STEREO. In order to observe the complete CME trajectory, we also include in our study the near-Earth *in-situ* observations from the *WIND* spacecraft. Changes in observed magnetic and plasma parameters provide indications of CME arrival at the Earth (Burlaga et al., 1981). We use the SOHO LASCO and

STEREO coronagraphs and arrival signatures from *WIND* to trace the CME propagation from the Sun to the Earth. A three-dimensional geometrical fitting technique is then used to reconstruct the observed CME structures based on the flux-rope geometry. We use the Graduated Cylindrical Shell (GCS) model for this purpose. In this chapter, we first describe the aforementioned instruments used for CME observations (section 2.2) followed by a detailed account of the shortlisting criteria for event selection (section 2.3) and the description of GCS fitting technique used for these selected CMEs (section 2.4).

2.2 Instruments and Observations

The SOHO mission carries the *Large Angle and Spectrometric Coronagraph* (LASCO; Brueckner et al., 1995) originally consisting of three solar coronagraphs which observe the solar corona from L1 Lagrangian point. After 1998 however, only two remain in working condition: the C2 and C3 coronagraphs with field of view (FOV) $1.5-6$ $R_\odot$ and $3.7-32$ $R_\odot$ respectively. LASCO was launched to investigate the outer layer of the Sun and the solar atmosphere. A solar coronagraph, as the name suggests, looks at the solar corona by creating an artificial eclipse. In other words, it uses an occulting disk to cover the Sun, thereby blocking the light from the photosphere so as to image the Thomson-scattered white light from the corona. The *SOHO LASCO CME CATALOG*[1] lists details of all the CMEs recorded by LASCO coronagraphs. It includes the Central Position Angle (CPA) and the sky-plane width of the CMEs based on which they are categorized into Halo (H) or Partial Halo (PH) CMEs. It also provides the first approximations of their speeds, acceleration and mass. Information from this catalog is the first step in selecting the CMEs for this study.

The *Sun–Earth Connection Coronal and Heliospheric Investigation* (SECCHI; Howard et al., 2008) instrument onboard the STEREO mission constitutes a set of five telescopes that observe the solar atmosphere and inner heliosphere. In October 2006, two STEREO spacecrafts were launched together into the heliocentric orbit. The STEREO Ahead (STA) and STEREO Behind (STB) drift away from the Earth at a rate of 22.5° per year. STA travels slightly faster than the Earth around the Sun while STB is slower. SECCHI includes- an Extreme UltraViolet Imager (EUVI), two white light coronagraphs (COR1 and COR2) and two Heliospheric Imagers (HI1 and HI2). Taken together they study the evolution of CMEs from the corona, thorough the interplanetary (IP) medium, up to and beyond the Earth. COR1 has a FOV of $1.4-4$ $R_\odot$ and COR2's FOV is $2-15$ $R_\odot$. HI observes the helio-

[1] http://cdaw.gsfc.nasa.gov/CME_list/

sphere from 12 – 318 $R_\odot$. STEREO's online resource[2] provides images of the evolving CME, showing the deflection as well as expansion of the CME as it propagates through the interplanetary medium from two different viewpoints (A and B).

A combination of data from all these instruments, namely : LASCO C2, COR2 A/B and HI1 has been used in our work to provide a continuous, three-perspective observation of coronal mass ejections originating in the solar corona and traveling towards the Earth ($\sim$ 215 $R_\odot$). In addition, we also include the *in-situ* observations from the *WIND*[3] spacecraft. Launched in 1994, *WIND* orbits the Sun at L1 Lagrangian point with the primary objective of collecting data for magnetospheric and ionospheric studies along with plasma processes in the near-Earth solar wind. The *Solar Wind Experiment* (SWE) aboard *WIND* includes sensors for recording the density, velocity and temperature of the ions in the solar wind. We use minute-averaged data for the solar wind flow speed and proton density about a day in advance of the CME arrival at the Earth to determine the conditions in the heliospheric plasma into which the CME propagates. Using the arrival signatures, HI1, COR2 and LASCO observations (in that order) the CMEs can be backtracked from the Earth to the Sun.

We however, begin with the CME identification in LASCO and COR2, continuing into the HI1 followed by identifying CME arrival using the ICME signatures in *WIND*. As an example, we show the white-light observation images for a CME on September 28, 2012 at 00:39 in all the three instruments in Figure 2.1. Panel (a) shows a Halo CME in LASCO C2 FOV. Panel (b) indicates the position of the STEREO spacecraft with respect to the Earth at 00:39 on the date of the event. Panel (c) shows a limb CME on the left side of the occulted Sun as observed from COR2 A, while Panel (d) shows the same event on the right side as seen from COR2 B.

For the three-dimensional (3D) reconstruction, we use the LASCO and STEREO A and B viewpoints. The geometry of CMEs as seen from STEREO A and B instruments are similar, therefore to accurately fit the GCS model, it is important to include LASCO observations. The LASCO view point gives crucial information about the orientation and dimensions of the CME, which are ambiguous if only SECHHI data is used. In general, the GCS fitting can be subjective leading to multiple parameter combinations that fit the observations, however, this degeneracy is broken by using the LASCO images which constrain the positional CME parameters (particularly the tilt angle). Extreme ultraviolet images (EUVI) have not been used in this procedure, because the use of LASCO images in conjunction with the STEREO data provides a good optimization of the CME parameters. Beyond the LASCO

[2]https://secchi.nrl.navy.mil/
[3]http://omniweb.gsfc.nasa.gov/

field of view, the tilt, longitude and latitude are taken to be constant, unless a change is clearly visible in the CME rotation. The EIT images are not always reliable in indicating the correct position of leading edge if the LASCO viewpoint is not used.

2.3 Selection Criteria

We analyze CMEs observed between 2010 and 2013. The criteria for selecting these events are described below.

1. **CME identification in SOHO LASCO CME CATALOG**
   As a first step, we use the comprehensive SOHO LASCO CME CATALOG to identify Halo (H) or Partial Halo (PH) CMEs. Partial halo CMEs have an angular width $> 120°$ while halo CMEs have an apparent angular span of $\approx 360°$. Studies show that in general halo or partial halo CMEs have a component that is Earth-directed (Zhao, 2004). In particular, halo-type CMEs are expected to be Earth-directed because they cover the disk center of the Sun which is also the Earth's projection on the Sun's disk. For each H/PH event identified in the catalog there exists a corresponding movie made from the compilation of LASCO C2 images for the event. We choose CMEs that are visible clearly in each image in the LASCO FOV and do not spill outside the image frame. We also include a pre-event image in the data. A pre-event image is taken right before the CME appears in the LASCO FOV (*i.e.* no CME is visible) and is used as the background image.

2. **CME identification in COR2**
   The LASCO listed CME event is then identified in the STEREO observations. We select only those events from C2 observations which are completely visible in both STEREO A (STA) and STEREO B (STB) simultaneously. Starting with the same initial time as in C2, the CME is tracked in both the COR2 instruments till it exits their FOV (~ 15 $R_\odot$). The STEREO orbit Tool[4] indicates the positions of both STA and STB at any time. Using the tool to identify the COR2 A/B positions and the direction in which the CME evolves, it can be determined if the CME is Earth-directed. For example, the event on September 28, 2012 (Figure 2.1) appears as a Halo CME in the LASCO catalog. This CME is visible as a limb CME in COR2. It appears on the left limb of the Sun when viewed from STA and on the right side when seen from STB, when the two spacecrafts were separated by 116°.

[4]https://stereo-ssc.nascom.nasa.gov/where.shtml

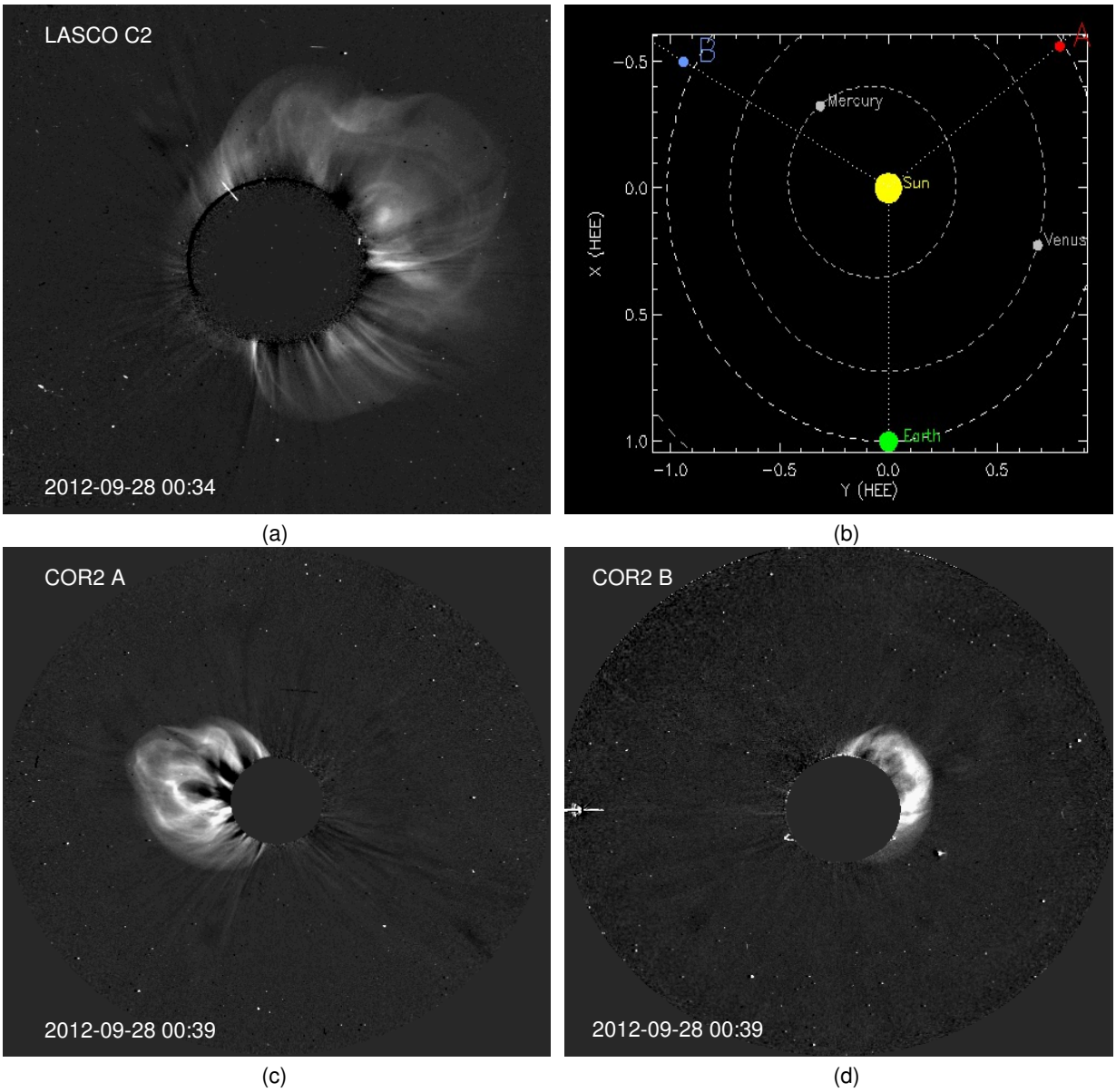


Figure 2.1: White-light images of a CME on September 28, 2012 in LASCO C2 (Panel a), COR2 A (Panel c) & COR2 B (Panel d) coronagraphs. Positions of the two STEREO spacecrafts during this event is shown in Panel b.

3. **Continuity in CME data**
   Only CMEs with continuous availability of images in both the coronagraphs were included in the sample *i.e.* we require that there are no gaps in the data. It is required for the expanding CME structure to stay within the image frame for all the instruments.

4. **Exclusion of events**
   CMEs with visible distortions and diffuse structures were excluded because these are difficult to fit into geometrical models and cannot be reconstructed properly. During phases of extreme activity of the Sun, we also find multiple events from the same or close by active regions (AR) which leads to a faster CME overtaking a preceding slower one, or a fast CME altering the environment into which the following slower CME travels. Therefore, we exclude events with CME-CME interactions because we are not equipped to handle the CME collision dynamics as of now.

5. **CME identification in HI**
   Once a CME is identified in both LASCO C2 and COR2 instruments, we track the event in the HI1 FOV. Using SECCHI movie tools, a CME can be seen in HI1 (up to ~ 80 $R_\odot$) after it leaves the COR2 FOV. In most cases, the images are diffuse and therefore one needs to be careful while tracking a CME in HI1.

6. **CME arrival signatures**
   To establish the complete Sun-Earth timeline of the CME, we investigate the ICME/shock arrival data from the *WIND* spacecraft for each CME. ICME signatures in *WIND* data include depressed plasma proton temperature, low plasma-β and strong, smoothly rotating magnetic field (Burlaga et al., 1981; Klein and Burlaga, 1982).

Using the above mentioned criteria we shortlist 38 Earth-directed CMEs. We also referred to various compiled lists of CMEs e.g. WIND ICME list[5], AFFECTS database[6], List of ICMEs by Richardson and Cane[7] and JHUAPL COR-CME Catalog (Vourlidas et al., 2017) to cross-reference the selected CMEs. We also referred to the Heliophysics Event Catalog[8] for information about source region (SR) positions and associated flare activity. The downloaded images for all events are prepared using the standard SolarSoft *sechhi_prep.pro* procedure. These are then fitted using a geometrical model for all time-stamps from the first appearance of CME in LASCO C2 up to the HI1 FOV. This fitting technique is described in the next section 2.4.

[5]https://wind.nasa.gov/ICMEindex.php
[6]http://www.affects-fp7.eu/services/cme-databases/
[7]http://www.srl.caltech.edu/ACE/ASC/DATA/level3/icmetable2.htm
[8]http://hec.helio-vo.eu/hec/

Table 2.1 lists details of all the CMEs studied in this work. The serial number (column 1) of each event is used throughout as a reference for the corresponding CME. Columns 2 and 3 indicate the date of the event and the time when it is first fit in C2 FOV using GCS fitting technique respectively. FR (Flux-rope) indicates if a three-part flux-rope structure was visible in the COR2 observations of the CME. We also indicate if the observed CME was a Halo (H) or a Partial Halo (PH) CME.

2.4 Fitting Technique

Coronal mass ejections are observed by white-light imaging of the solar corona, i.e. the coronagraphs measure the light from the photosphere which is Thomson scattered by free electrons in the coronal plasma (Billings, 1966) along the light of sight. Coronagraphs yield two-dimensional white-light images in the plane of the sky. It is therefore, difficult to obtain a true three-dimensional geometrical reconstruction of CMEs, the understanding of which is an important tool in developing a physical model for CME propagation.
A coronal mass ejection typically has a three-part structure- a bright front, followed by a dark cavity and a bright core (Illing and Hundhausen, 1985). LASCO observations have revealed detailed structure in the form of circular striations around the cavity. This gave rise to the widespread acceptance of CMEs as flux-rope like structures (Thernisien et al., 2006). Various geometrical models are used for fitting and characterizing the CME structure, *e.g.*, the Cone model (Howard et al., 1982), the Elliptical Model (Kahler and Webb, 2007), the Graduated Cylindrical Shell (GCS) model (Thernisien et al., 2006, 2009). With many theoretical models fitting the idealized flux-ropes and successfully reproducing the observations (*e.g.,* Chen et al., 1997), the term "flux-rope CME" has gradually substituted the "three-part CME". CME properties are also shown to be consistent with these theorized flux-ropes (Vourlidas et al., 2000; Krall et al., 2005). In this study, we use one such theoretical model called the Graduated Cylindrical Shell (GCS) model (Thernisien et al., 2009; Thernisien, 2011) for the geometrical fitting of the white-light CME images.

2.4.1 Graduated Cylindrical Shell (GCS) Model

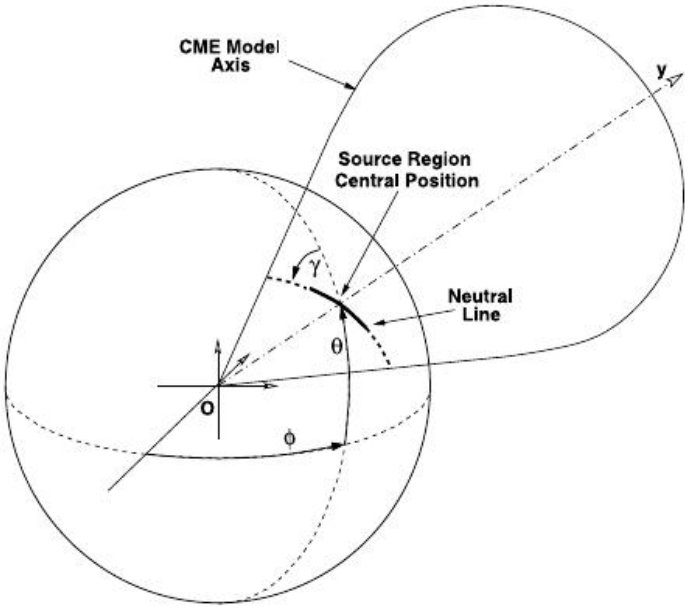
The Graduated Cylindrical Shell (GCS) model envisages a CME as two conical legs attached to the Sun with a tubular section in between, forming the main body of the CME (Thernisien et al., 2006, 2009). It fits a helical flux-rope like structure to the visible CME by varying a set of six parameters. Panel (a) of Figure 2.2 shows the location of the GCS model with respect

to the solar surface. Three parameters define the CME position: Carrington Longitude (ϕ), Latitude (θ) and Tilt angle (γ). These quantities represent the Euler angles that relate the Heliocentric Earth Ecliptic (HEE) co-ordinate system to the model axes. Panel (b) of Figure 2.2 shows the schematic of the GCS model in both face-on and edge on views. The structural parameters that define the 3D model are: Height of the leading edge (R), Aspect ratio (κ) and Half angle (α). The quantity R is measured from the center of the Sun while $\kappa = sin(\delta)$, where δ is the half angle of the cone. The half angle α is the angle between the axis of the leg and the y-axis. Using R, κ & α, all physical parameters that represent the CME structure can be derived using the detailed geometrical description in Thernisien (2011). Each image containing the CME structure is fitted using these six parameters. For a 3D geometrical reconstruction of the flux-rope structure, CME images from LASCO C2, COR2 A & B are fitted simultaneously. These parameters are varied to obtain the best fit to the evolving CME. The graphic user interface (GUI) using the SSWIDL *scraytrace* routine provides an interactive way of varying the GCS parameters and displays these changes simultaneously in the wire-frame which is overlaid on top of the images in each instrument frame. An example of the fitting technique is shown in Figure 2.3. It shows the GUI wherein the GCS parameters can be varied to get the optimal fitting of the yellow wire-mesh like flux-rope structure to overlap the visible CME in the images. It is important to not lose sight of the basic structure of the CME while fitting it at each time-stamp. Therefore, it is recommended to focus on a strikingly visible feature in the CME image and use the parameter variation to fit it in all images. In particular, we try to fit the leading edge of the CME with the outer front of the wire-mesh structure. In most cases, depending on how the CME deflects the longitude and latitude vary accordingly. Since our CMEs are Earth-directed, we use the longitudinal position of the Earth (Carrington Longitude) as a first estimate of the CME longitude. If there is not much deflection, these estimates provide a good approximation. We also consider the location of the associated flare (if any) ($http://hec.helio-vo.eu/hec/hec_gui.php$) and/or the position of the source region of the CME ($https://www.solarmonitor.org$). The actual position can still be different from these values, however, they give a good initial approximation for the longitude and latitude. We first vary the longitude ϕ, latitude θ and the height of the leading edge (R) to fit the CME front so that the outer edge of the wire-frame matches with the CME leading edge in all three instrument frames simultaneously. The tilt angle (γ) is also adjusted according to the visible CME structure. Since the CME expands as it propagates, the spatial extent is covered by varying the aspect ratio (κ) parameter and the angular width is adjusted by changing the half angle (α). All the variations in parameters should be such that the wire-frame overlaps the CME structure in all three instrument images simultaneously. With an optimized set of these six parameters we get a well-fitting match with the observed CME. This procedure is repeated for all images sequentially and the

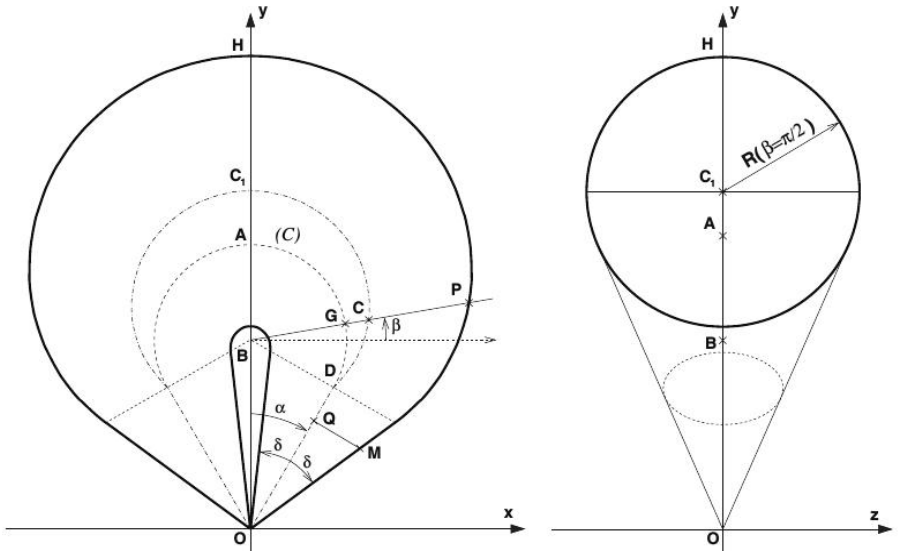
model is fit at all time-stamps. In cases where deflection is not so significant the positional parameters vary only slightly.

When the CME transitions from the COR2 to the HI1 FOV, it is important to maintain the chronological continuity. There should not be a large data gap (more than 1-2 hours) between the data from these two instruments. In HI1, the CME images appear somewhat diffuse; therefore, it is important to properly track the leading edge from COR2 to HI1. Since the CME structure is visibly less distinct, we keep the positional parameters constant unless a significant deflection is seen in the images and vary the other parameters accordingly. In HI1, images are fitted using the GCS procedure at successive time-stamps up to 80 $R_\odot$. Finally we get a 3D fit to all CME images beginning from LASCO C2, COR2 A & B, followed by HI1 at each time-stamp. This method is repeated carefully for all the CMEs in our sample set to get the 3D reconstructed CME evolution from $\approx$ 3 $R_\odot$ up to 80 $R_\odot$. With the observational parameters derived from the GCS fitting routine, other physical parameters can be estimated as well. Using the geometrical description in Thernisien (2011), we can calculate (at each time-stamp), the cross-sectional width of the CME and the circular cross-section radius (minor radius).

Once we have the complete height-time evolution of the CME (height of the leading edge), we make estimates of the initial velocity using a third degree polynomial. The GCS height-time profile is fit to determine the local velocity which is later fed into the force model to predict the complete CME trajectory. Details of the GCS parameters of each CME at the first observed time are given in Table 2.2. The serial number corresponds to event described in Table 2.1. The 8 events from Sachdeva et al. (2015) (marked with an asterisk $*$) have observations up to the HI2 FOV, while the remaining events have been fitted up to HI1 FOV. h_0 is the first observed height at which the GCS fit is done at the time indicated in Table 2.1. v_0 is the CME initial velocity at h_0. GCS parameters - Carrington Longitude ϕ, Latitude θ, Tilt angle γ, Aspect ratio κ and Half angle α are given at the first observed height h_0 for each CME. The height-time evolution data as well as other physical parameters for each reconstructed CME can now be used for analyzing the CME dynamics.

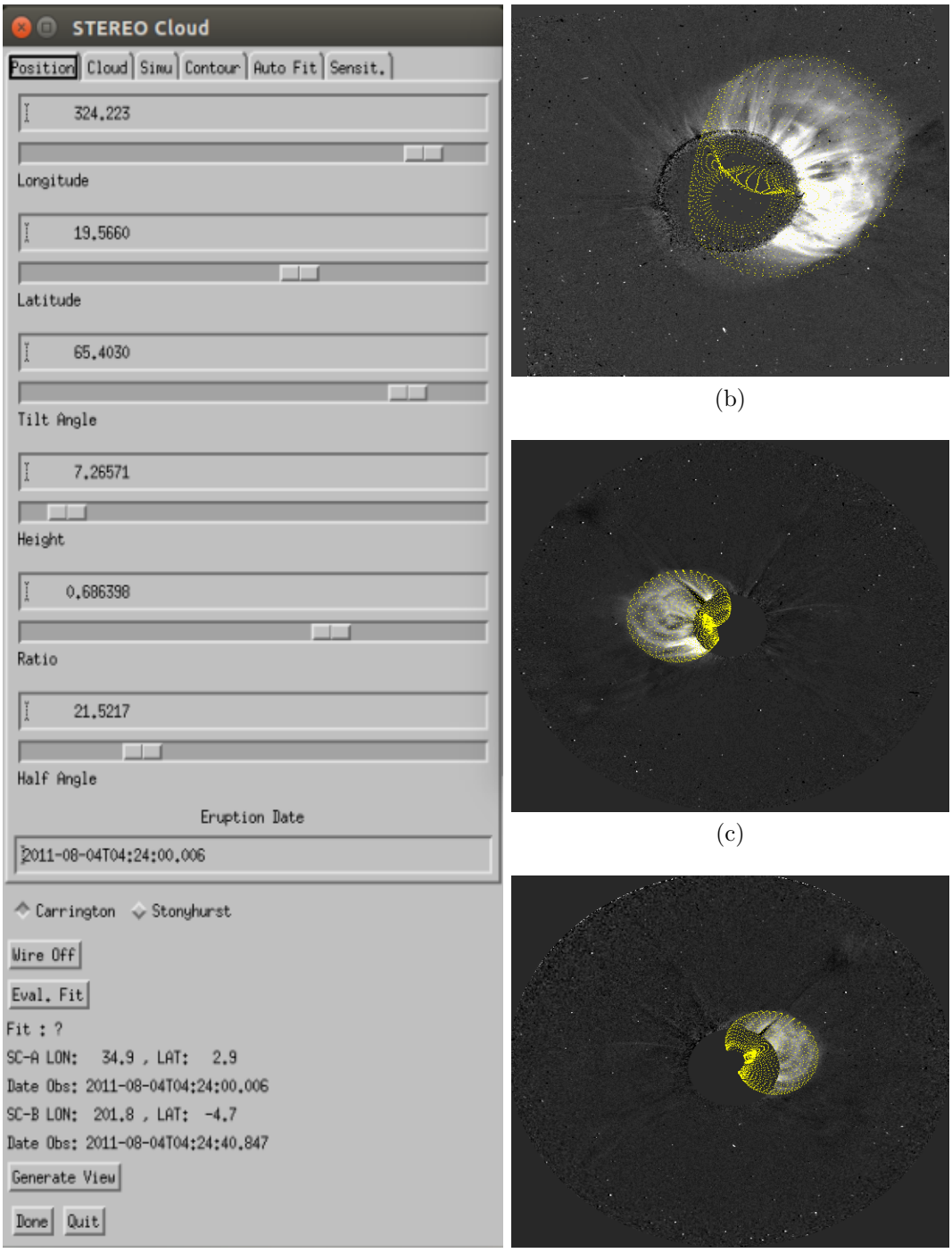


(a) Location of the GCS model in space



(b) GCS geometry face-on and edge on.

Figure 2.2: Geometrical representation of the GCS model adapted from Thernisien (2011)



(a) (b) (c) (d)

Figure 2.3: Panel a is the graphic user interface indicating six GCS parameters that can be varied as shown. Panels b, c and d show the corresponding fit of the wire-mesh (yellow) structure to the CMEs in C2, COR2 A and COR2 B images respectively for an event on August 4, 2011 at 4:24 UT.

Table 2.1: Details of observed characteristics of the CMEs in the sample set. First column is the serial number of each event with which it is referenced throughout the thesis. For each event the observation date (Date) and time when it is first fitted in C2 FOV is mentioned. FR indicates if a distinct flux-rope structure was observed in COR2 FOV. Cross (×) indicates that a FR structure was seen. H/PH indicate if it is a Halo or Partial Halo CME as seen in LASCO.

No.	Date	Time (U.T.)	FR	H/PH
1	2010 Mar. 19	11:39	×	H
2	2010 Apr. 03	10:24	×	H
3	2010 Apr. 08	03:24	–	PH
4	2010 Jun. 16	15:24	×	PH
5	2010 Sep. 11	02:24	×	PH
6	2010 Oct. 26	07:39	×	–
7	2010 Dec. 23	05:54	×	PH
8	2011 Jan. 24	03:54	–	–
9	2011 Feb. 15	02:24	–	H
10	2011 Mar. 03	05:54	×	PH
11	2011 Mar. 25	07:00	–	H
12	2011 Apr. 08	23:39	–	H
13	2011 Jun. 14	07:24	×	PH
14	2011 Jun. 21	03:54	×	H
15	2011 Jul. 09	00:54	×	PH
16	2011 Aug. 08	04:24	–	H
17	2011 Sep. 13	23:39	×	PH
18	2011 Oct. 22	10:54	–	H
19	2011 Oct. 26	12:39	–	PH
20	2011 Oct. 27	12:39	×	H
21	2012 Jan. 19	15:24	×	H
22	2012 Jan. 23	03:24	×	H
23	2012 Jan. 27	17:54	×	H
24	2012 Mar. 13	17:39	×	H
25	2012 Apr. 19	15:39	–	PH
26	2012 Jun. 14	14:24	×	H
27	2012 Jul. 12	16:54	×	H
28	2012 Sep. 28	00:24	×	H
29	2012 Oct. 05	03:39	×	PH
30	2012 Oct. 27	17:24	×	H
31	2012 Nov. 09	14:54	×	–
32	2012 Nov. 23	14:39	×	H
33	2013 Mar. 15	06:54	–	H
34	2013 Apr. 11	07:39	–	H
35	2013 Jun. 28	02:24	–	H
36	2013 Sep. 29	22:24	×	H
37	2013 Nov. 07	00:24	–	H
38	2013 Dec. 07	08:24	–	H

Table 2.2: CME no. indicates the serial number of the CME as referenced in Table 2.1. h_0 is the observed GCS height at the first observation and v_0 is the derived velocity at h_0. GCS parameters at h_0 are given by Carrington longitude (ϕ), heliographic latitude (θ), tilt (γ), aspect ratio (κ) and half angle (α). Fast CMEs are indicated by a superscript (f) in their serial number. Events from Sachdeva et al. (2015) are indicated by a superscript($*$) in their corresponding serial number.

			GCS Parameters at h_0				
No.	h_0	v_0	ϕ	θ	γ	κ	α
	($R_\odot$)	($km\,s^{-1}$)	(°)	(°)	(°)		(°)
1^*	3.5	162	119	-10	-35	0.28	10
2^{*f}	5.5	916	267	-25	33	0.34	25
3^*	2.9	468	180	17	-18	0.20	22
4^*	5.7	193	336	0.5	-15	0.23	9.5
5^*	4.0	444	260	23	-49	0.41	18
6^*	5.3	215	74	-31	-55	0.25	22
7	3.7	147	29	-28	-15	0.40	18
8	4.4	276	336	-15	-15	0.30	22
9^*	4.4	832	30	-6	30	0.47	27
10	4.9	349	175	-22	8	0.35	21
11^*	4.8	47	207	1	9	0.21	37
12	4.7	300	41	6	-6	0.30	35
13	3.6	562	202	1	36	0.26	57
14^f	8.4	1168	129	5	-8	0.45	14
15^f	4.1	903	264	17	15	0.35	18
16^f	7.3	1638	324	19	65	0.69	29
17	3.8	493	134	19	-38	0.43	41
18^f	4.0	1276	54	44	16	0.60	45
19	7.8	889	302	7	-1	0.46	9
20	5.3	882	223	29	16	0.36	16
21^f	4.6	1823	212	44	90	0.47	58
22^f	4.0	1910	206	28	58	0.48	41
23^f	3.5	2397	193	30	69	0.38	41
24^f	3.9	1837	302	21	-40	0.74	73
25	4.1	648	82	-28	0.0	0.27	30
26^f	6.2	1152	92	-22	-87	0.38	20
27^f	4.4	1248	88	-10	78	0.45	35
28^f	6.7	1305	165	17	86	0.42	42
29	4.4	461	56	-24	37	0.30	31
30	7.3	380	118	8	-36	0.20	40
31	3.8	602	285	-18	7	0.48	35
32	6.3	492	91	-21	-66	0.52	10
33^f	4.7	1504	76	-7	-86	0.31	40
34^f	5.9	1115	77	-1	90	0.14	47
35^f	6.6	1637	177	-35	-20	0.41	5
36^f	4.9	1217	360	21	90	0.38	47
37^f	5.9	975	304	-30	-75	0.34	12
38^f	6.8	1039	221	32	51	0.36	47

Chapter 3

CME dynamics and propagation

We discuss the major forces that govern CME propagation. These are : Lorentz driving force, solar wind aerodynamic drag and gravity. We motivate and investigate the phenomenological expressions used to describe these forces. We consider the torus instability model for Lorentz forces and a 1D drag-based model to describe the CME-solar wind interaction. Each of the parameters that appear in the force equation is discussed in this chapter and details of the models used for their calculation are provided. The method for force analysis is also outlined for both the forces.

3.1 Introduction

CMEs have been widely observed and studied to understand the mechanisms that trigger their eruption and cause their propagation in the interplanetary (IP) space. The complete CME evolution is typically divided into two phases; the initial eruption and acceleration phase followed by the propagation phase. Gopalswamy (2013) describes the CME acceleration as the sum of accelerations due to each of the three forces that affect CME propagation. These are, Lorentz force, aerodynamic drag and gravity. Similarly, Zhang and Dere (2006) describe three distinct phases of CME propagation: 1) Initiation phase of slow rise of CMEs, 2) phase of fast acceleration of CMEs and 3) propagation phase in which the CMEs undergo relatively minor evolution. They club the latter two phases and term it "residual acceleration" (*e.g.* Subramanian and Vourlidas, 2007; Bein et al., 2011). We describe the Lorentz driving force that is responsible for initial CME acceleration in section 3.2.1 and the

aerodynamic drag due to interaction between the CME and ambient solar wind in section 3.2.2. The solar gravitational pull causes CMEs to decelerate very close to the Sun (Shen et al., 2012); however, its effects are much smaller compared to the accelerating Lorentz forces *i.e.* gravity does not affect CME dynamics (Chen and Krall, 2003). Therefore, for simplicity we neglect gravity in this study. We outline the models that are used to calculate the two governing forces (Lorentz force and aerodynamic drag) along with the models/definitions used for evaluating the physical parameters required in the force equations. We also describe the methods for the aerodynamic drag and Lorentz force analysis in this chapter.

3.2 Forces acting on CMEs

3.2.1 Lorentz driving force

Initial CME triggering can be attributed to various mechanisms that lead to magnetic rearrangement, loss of equilibrium or some instability that causes the CME to erupt (Chen, 2011). In other words, CME eruption can be described as the disruption in the equilibrium of the magnetic field configuration (*e.g.* Chen, 1989; Chen and Garren, 1993). Comparisons between the data and theory related to the dynamics of expanding CME structure has shown that CMEs are driven by Lorentz forces ($J \times B$) from very early on in their evolution. In order to drive these magnetized structures, the Lorentz forces must involve misaligned currents and magnetic fields. This means that the flux-rope CMEs are required to be non force-free to be accelerated by Lorentz forces (Subramanian et al., 2014). Manoharan et al. (2004); Manoharan (2006); Subramanian and Vourlidas (2007) have shown, using observational evidence that the magnetic energy carried by flux-rope CMEs in sufficient to drive them from the Sun to the Earth. However, the actual nature of these Lorentz forces is still unclear. While some authors include it in the initial eruption process (*e.g.* Isenberg and Forbes, 2007; Kliem et al., 2014), others assume that the Lorentz force time profile follows the temporal evolution of the soft X-ray flux (*e.g.* Chen and Kunkel, 2010).
Most Lorentz force prescriptions model the CME morphology like an expanding current carrying loop-like structure with toroidal and poloidal magnetic fields and corresponding current components (*e.g.,* Chen, 1989; Garren and Chen, 1994)). Olmedo et al. (2013) describe the action of Lorentz force by considering the forces acting on elliptical current carrying loops. In addition, Kumar and Rust (1996) use the arguments of magnetic helicity conservation in their model which considers a current-core helical flux-rope CME and apply it to a torus-shaped cloud. Results of numerical simulations also support the driving action of Lorentz forces. These include MHD simulations of

CME initiation which involves reconnection (magnetic breakout model) (*e.g.* Antiochos et al., 1999; Moore et al., 2001; Karpen et al., 2012). Other MHD models that involve loss of equilibrium are given by Forbes and Isenberg (1991); Isenberg et al. (1993) and Shen et al. (2012).

CME eruption has also been explained by the kink instability (Török et al., 2004) and the torus instability (TI) (Kliem and Török, 2006). The torus instability models CMEs as current carrying rings that expand as they evolve. Kliem and Török (2006) consider the expansion instability of the ring in low-beta magnetic plasma in the presence of an overlying magnetic field and compare the properties with those of solar CMEs. For TI it is required for the overlying poloidal magnetic field to decrease rapidly enough so that the CME can erupt. When this field falls sufficiently fast, an instability occurs and the CME launches outwards with a whiplash-like action. In this study, we follow this prescription of Lorentz force as the major driving force acting on the CMEs.
The TI model does not include the effects of reconnection on the CME dynamics. Welsch (2017) state that in order for the CME to erupt through the field overlying the magnetized structure, the Kliem and Török (2006) model must include the dynamic effects that occur due to the reconfiguration of field lines. We consider the original TI model as described in Kliem and Török (2006) for modeling the Lorentz forces acting on solar coronal mass ejections and include it in the force equation described in Section 3.3.

3.2.2 Aerodynamic drag force

As the CME propagates into the interplanetary space, it couples with the ambient solar wind via momentum transfer. The action of viscous forces on the CME boundary causes the CMEs to slow down or accelerate depending on their speed relative to the speed of the surrounding medium (solar wind) (Borgazzi et al., 2009). Manoharan (2006); Maloney et al. (2009); Gopalswamy (2013) and others found that CMEs erupting with speeds lesser than the ambient solar wind speed were dragged up while those with speeds exceeding the solar wind speed were decelerated. Lewis and Simnett (2002) arrived at similar conclusions based on their study of an average "representative" CME using coronagraph observations. Various drag-based models that take into account aerodynamic drag force only due to interaction with the solar wind include Cargill (2004); Vršnak et al. (2010, 2013); Mishra and Srivastava (2013) and Temmer and Nitta (2015).

Other dynamical CME models used for modeling the CME propagation include ENLIL, which is a three-dimensional (3D) magneto-hydrodynamic (MHD) model (e.g., Odstrčil and Pizzo, 1999; Odstrcil et al., 2004; Taktakishvili et al., 2009; Lee et al., 2013; Vršnak et al., 2014; Mays et al., 2015) and,

the Global MHD model using data-driven Eruptive Event Generator Gibson-Low (EEGGL) (e.g. Jin et al., 2017). CME and Shock propagation Models like the Shock Time of Arrival Model (STOA), Interplanetary Shock Propagation model (ISPM) and Hakamada-Akasofu-Fry version 2 model (e.g., Fry et al., 2003; McKenna-Lawlor et al., 2006), other hybrid models (Wu et al., 2007) and the Space Weather Modeling Framework (SWMF; Lugaz et al., 2007; Tóth et al., 2007) are also often used to model CME propagation.

Most models that describe the momentum coupling between the CME and the solar wind use empirical drag parameters. Cargill (2004) uses 2.5D MHD simulation results to determine the drag coefficient, $C_{\rm D}$. Subramanian et al. (2012); Sachdeva et al. (2015) describe a microphysical prescription for the collisionless solar wind viscosity in order to determine the drag coefficient ($C_{\rm D}$). The dimensionless drag coefficient is representative of the strength of the coupling interaction between the CME and the solar wind. The aerodynamic drag force on CMEs is typically assumed to be proportional to the square of the CME velocity relative to the solar wind speed (*e.g.* Cargill, 2004; Subramanian et al., 2012; Vršnak et al., 2014; Sachdeva et al., 2015). This formulation is used for high Reynolds number flows past a solid body.

Landau and Lifshitz (1959) describe a scenario for a solid body moving through a fluid at high Reynolds number. The bulk flow (considered to be a potential flow) and the solid body are separated by a turbulent boundary layer. This description is relevant for CMEs, as they are over-pressured structures in a high Reynolds number flow. The "solid body" law requires that the tangential and normal velocities vanish at the boundary (which is thin, owing to large Reynolds number). The turbulence in the boundary layer arises because the velocity transitions from its bulk value to zero on the boundary over a very short distance and nonlinear terms in the Navier-Stokes equation assume importance giving rise to turbulence.

While some believe that the Lorentz forces play an important role in governing the CME dynamics only up to a few solar radii (*e.g.* Vršnak, 2006), others state that the solar wind drag is the dominant force affecting CMEs from very early on and model the CME trajectory using drag-based models (Lewis and Simnett, 2002; Cargill, 2004). Zhang and Dere (2006) suggest that the CME initiation and initial acceleration takes place < 2 R$_\odot$. On the other hand, Byrne et al. (2010) find that drag dominates the CME dynamics beyond 7 R$_\odot$. Temmer et al. (2011); Vršnak et al. (2013); Iju et al. (2014); Rollett et al. (2016) mention that ICMEs equilibrate with the solar wind speeds within ~ 0.5 AU. In spite of significant progress in modeling the Sun-Earth propagation of CMEs, predictions of travel time and speeds of Earth-directed CMEs are still limited in their accuracy (Zhao and Dryer, 2014) even for relatively simple events that do not involve CME-CME interactions (*e.g.* Temmer et al., 2012). Our understanding of how the Lorentz forces operate,

at what heights and when they cease to be important is not very robust as well.
We now describe the equation for the net force acting on CMEs (section 3.3) based on particular prescriptions of the two contributing forces.

3.3 Force Equation

The equation of motion for CMEs is given by:

$$F = m_{cme}\frac{d^2R}{dt^2}$$

where F is the total force, m_{cme} is the CME mass, R is the heliocentric distance of the leading edge of the CME and t represents time. F includes the Lorentz and aerodynamic drag forces (gravity is neglected),

$$\begin{aligned} F &= F_{Lorentz} + F_{drag} \\ &= \left\{\left[\frac{\pi I^2}{c^2}\left(ln\left(\frac{8R}{R_{cme}}\right) - \frac{3}{2} + \frac{l_i}{2}\right)\right] - \frac{(\pi R) I B_{ext}(R)}{c}\right\} \\ &\quad - \frac{1}{2}\, C_{\rm D}\, A_{cme}\, n_{sw}\, m_p \left(V_{cme} - V_{sw}\right) \left|V_{cme} - V_{sw}\right| \end{aligned} \tag{3.1}$$

$F_{Lorentz}$ and F_{drag} denote the Lorentz and aerodynamic drag forces respectively (in cgs units). $F_{Lorentz}$ is the net Lorentz force ($(1/c)J \times B$) that acts on a CME in the direction of the major radius. It includes the two terms in the curly brackets (see, *e.g.* Shafranov, 1966; Kliem and Török, 2006). The first term denotes the Lorentz self-forces acting on the expanding CME in the radially outward direction while the second term is the inward force due to an external poloidal magnetic field (B_{ext}) that holds down the expanding CME. CME current is represented by I, R_{cme} is the minor radius of the CME, c is the speed of light and l_i is the internal inductance.
The term involving $C_{\rm D}$ in the force equation represents the drag force acting on the CME (F_{drag}). The drag coefficient $C_{\rm D}$ denotes the strength of the interaction between the CME and the ambient solar wind (Subramanian et al., 2012; Sachdeva et al., 2015). The negative sign ensures that the solar wind can "pull up" a CME (if $V_{cme} < V_{sw}$) and also "drag it down" (if $V_{cme} > V_{sw}$). A_{cme} is the cross-sectional area of the CME, n_{sw} is the solar wind density, m_p is the proton mass, V_{cme} and V_{sw} denote the CME and solar wind speeds respectively. Non-radial components of forces have not been considered in this model (Byrne et al., 2010).

Equation 3.1 thus describes a full force equation in terms of various CME parameters. Models used for the calculation of each of these parameters are described in detail in the sections 3.4 and 3.5. We note that most physical quantities used in this analysis are observationally derived using the Graduated Cylindrical Shell (GCS) fitting procedure described in Chapter 2.

3.4 Solar wind Drag Model

The interaction between ambient solar wind and CMEs is given by the following equation (see, Equation 3.1):

$$F_{drag} = m_{cme}\frac{dV_{cme}}{dt} = -\frac{1}{2}C_{\rm D}\,A_{cme}\,n_{sw}\,m_p\left(V_{cme}-V_{sw}\right)\left|V_{cme}-V_{sw}\right|, \tag{3.2}$$

F_{drag} is the aerodynamic drag force due to momentum coupling between the CME and solar wind, m_{cme} is CME mass, V_{cme} is CME speed, $C_{\rm D}$ is the dimensionless drag coefficient, A_{cme} is CME cross-sectional area, n_{sw} is the solar wind proton density, m_p denotes the proton mass and V_{sw} is the ambient solar wind speed. The negative sign ensures that the solar wind can be both driving as well as a decelerating force. A fast CME propagating into a relatively slower solar wind is "dragged down" by it while a slow CME is "picked up" by a faster solar wind. The drag acceleration is considered to have a quadratic dependence on the CME-solar wind relative speed in accordance with the law for solid bodies moving at high Reynolds numbers (Landau and Lifshitz, 1959).

Cargill (2004); Vršnak et al. (2010, 2013) prescribe the drag-based model in terms of the γ parameter described below:

$$\frac{F_{drag}}{m_{cme}} \equiv a_d = -\gamma\left(V_{cme}-V_{sw}\right)\left|V_{cme}-V_{sw}\right|, \tag{3.3}$$

where, a_d is the acceleration and $\gamma\,(\mathrm{cm}^{-1})$ is given by

$$\gamma = C_{\rm D}\frac{n_{sw}m_pA_{cme}}{m_{cme}}, \tag{3.4}$$

which depends on the solar wind density (n_{sw}), cross-sectional area (A_{sme}) and the CME mass (m_{cme}). Vršnak et al. (2013) use this analytical equation to explicitly solve for the Sun-Earth transit time and speed of CMEs with the assumption that $\gamma(r)$ = constant. In the following sections, we describe the models used for each of the parameters that appear in the drag equation (Equation 3.2) and their calculation.

3.4.1 Drag Coefficient $C_{\rm D}$

The strength of the momentum coupling between a CME and the ambient solar wind is represented by the drag parameter $C_{\rm D}$. Most drag-based models consider an empirical drag coefficient. However, we consider a microphysical prescription for $C_{\rm D}$ using collisionless solar wind viscosity as described in Subramanian et al. (2012) and Sachdeva et al. (2015). Let ν_{sw} be the viscosity

in the ambient collisionless solar wind, which arises from resonant scattering of the solar wind protons with the turbulent Alfvén wave spectrum. It can be described with an expression for turbulent viscosity (*e.g.,* Verma, 1996) given by :

$$\nu_{sw} = \sqrt{6}\,\frac{2}{15}\,v_{\rm rms}\,\lambda\,, \tag{3.5}$$

where $v_{\rm rms} \equiv (3kT_i/m_p)^{1/2}$ is the rms speed of solar wind protons and λ is the mean free path. The ion inertial length is taken to be the mean free path here (Leamon et al., 2000; Smith et al., 2001; Bruno and Trenchi, 2014) and is given by :

$$\lambda \;=\; \frac{v_a}{\Omega_i} \;=\; \frac{c}{\omega_p} \;\sim\; 228\; n_{sw}^{-1/2}\; k\,m\,, \tag{3.6}$$

where, v_a is the Alfvén speed, Ω_i is the ion cyclotron frequency, c is the light speed, ω_p is the ion plasma frequency and n_{sw} is the ambient solar wind density. Coles and Harmon (1989) use a similar prescription for the mean free path which is also used in Subramanian et al. (2012). However, their prescription is a factor of 3 larger than the ion inertial length given by Equation 3.6. The Reynolds number (Re) is a dimensionless ratio of the inertial and viscous forces in a fluid. For CMEs, it is defined by:

$$Re \equiv \frac{(V_{cme} - V_{sw})\,R_{cme}}{\nu_{sw}} \;=\; \frac{(V_{cme} - V_{sw})\,R_{cme}\,n_{sw}\,m_p}{\eta_{hyb}}, \tag{3.7}$$

where the quantity ν_{sw} ($\rm cm^2\,s^{-1}$) is the solar wind viscosity and $\eta_{hyb} \equiv n_{sw}\,m_p\,\nu_{sw}$. The dimensionless coefficient of drag, $C_{\rm D}$ is expressed as a function of the Reynolds number using a fit to the data from Achenbach (1972) for the drag on a sphere at high Reynolds numbers in the super-critical regime:

$$C_{\rm D} = 0.148 - 4.3 \times 10^4\,Re^{-1} + 9.8 \times 10^{-9}\,Re \tag{3.8}$$

The above definition for $C_{\rm D}$ was experimentally determined for subsonic, high Reynolds number flow past a solid metal sphere (Achenbach, 1972). The drag force acting on CMEs described by Equation 3.2 appeals to a high Reynolds number, solid body law and the prescription for drag coefficient in Equation 3.8 is consistent with these assumptions. Russell et al. (2005) and Jian et al. (2006) show that CMEs are overpressured structures that do not deform in response to tangential stresses. That is, the total (magnetic + particle) pressure exhibits a substantial jump across a typical magnetic cloud boundary, suggestive of a solid-body like behavior. The drag formula given by Achenbach (1972) has also been verified by modern detached-eddy simulations of high Reynolds number flows in the super-critical regime (e.g., Constantinescu and Squires, 2004), which is the regime we are interested in. Although Equation 3.8 is derived experimentally for subsonic flows, we note that the CME motion through the solar wind is supersonic. In order to justify the applicability of this definition in the subsonic regime, we appeal to

the Morokovin hypothesis, which has been verified extensively via numerical simulations (*e.g.,* Duan et al., 2011). According to this hypothesis, a subsonic turbulent drag law is valid even for supersonic flows as long as the fluctuations in the turbulent boundary layer are incompressible, or subsonic. To a very good approximation, the turbulent fluctuations in the ambient solar wind are certainly incompressible (*e.g.,* Shaikh and Zank, 2010), therefore, the drag parameter prescription holds for CMEs as well. This is also evident from the small values of the density fluctuations $\Delta n/n$ in the ambient solar wind (*e.g.,* Bisoi et al., 2014; Sasikumar Raja et al., 2016). Arunbabu et al. (2013) show that the fluctuations in the magnetic field ($\Delta B/B$) in the turbulent sheath region, between the shock and the CME are also as small as 10%. Since magnetic field fluctuations can be considered to be a proxy for the $\Delta n/n$ values (*e.g.,* Spangler, 2002), it follows that the turbulent density fluctuations in the sheath region are also fairly incompressible. Therefore, the drag coefficient model as described here is quite relevant to describe the momentum coupling between CMEs and the solar wind. For completeness, in addition to the $C_{\rm D}$ prescription described above, we also use (empirical) constant $C_{\rm D}$ values lying within and outside the range of values predicted by this model.

3.4.2 CME Cross-sectional Area

The CME area (A_{cme}) in Equation 3.2 is the area of the elliptical cross-section in the x-z plane of the flux-rope CME and is calculated using,

$$A_{cme} = \pi \, R_{cme} \, W_{cme} \tag{3.9}$$

The quantity R_{cme} is the radius of the circular cross-section of the CME as seen edge-on (also called the minor radius). W_{cme} is the maximum value of the face-on half-width of the CME, or the major radius of the elliptical cross-section (Figure 2.2). Both these quantities are derived using the height of the leading edge R, half angle α and aspect ratio κ from the GCS fitting procedure (Thernisien, 2011). The CME cross-sectional area is thus calculated using observationally fitted parameters for each observed height/time.

3.4.3 Models for Solar wind parameters

The solar wind proton number density is a function of the observed GCS height of the leading edge, R. It is calculated using a modified version of the LeBlanc electron density model. The original model of Leblanc et al. (1998) (Equation 3.10) considers the number density at 1 AU to be 7.2 cm^{-3}; and

is given by:

$$n(R) = \left[3.3 \times 10^5 R^{-2} + 4.1 \times 10^6 R^{-4} + 8 \times 10^7 R^{-6}\right] \text{ cm}^{-3}, \quad (3.10)$$

However, we take the proton density at 1 AU (n_{wind}) to be that observed *in-situ* about one-two days before the arrival of the CME and its associated shock (if there is a shock). The density model we use is thus given by,

$$n_{sw}(R) = \left(\frac{n_{wind}}{7.2}\right)\left[3.3\times10^5 R^{-2}+4.1\times10^6 R^{-4}+8\times10^7 R^{-6}\right] \text{ cm}^{-3} \quad (3.11)$$

The quantity $n_{sw}(R)$ denotes the density of the ambient solar wind into which a CME propagates. The correction factor, $n_{wind}/7.2$ ensures that the modeled density at 1 AU from Equation 3.11 is same as the proton number density observed *in-situ* by the *WIND* spacecraft near the Earth. The modified LeBlanc model is used to extrapolate the measured 1 AU solar wind proton number density Sunwards. The quantity n_{wind} for all CME events in the sample is given in Table 3.1.

Another important parameter that affects the CME propagation significantly is the solar wind speed (*e.g.,* Temmer et al., 2011). Denoted by V_{sw} in the drag model (Equation 3.2), the solar wind speed is modeled as a function of the heliocentric distance (R) using the prescription given by Sheeley et al. (1997, 1999):

$$V_{sw}^2(R) = v_{wind}^2 \left[1 - e^{-\frac{(R-r_0)}{r_a}}\right], \quad (3.12)$$

where v_{wind} is the near-Earth solar wind speed observed *in-situ* by the *WIND* spacecraft (Table 3.1). Like n_{wind}, the quantity v_{wind} is also observed approximately one-two days in advance of the CME arrival, which essentially describes the solar wind environment that the CME will propagate into. In the solar wind speed model, r_0 denotes the heliocentric distance where the solar wind speed is zero and is taken to be 1.5 $R_\odot$ in this work. The quantity r_a, is the e-folding distance over which the asymptotic speed v_{wind} is reached. r_a is taken to be 50 $R_\odot$ for all CMEs. Both the quantities, n_{sw} and V_{sw} are therefore, observationally derived using the GCS parameters as well as *in-situ* observations.

3.4.4 Calculation of CME Mass

The CME structure is visible in the white-light images observed by coronagraphs as a projection on the Plane of the Sky (POS), which is the plane perpendicular to the Sun-spacecraft line. Quantities like height, width, brightness, speed, mass etc. are derived from these projected CME structures on the POS. This leads to a slight discrepancy between the actual and observed quantities due to projection effects.

With multi-spacecraft observations from different positions, methods to determine the actual CME parameters (correcting for projection effects) have been developed. The STEREO COR2 A & B coronagraphs provide two projected images of an event erupting from the Sun along the Line of Sight (LOS). Using STEREO A/B and LASCO observations it is possible to obtain the actual CME parameters and minimize projection effects. The observed CME intensities, once calibrated to units of mean-solar brightness give two values of the projected CME mass, one from each STEREO COR2 spacecraft (A & B). The mass values of the same observed CME structure from both instruments are generally slightly different. The "true" CME mass is the mass which is corrected for the projection effects due to the difference in the LOS of each instrument. We use the method outlined in Colaninno and Vourlidas (2009) to calculate the "true" CME mass for all the events in our sample. For each CME, we have the projected mass values from COR2 A & B coronagraphs. In the method briefly described here, it is required that the total CME mass must be equal for both these coronagraphs. Colaninno and Vourlidas (2009) follow the Thomson scattering calculation outlined in Billings (1966) and given by:

$$m = \frac{B_{obs}}{B_e(\theta)} \times 1.97 \times 10^{-24} \quad gm, \tag{3.13}$$

where, m is the mass at each pixel, B_{obs} is the observed brightness and $B_e(\theta)$ is the brightness of a single electron at an angular distance θ. θ is the angle along the LOS away from the POS. This method of mass estimation has been used by Vourlidas et al. (2000); Subramanian and Vourlidas (2007); Colaninno and Vourlidas (2009).

From the GCS fitting procedure, and using the *make_cme_mass_fits.pro* IDL routine we obtain the derived CME mass simultaneously for each viewpoint (COR2 A/B). In principle, since the two instruments observe the same volume of material from different angles, the mass observed in each should be the same. If this is not the case, the error must lie in the usage of an incorrect angle in the Thomson Scattering calculation (Equation 3.13). From Colaninno and Vourlidas (2009),

$$\frac{M_A}{M_B} = \frac{f_m(\theta + \Delta_{sc}/2)M_T}{f_m(\theta - \Delta_{sc}/2)M_T} , \tag{3.14}$$

where, M_A and M_B are observed masses from COR2 A and B respectively and,

$$f_m(\theta) = \frac{B_e(\theta)}{B_e(\theta = 0^\circ)} , \tag{3.15}$$

is the ratio of brightness of an electron at θ and on the POS ($\theta = 0^\circ$). Δ_{sc} is the angular separation of the two spacecrafts. We estimate the θ for which Equation 3.14 holds true. For this value of θ we calculate,

$$M_A - M_B = M_T \left[f_m(\theta + \Delta_{sc}/2) - f_m(\theta - \Delta_{sc}/2) \right], \tag{3.16}$$

at each height for each CME in the COR2 FOV. The quantity M_T is the true CME mass. It increases with height (Vourlidas et al., 2000), and beyond the COR2 FOV ($\sim$ 15 $R_\odot$) it is taken to be constant and equal to the last observed value in the COR2 FOV. The true mass (M_T) for each CME is calculated at each GCS observed height using this technique. We also include the Virtual Mass (M_v) (*e.g.,* Cargill et al., 1996; Cargill, 2004) in our calculations (Refer Appendix 6.1).

Total CME mass, $m_{cme} = M_T + M_v$, is written as,

$$m_{cme} = M_T \left[1 + \frac{1}{2} \frac{n_{sw}(R)\, m_p}{M_T} A_{cme} R \right] \tag{3.17}$$

For all CMEs, m_{cme} at the last observed height (h_{COR}) in the COR2 FOV, is given in Table 3.1.

The above section describes models used for evaluating each parameter in the drag force equation using various observed parameters (GCS and *in-situ*). In order to calculate the speed of the CME, we solve Equation 3.2 using these prescriptions. The details are described in the sections below.

3.4.5 Solving for V_{cme}

The drag force Equation 3.2 is a simple 1D model which describes the momentum coupling between CMEs and solar wind and is prescribed in terms of parameters derived using observations (wherever applicable). To calculate the CME velocity profile (V_{cme} as a function of time) we require an estimate for the CME initial speed (v_0) at the first observed height (h_0). This initial velocity (v_0 at h_0) is calculated by fitting a 3^{rd} degree polynomial to the GCS fitted height-time profile for each CME in the event sample and is used as the initial condition when the differential equation for V_{cme} is solved from h_0 onwards (Table 2.2). For each event, the drag-only model (Equation 3.2) is initiated (a) from the first data point (h_0) and (b) at progressively larger heights. At each height, the corresponding parameters at that height are used in the model. The solutions for V_{cme} from Equation 3.2 are integrated to obtain a height-time profile predicted by this model, that includes only the solar wind drag force. We then compare this modeled height-time solution with the observed CME profile obtained from the GCS fitting technique described earlier in Chapter 2. The initiation height at which the model and observed height-time profiles show a good agreement is denoted by $\widetilde{h}_0$. The magnitude of the aerodynamic drag force above $\widetilde{h}_0$ is computed from the force Equation 3.2 using the corresponding parameters and model solutions. Results from this analysis are described in detail in Chapter 4 for all the events.

3.5 The TI Lorentz Force Model

The Lorentz force model based on the torus instability (TI) (section3.2.1) is described in terms of two competing $(J \times B)$ factors. One is due to the Lorentz self-forces acting radially outwards on the flux-rope and the other is due to the overlying external poloidal field that tends to hold down the CME. The total Lorentz force acting on an expanding CME can be expressed in terms of the CME current I, the height of the leading edge R and the external poloidal magnetic field $B_{ext}(\propto R^{-n})$ which is required to fall sufficiently fast for the CME to escape (see, *e.g.* Shafranov, 1966; Kliem and Török, 2006):

$$F_{Lorentz} = \frac{\pi I^2}{c^2}\left(ln\left(\frac{8R}{R_{cme}}\right) - \frac{3}{2} + \frac{l_i}{2}\right) - \frac{(\pi R) I B_{ext}(R)}{c}, \tag{3.18}$$

where c is the speed of light, R_{cme} is CME minor radius and l_i is the internal inductance which is taken to be $l_i = 1/2$. The ratio R/R_{cme} is the aspect ratio determined by GCS derived parameters. The decay index n needs to be above a critical value n_{cr}, for the torus instability to be operative, ensuring CME eruption (Kliem and Török, 2006). For each CME, we choose a value of n that is $> n_{cr}$. Both these quantities are listed in Table 3.1 for each event. In the sections below, we describe how the CME current (and hence, the Lorentz force) is calculated as described in Sachdeva et al. (2017). We note that the CME minor radius (R_{cme}) is referenced as "b" in Sachdeva et al. (2017).

3.5.1 CME current

The CME axial current, I is determined by the conservation of total (i.e. flux-rope + external) magnetic flux enclosed by a current carrying ring which is given by (Kliem and Török, 2006):

$$\Psi_{total} = \Psi_{int} + \Psi_{ext} ,$$

where, Ψ_{int} and Ψ_{ext} are internal (flux-rope) and external magnetic flux given by (in cgs units):

$$\begin{aligned} \Psi_{int} &= cL\,I \\ \Psi_{ext} &= -\int B_{ext}.da = -2\pi \int_0^R B_{ext}(r)\, r\, dr , \end{aligned}$$

where, L is the inductance.

Conservation of total magnetic flux requires,

$$\begin{aligned} \Psi_{total}\left(h_{eq}\right) &= \Psi_{total}\left(R\right) \\ \Rightarrow \Psi_{int}(h_{eq}) - 2\pi \int_0^{h_{eq}} B_{ext}(r) r dr &= \Psi_{int}(R) - 2\pi \int_0^{R} B_{ext}(r) r dr \\ \Rightarrow L_{eq} I_{eq} - \frac{2\pi}{c} \int_0^{h_{eq}} B_{ext}(r) r dr &= L(R)\, I(R) - \frac{2\pi}{c} \int_0^{R} B_{ext}(r) r dr \end{aligned} \tag{3.19}$$

The quantities with subscript "eq" represent values at the pre-eruption equilibrium position (h_{eq}), where the total Lorentz force acting on a CME is zero (*i.e.* from Equation 3.18, $F_{Lorentz} = 0$). As described by Chen (1989), the inductance L is given by:

$$L = \frac{4\pi R}{c^2}\left[ln\left(\frac{8R}{R_{cme}}\right) - 2 + l_i/2\right] \tag{3.20}$$

When substituted in Equation 3.19, it gives the axial CME current carried by the CME,

$$I = \frac{c^{'}_{eq} I_{eq} h_{eq}}{c^{'} R}\left(1 + \frac{(c^{'}_{eq} + \frac{1}{2})}{2c^{'}_{eq}(2-n)}\left[\left(\frac{R}{h_{eq}}\right)^{2-n} - 1\right]\right), \tag{3.21}$$

where,

$$\begin{aligned} c^{'}(R) &= \left[ln(8R/R_{cme}) - 2 + l_i/2\right] \\ c^{'}_{eq} &= c^{'}(R = h_{eq}) = \left[ln(8h_{eq}/R_{cme}(h_{eq})) - 2 + l_i/2\right] \end{aligned}$$

The equilibrium current I_{eq} and external field at equilibrium ($B_{ext}(h_{eq})$) are related via,

$$I_{eq} = \frac{B_{\rm ext}(h_{eq}) h_{eq} c}{c^{'}_{eq} + \frac{1}{2}}. \tag{3.22}$$

In this study, the equilibrium position, h_{eq} is taken to be equal to 1.05 $R_\odot$. $n > n_{cr} = 3/2 - 1/(4c^{'}_{eq})$ is chosen to be such that, $|F_{drag}| > F_{Lorentz}$ for $R > \widetilde{h}_0$ (see, Appendix 6.2.5 for details). The CME current is evaluated using observationally derived CME parameters determined from the GCS fit (R and R_{cme}). The details are described in Appendix 6.2.

3.5.2 Calculating the CME current I

The external poloidal field, B_{ext} ($\propto R^{-n}$) is related to the equilibrium current by Equation 3.22. In order to determine the CME current I, either I_{eq} or $B_{ext}(h_{eq})$ is required. For a given value of n, the external field at equilibrium

($B_{ext}(h_{eq})$) is determined by equating the solar wind drag and Lorentz forces at the height $\widetilde{h}_0$. Basically, it is required that $|F_{drag}(\widetilde{h}_0)| = F_{Lorentz}(\widetilde{h}_0)$. This constrains the equilibrium current I_{eq}.

Using Equations 3.21, 3.22 and $B_{ext}(R) = B_{ext}(h_{eq})(R/h_{eq})^{-n}$ in Equation 3.18, the Lorentz force acting on a CME can be calculated (in dynes). With the external field, $B_{ext}(h_{eq})$ at equilibrium (and hence, the current I_{eq} at h_{eq}), we can calculate the CME current (I) values at each observed height. The Lorentz force magnitude can then be calculated using the current (I) estimates and the ratio R/R_{cme} from the GCS fittings for all heights starting from the first observed height h_0. Between h_{eq} and h_0 due to FOV constraints of the coronagraphs, we do not have the GCS observations of the CME. In this range, we assume that the CME expands self-similarly. For $R < h_0$, we assume R/R_{cme} to be the same as its value at h_0 and calculate the Lorentz force magnitude. The expression used to determine the Lorentz force magnitude is described in detail in the Appendix 6.2.

3.5.3 Lorentz force profile

The Lorentz force profile shows a steep increase from the equilibrium position (h_{eq}), and peaks at h_{peak}, beyond which it decreases gradually. An example is shown in Figure 3.1 for CME 1 (Table 2.1). The two terms in Equation 3.18 add up to give this resultant observed Lorentz force profile.

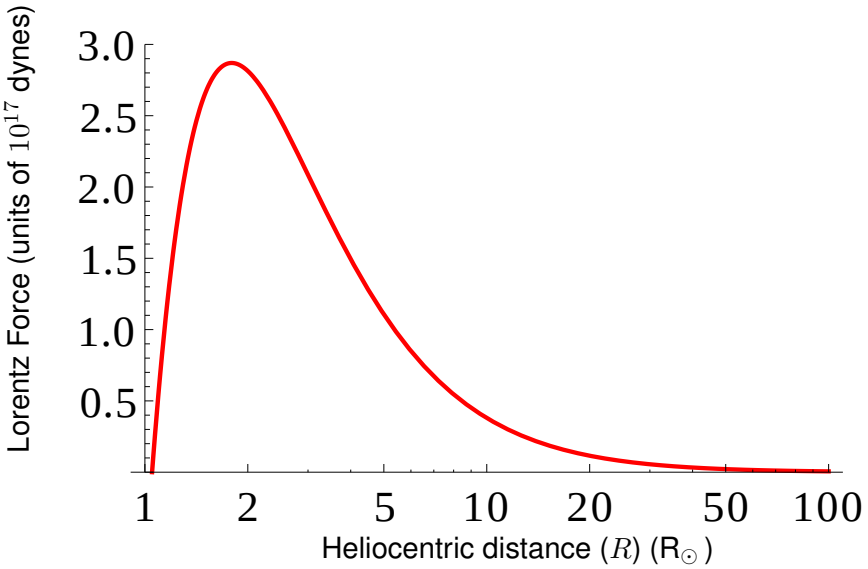


Figure 3.1: Lorentz force profile with respect to heliocentric distance for a set of parameters given by: $n = 2.5$, $B_{ext}(h_{eq}) = 0.013\,G$ and $R/R_{cme} = 4.56$. The force increases from $h_{eq} = 1.05$ $R_\odot$ to peak at 1.75 $R_\odot$ and then decreases. X-axis is plotted on a logarithmic scale for clarity.

We rewrite the terms in Lorentz force equation (Equation 3.18) individually:

$$Term\,1 = \frac{\pi I^2}{c^2}\left(ln\left(\frac{8R}{R_{cme}}\right) - \frac{3}{2} + \frac{l_i}{2}\right) \quad (3.23)$$

$$Term\,2 = -\frac{(\pi R) I B_{ext}(R)}{c} \quad (3.24)$$

$$F_{Lorentz} = Term\,1 + Term\,2$$

Figure 3.2 plots Term 1 (Lorentz self-force) (blue) and Term 2 (force due to external field) (green) *versus* the heliocentric distance (R), for a set of parameter values. When added together they result in the Lorentz force profile (red). The first term (Term 1) dominates over Term 2.

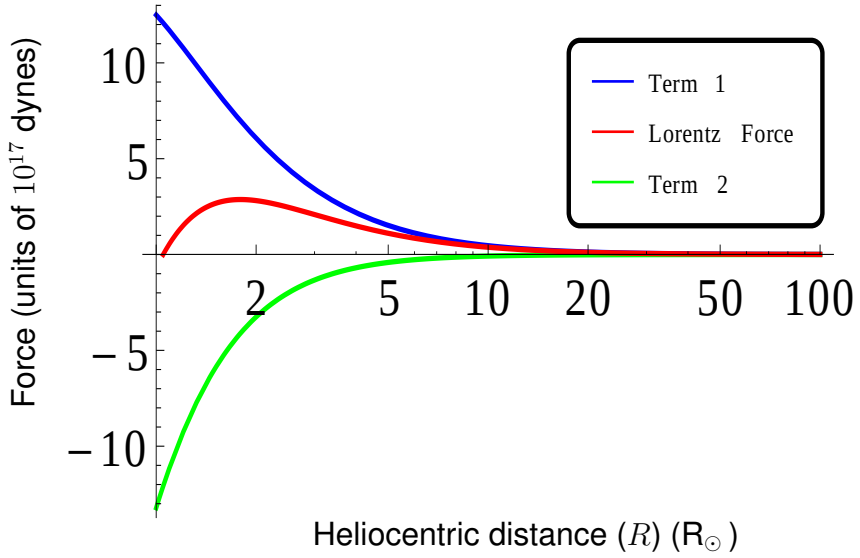


Figure 3.2: Individual terms in the Lorentz force equation (Equation 3.18) and the resultant force profile with respect to heliocentric distance (R) for a set of parameters given by: $n = 2.5$, $B_{ext}(h_{eq}) = 0.013\,G$ and $R/R_{cme} = 4.56$ are shown here. First term represents the Lorentz self-force (blue) and the second term is the force due to the external poloidal field (green). The resultant Lorentz force profile is shown in red color. X-axis is plotted on a logarithmic scale for clarity.

The peak denotes the height where,

$$\frac{d\,F_{Lorentz}}{dR} = 0 \quad at \quad R = h_{peak}$$

and,

$$\frac{d\,F_{Lorentz}}{dR} > 0 \quad for \quad R < h_{peak}$$

$$\frac{d\,F_{Lorentz}}{dR} < 0 \quad for \quad R > h_{peak}$$

h_{peak} is therefore, the height where the Lorentz force has the maximum magnitude, beyond which it decreases.

The model framework for the two major forces governing CME propagation described in the preceding sections is used to determine the heliocentric distances at which they dominate CME dynamics. Results of solar wind drag and Lorentz force analysis are described in Chapter 4.

Table 3.1: Column 1 represents the CME no. with reference to Table 2.1. Columns 2 and 3 denote the *in-situ* solar wind proton density and speed observed at 1 AU, one-two days in advance of the CME arrival. Column 4 is the final observed height (h_{COR}) in the COR2 FOV and column 5 indicates the mass at this height in units of 10^{15} gms. Columns 6 and 7 list the critical decay index ($n_{cr} = 3/2 - 1/4c'_{eq}$) and the decay index ($n$) chosen for each CME, respectively.

No.	n_{wind} (cm^{-3})	v_{wind} (kms^{-1})	COR2 final height(h_{COR}) ($R_\odot$)	Mass at h_{COR} (10^{15}gm)	n_{cr}	n
1*	3.60	380	15.43	2.90	1.36	2.5
2*^{f}	7.10	470	14.28	5.85	1.35	1.6
3*	3.60	440	12.57	7.30	1.38	1.9
4*	3.50	500	15.86	2.30	1.37	2.5
5*	4.00	320	15.93	7.65	1.34	1.6
6*	3.80	350	15.43	7.14	1.37	1.7
7	6.10	321	17.60	4.15	1.34	1.6
8	9.00	320	15.29	7.86	1.36	1.6
9*	2.50	440	16.36	5.35	1.33	2.1
10	2.25	550	14.07	3.13	1.35	2.5
11*	3.00	360	16.71	4.72	1.38	1.9
12	5.00	375	14.52	5.61	1.36	2.5
13	3.70	455	18.52	10.30	1.37	1.6
14^f	8.00	470	16.86	4.98	1.33	1.6
15^f	7.50	445	13.94	3.17	1.35	1.9
16^f	2.00	355	16.01	6.17	1.29	1.6
17	2.13	468	14.89	4.87	1.33	1.7
18^f	8.00	300	18.22	1.31	1.31	2.1
19	3.00	260	16.37	3.61	1.33	2.1
20	8.42	411	14.22	3.01	1.35	2.2
21^f	7.00	310	18.22	9.17	1.33	3.0
22^f	6.00	416	13.92	14.76	1.32	3.0
23^f	4.00	420	17.60	12.45	1.34	3.0
24^f	1.00	533	15.79	10.04	1.29	1.9
25	10.00	325	16.37	5.93	1.37	1.6
26^f	3.23	324	14.83	5.65	1.35	1.6
27^f	3.20	355	13.91	14.80	1.33	1.6
28^f	7.00	320	15.78	8.96	1.34	1.6
29	6.00	320	15.46	6.72	1.36	1.6
30	5.00	280	12.37	3.70	1.38	1.6
31	13.00	290	15.14	5.19	1.33	2.9
32	7.00	370	16.68	3.45	1.32	1.7
33^f	4.50	470	19.14	1.74	1.36	1.8
34^f	3.30	445	16.37	15.10	1.39	1.6
35^f	10.00	420	12.68	3.33	1.34	2.5
36^f	11.00	260	16.37	13.73	1.34	2.1
37^f	5.50	381	18.83	5.25	1.35	1.7
38^f	15.00	367	16.68	4.87	1.35	1.9

Chapter 4

Results and Discussion

Using coronagraph data we shortlist a set of 38 CMEs for this study. For all CMEs in our sample, we solve the 1D solar wind drag model to first determine the heliocentric distances beyond which the solar wind drag dominates CME dynamics. We then compute the Lorentz force acting on the CMEs based on the torus instability model. Comparative analysis of the two forces at different heights and the individual force profiles are discussed in this chapter for all the events. These results have been published in Sachdeva et al. (2015) and Sachdeva et al. (2017).

4.1 Introduction

In order to understand CME dynamics, it is essential to investigate the forces that act on it as it propagates through the interplanetary medium. The two major forces in this regard are the solar wind aerodynamic drag and Lorentz force. We seek to quantify the relative contributions of each of these forces as a function of the heliocentric distance. First, we use the solar wind drag-only model to determine the height beyond which the drag is dominant. Then, we evaluate the magnitude of the Lorentz force that accelerates the CMEs, using the torus instability model prescription. We begin with a brief discussion of the CME sample set, followed by the force analysis method used to determine the heights where these forces govern the CME propagation by comparing the model predictions with observations. Results for all the CMEs in our sample are described in this chapter.

4.2 Sample Description

Using STEREO, SOHO LASCO and *WIND* observations we build a sample of 38 Earth-directed CMEs based on the selection criteria described in Chapter 2. These instruments provide continuous tracking of the CMEs from three view-points which makes this a well-observed sample with detailed observations of 3D evolution of these CMEs. Using the geometrical fitting technique of Graduated Cylindrical Shell (GCS) model, these CMEs are 3D reconstructed. The GCS fitting provides information regarding various geometrical parameters like the observed height-time profile, CME minor radius and derived parameters like CME area and width. Our sample includes CMEs with initial velocities ranging between $47 - 2400$ km s^{-1} . 18 of these CMEs are labeled as "fast" CMEs having initial speeds, $v_0 > 900$ km s^{-1} while the remaining are slow CMEs.

Figure 4.1 shows the initial observed height (h_0), fitted using the GCS technique plotted as a function of the initial velocity of each CME. Blue spheres indicate slow CMEs and black spheres represent fast CMEs. We do not find any significant distinction in this regard, between the slow and fast CMEs. This color scheme (blue spheres - slow CMEs and black spheres - fast CMEs) is followed throughout this work. About 60 % CMEs in our sample have the first observed height as low as $3-5$ R$_\odot$. The limited time cadence of the LASCO C2 coronagraph might affect the h_0 values for fast CMEs. Owing to this, faster CMEs have fewer data points in the range $3-10$ R$_\odot$.

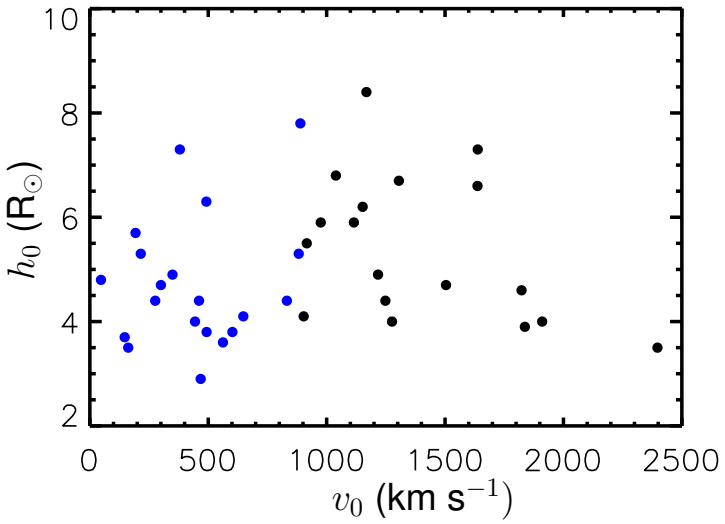


Figure 4.1: Initial observed GCS fitted height (h_0) at the first time-stamp is shown in the figure for each CME in our sample referenced by the CME initial velocity (v_0). Blue spheres indicate slow CMEs and black spheres represent fast CMEs. Details in Table 2.2

4.3 Part 1 - Aerodynamic Drag

The first part of this work focuses on studying the affects of the solar wind aerodynamic drag on CMEs using the drag-only model described in detail in Chapter 3. Assuming that only drag force is acting, we consider the 1D drag-only model (Equation 3.2). In other words, Lorentz forces are not included, and we consider only the F_{drag} term in Equation 3.1. This drag model incorporates a physical prescription for the collisionless solar wind viscosity which determines the non-constant drag coefficient ($C_{\rm D}$) definition (Equation 3.8). Using observationally derived parameters (from GCS fitting) and *in-situ* observations, we determine the quantities, A_{cme}, V_{sw}, n_{sw} and $C_{\rm D}$. Then we solve the drag equation and compare the model solutions with the height-time data.

The 1D differential equation for drag force (Equation 3.2) is solved for all events, (a) from the first observed height and (b) at progressively larger heights. At each height the parameters corresponding to that particular heliocentric distance are used. The initial velocity, determined via polynomial fitting to the data is used as an initial condition to the equation. It corresponds to the height at which the model is initiated. The solution of this 1D aerodynamic drag equation is a model-predicted velocity profile of each CME (subjected exclusively to a drag force). The output of Equation 3.2 is then integrated to obtain a height-time trajectory predicted by the model which is compared to the observed height-time profile.

These observed height-time profiles (from GCS fitting) and the model predictions are shown in Panel (a) of Figures 4.9 – 4.27 for all CMEs in the sample. Each plot is marked by the CME number with which it is referenced in Table 2.1. Plots for fast CMEs (initial velocity $v_0 > 900\,km\,s^{-1}$) are indicated by a (f) in the CME serial number. Observed height-time data points from the GCS fitting (see Chapter 2) are denoted by black diamond symbols in all the plots. The dash-dotted line (red) shows the model predicted height-time profiles when the drag-only model is initiated from the first observed height (h_0). On the other hand, the solid (blue) line indicates the model solutions when it is initiated at a later height ($\widetilde{h}_0$).

A jump in the height-points is seen in some plots. This is due to a change in the observing instrument. In particular, while transitioning from COR2 to HI1 instrument, there is a time-gap in the observations which leads to a jump in fitted height. Sometimes, the HI1 observations are too faint initially for a clear GCS fit and the later images when fitted can lead to a few missing height points. Error bars (± 0.2 $R_\odot$ for COR2, ± 1 $R_\odot$ for HI1 and ± 10 $R_\odot$ for HI2) are shown in all the plots.

4.3.1 Fast CMEs

CMEs with initial velocity $v_0 > 900$ km s^{-1} are referred to as "fast" CMEs in this study. These are indicated by a superscript (f) in Table 2.2 in Chapter 2 and all subsequent tables. Plots titled "f" in Figures 4.9 – 4.27 show the observed and predicted height-time profiles for all the 18 fast CMEs in our sample. Each plot indicates the modeled (red dash-dotted line) and observed height-time (black diamond symbols) profile for fast CMEs. When the 1D drag-only force equation is solved for all the events, we find that the model solutions agree reasonably well with the observed CME trajectory from the first data point (h_0) for the fast CMEs. In other words, for fast CMEs, the drag force is dominant from as early as the first observed height (in the range 3.5-8.4 R$_\odot$). How well the predicted model solutions fit the data is determined using the coefficient of determination (also called R squared). Model solutions with $R^2 > 98\%$ are considered acceptable.

For some events we note that the height-time plots look roughly like a straight line. This might suggest that the CME speed is nearly constant (*e.g.*, CMEs 15, 16, 27, 34); however, this is not the case. The profile looks like a straight line when the complete height-range is scaled down to fit the frame. In fact, in most cases the CME speeds decrease by 20-60 % of the initial speeds. We also see curved profiles in events CME 21, 22, 35, 36 etc. In some cases, the modeled CMEs are slightly faster than the observed CMEs (*e.g.,* CMEs 2, 9, 19, 20). That is, the model predicts that the CME reaches the final observed height (h_f; Table 4.1) earlier than it is actually observed. Some predicted profiles agree quite well with the data (*e.g.*, CMEs 16, 26, 28, 34, 36 and 37). About 5 of the 18 fast CMEs, decelerate by more than $\sim$ 500 km s^{-1} from their initial height up to the last predicted height $\widetilde{h}_f$ (see, Table 4.1). The first observed height (h_0) for fast CMEs in our sample lies between 3.5 and 8.5 R$_\odot$. Since the drag-only model considers only the effects of aerodynamic drag force, it can be claimed that solar wind aerodynamic drag is the dominant force for these CMEs, from as low as 3.5 R$_\odot$. This result is in general consensus with most existing reports on fast CMEs being drag dominated above only a few solar radii.

4.3.2 Slow CMEs

Next, we consider the remaining 20 (slower) CMEs in our sample. These CMEs have initial velocities ranging between $47 - 900$ km s^{-1} . In general, it is believed that Lorentz self-forces are dominant for the initial part of CME trajectory, while aerodynamic drag takes over at larger heights (*e.g.*, Michalek et al., 2015). Some authors (*e.g.*, Lewis and Simnett, 2002) claim that slow CMEs are exclusively dragged *up* by the solar wind. Mishra and Srivastava

(2013) apply the drag-based model to explain observations of slow CMEs over their entire trajectory while others, (*e.g.*, Byrne et al., 2010; Carley et al., 2012; Gopalswamy, 2013) think that solar wind aerodynamic drag becomes dominant for slow CMEs beyond a few solar radii.

When the drag-only model analysis (as described for fast CMEs) is repeated for the slower events in the sample, we find a considerable discrepancy between the modeled and observed CME profiles. This is evident from plots for slower CMEs in Figures 4.9 – 4.27. The height-time data and the model predicted solutions (red dash-dotted line) disagree substantially for these CMEs when the model is initiated from the first observed height (h_0) which lies in the range $2.9-7.8$ $R_\odot$ for slow CMEs. This means that the momentum coupling between the CME and solar wind alone is not sufficient to describe the observed CME dynamics for these CMEs in our sample. Therefore, these events cannot be considered drag-dominated from the start. In order to find the height beyond which the solar wind aerodynamic drag "takes over" their propagation, we initiate the drag-only model at progressively later heights. In other words, we begin solving the drag equation at larger heights to find the height at which the predicted and observed height-time profiles agree reasonably well with each other. Our method is depicted as a flowchart in Figure 4.2. The height at which this agreement is achieved is denoted by $\widetilde{h}_0$ and the corresponding CME velocity at this height which is used as an initial condition is denoted by $\widetilde{v}_0$.

In the plots for slower CMEs in Figures 4.9 – 4.27, the predicted solutions when the model is initiated at $\widetilde{h}_0$, are indicated by a blue solid line. The quantities $\widetilde{h}_0$ and corresponding $\widetilde{v}_0$ are listed in Table 4.1 for all the CMEs. For fast CMEs (described in the previous section), the initiation height $\widetilde{h}_0$ is same as the first observed height h_0 and so is the initial velocity i.e. $\widetilde{v}_0$ is same as v_0. Since the model we use (Equation 3.2) does not include any other force except the solar wind drag, it can be definitively stated that the slower CMEs in our sample ($v_0 < 900$ km s^{-1}) are not drag-dominated below the height $\widetilde{h}_0$. We find that the height $\widetilde{h}_0$ lies between $12-50$ $R_\odot$ for these slow CMEs (Table 4.1). In other words, the ambient solar wind drag force can be considered to be the dominant force influencing the CME trajectory beyond $12-50$ $R_\odot$ for the slow CMEs in our sample.

Figure 4.3 shows this heliocentric distance ($\widetilde{h}_0$) corresponding to the initial velocity (v_0) of each CME. Independent studies using empirical fitting parameters have also confirmed that slower CMEs are drag-dominated only beyond ≈ 20 $R_\odot$ (*e.g.*, Temmer and Nitta, 2015, Žic et al., 2015). Borgazzi et al. (2009) discuss the CME dynamics using drag-only models only beyond ~ 30 $R_\odot$. It can be concluded therefore, that below these heights, other forces, such as Lorentz forces must be taken into account. The solar wind interaction with CMEs tends to equilibrate their speeds, *i.e.* a CME will

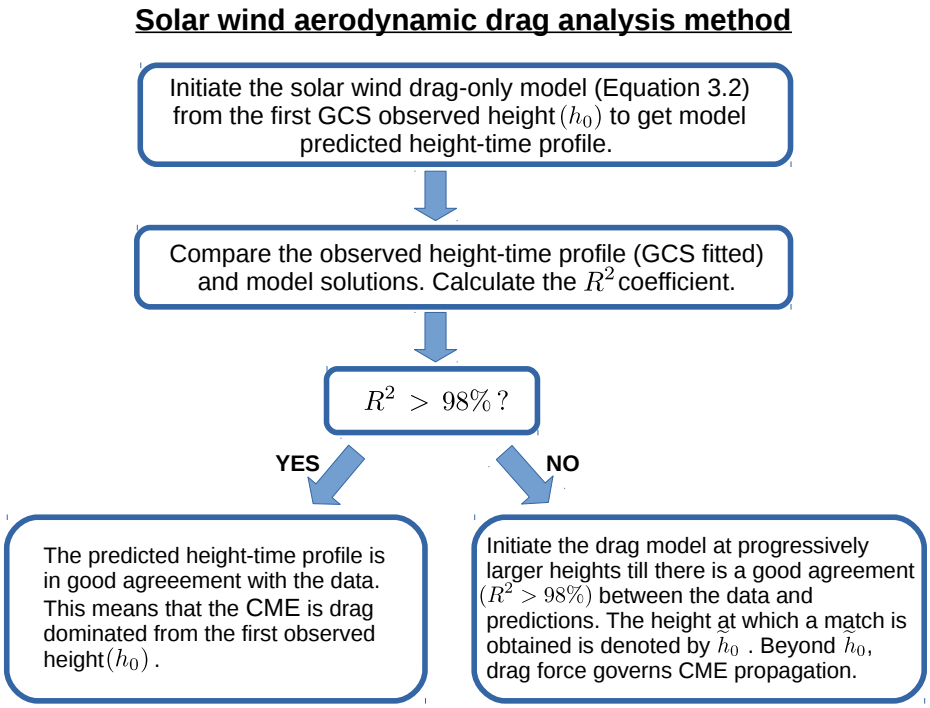


Figure 4.2: Flowchart describing the solar wind drag force analysis method for all CMEs.

accelerate or decelerate to match the speed of the solar wind. An important point to note here is that most of the slower CMEs show little or no evolution in their speeds beyond $\widetilde{h}_0$. CME 31 decelerates the most above $\widetilde{h}_0$, from $\widetilde{v}_0 \sim 597$ km s^{-1} to ~ 470 km s^{-1} at $\widetilde{h}_f$. For several slow CMEs, the speeds stay roughly constant for heliocentric distances $> \widetilde{h}_0$. Above this height, the drag-based model tends to perform quite well, therefore, it can be said that the ambient solar wind aerodynamic drag does not do much for these CMEs. Since the deceleration is so small, using models with constant $C_{\rm D} \sim 0$ yield good results. Therefore, initiating drag-only models above $\widetilde{h}_0$ does not constrain these models to any significant extent, and only reinforces the fact that most slow CMEs do not accelerate or decelerate much beyond $\widetilde{h}_0$.

Final height: observations versus model predictions

Column 4 in Table 4.1 indicates the final observed height (h_f) derived from the GCS fitting for all CMEs. For CMEs that are indicated with a superscript $*$, the observations extend up to HI2 (Sachdeva et al., 2015) while the remaining events are observed till the HI1 FOV (~ 80 R$_\odot$). $\widetilde{h}_f$ (Column 5 of Table 4.1) denotes the final predicted height when the drag-only model is initiated at $\widetilde{h}_0$. The difference between them is represented by the quan-

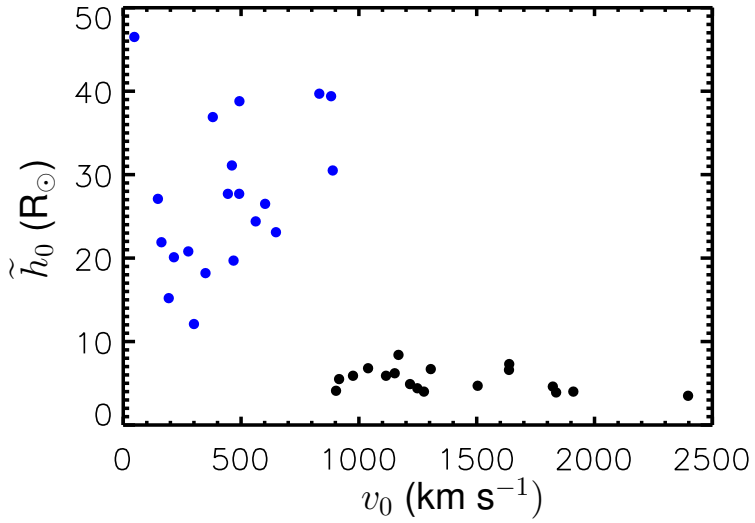


Figure 4.3: Height beyond which the solar wind drag model solutions match the observed CME propagation ($\widetilde{h}_0$) is plotted as a function of CME initial velocity. Blue spheres indicate slow CMEs and black spheres represent fast CMEs. Details in Table 4.1.

tity $\Delta\widetilde{h}_f = h_f - \widetilde{h}_f$. For all CMEs except CME 2, $0.2 < \Delta\widetilde{h}_f < 10$ $R_\odot$. For CME 2, $\Delta\widetilde{h}_f$ is -31.7 $R_\odot$. A positive $\Delta\widetilde{h}_f$ indicates that the model underpredicts the final height (when compared to the observed height h_f) and vice-versa. We find that for about 79 % of the CMEs in the sample, $\Delta\widetilde{h}_f$ is less than 5 $R_\odot$. This is another indication of how well the drag-only model predicts the observed trajectory.

C_D prescription (Equation 3.8) versus constant C_D

The last column of Table 4.1 lists the range of values of the drag coefficient C_D derived using Equation 3.8 (Subramanian et al. (2012) prescription for C_D), for all the CMEs. We also use constant C_D values and solve the Equation 3.2. Constant C_D models with values outside the range mentioned in Table 4.1 perform poorly. As an example, we show this result for CME 2 in Figure 4.9. The model solutions with constant C_Ds of 0.1 (green dash-dotted line) and 5 (brown dash-dotted line) disagree considerably with the observed height-time data for CME 2. The Subramanian et al. (2012) prescription for drag coefficient (Equation 3.8) is therefore a good guide for constant C_D models. In other words, only those constant C_D drag-only models with C_D values that are close to those predicted by Equation 3.8 agree reasonably well with the data.

How robust are our conclusions?

We consider as an example, CME 2 which has a starting speed of 916 $\mathrm{km\,s^{-1}}$ and decelerates to $\sim 715\ km\,s^{-1}$. The Sun-Earth travel time for CME 2 was observed to be $\approx$ 60 hours and the model predicts that the CME arrives at the Earth around 8 hours earlier. This means that modeled CME is somewhat faster than the observed one representing an error of 14%. Our time of arrival (ToA) errors are comparable to the values of $\approx$ 10-12 hours obtained from MHD models (Mays et al., 2015) and drag-based models (Shi et al., 2015). Although we have used observational data (obtained by GCS fitting) as much as possible for the model, there is some room for uncertainty in the quantity r_a (Equation 3.12). We find that a 50 % increase(decrease) in r_a results in a 3.7% increase(decrease) in the predicted CME travel time. Thus, our results are not very sensitive to the precise value of r_a. Errors in the GCS flux-rope fitting procedure can also lead to errors in the measured cross-sectional area of the CME. When A_{cme} is decreased by 50 %, the CME travel time decreases by 6 %.

To summarize, we find that CMEs that travel with initial velocity $v_0 >$ 900 km $\mathrm{s^{-1}}$, are drag-dominated from very early on. The solar wind decelerates fast CMEs from heights as low as $3.5-4\ \mathrm{R_\odot}$. However, in case of slower CMEs, momentum coupling with the ambient solar wind does not satisfactorily describe the observed dynamics from very low heights. Instead, we find that these CMEs are drag dominated only above $12-50\ \mathrm{R_\odot}$. This conclusion is independent of the specific C_D model used (Subramanian et al. (2012); Sachdeva et al. (2015) or a constant C_D). We now investigate the effect of forces at heights $< \widetilde{h}_0$. We also use Equation 3.2 to calculate the magnitude of the drag force for heights $> \widetilde{h}_0$ for all CMEs.

4.4 Part 2 - Lorentz Force

We now consider the F_{Lorentz} term in Equation 3.1 which describes the driving Lorentz force acting on CMEs. Most Lorentz force models concerned with CME initiation predict that the total Lorentz force profile increases up to a peak at a certain heliocentric distance and decreases thereafter. Various models described in literature cater to such a profile by either tailoring the injected poloidal flux (or equivalently, the driving current) (Chen and Kunkel, 2010) or rely on the external Lorentz forces to decrease rapidly enough (with heliocentric distance) for the CME to "launch" (Kliem and Török, 2006; torus instability (TI) model). Kliem et al. (2014) have also shown the equivalence of TI and the catastrophe mechanism for CME eruption (Forbes and Isenberg, 1991).

To evaluate the magnitude of the Lorentz force acting on CMEs, we require the CME current (I) and equilibrium current (I_{eq}) at h_{eq} (which relates to the equilibrium value of external field $B_{ext}(h_{eq})$), calculated using Equations 3.21 and 3.22 (section 3.5.1). The final expression used for the Lorentz force acting on a CME is given by Equation 6.14 in Appendix 6.2. For each CME, we use the quantities derived from the GCS fitting technique to calculate the Lorentz force. The decay index n (Table 3.1) is such that the drag force is larger in magnitude compared to the Lorentz force above $\widetilde{h}_0$; it also ensures, $n > n_{cr}$. Thus, n is the minimum value that requires $|F_{drag}| > F_{Lorentz}$ for $R > \widetilde{h}_0$. For a given value of n, the quantity I_{eq} (and equivalently $B_{ext}(h_{eq})$) is determined by the condition $|F_{drag}(\widetilde{h}_0)| = F_{Lorentz}(\widetilde{h}_0)$. Thus, by equating the two forces at $\widetilde{h}_0$, the equilibrium current (I_{eq}) and hence, the external poloidal field (B_{ext}) at equilibrium (h_{eq}) can be constrained. For the sake of concreteness the equilibrium position of the flux rope (where the Lorentz self-force and external forces balance each other) is taken to be $h_{eq} = 1.05$ R$_\odot$ for all CMEs in our sample.

The GCS fittings to the CME events begin at the time of first observation in the COR2 FOV. This observed GCS height denoted by h_0 (Table 2.1) lies between 2.9 – 8.4 R$_\odot$ for our sample. Other derived GCS parameters like the flux-rope aspect ratio (R/R_{cme}), (R_{cme} is the minor radius), are also available at each observed height (R) beginning from h_0 (first observed height). We assume that the aspect ratio at heliocentric distances between h_{eq} and h_0 is the same as the ratio at h_0. In other words, we assume that the CME expands self-similarly from h_{eq} to h_0. For heights beyond h_0, the aspect ratio is obtained using the observed quantities R and minor radius R_{cme} derived using the GCS technique.

For each CME, we calculate the Lorentz force between h_{eq} and the final observed height (h_f) with observed values of R, minor radius (R_{cme}) and $l_i = 1/2$. In Figures 4.9 – 4.27, each plot in Panel (b) shows the Lorentz force profile versus the heliocentric distance of the CME leading edge (R) for all CMEs. The red solid line indicates the Lorentz force evaluated at heights between h_{eq} and h_0 (using a constant R/R_{cme}). Beyond h_0, the open diamond symbols (connected by a red dotted line) represent the Lorentz force derived using observations. The blue vertical dashed line denotes the position of $\widetilde{h}_0$ which is the height at which solar wind drag takes over. In case of fast CMEs (indicated by f, alongside the CME number), this line indicates the position of the first observed height (h_0).

For each CME, I_{eq} and $B_{ext}(h_{eq})$ are listed in Table 4.2 . The equilibrium current (I_{eq}) is in units of 10^{10} Amperes. These estimates are in general agreement with the average axial current calculated by Subramanian and Vourlidas (2007). B_{ext} at $h_{eq}(= 1.05$ R$_\odot)$ is in units of 10^{-1} Gauss. Figure 4.4 shows the equilibrium CME current and magnetic field for all the CMEs as

a function of the initial velocity. In general, for slower CMEs (blue spheres), both these quantities are smaller in magnitude when compared to their values for faster CMEs. The Lorentz force magnitude (in units of 10^{17} dynes) at $\widetilde{h}_0$ is also indicated in Table 4.2 for all CMEs. It is equal to the absolute drag force at this height. Panel (a) of Figure 4.5 depicts the magnitude of the Lorentz force at $\widetilde{h}_0$ versus the initial velocity (v_0) for each CME in our sample. It is equal to the absolute magnitude of the drag force at this height.

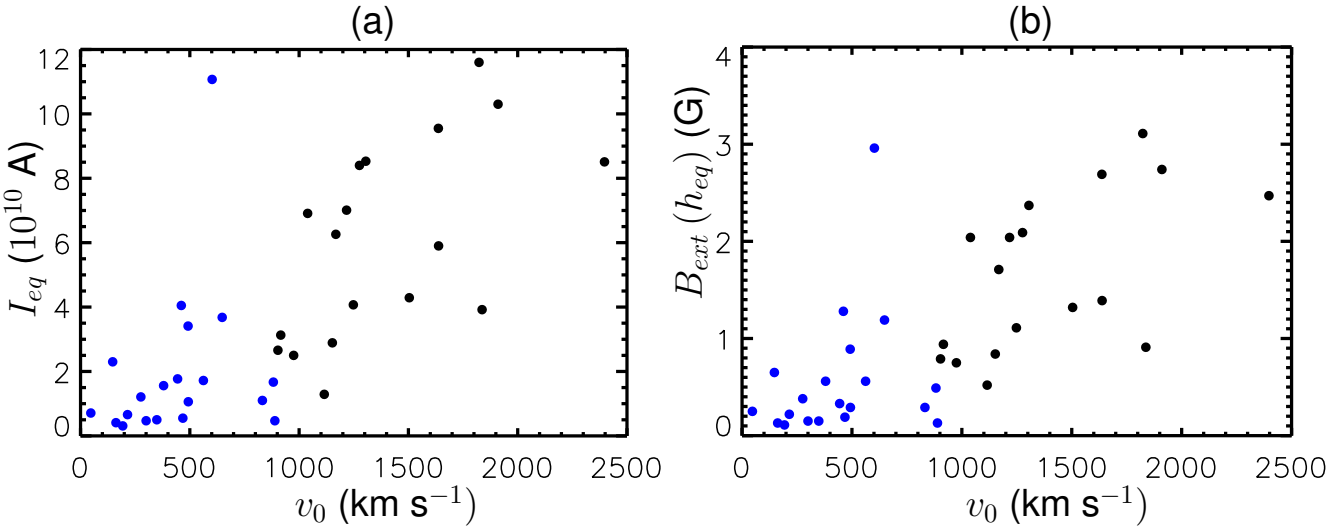


Figure 4.4: Plots of Lorentz force parameters, CME current and external magnetic field at equilibrium, as a function of CME initial velocity (v_0). Panel (a) shows the CME current (I_{eq}) at equilibrium position (h_{eq}) *versus* the CME initial velocity (v_0). Panel (b) is a plot of the external poloidal magnetic field ($B_{ext}(h_{eq})$) at the equilibrium height (h_{eq}) *versus* the initial velocity (v_0). Details in Table 4.2.

Lorentz force peak at h_{peak}

For both fast and slow CMEs, we note that the Lorentz force profile increases steeply from h_{eq} to reach its maximum at a height denoted by "h_{peak}" (in Table 4.2) and then decreases gradually. This quantity h_{peak} lies in the range, $1.65-2.45$ R$_\odot$. Panel (b) of Figure 4.5 plots the quantity h_{peak} for each CME as a function of the CME initial velocity (v_0; Table 2.2). The blue symbols represent slow CMEs ($v_0 < 900$ km s^{-1}) while symbols in black represent fast CMEs ($v_0 > 900$ km s^{-1}). There are no noticeable trends distinguishing slow and fast CMEs.

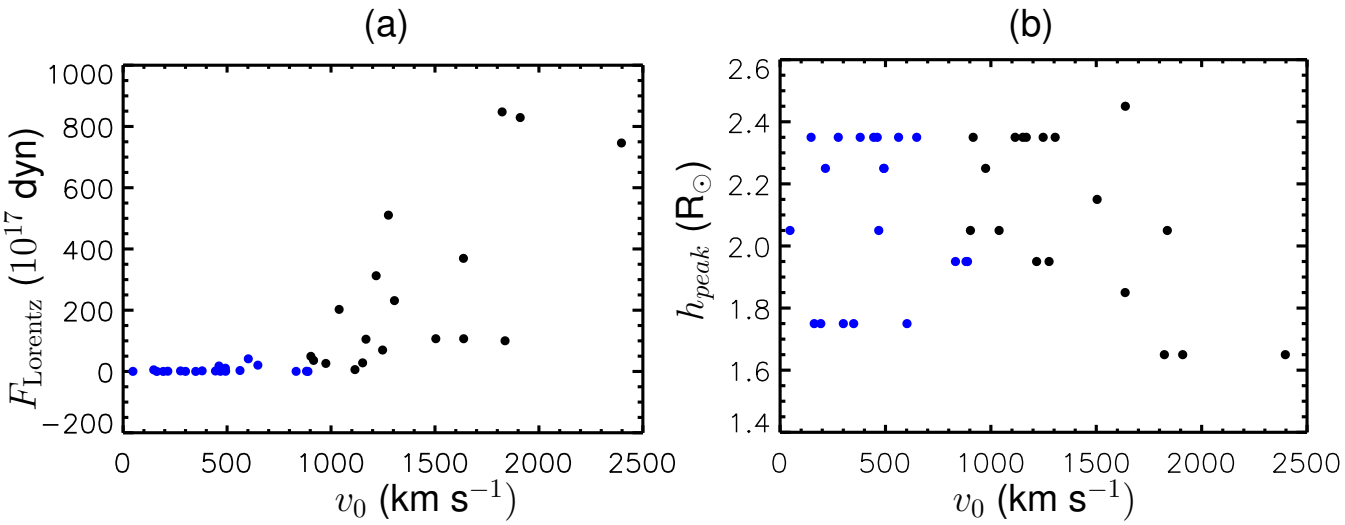


Figure 4.5: Panel (a) depicts the magnitude of the Lorentz force ($F_{\rm Lorentz}$) at $\widetilde{h}_0$ in units of 10^{17} dyn as a function of CME initial velocity, v_0. Panel (b) shows the heliocentric distance, h_{peak} where the Lorentz force achieves its maximum value as a function of CME initial velocity, v_0 (see Table 4.2. Symbols in blue represent slow CMEs (*i.e.* $v_0 < 900$ km s^{-1}) and symbols in black represent fast CMEs ($v_0 > 900$ km s^{-1}).

The Fall %

A measure of how much the Lorentz force falls from its maximum value (at h_{peak}) till the height $\widetilde{h}_0$ is indicated by the quantity $Fall\,\%$ in Table 4.2. Figure 4.6 plots the $Fall\,\%$ for all events in our sample as a function of the CME initial speed (v_0) in Panel (a), and $\widetilde{h}_0 = h_0$ in Panel (b). It can be seen clearly that the $Fall\,\%$ is larger for slower CMEs (larger $\widetilde{h}_0$) in comparison to faster ones. Since fast CMEs are drag dominated from relatively early on ($\widetilde{h}_0 = h_0$), the Lorentz force decrease from its maximum value at h_{peak} is smaller compared to the decrease in case of slower CMEs ($\widetilde{h}_0 \sim 12-50$ R$_\odot$). For slower CMEs, the $Fall\,\%$ at $\widetilde{h}_0$ ($12-50$ R$_\odot$) lies between 70–98 % while for faster CMEs, it is between 20–60 % .

The decay index (n; Table 3.1) for the external poloidal field is represented in a scatterplot in Figure 4.7. We see no clear trend for n with regard to slow and fast CMEs. However, the highest n values are typically associated with the faster CMEs in the sample. n lies in the range $1.6 - 3$.

For a fixed value of n, we note that an increase in h_{eq} by 14 % increases the peak force position value by $\sim$ 15%. It decreases the $Fall\,\%$ of the Lorentz force at $\widetilde{h}_0$ (relative to its peak value) by 5%. For a fixed value of $h_{eq}(= 1.05R_\odot)$, an increase in n by 31% decreases the peak position by 17%. It also increases the $Fall\,\%$ of the Lorentz force at $\widetilde{h}_0$ (relative to its peak

value) by 19.5%.

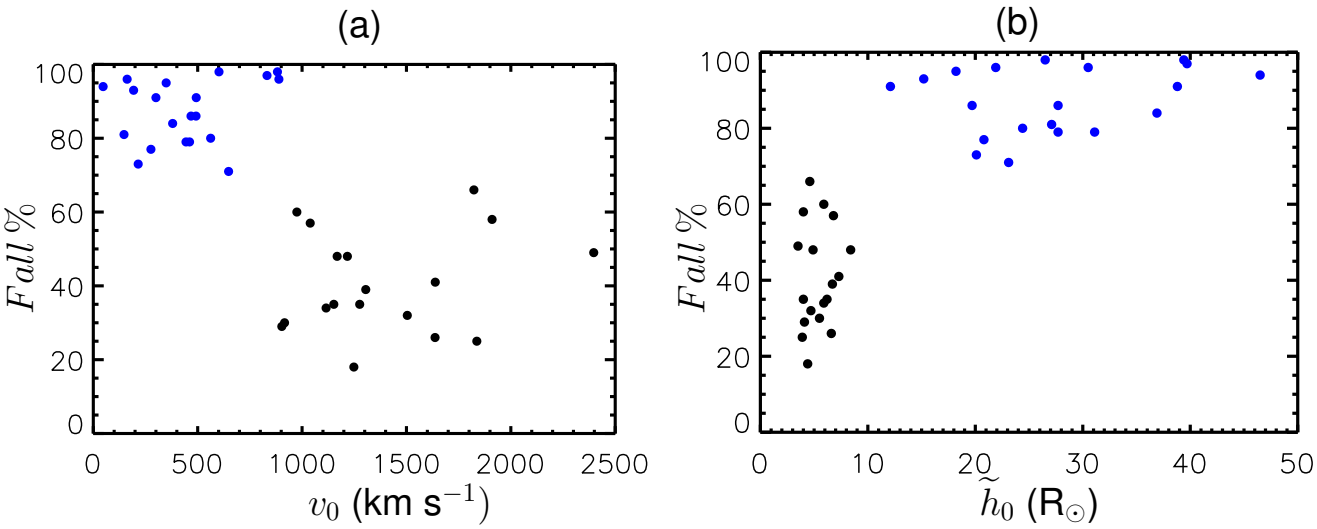


Figure 4.6: Plot of the Lorentz force $Fall\,\%$ *versus* CME initial velocity (v_0) in Panel (a) and $\widetilde{h}_0$ in Panel (b) (see, Table 4.2).

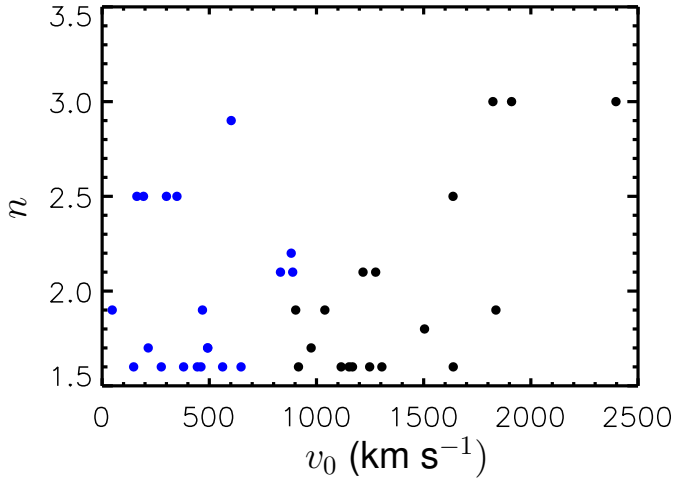


Figure 4.7: Plot of decay index (n) corresponding to CME initial velocity (v_0) (see, Table 3.1).

4.4.1 Lorentz force vs aerodynamic drag

In Panel (b) of Figures 4.9–4.27, the filled green circles represent absolute value of the aerodynamic drag force (F_{drag}) beginning at $\widetilde{h}_0$. We note that for all CMEs, the Lorentz force peaks between 1.65–2.45 $R_\odot$ but becomes negligible only by 12–50 $R_\odot$ for the slower CMEs in the sample. This means that the Lorentz force dominates the CME propagation at heights up to 12–50 $R_\odot$ for slower CMEs, beyond which the solar wind aerodynamic drag

takes over. The effects of Lorentz force for slower CMEs is therefore quite pronounced well beyond a few solar radii. However, in case of faster CMEs in our sample, the Lorentz force becomes negligible (compared to the solar wind drag) from as early as 3.5 – 4 $R_\odot$. In fact, the solar wind drag is significantly larger in magnitude in comparison to the Lorentz force beyond h_0 for fast CMEs.

Vršnak (2016) investigate the CME-flare relationship by illustrating how the CME eruption, driven by MHD (magneto-hydrodynamic) instabilities (i.e., Kink or Torus) as well as the CME acceleration and propagation are affected by magnetic reconnection. They also discuss a feedback relationship between the flare and ejection through reconnection. They find that in the absence of magnetic reconnection, the Lorentz force (or acceleration) that drives the CMEs decreases rapidly. This does not explain the observed acceleration which can be as high as several kms^{-2}. To achieve these strong accelerations, they introduce reconnection which increasingly adds poloidal flux strengthening the forces acting on the flux-rope (Chen, 1989).

Vršnak (2016) also suggest that the eruption acceleration is closely related to the impulsive phase of the flare (e.g., Hard X-ray, microwave bursts, Soft X-ray flux) (*e.g.,* Zhang et al., 2001; Vršnak et al., 2004; Zhang et al., 2004). Based on their study, CME acceleration (*i.e.*, Lorentz force) peaks at larger heights for more gradual events. Due to the addition of the poloidal flux, the Lorentz force driving is prolonged for slower events, which is also what we observe. We find that in the case of slower CMEs, the Lorentz forces are dominant upto 12-50 $R_\odot$, beyond which they become negligible and the aerodynamic drag takes over.

We conclude that the drag-only model accounts well for the observed CME trajectory when initiated at (or beyond) $\widetilde{h}_0$. This means that the Lorentz force is not important beyond this height. However, below $\widetilde{h}_0$, the Lorentz force is appreciable and governs the CME propagation. We find this to be true for 36 out of 38 CMEs in our sample. Two slow CMEs (CME 4 and CME 10) are exceptions.

Relative difference between the two forces ($F_{\rm diff}\%$)

The difference between the solar wind drag force and Lorentz driving force beyond $\widetilde{h}_0$ is significantly pronounced in case of fast CMEs as can be seen from Figures 4.9–4.27. We define a quantity,

$$F_{\rm diff}\% \;=\; \frac{(F_{drag} - F_{Lorentz})}{F_{drag}} \times 100\,\% \;,$$

which measures the relative difference between the two forces. $F_{\rm diff}$ (last column in Table 4.2) is evaluated at 40 $R_\odot$ for all events except for CME 11.

Since for CME 11, $\widetilde{h}_0 \sim 46$ R$_\odot$, $F_{\rm diff}$ is evaluated at 50 R$_\odot$ for this event and indicated by a superscript $^{\circledast}$ in Table 4.2. Figure 4.8, plots $F_{\rm diff}$% *versus* the CME initial velocity (v_0). As before, the blue circles indicate slow CMEs and black ones indicate fast CMEs. The solar wind aerodynamic drag is about 50-90 % larger than the Lorentz force at 40 R$_\odot$ for most of the fast CMEs. For slower events, however, this range lies between 0.2% and 30 %.

For some slow CMEs, the Lorentz force is only slightly smaller that the drag force even much beyond $\widetilde{h}_0$. For CMEs 4 and 10, we find that the Lorentz force magnitude is in fact larger than the solar wind drag force. This could be because the computed Lorentz force is an overestimate. In determining the Lorentz force, the torus instability model assumes the total magnetic flux to be frozen in. However, this assumption may not be entirely true. The magnetic energy is dissipated in heating the CME plasma and/or CME expansion and the total magnetic flux may not be conserved. For slower CMEs, our results suggest that it is important to take into account the energy expended in CME expansion and internal heating (*e.g.*, Kumar and Rust, 1996; Wang et al., 2009; Emslie et al., 2012).

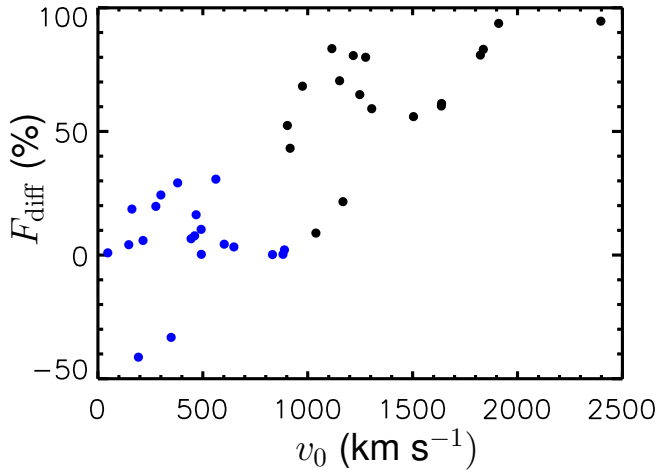


Figure 4.8: Plot of relative difference between drag and Lorentz forces as a function of CME initial velocity, v_0. $F_{\rm diff}$ % is calculated at 40 R$_\odot$ for all CMEs except CME 11, for which it is evaluated at 50 R$_\odot$ (see, Table 4.2). The blue circles represent slow CMEs and the black ones represent fast CMEs.

Reiterating the results described in Tables 4.1 and 4.2:

1. We determine the height at which solar wind drag dominates the CME dynamics. For each CME, this height ($\widetilde{h}_0$) is given in Table 4.1 together with the initiation velocity ($\widetilde{v}_0$) at this height. Fast CMEs ($v_0 > 900$ km s^{-1}) are drag dominated from very early on ($\widetilde{h}_0 = h_0 = 3.5$–$8$ R$_\odot$). For slower CMEs ($v_0 < 900$ km s^{-1}), $\widetilde{h}_0$ ranges between 12–50 R$_\odot$.

2. The difference between observed final height (h_f) and the model predicted final height $\widetilde{h}_f$ is given by $\Delta\widetilde{h}_f$. This difference lies between 0.2-10 for most of the CMEs, indicating that the drag model fits the observations well in this respect.

3. We note that the decay index n ranges from 1.6–3. The fastest CMEs typically have the highest values of n.

4. The height at which the Lorentz force peaks (h_{peak}) lies between 1.65–2.45 $R_\odot$.

5. The $Fall\,\%$ is the amount by which the Lorentz force decreases from its maximum value at h_{peak} up to $\widetilde{h}_0$. This quantity is larger for slower CMEs, $50 < Fall\,\% < 90$ as compared to faster CMEs, $20 < Fall\,\% < 60$.

6. Finally, the quantity $F_{\rm diff}\%$ evaluated at 40 $R_\odot$ (except for CME 11, where it is evaluated at 50 $R_\odot$) denotes the relative percentage difference between the two forces. For fast CMEs, $50 < F_{\rm diff}\,\% < 90$ whereas $0.2 < F_{\rm diff}\,\% < 30$ for slower ones.

A thorough understanding of "how" and "where" of the forces that affect CME propagation is needed to build reliable models for accurately predicting the CME arrival time and speed at the Earth. This work is the first systematic study in this regard using a diverse CME sample set (to the best of our knowledge). The force analysis described in this work will provide a physical basis for inputs to space weather forecast models.

Table 4.1: Parameters and results of the drag analysis for all CMEs in the sample. The first column is the serial number of each event with which it is referenced. $\widetilde{h}_0$ is the height at which the drag force takes over the CME dynamics and $\widetilde{v}_0$ is the corresponding speed at this height. h_f is the final observed GCS height. $\widetilde{h}_f$ is the model predicted final height at the same time instant as h_f. $\Delta\widetilde{h}_f = h_f = \widetilde{h}_f$. The last column indicates the predicted range of C_D values using the Subramanian et al. (2012) prescription.

No.	$\widetilde{h}_0$ ($R_\odot$)	$\widetilde{v}_0$ (kms^{-1})	h_f ($R_\odot$)	$\widetilde{h}_f$ ($R_\odot$)	$\Delta\widetilde{h}_f$ ($R_\odot$)	C_D range
1*	21.9	383	155.4	148.3	7.1	0.1-0.3
2^{*f}	5.5	916	210.0	241.7	-31.7	0.6-1.3
3*	19.7	506	195.1	191.8	3.3	0.21-0.37
4*	15.2	437	163.3	159.0	4.3	0.19-0.29
5*	27.7	490	150.3	149.1	1.2	0.38-0.55
6*	20.1	445	131.5	141.8	-10.3	0.27-0.45
7	27.1	583	59.7	60.2	-0.5	0.63-0.76
8	20.8	454	55.9	56.4	-0.5	0.46-0.53
9*	39.7	530	188.6	190.7	-2.1	0.25-0.38
10	18.2	511	42.2	42.9	-0.7	0.22-0.31
11*	46.5	456	211.0	212.0	-1.0	0.27-0.34
12	12.1	373	48.9	52.3	-3.4	0.21-0.33
13	24.4	767	77.8	76.8	1.0	0.55-0.64
14^f	8.4	1168	80.9	84.5	-3.6	1.0-1.9
15^f	4.1	903	67.7	70.4	-2.7	0.67-1.44
16^f	7.3	1638	67.1	61.3	5.8	1.41-1.93
17	38.8	636	73.6	69.4	4.2	0.38-0.42
18^f	4.0	1276	55.1	58.6	-3.5	1.63-3.05
19	30.5	313	52.6	53.1	-0.5	0.25-0.3
20	39.4	491	75.4	74.7	0.7	0.34-0.45
21^f	4.6	1823	100.0	91.6	8.4	1.4-3.4
22^f	4.0	1910	86.8	90.7	-3.9	1.87-3.5
23^f	3.5	2397	92.0	99.7	-7.7	1.7-3.23
24^f	3.9	1837	71.4	81.4	-10.0	1.24-1.83
25	23.1	684	77.9	77.5	0.4	0.76-1.1
26^f	6.2	1152	85.5	85.2	0.3	0.93-1.22
27^f	4.4	1248	72.3	82.2	-9.9	1.12-1.58
28^f	6.7	1305	87.4	86.2	1.2	1.44-2.3
29	31.1	790	70.8	70.3	0.5	0.85-1.03
30	36.9	570	88.6	89.9	-1.3	0.51-0.66
31	26.5	597	88.9	89.2	-0.3	0.77-1.38
32	27.7	668	58.5	58.3	0.2	0.8-0.98
33^f	4.7	1504	90.5	84.4	6.1	0.76-1.68
34^f	5.9	1115	86.2	84.1	2.1	0.59-0.76
35^f	6.6	1637	60.9	65.0	-4.1	1.21-2.99
36^f	4.9	1217	77.6	77.9	-0.3	1.35-2.42
37^f	5.9	975	78.2	79.1	-0.9	0.84-1.22
38^f	6.8	1039	48.7	51.4	-2.7	0.96-2.1

Table 4.2: Column 1 is the CME serial number. I_{eq} is the axial CME current at equilibrium (h_{eq}). $B_{ext}(h_{eq})$ is the external magnetic field at equilibrium. F_{Lorentz} is the Lorentz force magnitude at $\widetilde{h}_0$ (equal to $|F_{drag}(\widetilde{h}_0)|$). The position of maximum Lorentz force is indicated by h_{peak}. The $Fall\%$ is the amount by which the Lorentz force decreases from its peak value (h_{peak}) to $\widetilde{h}_0$. The last column indicates $F_{\text{diff}} = (\frac{F_{drag}-F_{Lorentz}}{F_{drag}}) \times 100\%$ at 40 $R_\odot$. For CME 11 ($^{\circledast}$), F_{diff} % is evaluated at 50 $R_\odot$.

No.	I_{eq} (10^{10} A)	$B_{ext}(h_{eq})$ (10^{-1} G)	$F_{Lorentz}(\widetilde{h}_0)$ (10^{17} dyn)	h_{peak} ($R_\odot$)	$Fall\%$ (%)	$F_{\text{diff}}\%$ (%)
1*	0.41	0.13	0.10	1.75	96	18.6
2^{*f}	3.13	0.94	36.12	2.35	30	43.2
3*	0.55	0.19	0.49	2.05	86	16.3
4*	0.31	0.11	0.12	1.75	93	-41.3
5*	1.77	0.33	1.52	2.35	79	6.6
6*	0.66	0.22	0.85	2.25	73	5.9
7	2.30	0.65	5.31	2.35	81	4.2
8	1.21	0.38	1.78	2.35	77	19.7
9*	1.10	0.29	0.42	1.95	97	0.2
10	0.50	0.15	0.19	1.75	95	-33.3
11*	0.71	0.25	0.29	2.05	94	0.9 $^{\circledast}$
12	0.47	0.15	0.33	1.75	91	24.3
13	1.72	0.56	3.11	2.35	80	30.7
14^f	6.26	1.71	105.37	2.35	48	21.6
15^f	2.66	0.79	49.41	2.05	29	52.4
16^f	5.90	1.39	106.87	2.45	41	61.3
17	1.06	0.29	0.67	2.25	91	0.3
18^f	8.40	2.09	510.45	1.95	35	80.0
19	0.47	0.13	0.11	1.95	96	2.1
20	1.67	0.49	0.79	1.95	98	0.3
21^f	11.60	3.11	847.54	1.65	66	80.9
22^f	10.30	2.74	829.15	1.65	58	93.7
23^f	8.51	2.47	746.12	1.65	49	94.6
24^f	3.92	0.91	100.22	2.05	25	83.2
25	3.68	1.19	20.68	2.35	71	3.3
26^f	2.89	0.84	28.15	2.35	35	70.5
27^f	4.07	1.11	70.02	2.35	18	64.9
28^f	8.53	2.37	231.39	2.35	39	59.2
29	4.05	1.28	17.89	2.35	79	7.8
30	1.56	0.56	2.05	2.35	84	29.2
31	11.07	2.96	41.31	1.75	98	4.4
32	3.41	0.89	10.64	2.25	86	10.4
33^f	4.29	1.32	106.99	2.15	32	56.0
34^f	1.29	0.52	6.13	2.35	34	83.5
35^f	9.55	2.69	369.41	1.85	26	60.3
36^f	7.06	2.04	312.65	1.95	48	80.7
37^f	2.50	0.75	26.29	2.25	60	68.3
38^f	6.91	2.04	202.65	2.05	57	8.9

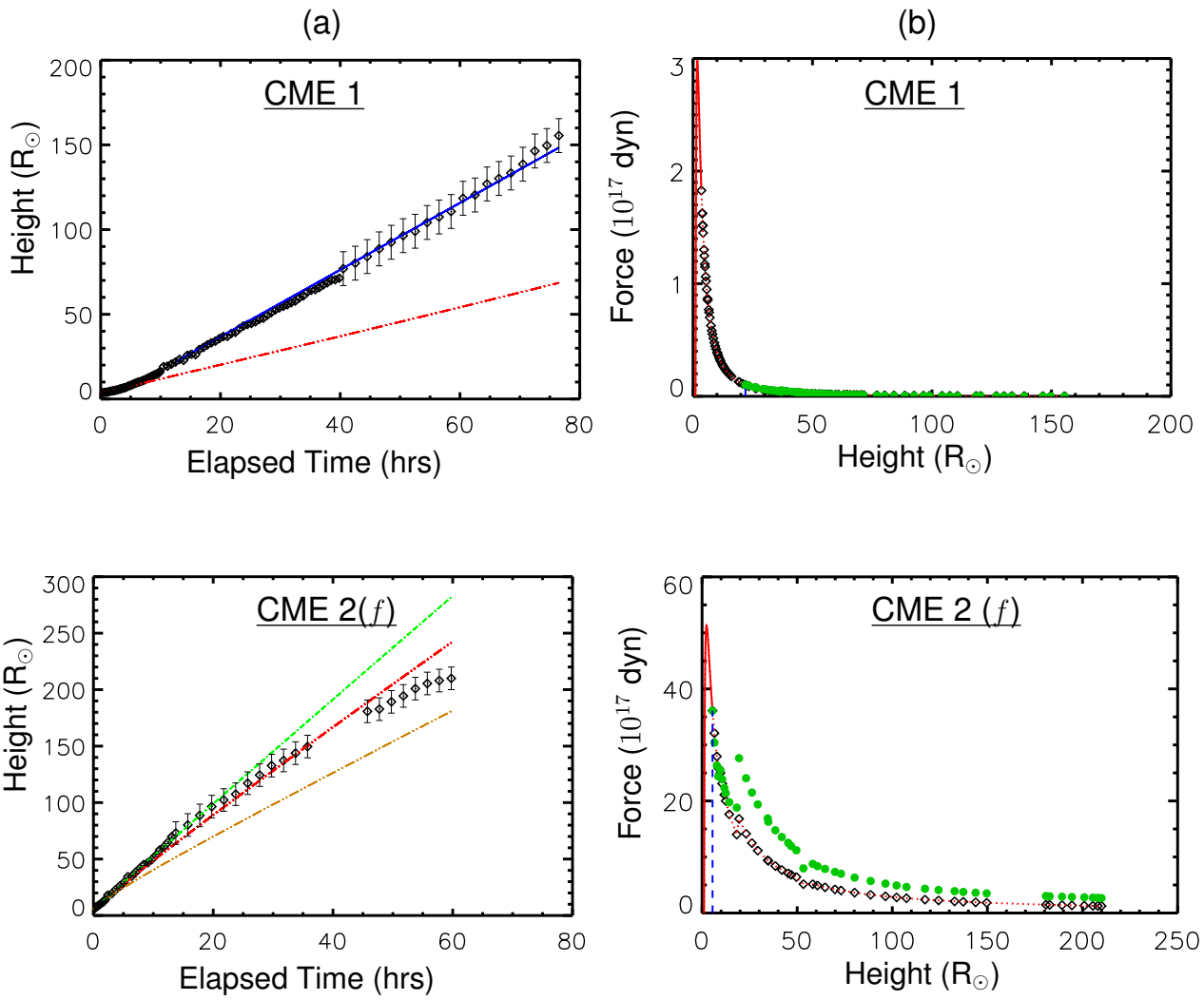


Figure 4.9: Panel (a) (first column) depicts the observed and predicted height-time profiles and Panel (b) (second column) shows the force profiles for CME 1 and CME 2. Each plot title indicates CME number referenced by Table 4.1. In Panel (a), the observed height-time data is shown with diamonds. The red dash-dotted line is the drag model solution when it is initiated from the first observed height, h_0. The blue solid line shows the predicted height-time trajectory when the drag model is initiated from height $\widetilde{h}_0$. The fast CMEs are indicated by a (f) along with the CME number. For CME 2, the height-time solutions using constant $C_{\rm D}$ of 0.1 (green dash-dotted line) and 5 (brown dash-dotted line) are also shown. In Panel (b), the open diamond symbols (connected by a red dotted line) represent the Lorentz force values derived observationally starting from h_0. The red solid line indicates the Lorentz force values for heights between h_{eq} and h_0. The filled green circles represent the absolute value of the solar wind drag force (beyond $\widetilde{h}_0$). The blue dashed vertical line indicates the height $\widetilde{h}_0$ (= h_0 for fast CMEs) at which the solar wind drag force takes over.

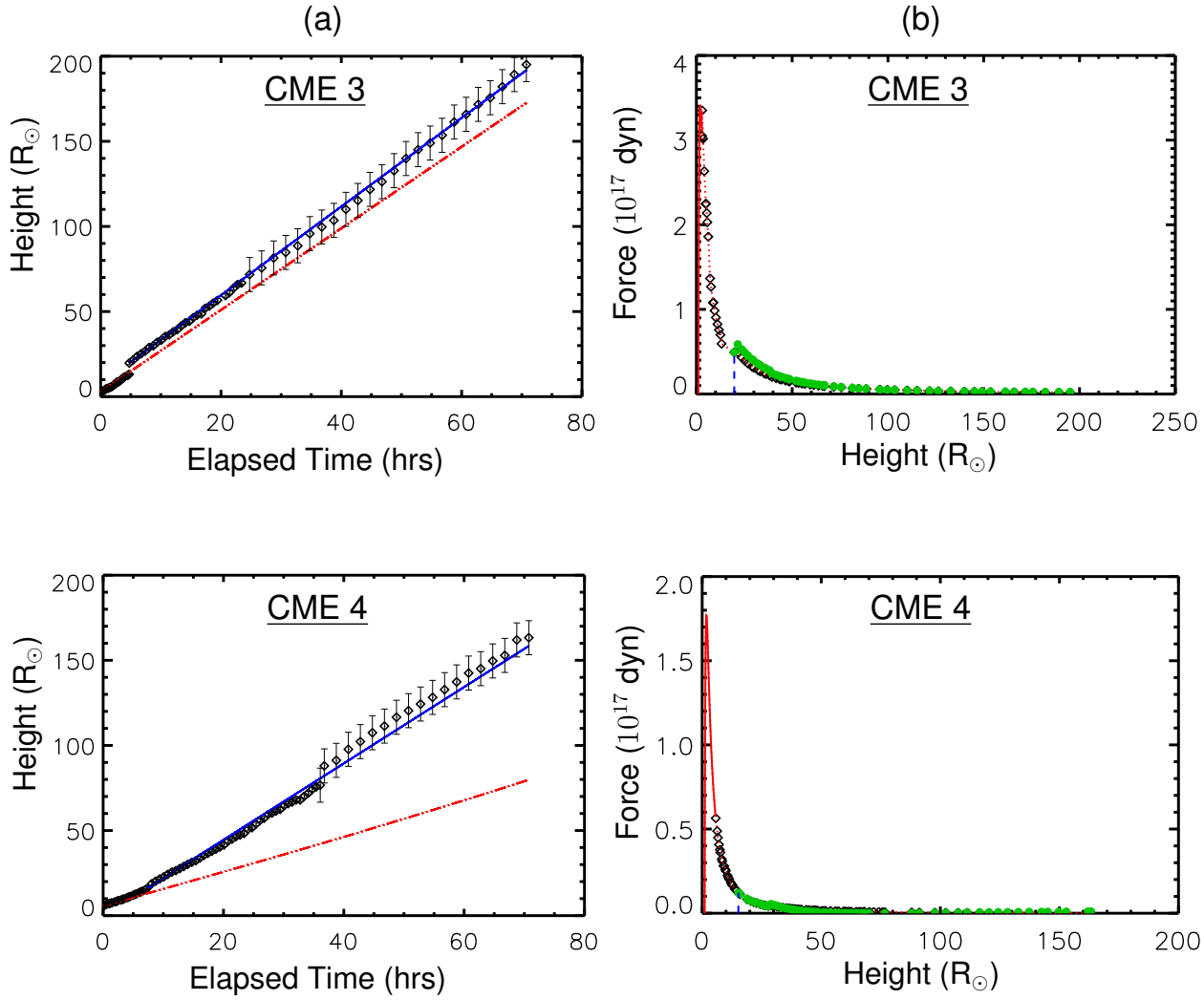


Figure 4.10: Panel (a) depicts the observed and predicted height-time profiles and Panel (b) shows the force profiles for CME 3 and CME 4. Each plot title indicates CME number referenced by Table 4.1. In Panel (a), the observed height-time data is shown with diamonds. The red dash-dotted line is the drag model solution when it is initiated from the first observed height, h_0. The blue solid line shows the predicted height-time trajectory when the drag model is initiated from height $\widetilde{h}_0$. The fast CMEs are indicated by a (f) along with the CME number. In Panel (b), the open diamond symbols (connected by red dotted line) represent the Lorentz force values derived observationally starting from h_0. The red solid line indicates the Lorentz force values for heights between h_{eq} and h_0. The filled green circles represent the absolute value of the solar wind drag force. The blue dashed vertical line indicates the height $\widetilde{h}_0$ $(= h_0$ for fast CMEs) at which the solar wind drag force takes over.

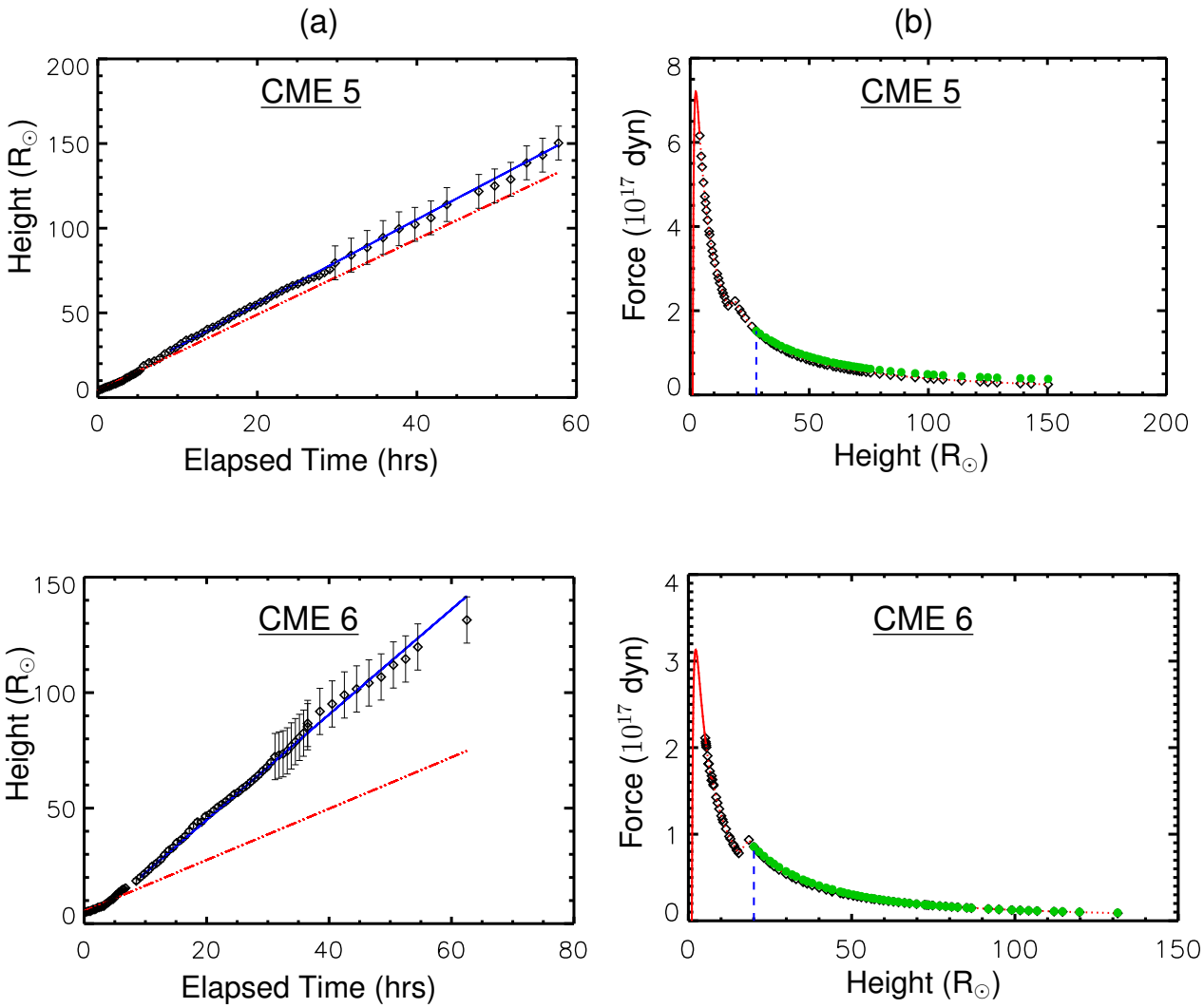


Figure 4.11: Height-time and Force profiles for CMEs 5 and 6. Caption same as Figure 4.10.

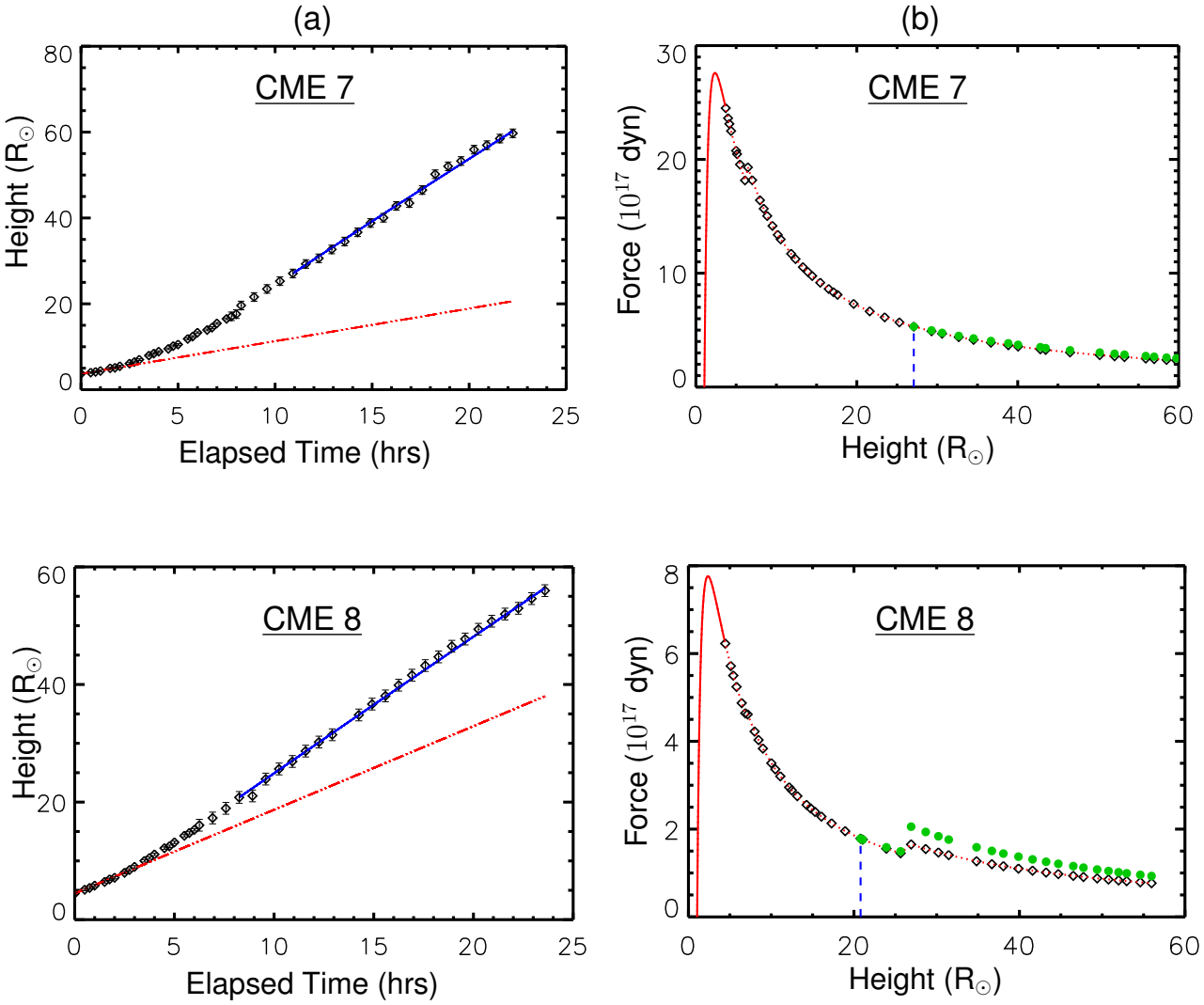


Figure 4.12: Height-time and Force profiles for CMEs 7 and 8. Caption same as Figure 4.10.

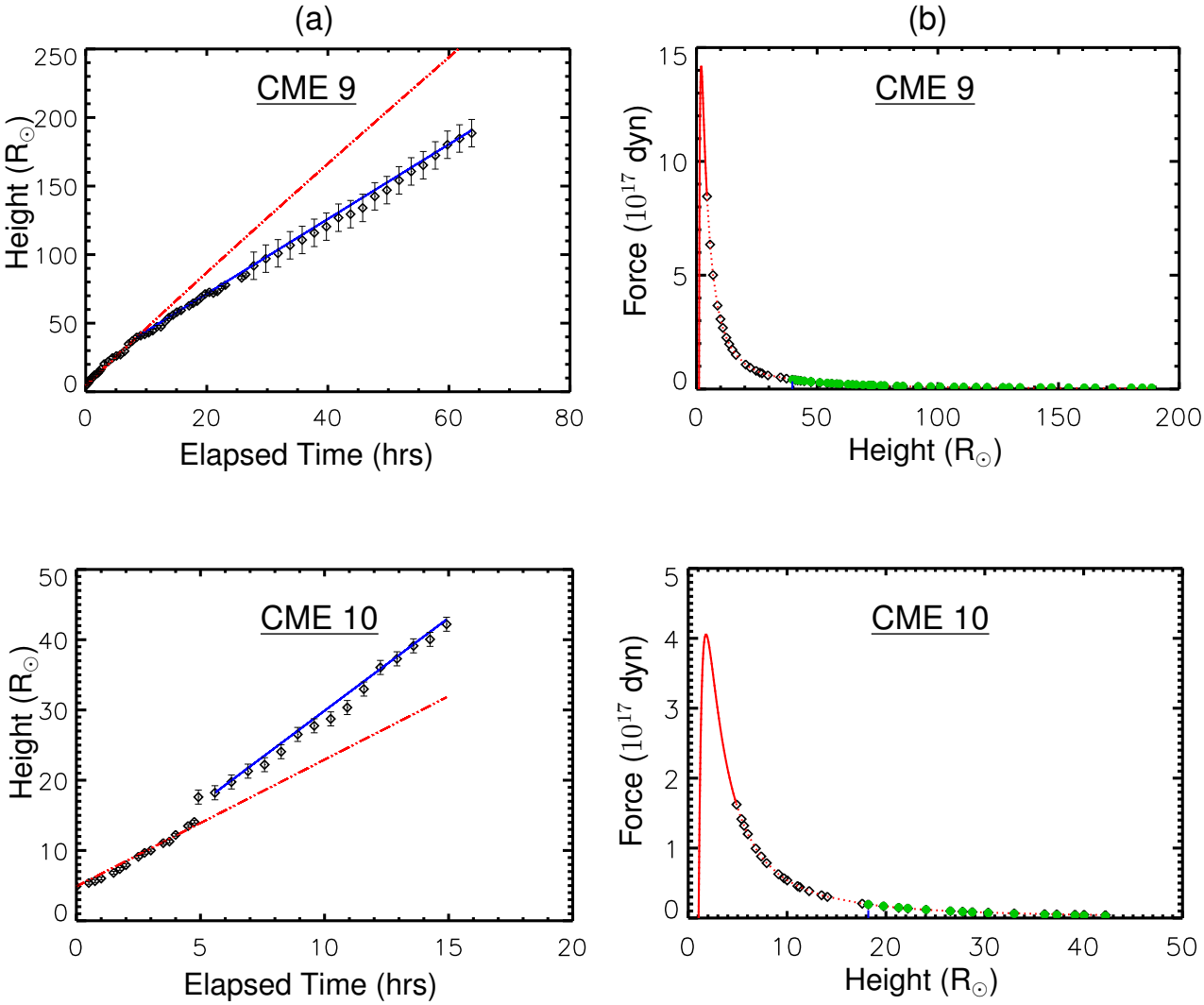


Figure 4.13: Height-time and Force profiles for CMEs 9 and 10. Caption same as Figure 4.10

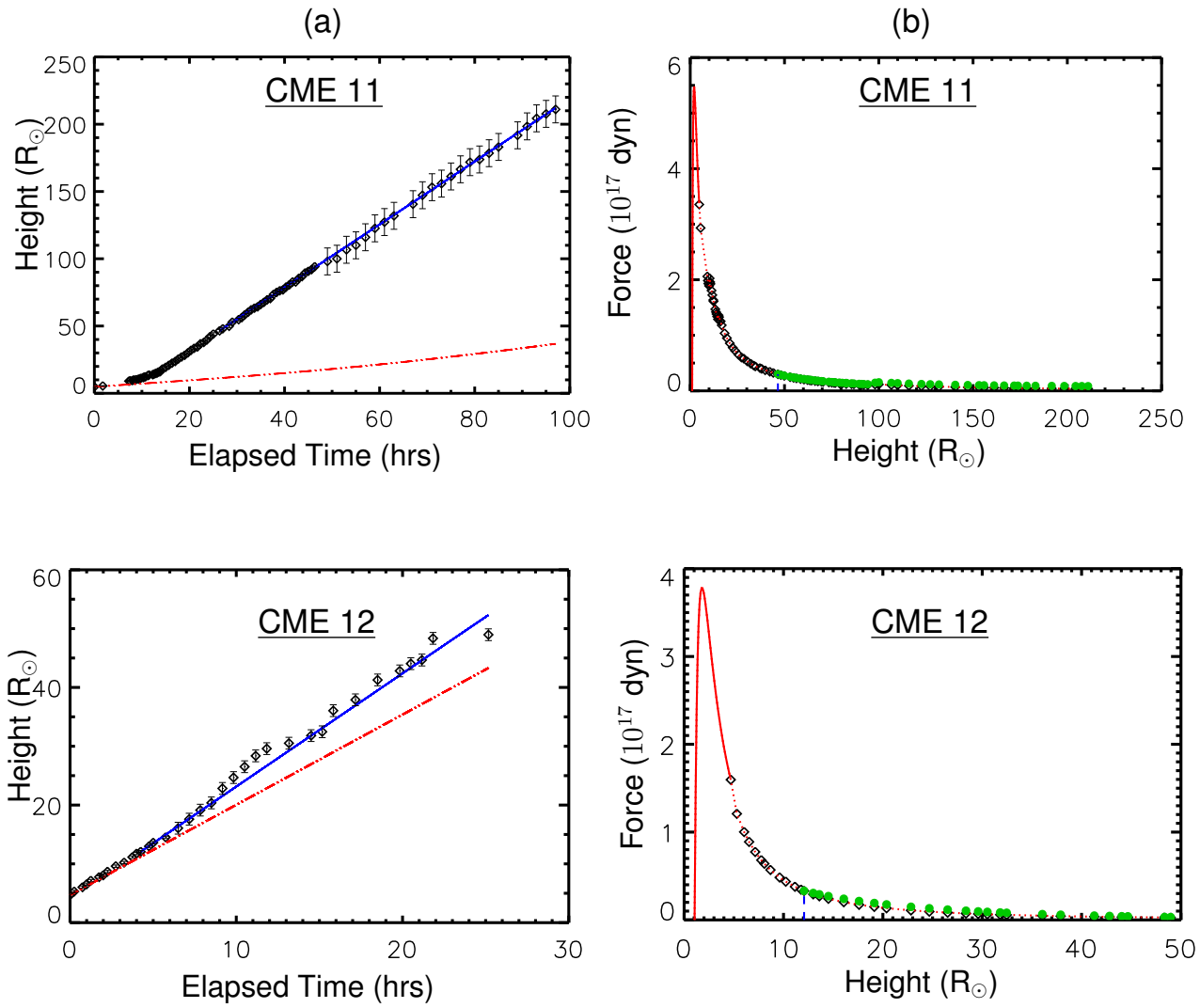


Figure 4.14: Height-time and Force profiles for CMEs 11 and 12. Caption same as Figure 4.10

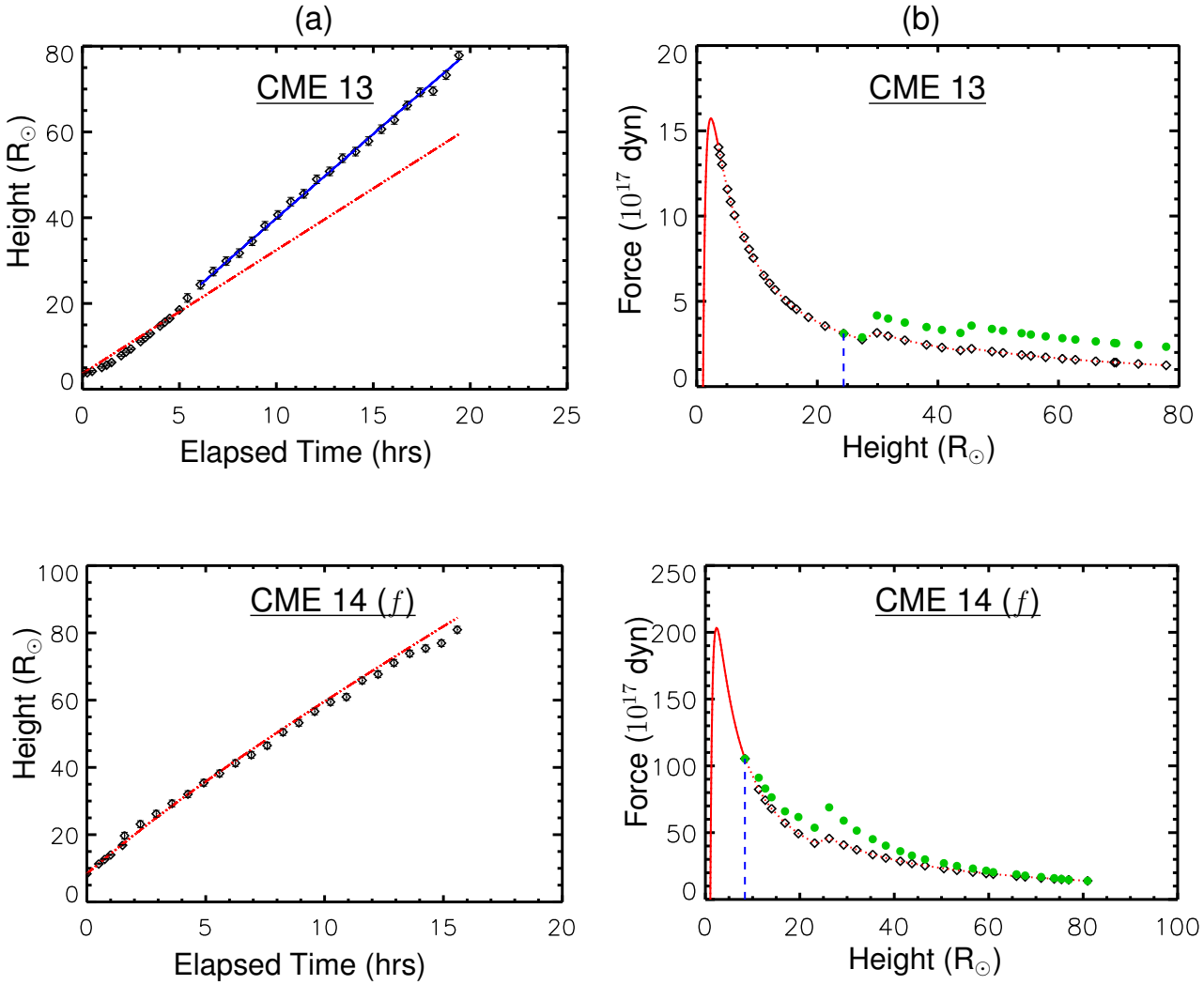


Figure 4.15: Height-time and Force profiles for CMEs 13 and 14. Caption same as Figure 4.10

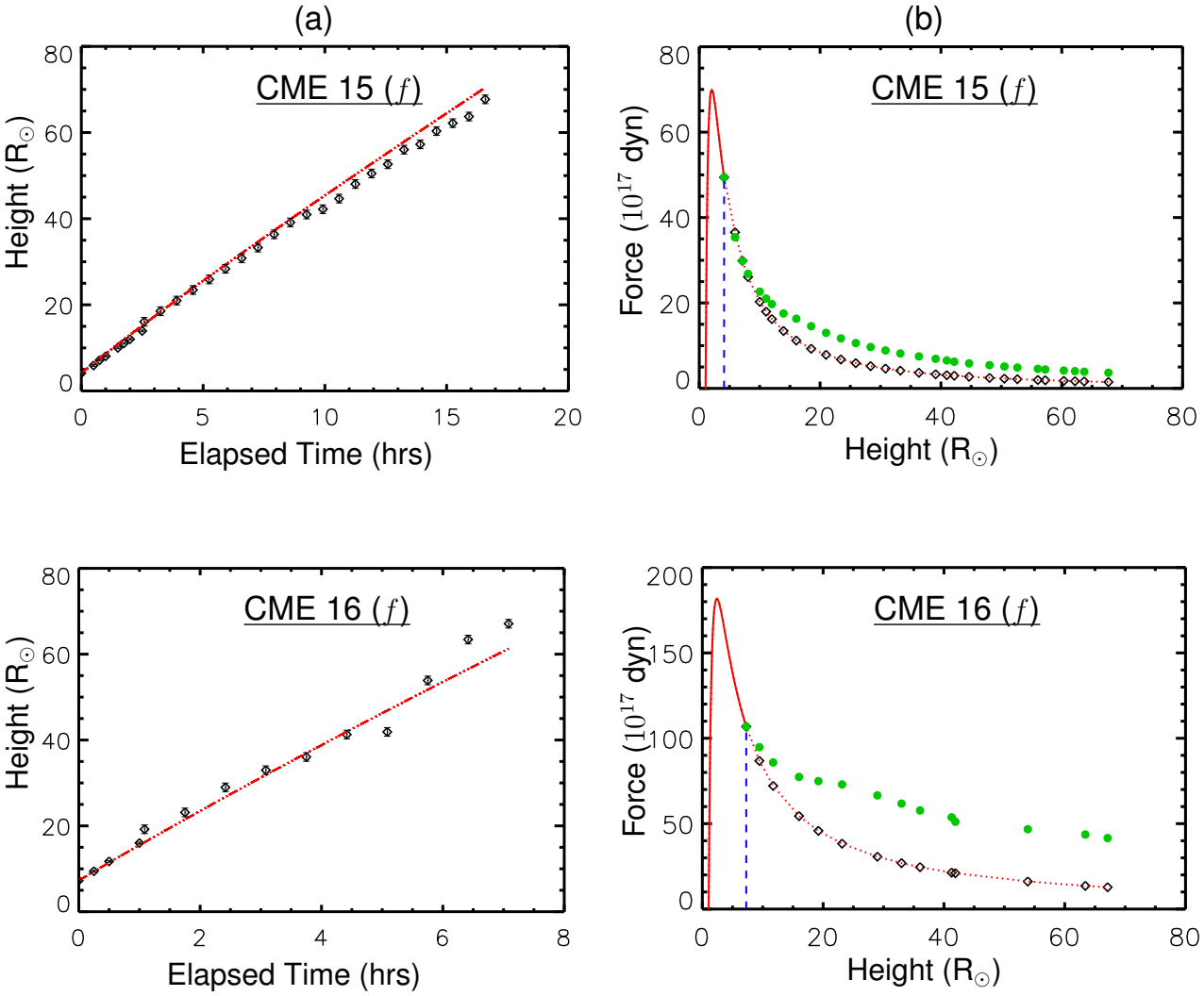


Figure 4.16: Height-time and Force profiles for CMEs 15 and 16. Caption same as Figure 4.10

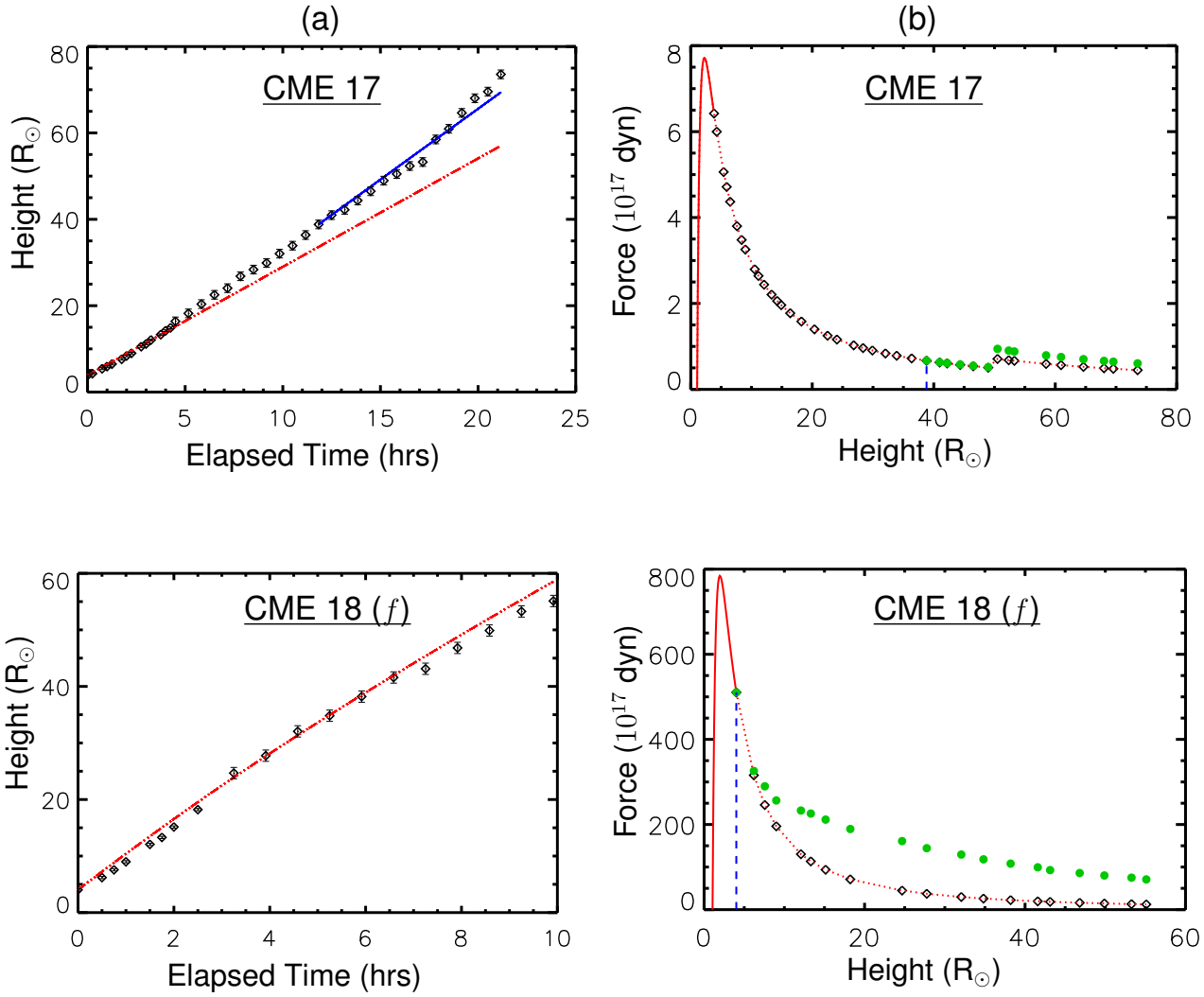


Figure 4.17: Height-time and Force profiles for CMEs 17 and 18. Caption same as Figure 4.10

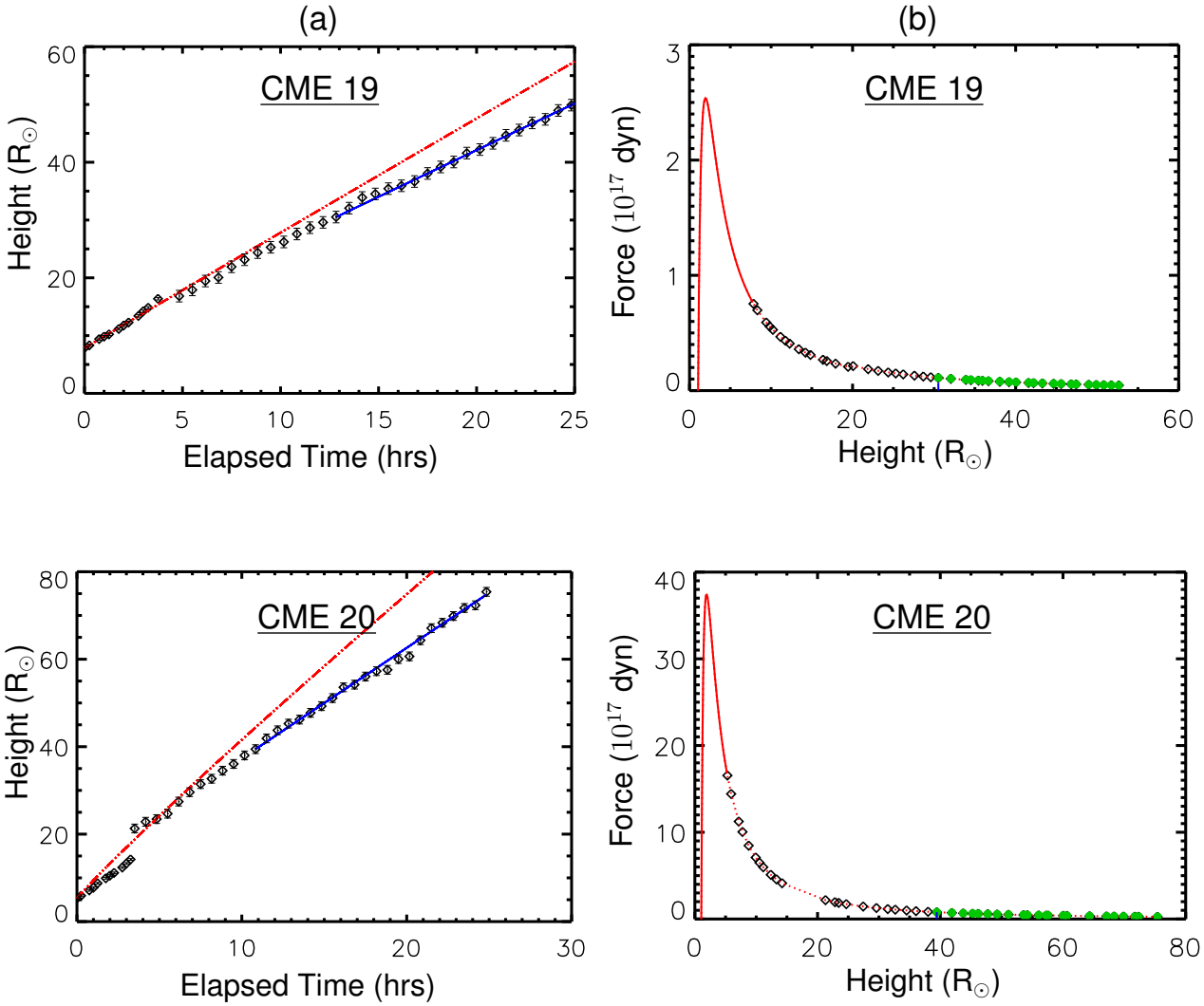


Figure 4.18: Height-time and Force profiles for CMEs 19 and 20. Caption same as Figure 4.10

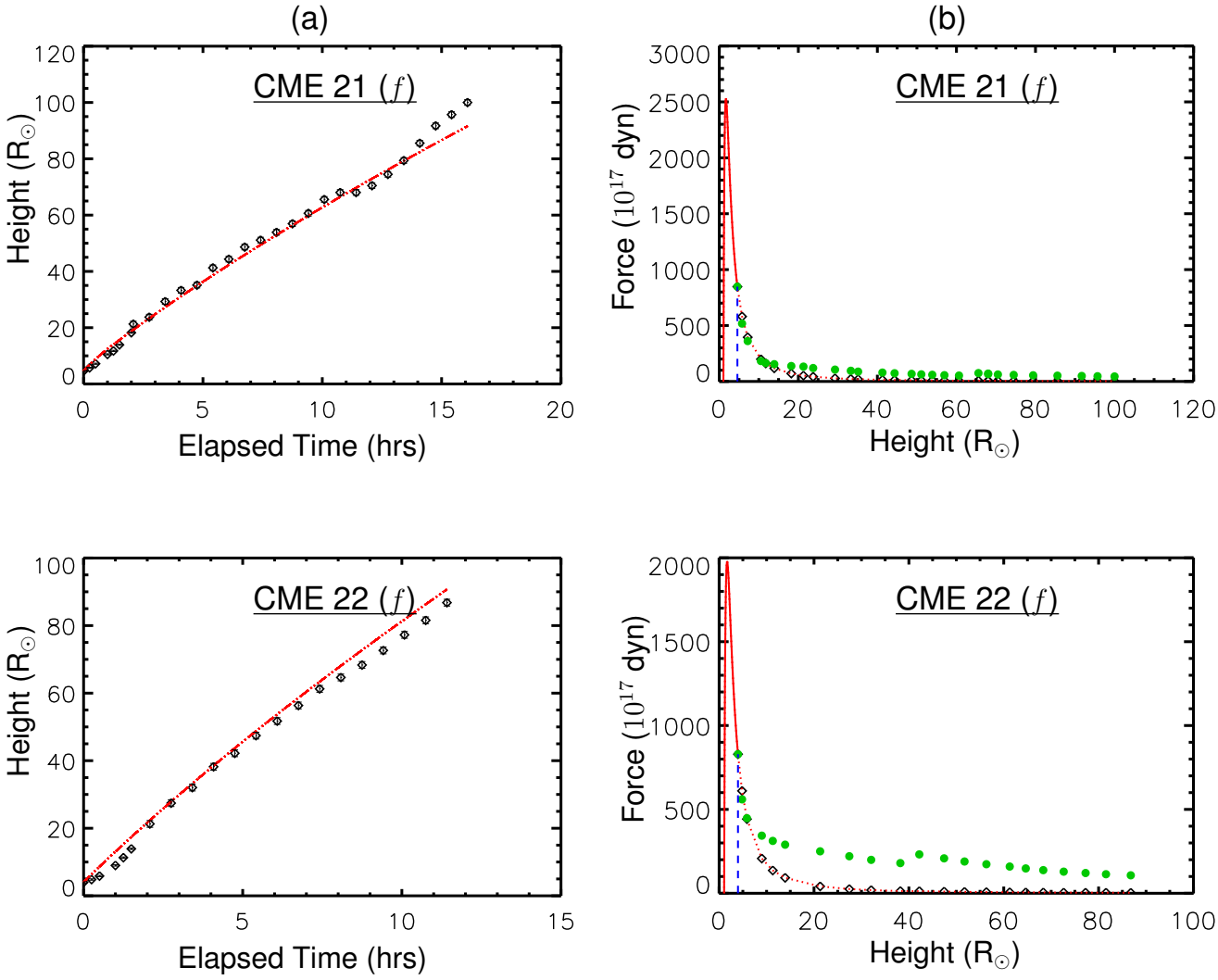


Figure 4.19: Height-time and Force profiles for CMEs 21 and 22. Caption same as Figure 4.10

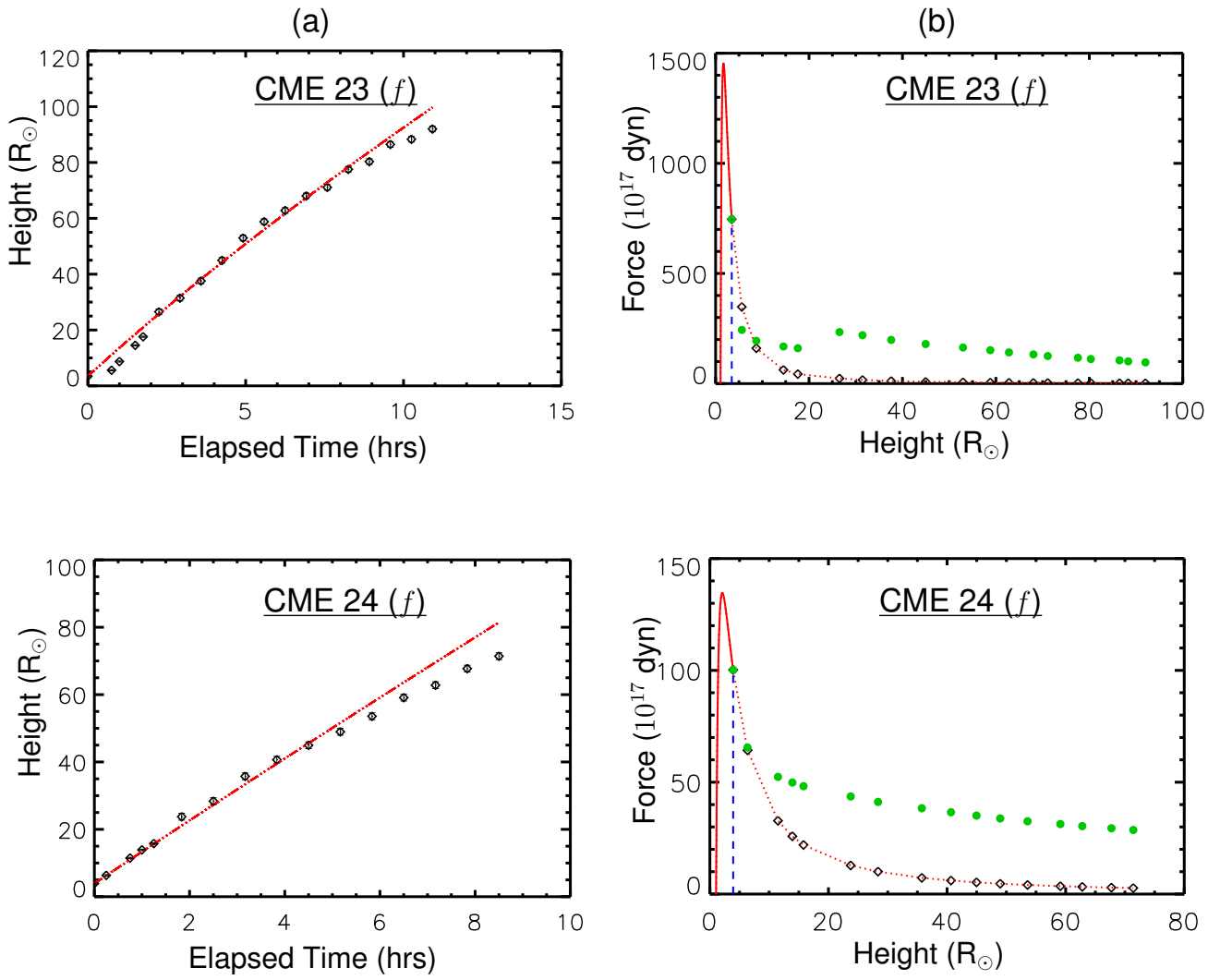


Figure 4.20: Height-time and Force profiles for CMEs 23 and 24. Caption same as Figure 4.10

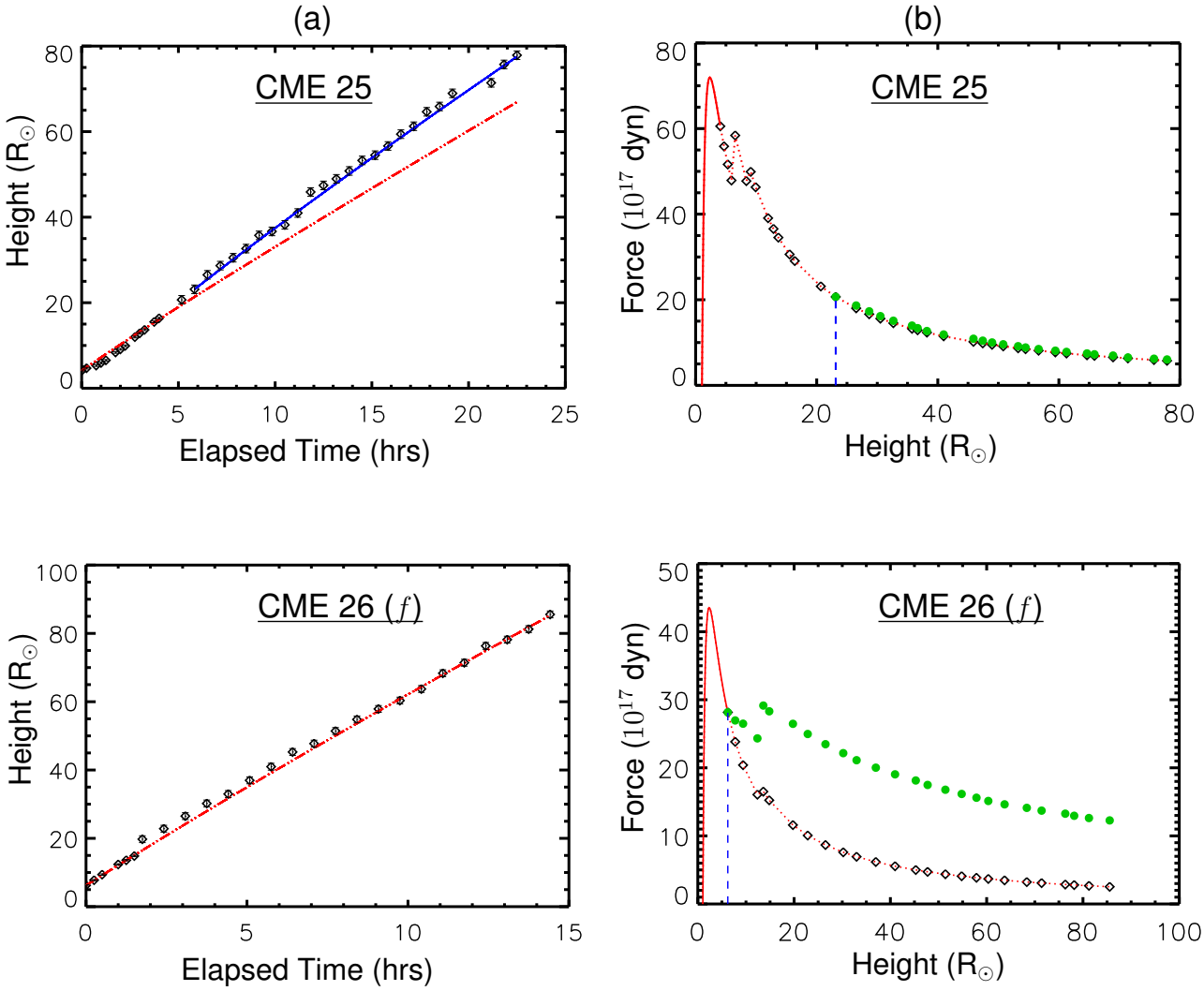


Figure 4.21: Height-time and Force profiles for CMEs 25 and 26. Caption same as Figure 4.10

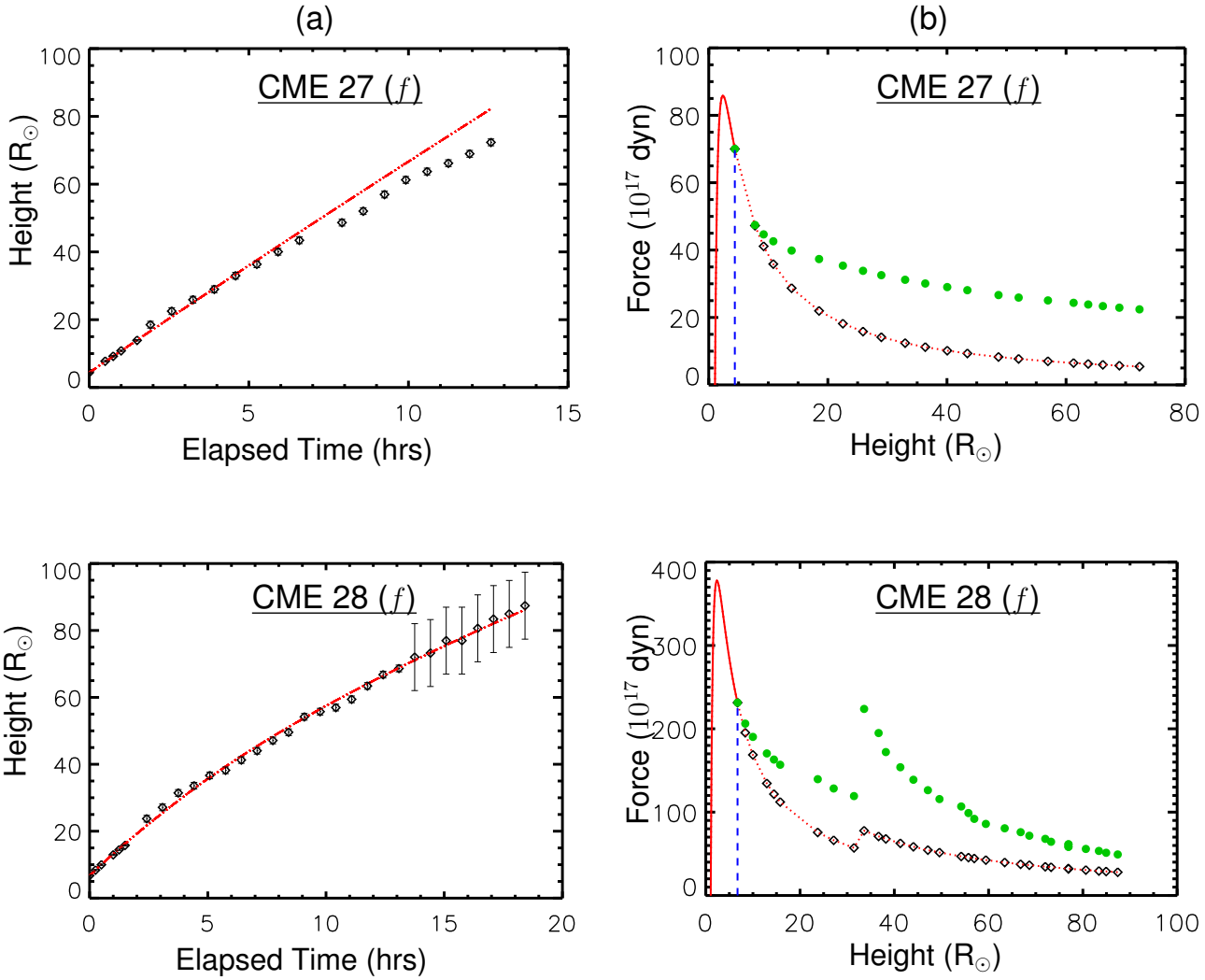


Figure 4.22: Height-time and Force profiles for CMEs 27 and 28. Caption same as Figure 4.10

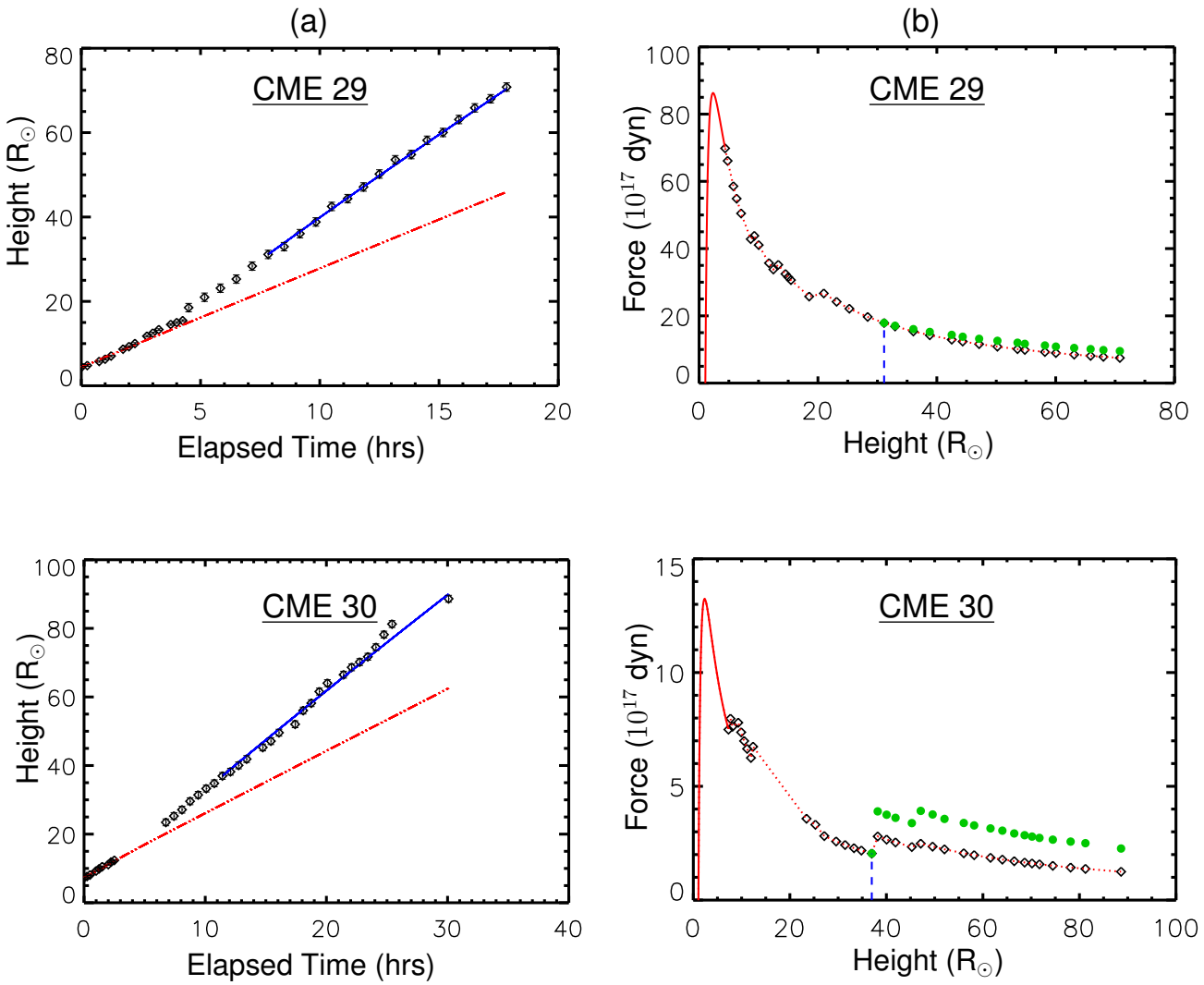


Figure 4.23: Height-time and Force profiles for CMEs 29 and 30. Caption same as Figure 4.10

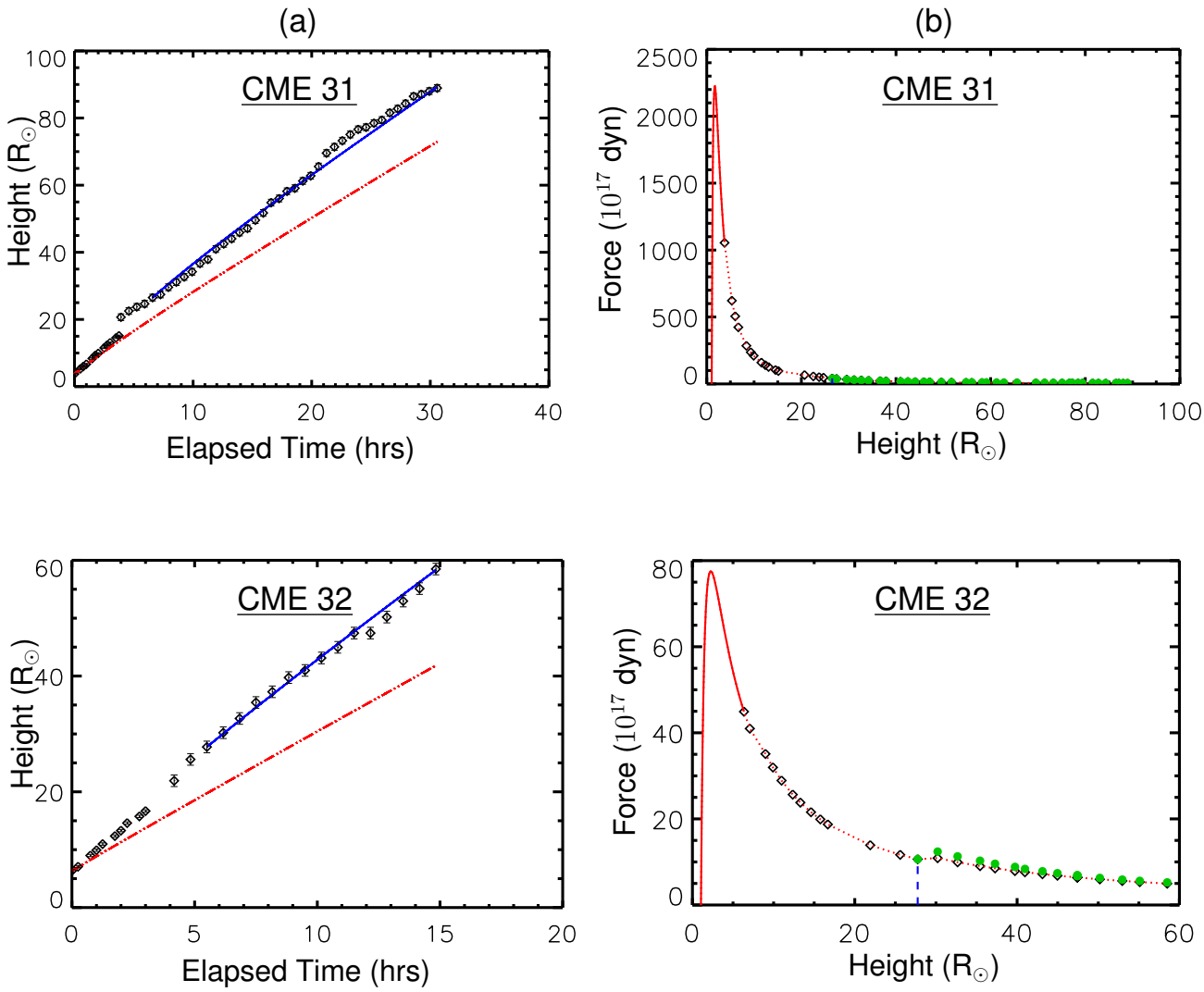


Figure 4.24: Height-time and Force profiles for CMEs 31 and 32. Caption same as Figure 4.10

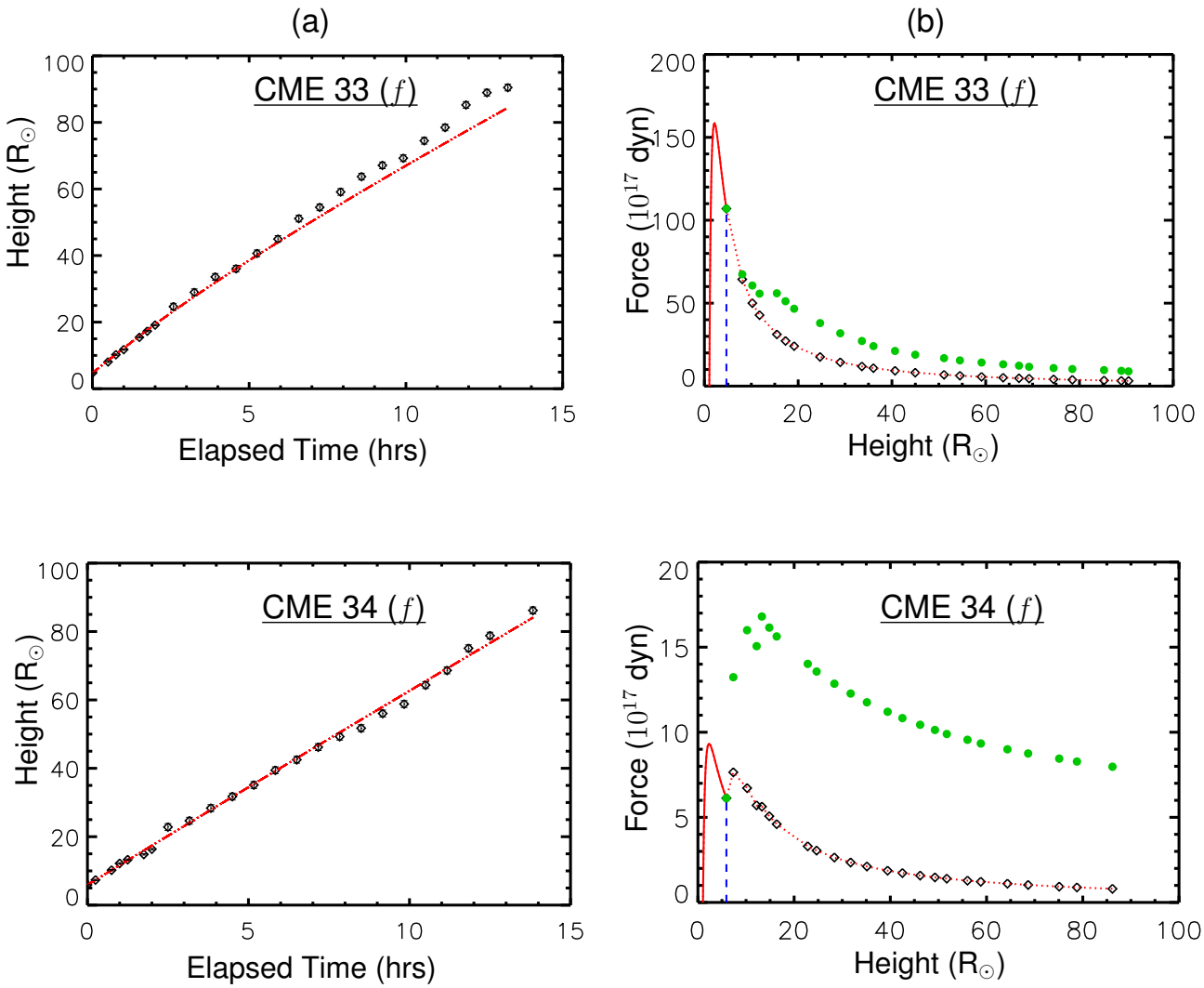


Figure 4.25: Height-time and Force profiles for CMEs 33 and 34. Caption same as Figure 4.10

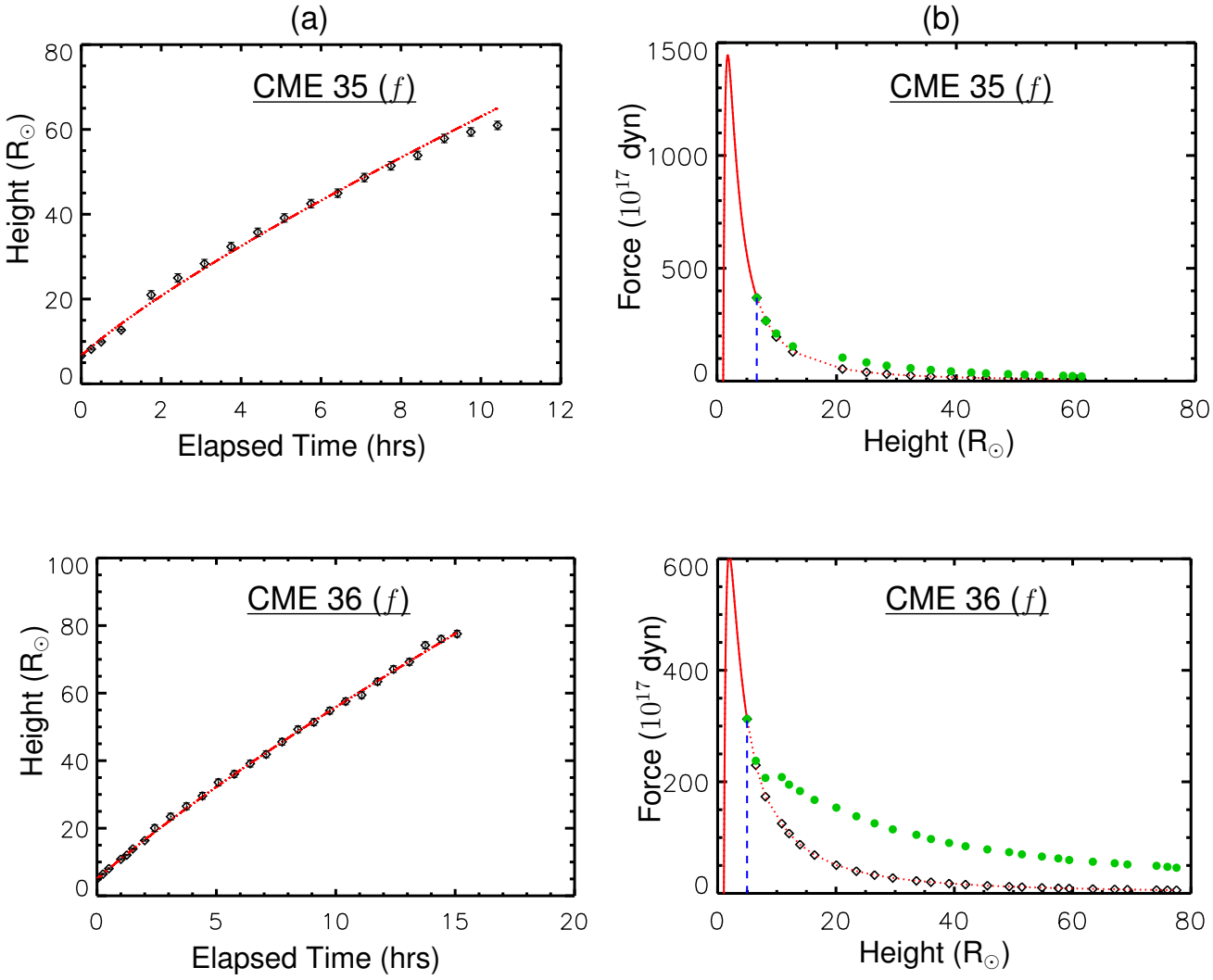


Figure 4.26: Height-time and Force profiles for CMEs 35 and 36. Caption same as Figure 4.10

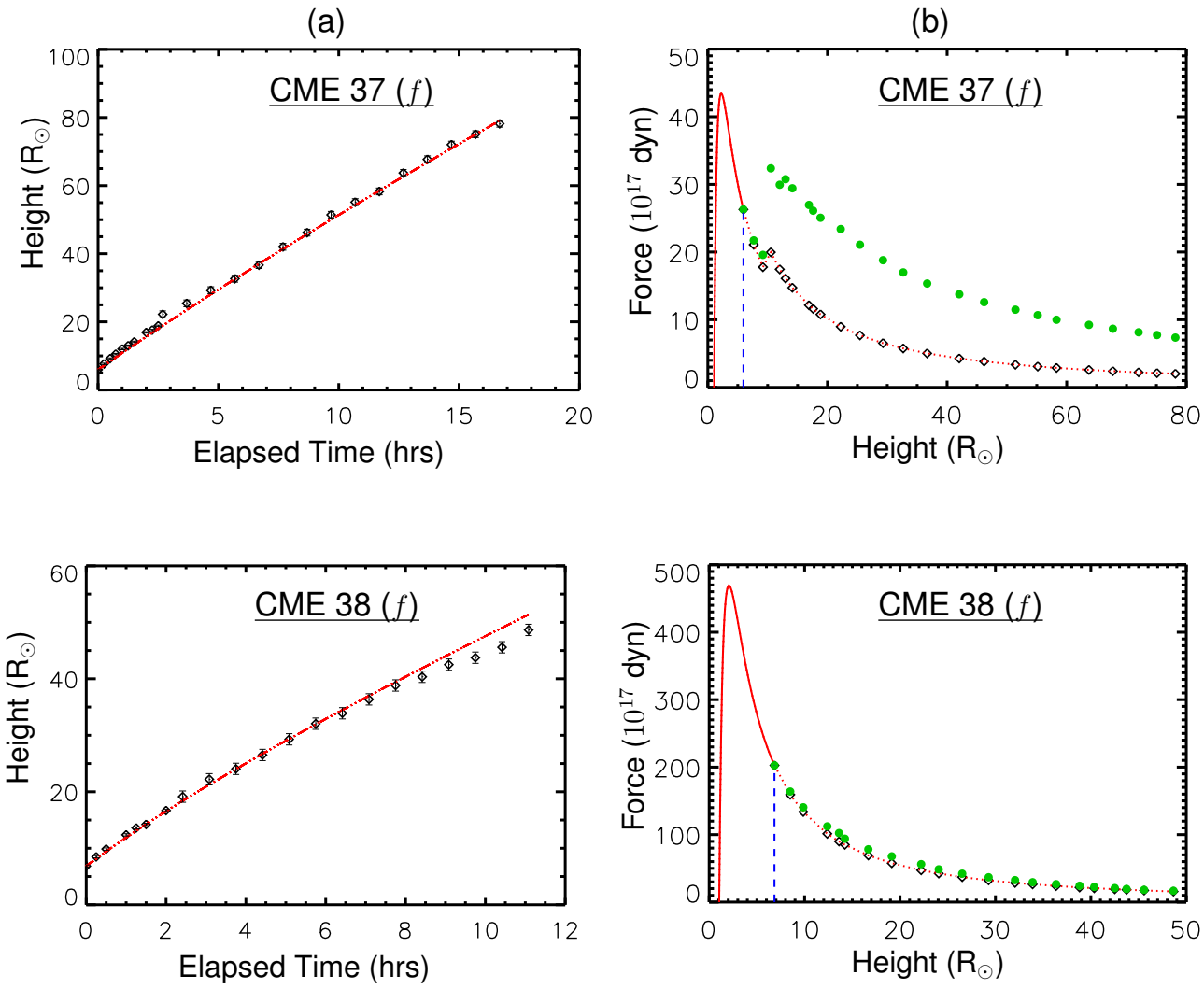


Figure 4.27: Height-time and Force profiles for CMEs 37 and 38. Caption same as Figure 4.10

Chapter 5

Future Work

In this chapter, we outline a plan for further analysis of the CME data sample described in this work. The first step is to expand the CME data set for improved statistical analysis to derive generalized conclusions for CMEs of all speed ranges. We can investigate the dissipation of magnetic energy and plasma heating using the expansion and CME evolution data. We can also explore the possibility of finding proxies, (e.g. Microwave radio emission, X-ray profiles) for the initiation phase of CMEs.

5.1 Expansion of CME sample

In the force analysis of a set of well-studied CMEs described in this thesis, we find an abrupt change in the value of the drag-model "initiation" height ($\widetilde{h}_0$) at 900 km s^{-1}. This speed is also used for differentiating between fast ($v_0 > 900$ km s^{-1}) and slow ($v_0 < 900$ km s^{-1}) CMEs. Figure 4.3, which is a plot of the drag initiation height ($\widetilde{h}_0$) *versus* CME initial velocity (v_0), shows this abrupt change in the value of $\widetilde{h}_0$ at 900 km s^{-1}. This is most likely a data selection artefact. In our sample of 38 CMEs, we have 9 events with initial velocity, $v_0 < 400$ km s^{-1}, 14 CMEs with $v_0 < 500$ km s^{-1} and 6 CMEs with $500 < v_0 < 900$ km s^{-1}. We thus have few medium speed CMEs ($500 < v_0 < 900$ km s^{-1}) - these are the ones that typically have $\widetilde{h}_0$ between $\sim$ 4 and 20 R$_\odot$. A larger sample having more medium speed CMEs ($500 < v_0 < 900$ km s^{-1}) will likely resolve this issue. Another factor that needs to be taken into consideration is the limited time cadence of the COR2 coronagraphs. This restriction leads to fewer data points in the initial stages of CME propagation, especially for faster CMEs. We find that $\widetilde{h}_0$ for the fast CMEs is the first observed height, and the missing data points could

in fact lead to even lower values of $\widetilde{h}_0$ for some of these events. Data from future coronagraphs with a higher time cadence (*e.g.* the *Visible Emission Line Coronagraph* (VELC) aboard ADITYA L1; Venkata et al. (2017)) could be useful in estimating $\widetilde{h}_0$ more accurately for fast CMEs. In summary, we plan to expand the CME sample to include CMEs that have initial velocities spanning a wider range with more events that have medium range initial speeds. This will be the key to generalizing our results.

5.2 Proxies for the initial acceleration phase of CMEs

CMEs in white-light can be well observed via coronagraphs only above 2-3 $R_\odot$; this is typically beyond the heights at which the Lorentz force peaks. This restriction leads to an uncertainty in calculating the CME launch speed. Due to unavailability of the CME height-time and expansion data in the low corona, we assume a self-similar expansion below the first observed height for all the events in our sample. An alternate approach could consist of estimating the CME initial speeds using X-ray or radio emission (Zhang and Dere, 2006). Chen (1996) use the soft X-ray profile as a proxy for CME current and Matamoros et al. (2017) investigate the feasibility of using the fluence of nonthermal microwave bursts to estimate the CME initial speeds. However, these studies need to be done with a larger CME sample.

We plan to investigate proxies in different wavelengths (particularly low-frequency radio lightcurves) for the CME initiation profile. CMEs with observations of the microwave lightcurve or X-ray profiles can be compared to the model derived Lorentz force profiles. A good match might indicate these lightcurves to be appropriate proxies for the initial CME evolution profile and can be used to determine CME parameters (like initial speeds) very early on. These proxies can provide important observational constraints on the Lorentz forces acting on CMEs. This is specially important for slow to medium speed CMEs, for which it has been shown that drag forces dominate only beyond 12–50 $R_\odot$.

The results from drag and Lorentz force analysis will be helpful in developing better physics-based models for the CME arrival predictions. However, this has been done so far only for past events which have been carefully studied. The purpose of this work is to ultimately promote models that forecast CME arrival based on the initial observations and estimates at the first detection of the CMEs in the LASCO FOV or from X-ray/radio signatures.

5.3 Plasma Heating

As described in Chapter 4 (section 4.4.1), we find that for some CMEs, the drag force is only slightly larger than the Lorentz force. In fact for two CMEs (CME 4 and CME10) in our sample, the drag force is slightly smaller than the Lorentz force. We suggest that one reason for this is that the Lorentz force is overestimated in our analysis. This could be due to the inherent assumption that the total magnetic flux is conserved, which might not be true. Therefore, we need to take into account any flux dissipation that may be present. We might also need to consider the energy expended, in CME expansion and in heating of the CME plasma (*e.g.* Kumar and Rust, 1996; Emslie et al., 2012). CME event analysis of Wang et al. (2009), suggests that heat is continuously injected into the CME plasma. With the availability of GCS measurements for the expansion of the CME along with translation, it will be interesting to see how the model predictions for describing the CME internal state match these observations. We would also like to explore if something can be concluded about the microphysics of the turbulent dissipation.

5.4 1D $\rightarrow$ 3D force Equation

We have discussed in detail a one-dimensional (1D) solar wind drag equation which entails the momentum coupling between CME and the ambient solar wind. Factors like front-flattening, rotation etc. of the CME are not taken into account. While this simple prescription provides reasonably accurate results when compared to observations, it is important to also account for the three-dimensional (3D) effects of propagation on the CMEs and how they alter the predicted trajectory. It is thus essential to also understand and modify the 1D force equation to a 3D equation (Isenberg and Forbes, 2007).

5.5 Solving a full force equation

The action of the two major forces governing CME propagation have been solved for, independently in this study as described in Chapter 3. Beginning with a drag-only model we determine the heights beyond which solar wind drag force dominates the CME dynamics. We then study the nature of Lorentz forces below and above this heliocentric distance. The next logical step is to combine observationally derived models for each of the two forces and solve the full-force equation. In other words, Equation 3.1 needs to be solved in its entirety, with each term described by physics-based prescriptions

and constrained by observations. This endeavor will require good approximations for the CME current or external magnetic field in order to calculate the Lorentz forces (Isenberg and Forbes, 2007; Savani et al., 2015). Various methods to estimate these include the calculation of CME flux content from flare ribbon brightenings (Longcope et al., 2007) or via poloidal flux injection method to estimate the field strength Kunkel and Chen (2010).

Chapter 6

Appendix

Detailed calculations for CME virtual mass and Lorentz force model as used in the estimation of drag and Lorentz force respectively is described in this Appendix. We show the equivalence of two Lorentz force models: torus instability (TI) model (Kliem and Török, 2006) and flux-injection model (Chen, 1996)). GCS fitting at one timestamp is shown for each CME and the corresponding parameters at that timestamp are given in Table 6.1.

6.1 CME Virtual Mass

The total CME mass (m_{cme}) is a summation of the "true" mass (M_T) which is corrected for projection effects and the virtual mass M_v, which is described by Landau and Lifshitz (1959) (p 31), as half the mass of the fluid displaced by a sphere moving in that fluid. The CME traveling in an ambient solar wind is also envisioned as a solid sphere propagating in a fluid, (see, Chapter 3), therefore we include the virtual mass correction to the true CME mass (M_T).

$$\begin{aligned} m_{cme} &= M_T + M_v \\ &= \mathrm{Vol}_{cme}\left[\rho_i + \frac{\rho_e}{2}\right] \end{aligned} \tag{6.1}$$

where, Vol_{cme} is the CME volume, ρ_i is density inside the CME and ρ_e is the external (solar wind) density.

$$\rho_i = \rho_{cme} = \frac{M_T}{\mathrm{Vol}_{cme}}$$
$$\rho_e = \rho_{sw} = n_{sw}(R)\, m_p$$

where, $n_{sw}(R)$ is the solar wind proton number density and m_p is the proton mass. Substituting in Equation 6.1,

$$\begin{aligned} m_{cme}(R) &= \mathrm{Vol}_{cme}\left[\frac{M_T}{\mathrm{Vol}_{cme}} + \frac{n_{sw}(R)m_p}{2}\right] \\ &= M_T\left[1 + \frac{n_{sw}(R)\,m_p}{2}\frac{\mathrm{Vol}_{cme}}{M_T}\right] \\ &= M_T\left[1 + \frac{n_{sw}(R)\,m_p}{2}\frac{A_{cme}R}{M_T}\right] \end{aligned} \tag{6.2}$$

using, $\mathrm{Vol}_{cme} = A_{cme}\,R$, where A_{cme} is the CME cross-sectional area and R is the heliocentric distance of the CME leading edge. Equation 6.2 defines the total CME mass as a function of the heliocentric distance (R). We find in our analysis however, that the addition of virtual mass does not change the results significantly.

6.2 The TI Lorentz Force Model

6.2.1 Net Lorentz force

The toroidal force acting on a current carrying loop is given by (see e.g., Shafranov, 1966, Chen, 1989):

$$F_{int} = \frac{I^2}{c^2 R}\left(ln\frac{8R}{R_{cme}} + \frac{l_i}{2} - \frac{3}{2}\right) \quad (in\ cgs) \tag{6.3}$$

where, F_{int} is the Lorentz force ($J \times B$) acting radially outwards per unit length of the flux rope, I is the toroidal current, R is the height and l_i is the internal inductance. In the presence of an external poloidal magnetic field (B_{ext}), the force with which the CME is held down is given by:

$$\begin{aligned} F_{ext} &= \frac{J \times B_{ext}(R)}{c} \\ &= \int I\frac{dl \times B_{ext}(R)}{c} \\ \frac{F_{ext}}{unit\ length} &= -\frac{IB_{ext}(R)}{c} \end{aligned} \tag{6.4}$$

The complete force balance equation is given by (Kliem and Török, 2006):

$$F_R = \frac{I^2}{c^2 R}\left(ln\left(\frac{8R}{R_{cme}}\right) + \frac{l_i}{2} - \frac{3}{2}\right) - \frac{IB_{ext}(R)}{c} \tag{6.5}$$

where, F_R is the Lorentz force per unit length acting on a current carrying loop (in cgs units). The total Lorentz force acting on the flux-rope is given by (Equation 3.18):

$$F_{Lorentz} = \frac{\pi I^2}{c^2}\left(ln\left(\frac{8R}{R_{cme}}\right) - \frac{3}{2} + \frac{l_i}{2}\right) - \frac{(\pi R) I B_{ext}(R)}{c} \tag{6.6}$$

6.2.2 CME current at equilibrium (I_{eq})

The equilibrium current (I_{eq}) is determined by equating the total force $F_{Lorentz}$ (Equation 6.6) to zero. At equilibrium ($R = h_{eq}$),

$$\frac{\pi I_{eq}^2}{c^2}\left(ln\left(\frac{8h_{eq}}{R_{cme}(h_{eq})}\right) - \frac{3}{2} + \frac{l_i}{2}\right) = \frac{(\pi h_{eq}) I_{eq} B_{ext}(h_{eq})}{c} \tag{6.7}$$

Using,

$$c^{'}(R) = \left[ln(8R/R_{cme}) - 2 + l_i/2\right]$$
$$c^{'}_{eq} = c^{'}(R = h_{eq}) = \left[ln(8h_{eq}/R_{cme}(h_{eq}) - 2 + l_i/2\right],$$

in Equation 6.7 we get,

$$\frac{I_{eq}}{c\ h_{eq}}(c^{'}_{eq} + \frac{1}{2}) = B_{ext}(h_{eq}) \tag{6.8}$$

The current at equilibrium is given by,

$$I_{eq} = \frac{B_{ext}(h_{eq}) h_{eq} c}{c^{'}_{eq} + \frac{1}{2}} \tag{6.9}$$

6.2.3 CME current I

The current carried by a flux-rope is determined by conserving the total magnetic flux (internal + external). Using $B_{ext}(R) = \hat{B} R^{-n}$ and equations of flux conservation (Equation 3.19), we get:

$$L_{eq} I_{eq} - \frac{2\pi}{c}\int_0^{h_{eq}} B_{ext}(r) r dr = L(R)\, I(R) - \frac{2\pi}{c}\int_0^{R} B_{ext}(r) r dr \tag{6.10}$$

where,

$$L = \frac{4\pi R}{c^2}\left[ln(8R/R_{cme}) - 2 + l_i/2\right]$$
$$L(R) = \frac{4\pi R}{c^2} c^{'}$$
$$L_{eq} = \frac{4\pi h_{eq}}{c^2} c^{'}_{eq} \tag{6.11}$$

From Equation 6.10,

$$\begin{aligned} L(R)\,I(R) &= L_{eq}\,I_{eq} + \frac{2\pi}{c}\hat{B}\left[\frac{R^{(2-n)}}{(2-n)} - \frac{h_{eq}^{(2-n)}}{(2-n)}\right] \\ &= L_{eq}\,I_{eq} + \frac{2\pi}{(2-n)\,c}\hat{B}h_{eq}^{(2-n)}\left[\left(\frac{R}{h_{eq}}\right)^{(2-n)} - 1\right] \\ I(R) &= \frac{L_{eq}\,I_{eq}}{L(R)} + \frac{2\pi}{(2-n)\,c}\frac{\hat{B}\,h_{eq}^{(2-n)}}{L(R)}\left[\left(\frac{R}{h_{eq}}\right)^{(2-n)} - 1\right] \end{aligned} \quad (6.12)$$

Using, Equations 6.11 and 6.9 in Equation 6.12,

$$\begin{aligned} I(R) &= \frac{c_{eq}^{'}\,h_{eq}I_{eq}}{c^{'}\,R} + \frac{2\pi}{(2-n)}\frac{(\hat{B}\,h_{eq}^{-n})\,h_{eq}^{2}}{L(R)\,c}\left[\left(\frac{R}{h_{eq}}\right)^{(2-n)} - 1\right] \\ &= \frac{c_{eq}^{'}\,h_{eq}I_{eq}}{c^{'}\,R}\left(1 + \frac{2\pi}{(2-n)}\frac{B_{ext}(h_{eq})\,h_{eq}c^{'}R}{L(R)\,c\,c_{eq}^{'}\,I_{eq}}\left[\left(\frac{R}{h_{eq}}\right)^{(2-n)} - 1\right]\right) \end{aligned}$$

The CME current is given by,

$$I(R) = \frac{c_{eq}^{'}\,h_{eq}I_{eq}}{c^{'}\,R}\left(1 + \frac{(c_{eq}^{'}+1/2)}{2\,c_{eq}^{'}\,(2-n)}\left[\left(\frac{R}{h_{eq}}\right)^{(2-n)} - 1\right]\right) \quad (6.13)$$

6.2.4 Final Lorentz force expression

We rewrite the Lorentz force (Equation 6.6) by substituting $I(R)$ (Equation 6.13) and I_{eq} (Equation 6.9),

$$\begin{aligned} F_{Lorentz} &= \frac{\pi\,I}{c}\left[\frac{I\,(c^{'}+1/2)}{c} - R\,B_{ext}(R)\right] \\ &= \frac{\pi\,c_{eq}^{'}\,h_{eq}\,I_{eq}\,Q}{c^{'}\,R\,c}\left[\frac{c_{eq}^{'}\,h_{eq}\,I_{eq}\,Q\,(c^{'}+1/2)}{c^{'}\,R\,c} - R\,B_{ext}\,(h_{eq})\left(\frac{R}{h_{eq}}\right)^{-n}\right] \end{aligned}$$

where,

$$B_{ext}(R) = B_{ext}(h_{eq})[R/h_{eq}]^{-n}$$

$$Q = \left(1 + \frac{(c_{eq}^{'}+1/2)}{2\,c_{eq}^{'}\,(2-n)}\left[\left(\frac{R}{h_{eq}}\right)^{(2-n)} - 1\right]\right)$$

Finally, we get the net Lorentz force acting on a CME in terms of the observed and derived GCS parameters (R, R_{cme}, $h_{eq} = 1.05$ R$_\odot$) and using $B_{ext}(h_{eq})$

from the force analysis,

$$F_{Lorentz} = \frac{\pi\, c_{eq}^{'}\,(B_{ext}(h_{eq}))^2\,(h_{eq})^2\,Q}{c^{'}\,(c_{eq}^{'}+1/2)}\left[\frac{c_{eq}^{'}\,Q}{(c_{eq}^{'}+1/2)}\frac{(c^{'}+1/2)}{c^{'}}\left(\frac{h_{eq}}{R}\right)^2-\left(\frac{R}{h_{eq}}\right)^{-n}\right] \tag{6.14}$$

6.2.5 Decay Index n

Kliem and Török (2006) describe the evolution of the major radius of an expanding current ring by :

$$\frac{d^2\rho}{d\tau^2} = \frac{c_{eq}^{'2}\rho^{-2}}{c^{'}(c_{eq}^{'}+1/2)}\left[1+\frac{(c_{eq}^{'}+1/2)}{2c_{eq}^{'}(2-n)}(\rho^{2-n}-1)\right]$$
$$\times\left[\frac{c^{'}+1/2}{c^{'}}\left(1+\frac{(c_{eq}^{'}+1/2)}{2c_{eq}^{'}(2-n)}(\rho^{2-n}-1)\right)-\frac{c_{eq}^{'}+1/2}{c_{eq}^{'}}\rho^{2-n}\right] \quad (n\neq 2)$$

where, $\rho = R/h_{eq}$, $\tau = t/T$ and,

$$T^2 = \frac{c_{eq}^{'}+1/2}{4}\frac{R_{cme}^2(h_{eq})}{B_{eq}^2/(4\pi\rho_{m0})}$$

where, ρ_{m0} is the mass density at equilibrium. Using Alfv́en speed defined as, $V_A = B_{eq}^2/(4\pi\rho_{m0})$ at equilibrium,

$$T = \frac{(c_{eq}^{'}+1/2)^{1/2}}{2}\frac{R_{cme}(h_{eq})}{V_A}$$

Assuming self-similar expansion, that is, $c^{'}(R) = constt.$, they derive the condition for instability using,

$$\frac{d}{d\rho}\left(\frac{d^2\rho}{d\tau^2}\right) > 0 \quad at\ \rho = 1$$

which gives the critical decay index,

$$n > n_{cr} = \frac{3}{2} - \frac{1}{4c_{eq}^{'}}$$

Since, $c^{'}$ depends logarithmically on R/R_{cme}, it varies very slowly, therefore, the assumption $c^{'}(R) = c_{eq}^{'}$ is valid. It is also seen that CMEs expand self-similarly (using GCS observations).

The decay index, n is chosen based on the following two conditions:

1. $n > n_{cr}$. The decay index for the external magnetic field should be greater than the critical decay index derived using the instability condition, which ensures the CME launch.

2. Since the solar wind aerodynamic drag is found to be dominant above the heights $R > \widetilde{h}_0$, the Lorentz force $F_{Lorentz}$ should be smaller in magnitude above these heights. We use the condition, $|F_{drag}| > F_{Lorentz}$ for $R > \widetilde{h}_0$.

We choose different values of $n > n_{cr}$, and check if $|F_{drag}| > F_{Lorentz}$ for $R > \widetilde{h}_0$ for that n. The smallest value of $n > n_{cr}$ for which this condition holds true is taken to be the value of the decay index which takes care of the instability condition as well as constrains the Lorentz force. A larger value of n indicates that the external field decays rapidly, typical to active regions from where fast CMEs erupt. It is seen that for our sample, the largest values of $n(\sim 3)$ correspond to fast events. Smaller n values indicate slower CMEs originating from erupting prominences.

6.3 Equivalence of two Lorentz force models

The Lorentz force prescription we use is based on torus instability model (TI) described in Kliem and Török (2006). It appeals to an overlying external magnetic field which decreases rapidly enough for the CME to launch (like a whiplash action). The external poloidal field is required to decay as $\propto R^{-n}$, where n is the decay index. Equation 6.6 represents the net Lorentz force acting on a current carrying loop. The two competing $J \times B$ terms in Equation 6.6 give a Lorentz force profile which increases to a peak and then decreases (Figure 3.2). The TI model assumes conservation of magnetic flux to derive the CME current (I) (see section 6.2.3, Equation 6.13). An example of CME current profile is shown in Figure 6.1 for CME 1. It decreases as a function of the heliocentric distance.

Another approach to Lorentz forces relies on a tailored injection of poloidal flux at the base of the flux-rope (Chen, 1996; Chen and Kunkel, 2010). The temporal profile of the accompanying soft X-ray flare is often used as a guide for the time profile of injected flux (or equivalently, the poloidal CME current). The force acting on a toroidal section of current carrying loop as described by Chen (1996) (based on Shafranov (1966)) is given by :

$$F_R = \frac{I_t^2}{c^2 R}\left[ln\left(\frac{8R}{R_{cme}}\right) + \frac{1}{2}\beta_p - \frac{1}{2}\frac{\bar{B}_t^2}{B_{pa}^2} + 2\left(\frac{R}{R_{cme}}\right)\frac{B_s}{B_{pa}} - 1 + \frac{li}{2}\right] \quad (6.15)$$

where, F_R is the Lorentz force per unit length in the major radial direction, I_t is the toroidal current, $\beta_p = 8\pi(\bar{p} - p_a)/B_{pa}^2$, $\bar{p}$ is the average pressure

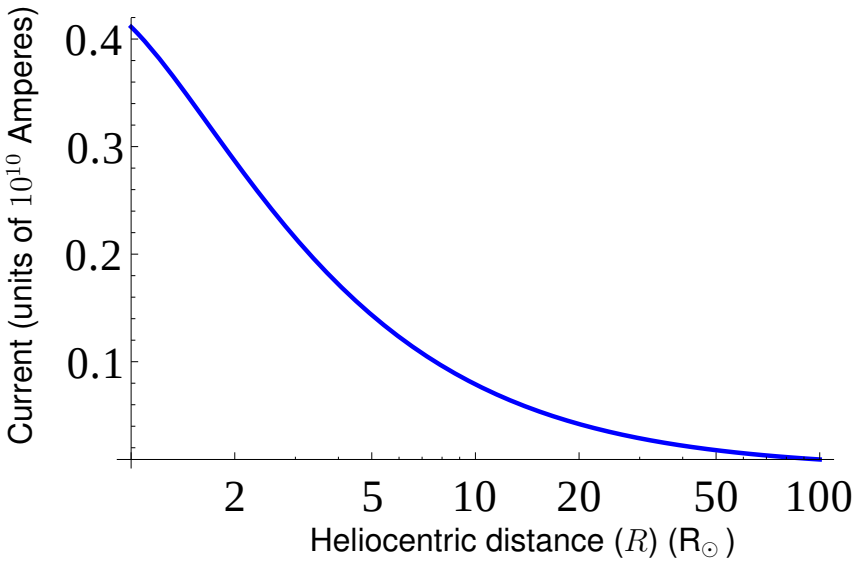


Figure 6.1: CME current profile (Equation 6.13) for parameters : $n = 2.5$, $I_{eq} = 0.41 \times 10^{10}$ A and $R/R_{cme} = 4.56$. The current decreases as a function of the heliocentric distance (R). X-axis scale is logarithmic.

inside the loop, p_a is the ambient coronal pressure, $\bar{B}_t$ is the average toroidal field and B_{pa} is the poloidal magnetic field inside the loop. B_s is the ambient field. The poloidal flux enclosed by the torus section is given by:

$$\Phi_p(t) \; = \; cL(t)I_t(t) \tag{6.16}$$

Using Equation 6.16 in 6.15, we get,

$$F_R \; = \; \frac{\Phi_p^2}{c^4 R L^2}\left[ln\left(\frac{8R}{b}\right) + \frac{1}{2}\beta_p - \frac{1}{2}\frac{\bar{B}_t^2}{B_{pa}^2} + 2\left(\frac{R}{a}\right)\frac{B_s}{B_{pa}} - 1 + \frac{li}{2}\right] \tag{6.17}$$

The injection of flux (by increasing the poloidal magnetic flux $\Phi_p(t)$) drives the initial flux rope out of equilibrium. For each CME, Chen and Kunkel (2010) adjust the function, $d\Phi_p(t)/dt$ to obtain best-fit solutions to the observed height-time profiles. The Lorentz force profile from this model also increases to a peak and then decreases. However, the toroidal current I_t from this prescription emulates the injected flux profile (Equation 6.16).

On comparing the TI and flux-injection models for Lorentz forces, we find that the ambient field is required to decay sufficiently in the TI model. However, no such restriction exists in the second approach. In fact, Chen (1996) describe a simple functional form for the external ambient field chosen to increase before decreasing as a function of height (Equation 16 in Chen (1996)). This provides stability to the initial flux rope against expansion in the major radial direction.

We assume a simplified version of Equation 6.15 specialized to small perturbations from equilibrium, given by :

$$F_R = \frac{I_t^2}{c^2 R}\left[ln\left(\frac{8R}{R_{cme}}\right) + \beta_p - \frac{3}{2} + \frac{li}{2}\right] \tag{6.18}$$

where, $\beta_p \simeq 1 - \frac{B_t^2}{B_p^2}$.

We compare the Lorentz forces from these two equations 6.18 and 6.5, to determine the functional form of current I_t (from flux-injection model) in terms of the current prescription from the TI model. For simplicity, we consider β_p is small (≈ 0).

$$\begin{aligned} \frac{I_t^2}{c^2 R}\left[ln\left(\frac{8R}{R_{cme}}\right) + \beta_p - \frac{3}{2} + \frac{li}{2}\right] &= \frac{I^2}{c^2 R}\left(ln\left(\frac{8R}{R_{cme}}\right) + \frac{l_i}{2} - \frac{3}{2}\right) - \frac{IB_{ext}(R)}{c} \\ I_t^2 &= I^2 - \frac{cRIB_{ext}(R)}{\left(ln\frac{8R}{R_{cme}} + \frac{l_i}{2} - \frac{3}{2}\right)} \end{aligned} \tag{6.19}$$

where, I is the CME current determined from the TI model (Equation 6.13) and $B_{ext}(R) = B_{ext}(h_{eq})\left(R/h_{eq}\right)^{-n}$.

As an example, we show the current profile (I_t) from the flux injection model for CME 1 determined using Equation 6.19 and CME parameters: $n = 2.5$, $I_{eq} = 0.41 \times 10^{10}$ A and $R/R_{cme} = 4.56$ in Figure 6.2.

The functional form of CME current I_t is given by (for $n = 2.5$):

$$I_t = \sqrt{\frac{C_1}{R^3} - \frac{C_2}{R^{2.5}} + \frac{C_3}{R^2}} \tag{6.20}$$

The constants C_1, C_2 and C_3 are determined for corresponding values of parameters, n, aspect ratio (R/R_{cme}) and $B_{ext}(h_{eq})$. For this event (with $n = 2.5$),

$$\begin{aligned} C_1 &= 4.9 \times 10^{38} \\ C_2 &= 1.3 \times 10^{39} \\ C_3 &= 8.4 \times 10^{38} \end{aligned}$$

Both the approaches for Lorentz forces acting on CMEs yield a solution that initially increases with time/height, reaches a maximum and subsequently decreases. The mathematical equivalence of their current prescriptions has been demonstrated above.

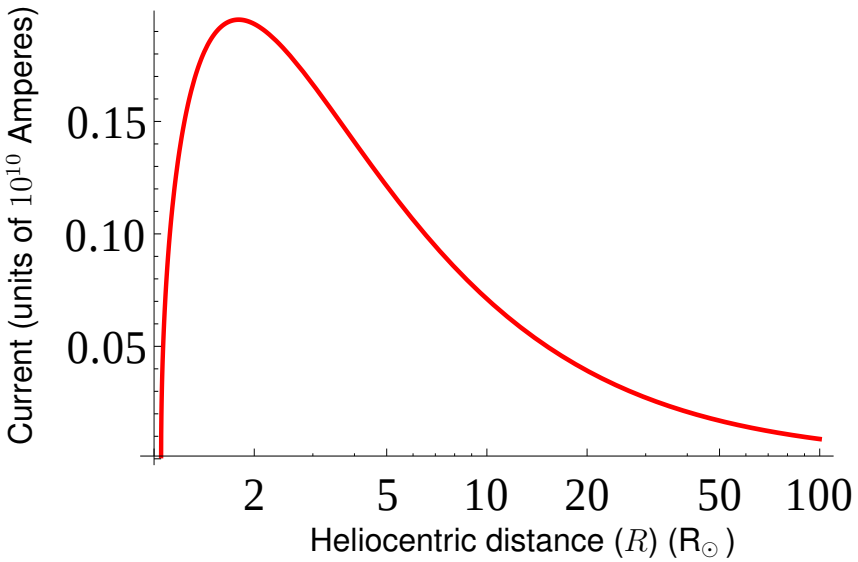


Figure 6.2: CME current using injection of poloidal flux (Chen, 1996) follows the Lorentz force profile. Current increases to a peak and then decreases as a function of the heliocentric distance (R). The x-axis scale is logarithmic.

6.4 GCS fittings for all CMEs

We show the a GCS model fit to the LASCO C2, COR2 A and COR2 B data for all CMEs at one timestamp. In Figures 6.3 to 6.40, the first row show the remote sensing observation data at a particular timestamp. The second row shows the GCS model fit to this data. The left panel is coronagraph image from STEREO COR 2A, middle panel is data from LASCO C2 and right panel is data from STEREO COR2 B. The flux-rope like wiremesh structure (yellow) represents the fitting to each coronagraph image using GCS technique. Only one figure per event is shown to keep the file compact. The caption for each figure indicates the date of CME event, time of observation at which the fit is shown and the corresponding height at that time using GCS fitting. Table 6.1 lists all the GCS parameters at the selected timestamp for each CME.

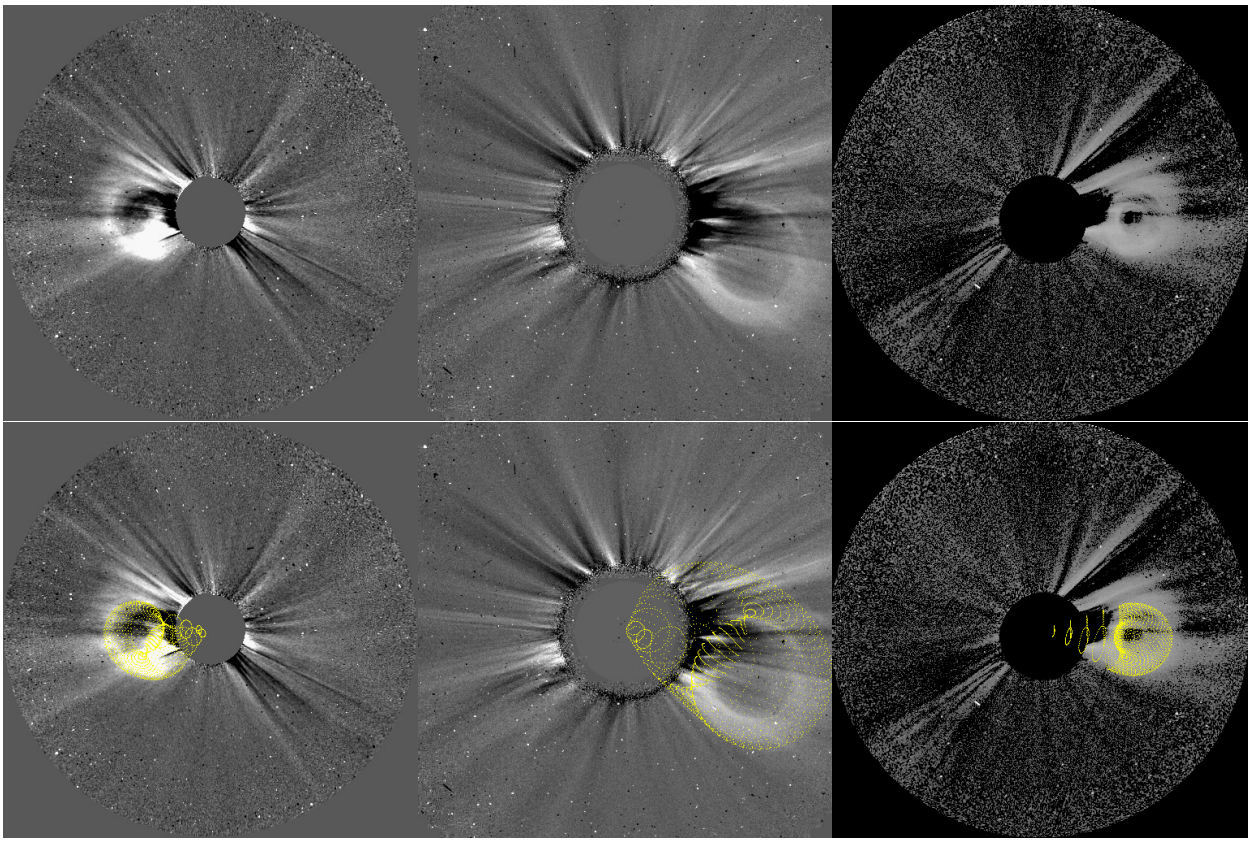


Figure 6.3: GCS fit for CME 1 on March 19, 2010 at 17:54 UT at height $H = 10.07$ $R_{\odot}$. Table 6.1 lists the GCS parameters for this event.

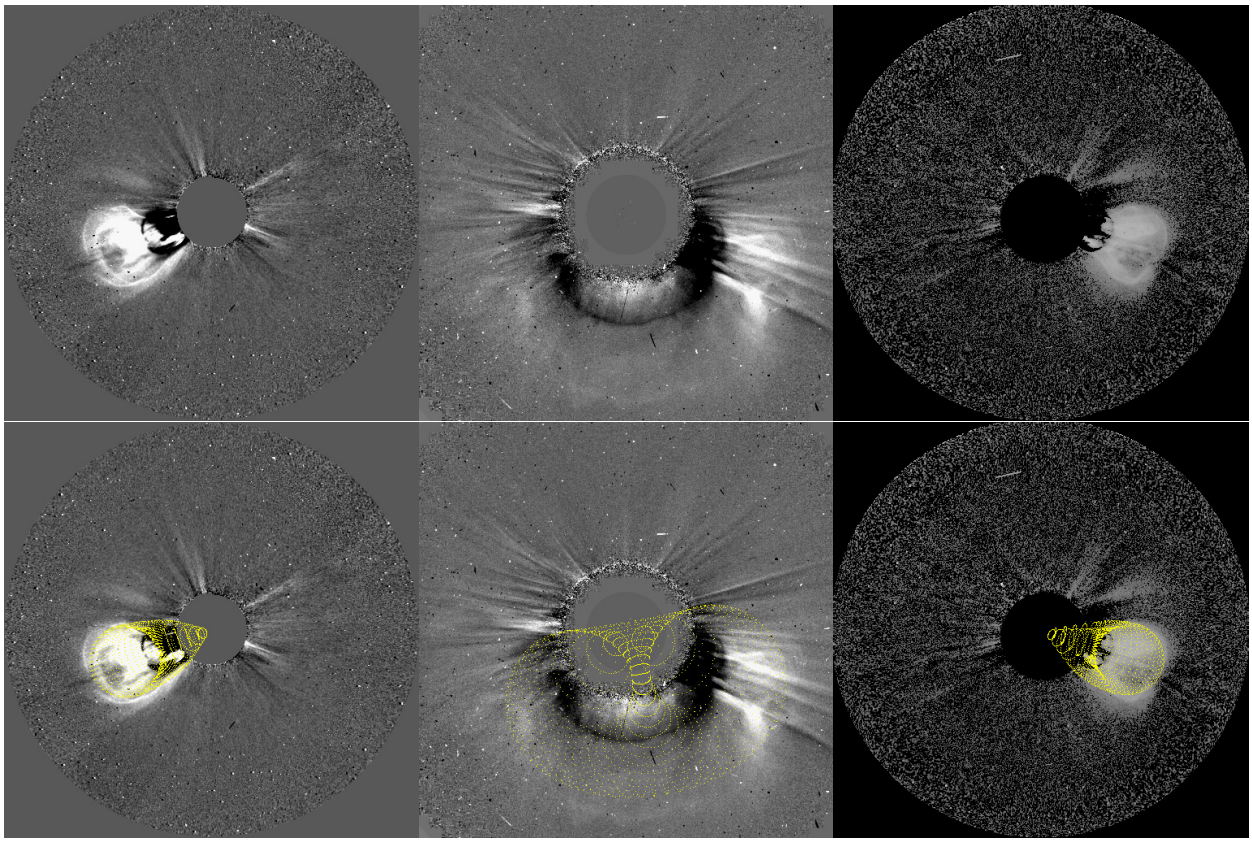


Figure 6.4: GCS fit for CME 2 on April 03, 2010 at 11:24 UT at height $H = 9.6\ \mathrm{R}_{\odot}$. Table 6.1 lists the GCS parameters for this event.

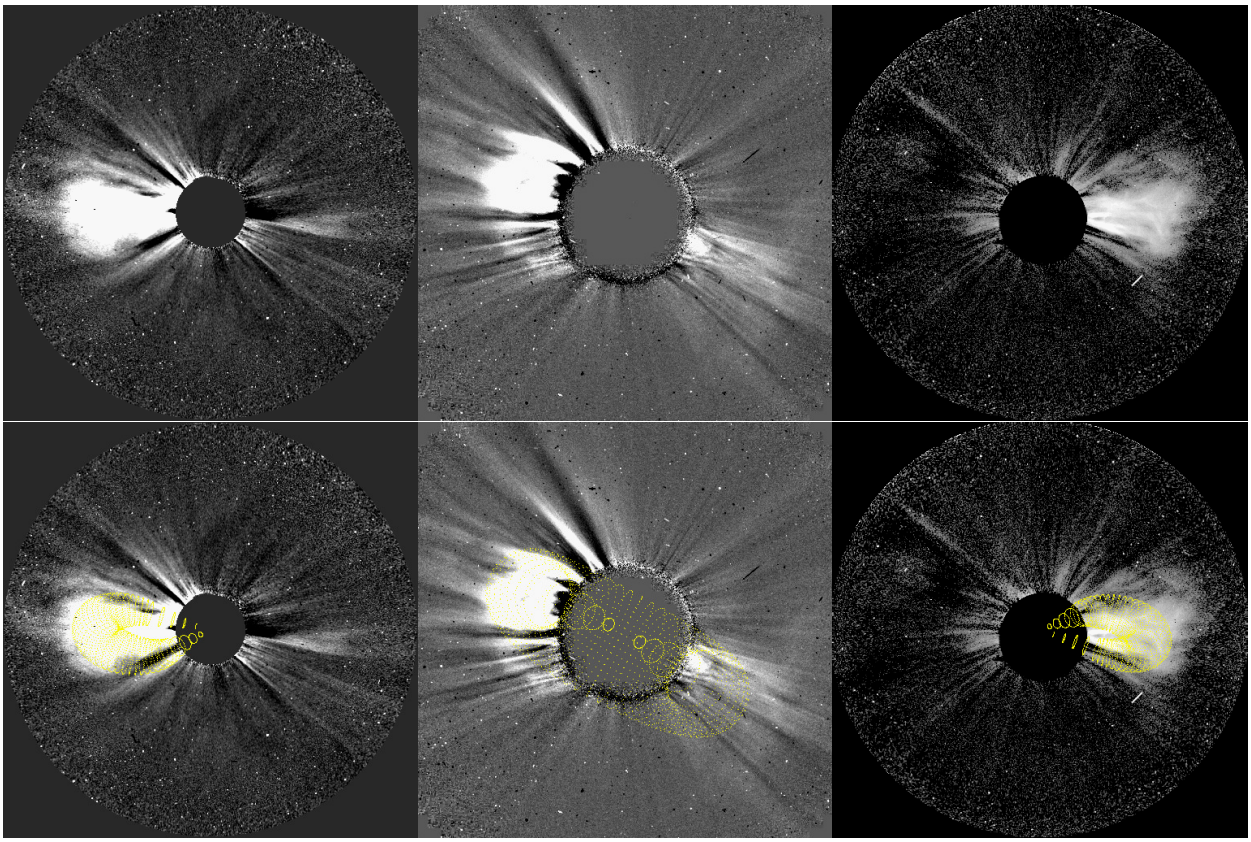


Figure 6.5: GCS fit for CME 3 on April 08, 2010 at 06:54 UT at height $H = 10.2\ \mathrm{R}_{\odot}$. Table 6.1 lists the GCS parameters for this event.

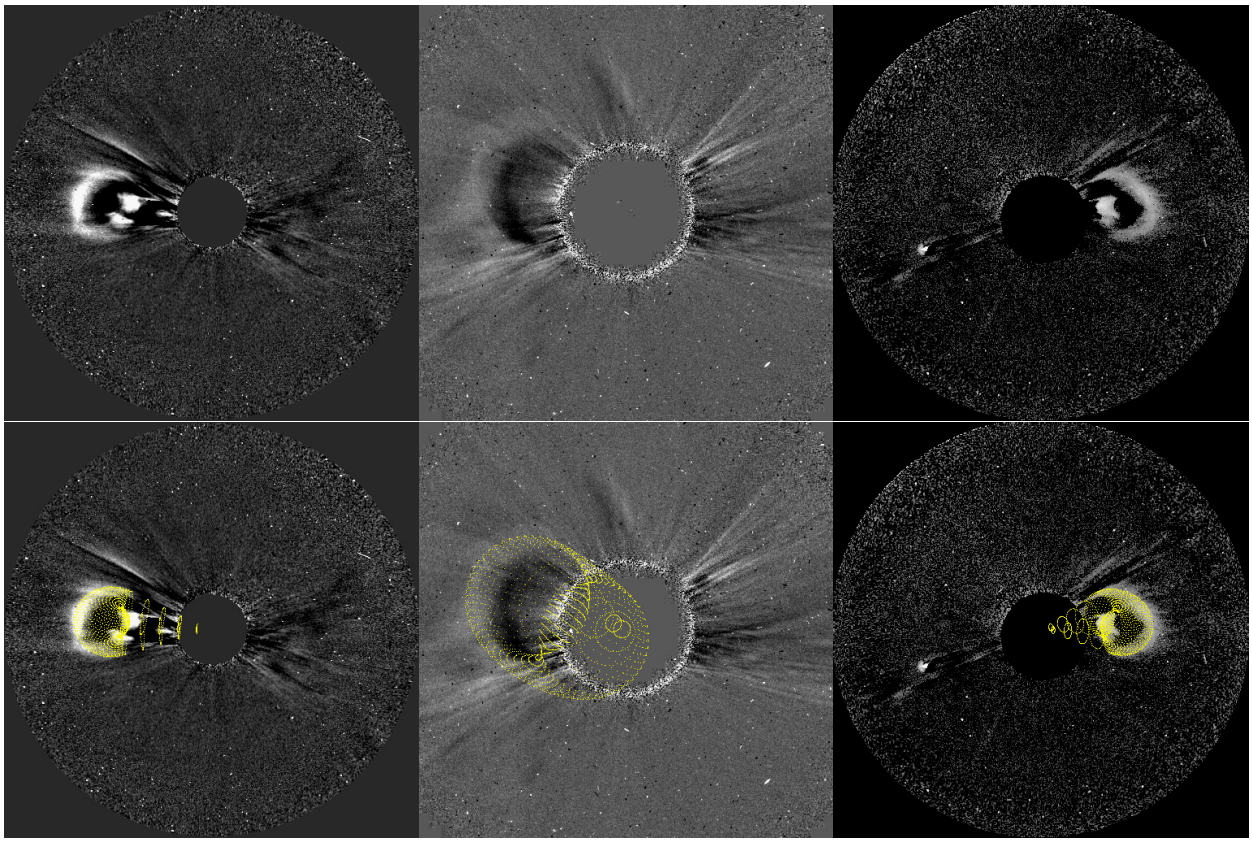


Figure 6.6: GCS fit for CME 4 on June 16, 2010 at 18:54 UT at height $H = 9.9$ $R_\odot$. Table 6.1 lists the GCS parameters for this event.

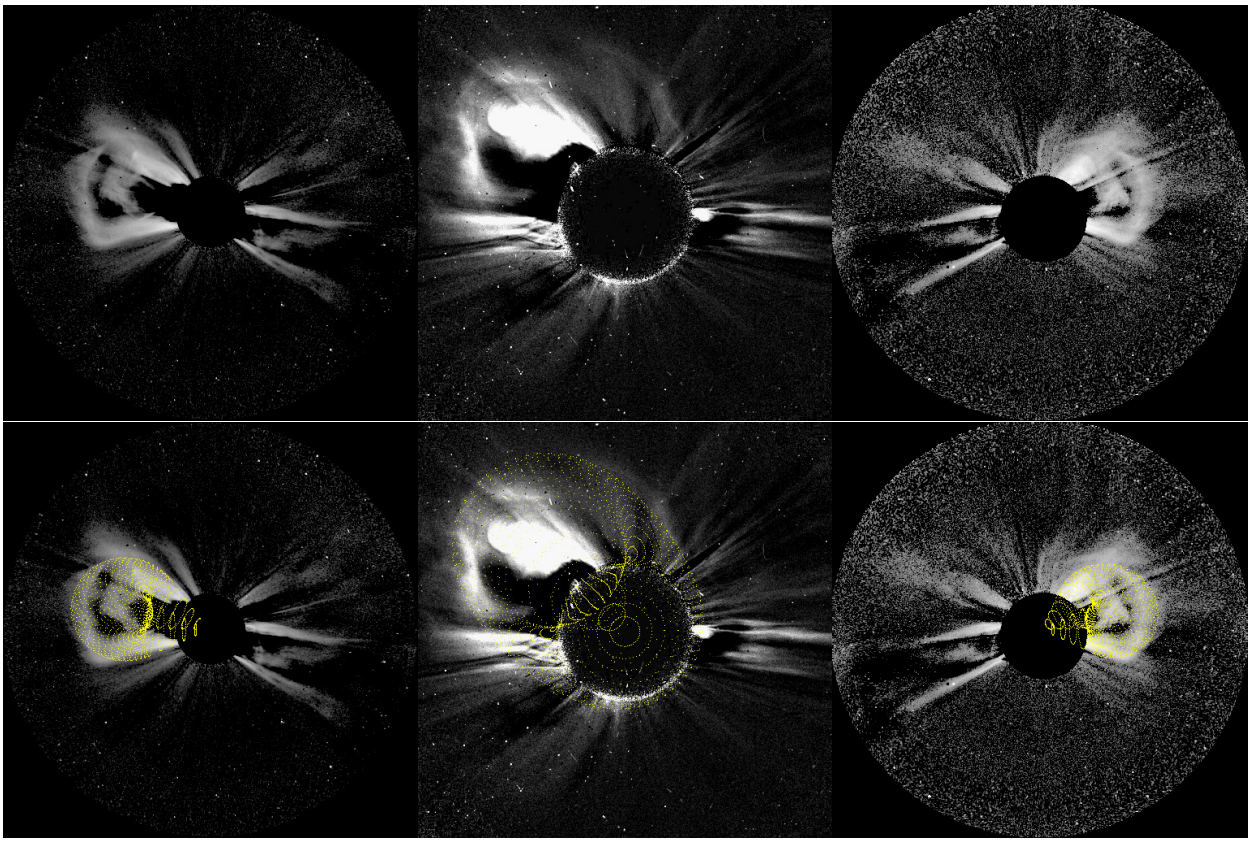


Figure 6.7: GCS fit for CME 5 on September 11, 2010 at 05:39 UT at height $H = 10.3$ $R_\odot$. Table 6.1 lists the GCS parameters for this event.

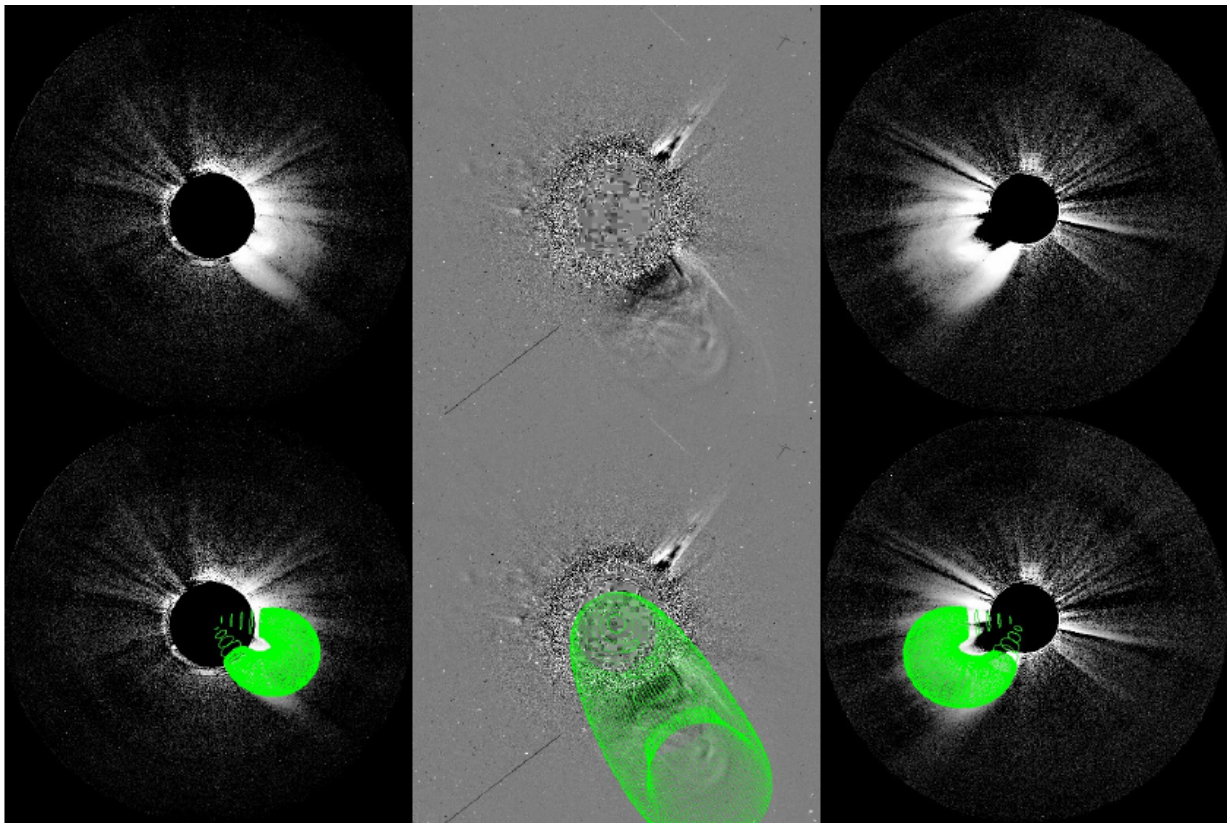


Figure 6.8: GCS fit for CME 6 on October 26, 2010 at 11:54 at height $H = 10.0\ \mathrm{R}_{\odot}$. Table 6.1 lists the GCS parameters for this event. This figure is adapted from Colaninno (2012) (Appendix).

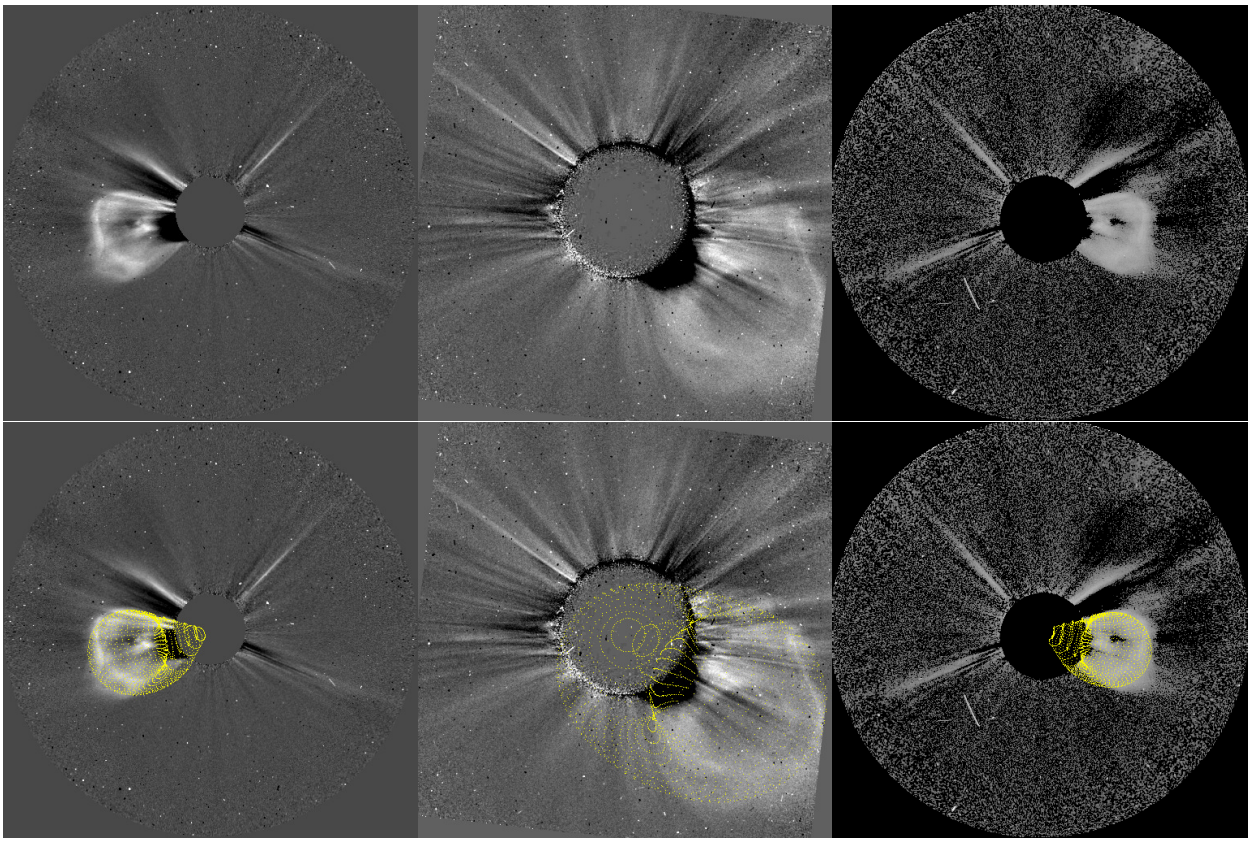


Figure 6.9: GCS fit for CME 7 on December 23, 2010 at 10:24 UT at height $H = 9.5$ $R_{\odot}$. Table 6.1 lists the GCS parameters for this event.

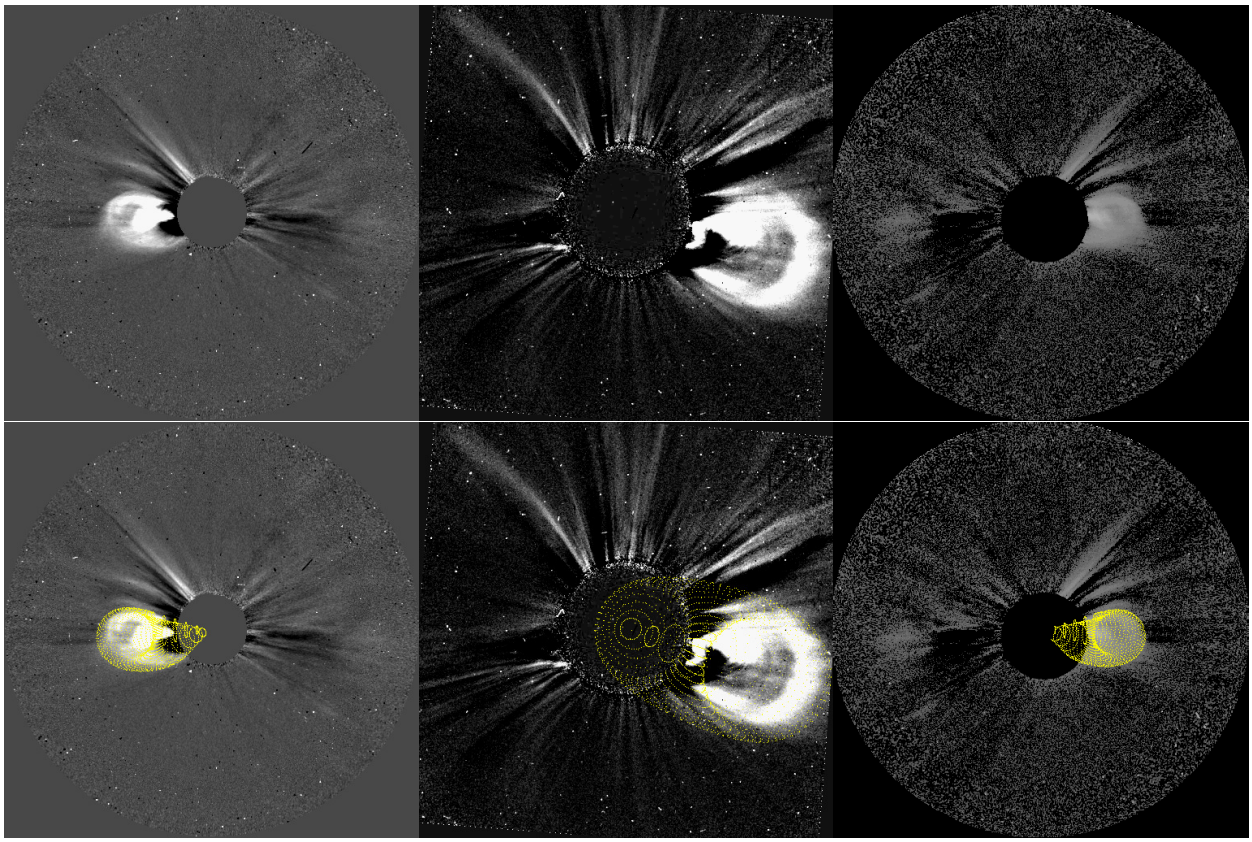


Figure 6.10: GCS fit for CME 8 on January 24, 2011 at 06:39 UT at height $H = 8.9$ $R_\odot$. Table 6.1 lists the GCS parameters for this event.

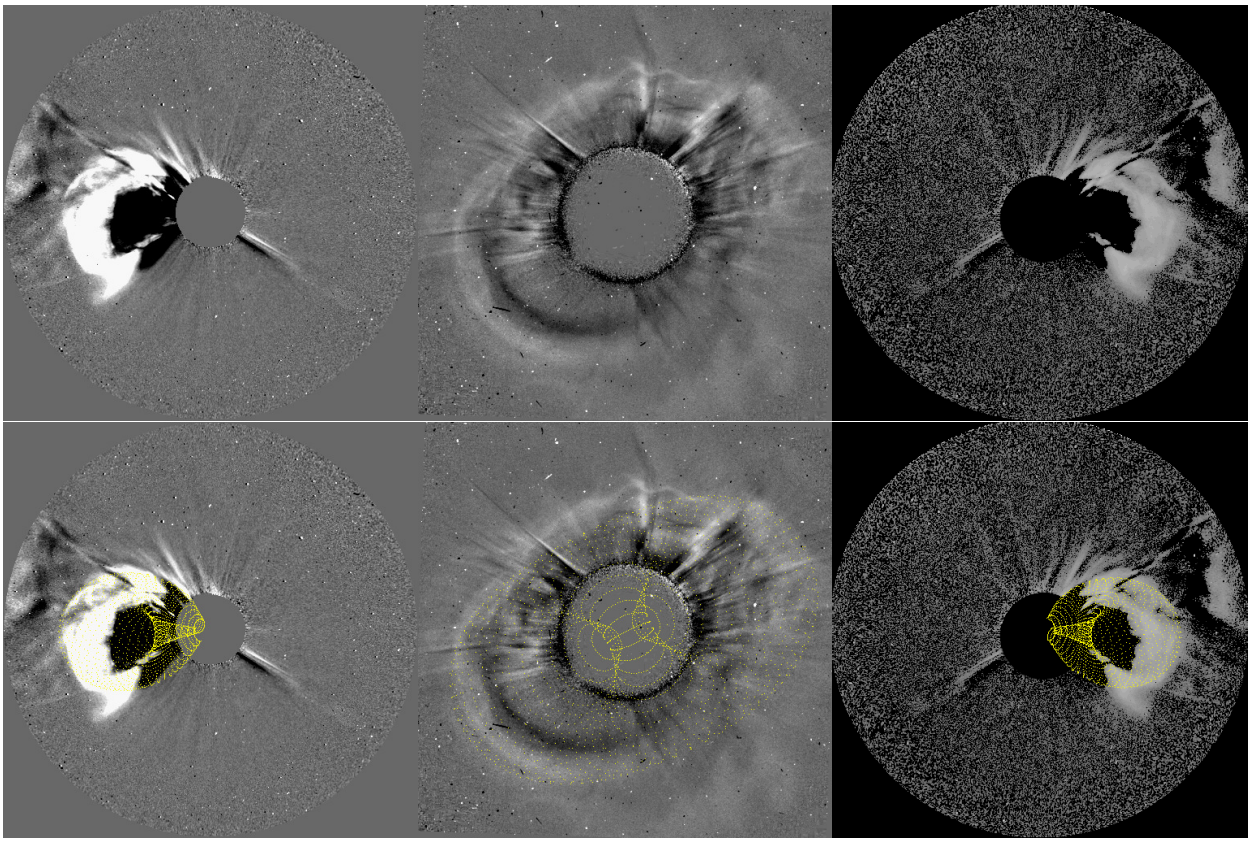


Figure 6.11: GCS fit for CME 9 on February 15, 2011 at 03:39 UT at height $H = 10.9\ \mathrm{R}_{\odot}$. Table 6.1 lists the GCS parameters for this event.

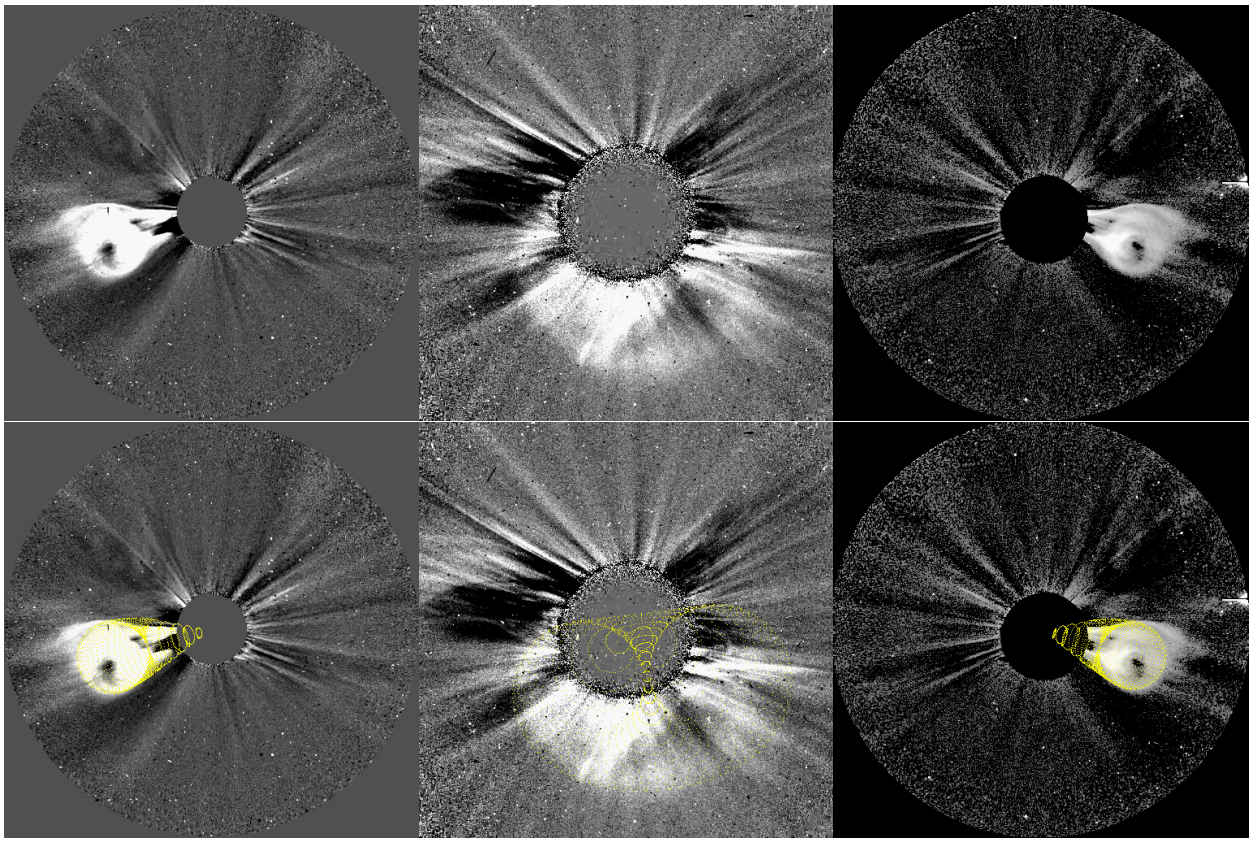


Figure 6.12: GCS fit for CME 10 on March 03, 2011 at 08:53 UT at height $H = 10.0$ $R_\odot$. Table 6.1 lists the GCS parameters for this event.

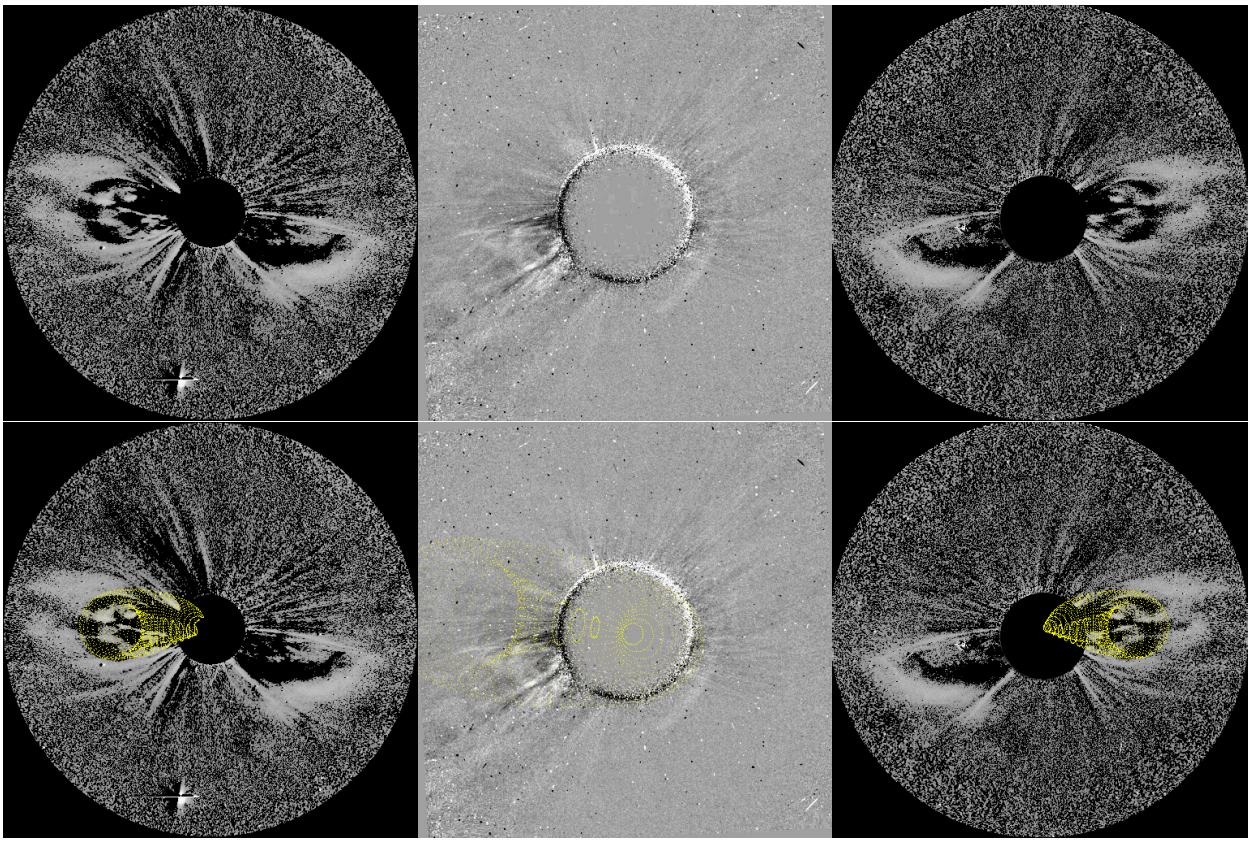


Figure 6.13: GCS fit for CME 11 on March 25, 2011 at 15:39 UT at height $H = 10.0$ $R_{\odot}$. Table 6.1 lists the GCS parameters for this event.

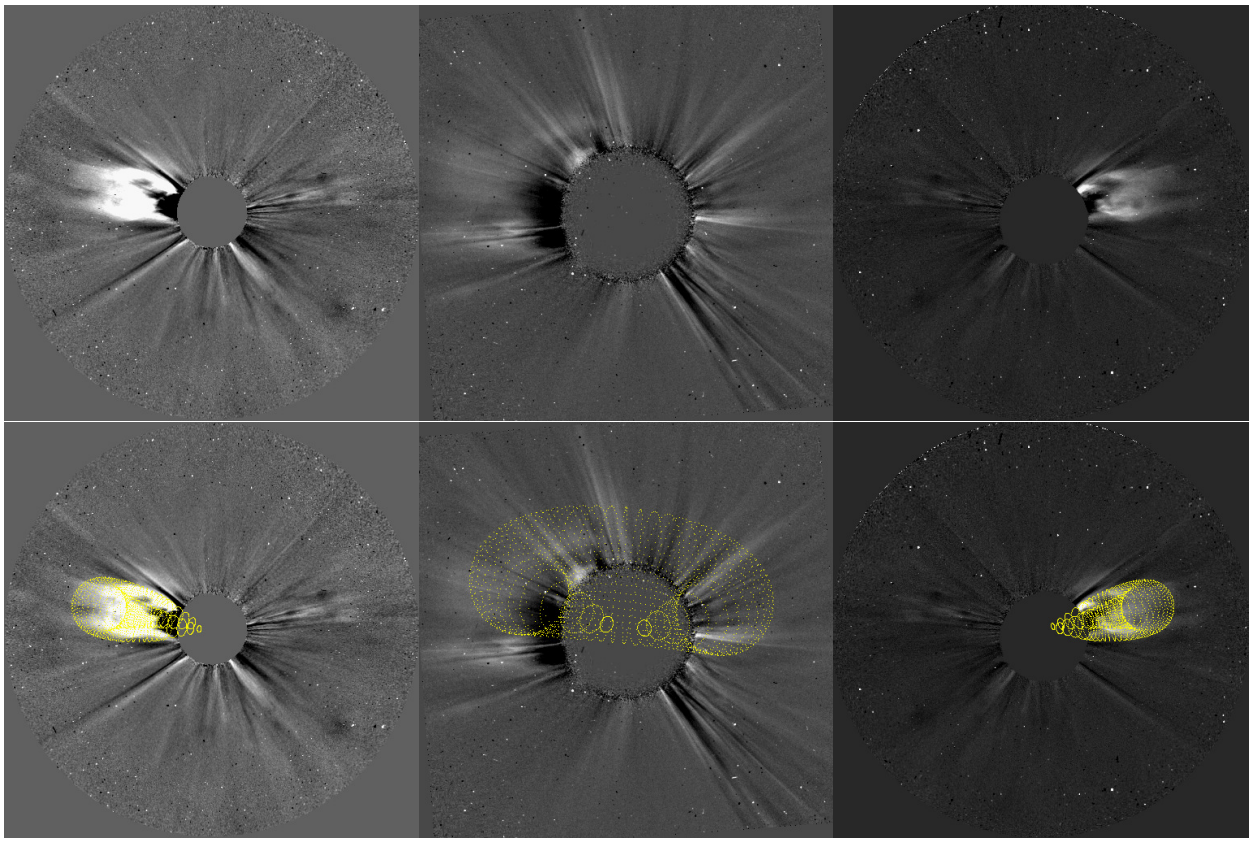


Figure 6.14: GCS fit for CME 12 on April 09, 2011 at 02:54 UT at height $H = 10.2\ \mathrm{R}_{\odot}$. Table 6.1 lists the GCS parameters for this event.

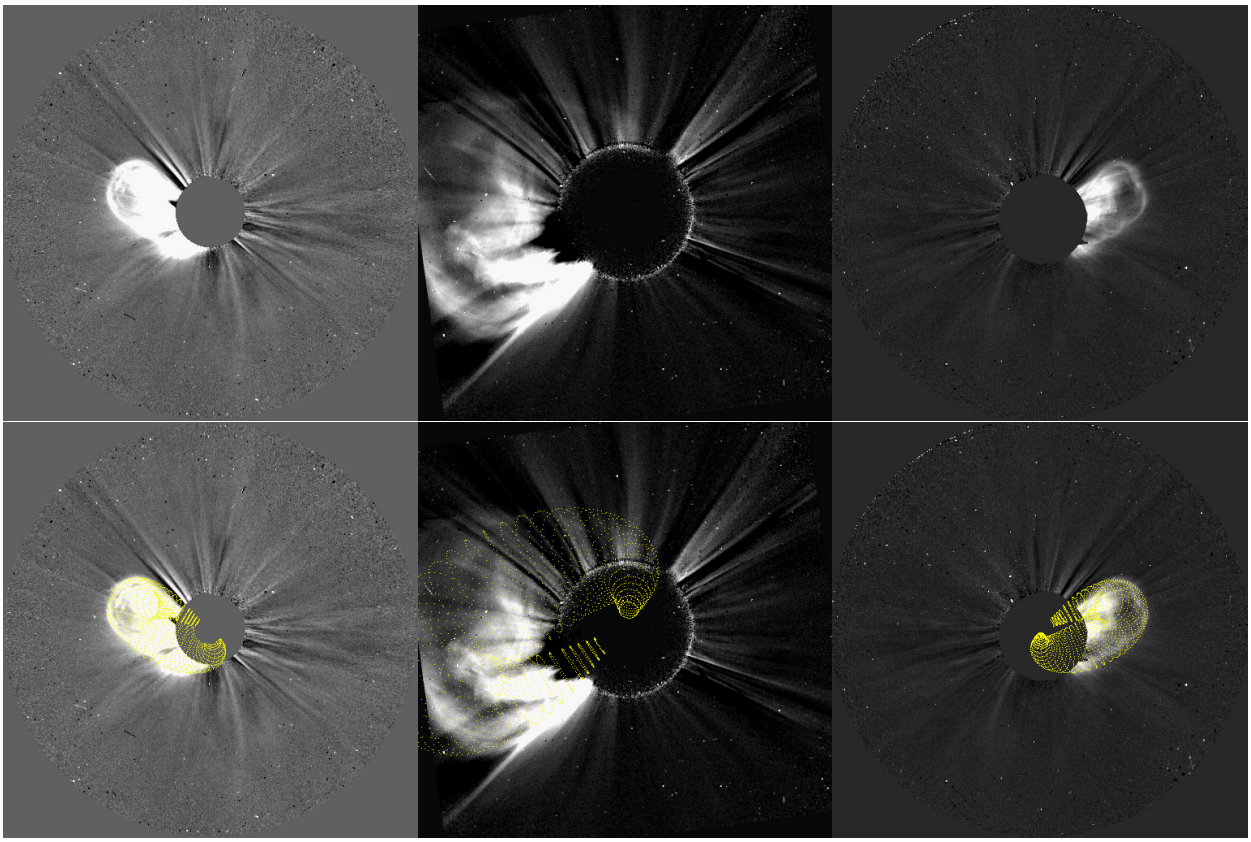


Figure 6.15: GCS fit for CME 13 on June 14, 2011 at 09:54 UT at height $H = 9.4\ \mathrm{R}_{\odot}$. Table 6.1 lists the GCS parameters for this event.

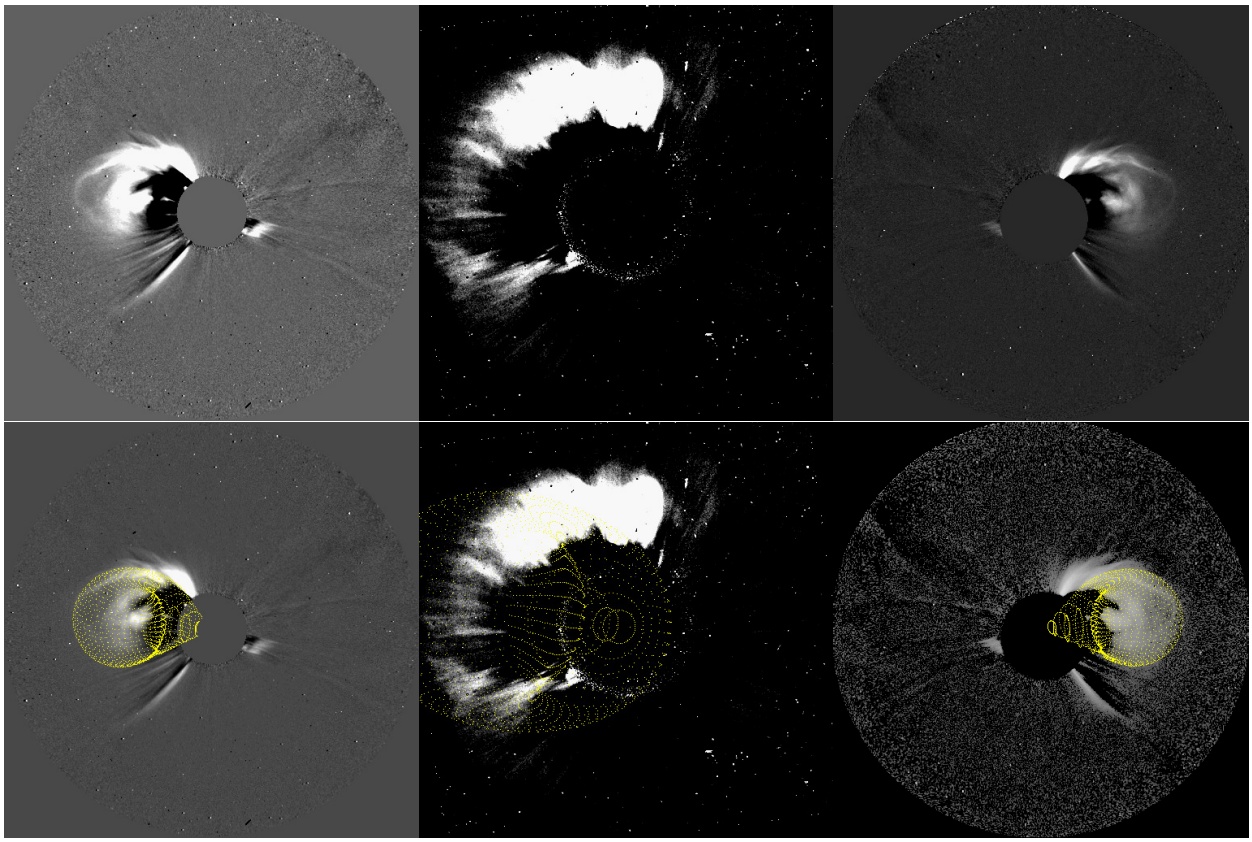


Figure 6.16: GCS fit for June 21, 2011 (CME 14) at 04:24 at height 11.3 $R_{\odot}$. Table 6.1 lists the GCS parameters for this event.

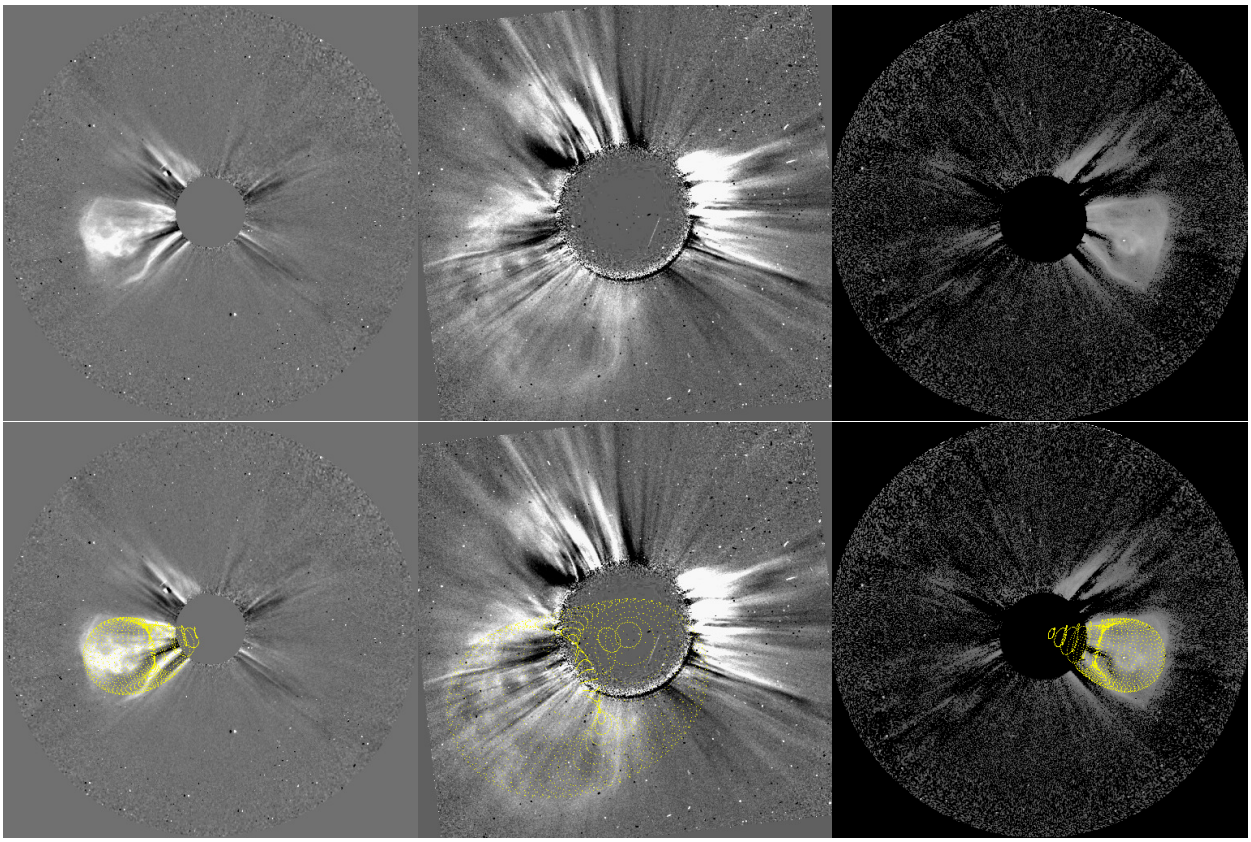


Figure 6.17: GCS fit for CME 15 on July 09, 2011 at 02:24 UT at height $H = 10.0$ $R_{\odot}$. Table 6.1 lists the GCS parameters for this event.

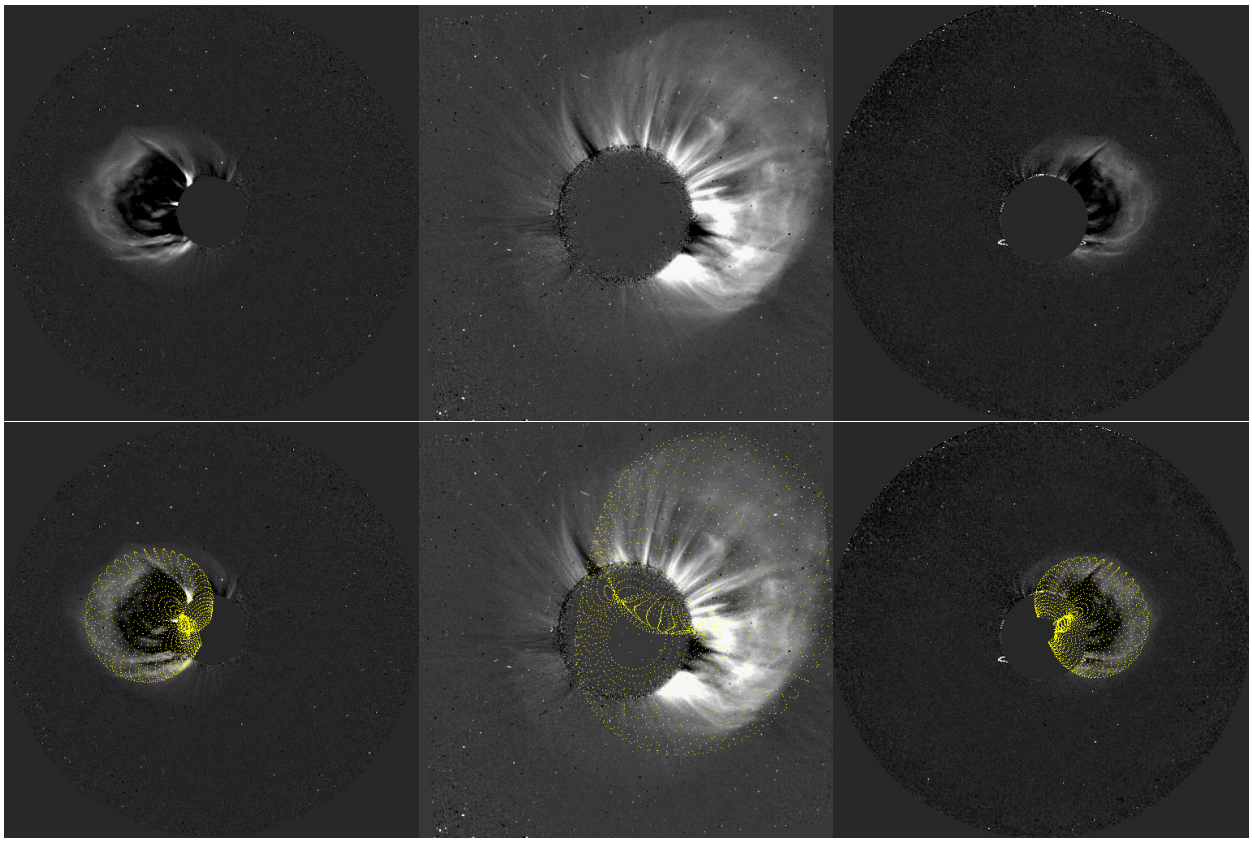


Figure 6.18: GCS fit for CME 16 on August 04, 2011 at 04:39 UT at height $H = 9.4$ $R_\odot$. Table 6.1 lists the GCS parameters for this event.

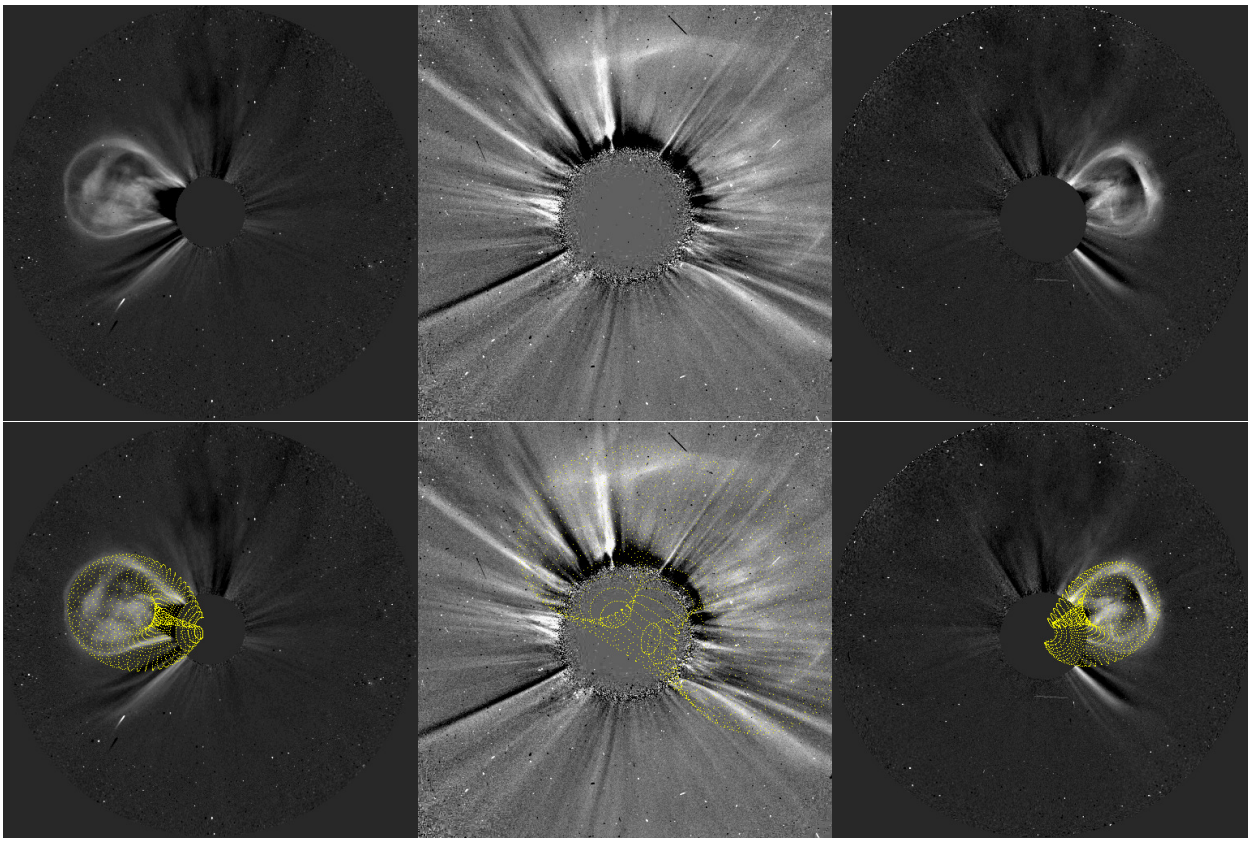


Figure 6.19: GCS fit for CME 17 on September 14, 2011 at 02:24 UT at height $H = 10.5\ \mathrm{R}_{\odot}$. Table 6.1 lists the GCS parameters for this event.

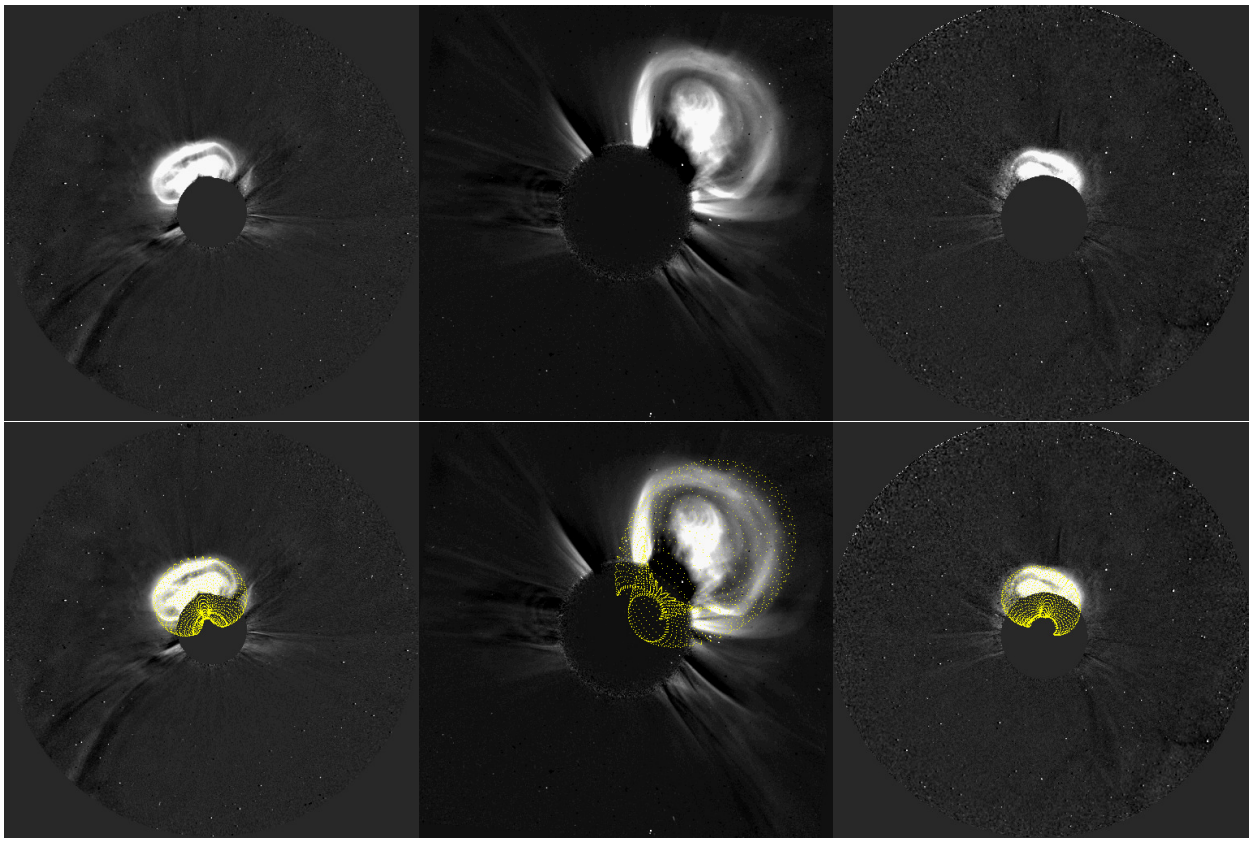


Figure 6.20: GCS fit for CME 18 on October 22, 2011 at 11:24 at height $H = 6.2$ $R_\odot$. Table 6.1 lists the GCS parameters for this event.

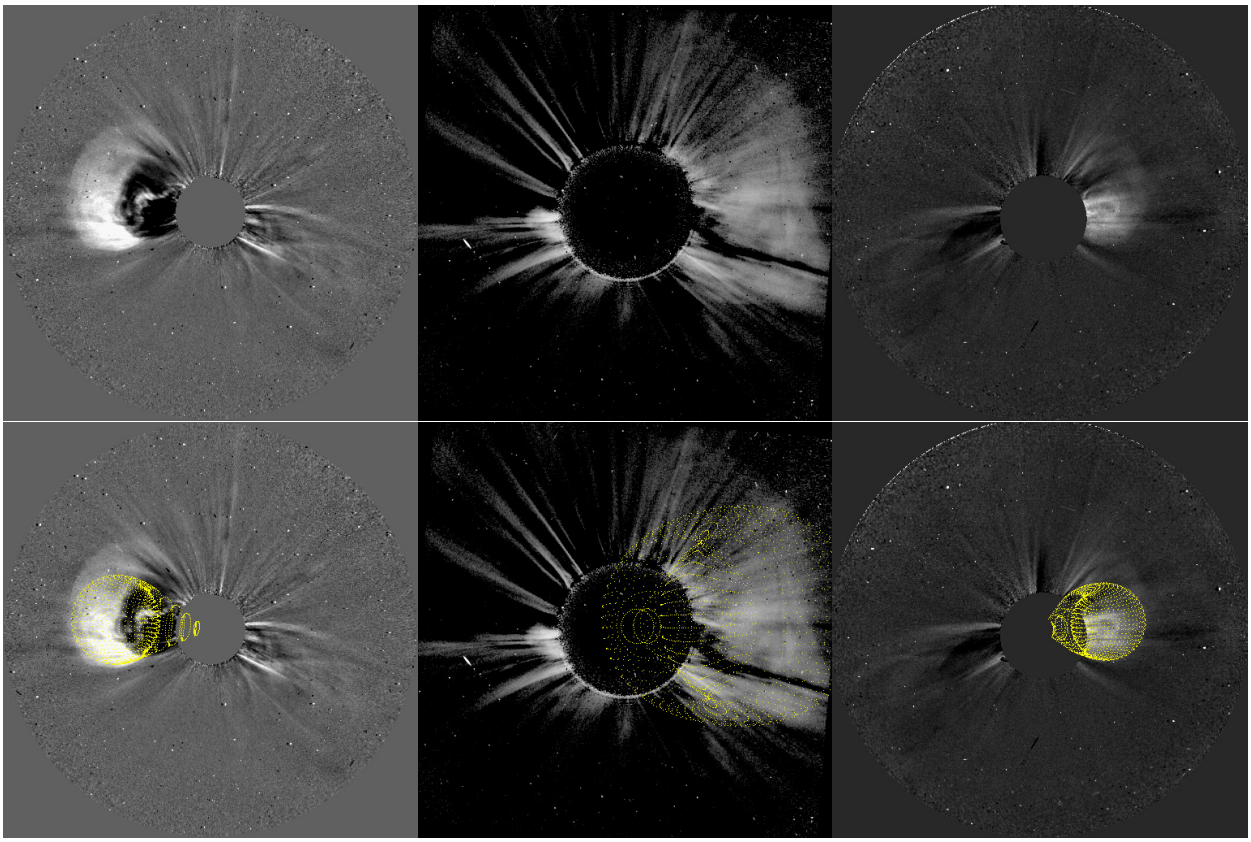


Figure 6.21: GCS fit for CME 19 on October 26, 2011 at 13:54 UT at height $H = 10.2$ $R_{\odot}$. Table 6.1 lists the GCS parameters for this event.

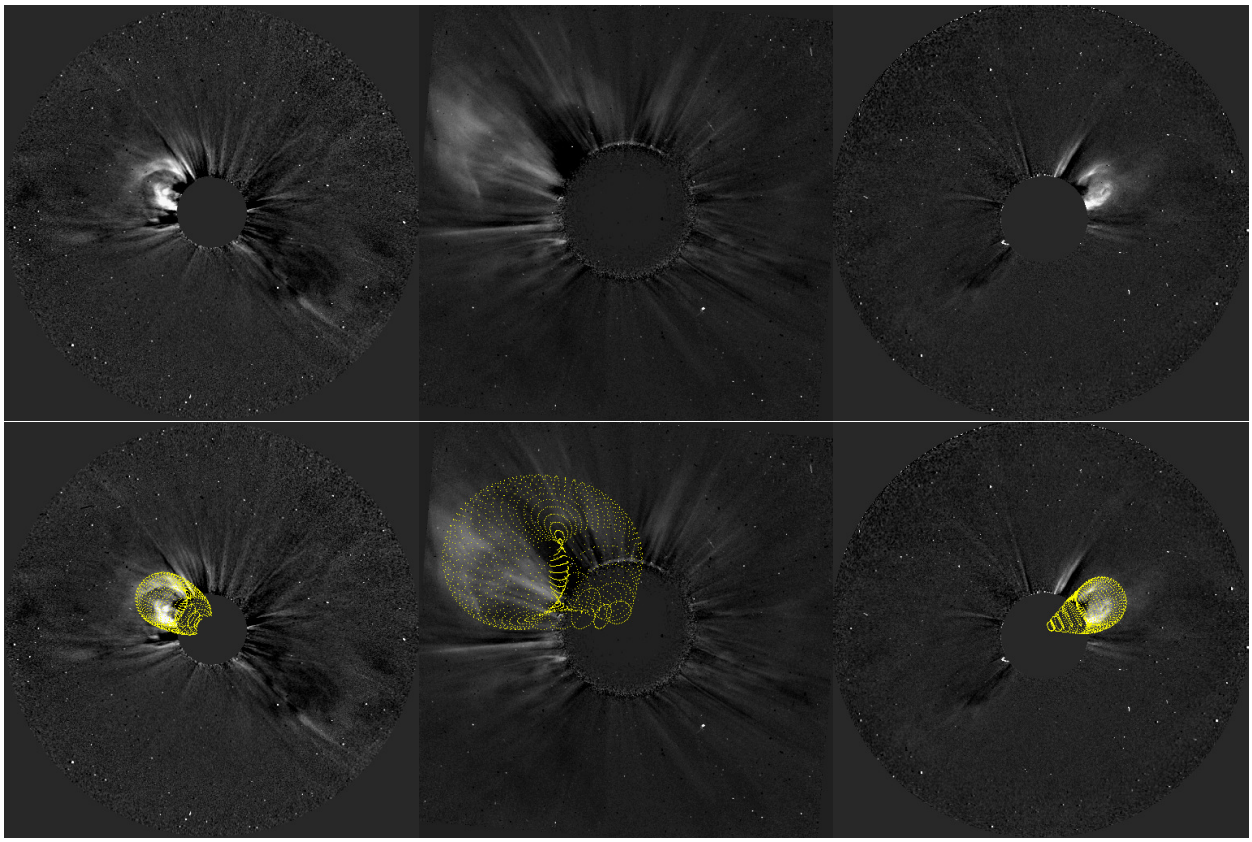


Figure 6.22: GCS fit for CME 20 on October 27, 2011 at 13:39 UT at height $H = 7.8$ $R_\odot$. Table 6.1 lists the GCS parameters for this event.

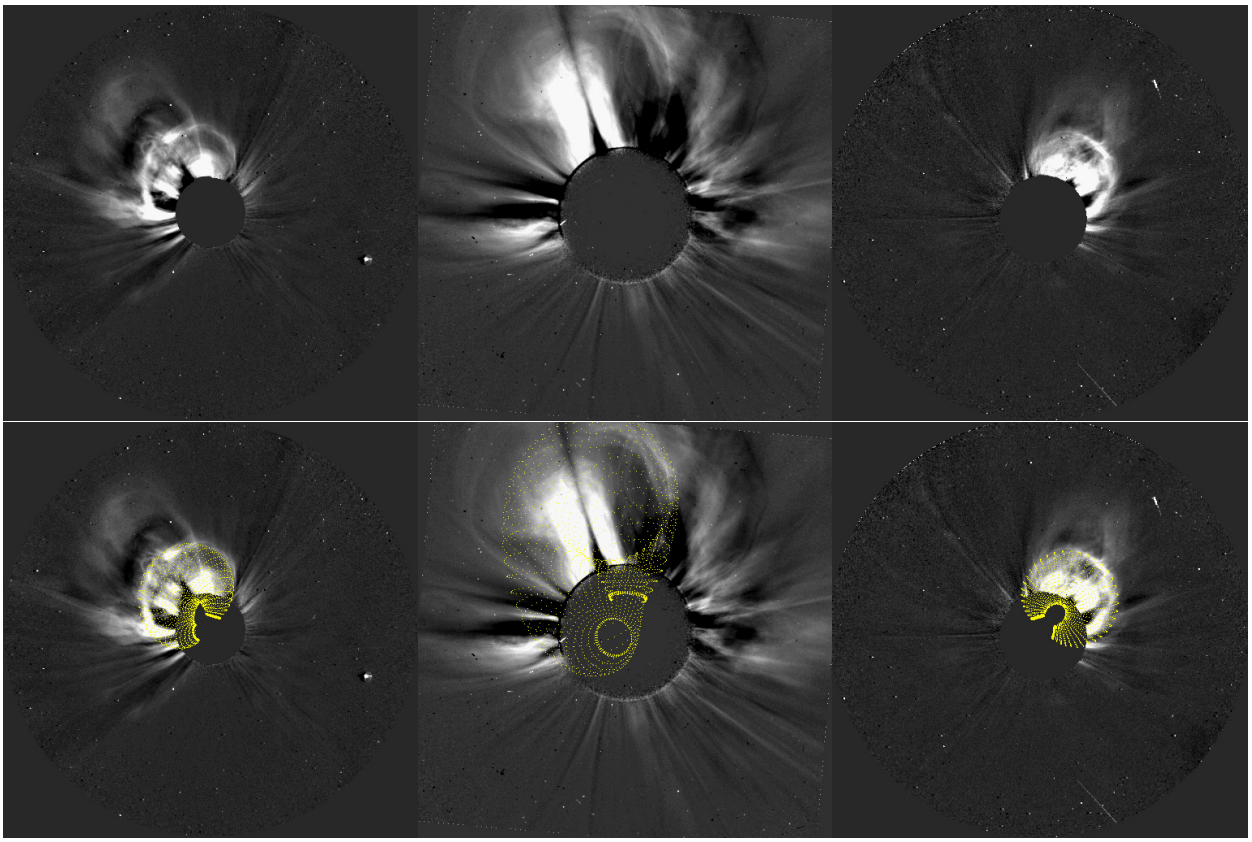


Figure 6.23: GCS fit for CME 21 on November 19, 2011 at 15:54 UT at height $H = 7.2$ $R_\odot$. Table 6.1 lists the GCS parameters for this event.

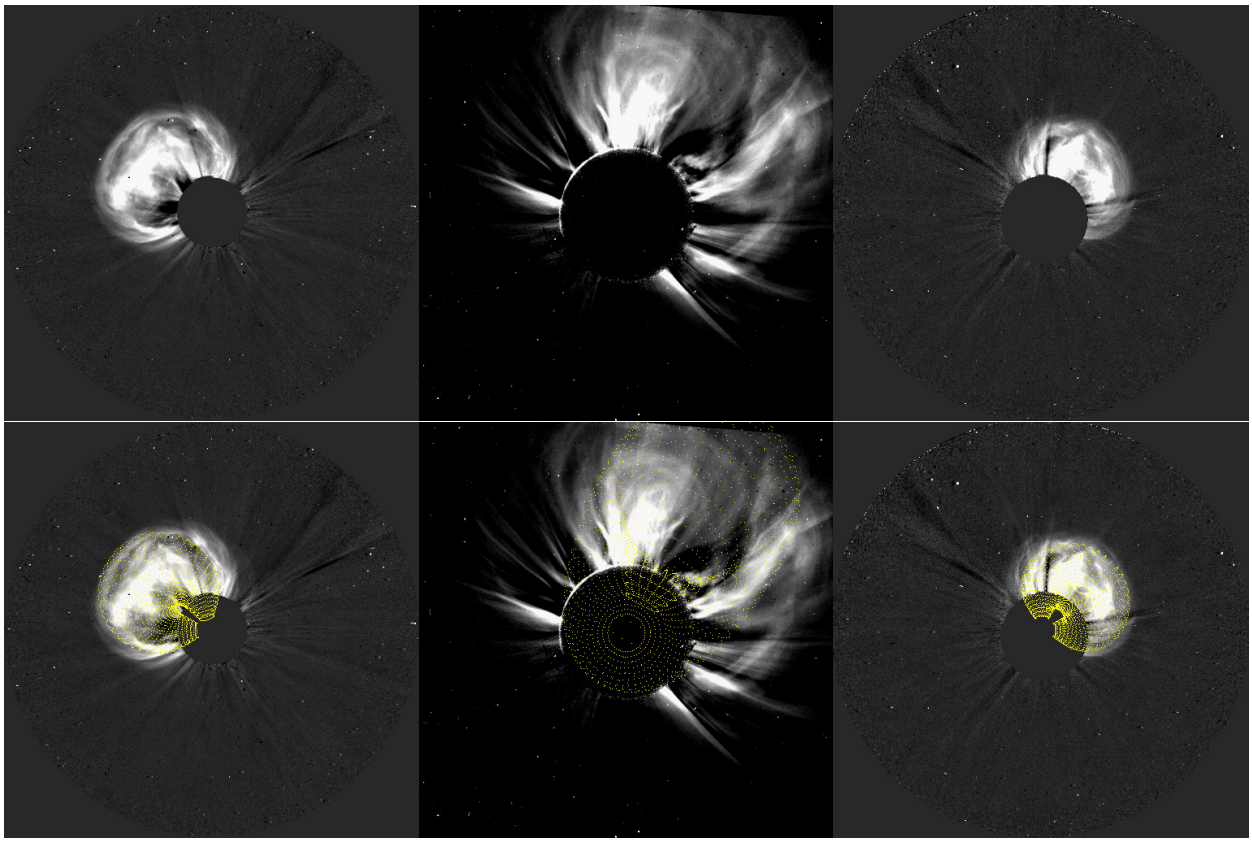


Figure 6.24: GCS fit for CME 22 on January 23, 2012 at 04:24 UT at height $H = 8.9$ $R_\odot$. Table 6.1 lists the GCS parameters for this event.

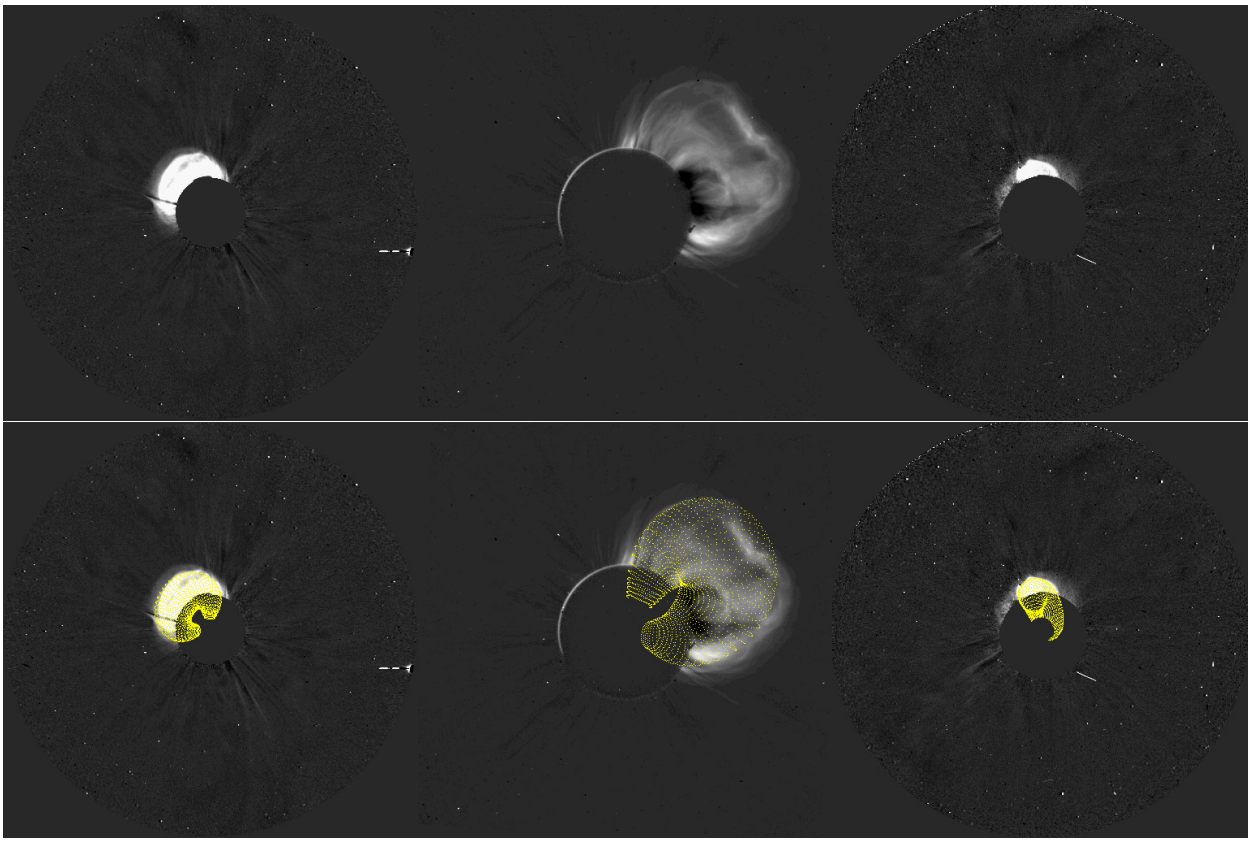


Figure 6.25: GCS fit for CME 23 on January 27, 2012 at 18:39 UT at height $H = 5.3$ $R_\odot$. Table 6.1 lists the GCS parameters for this event.

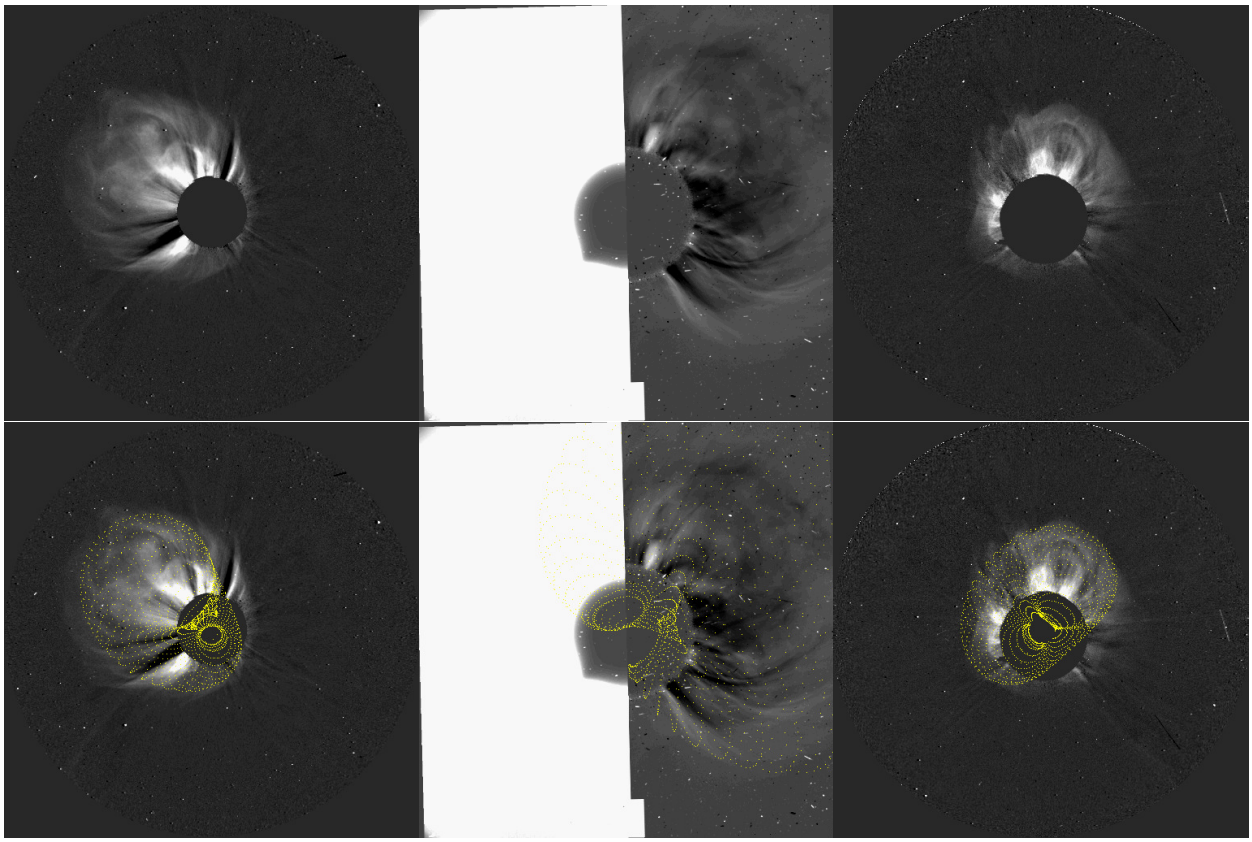


Figure 6.26: GCS fit for CME 24 on March 13, 2012 at 18:24 UT at height $H = 11.5\ \mathrm{R}_{\odot}$. Table 6.1 lists the GCS parameters for this event.

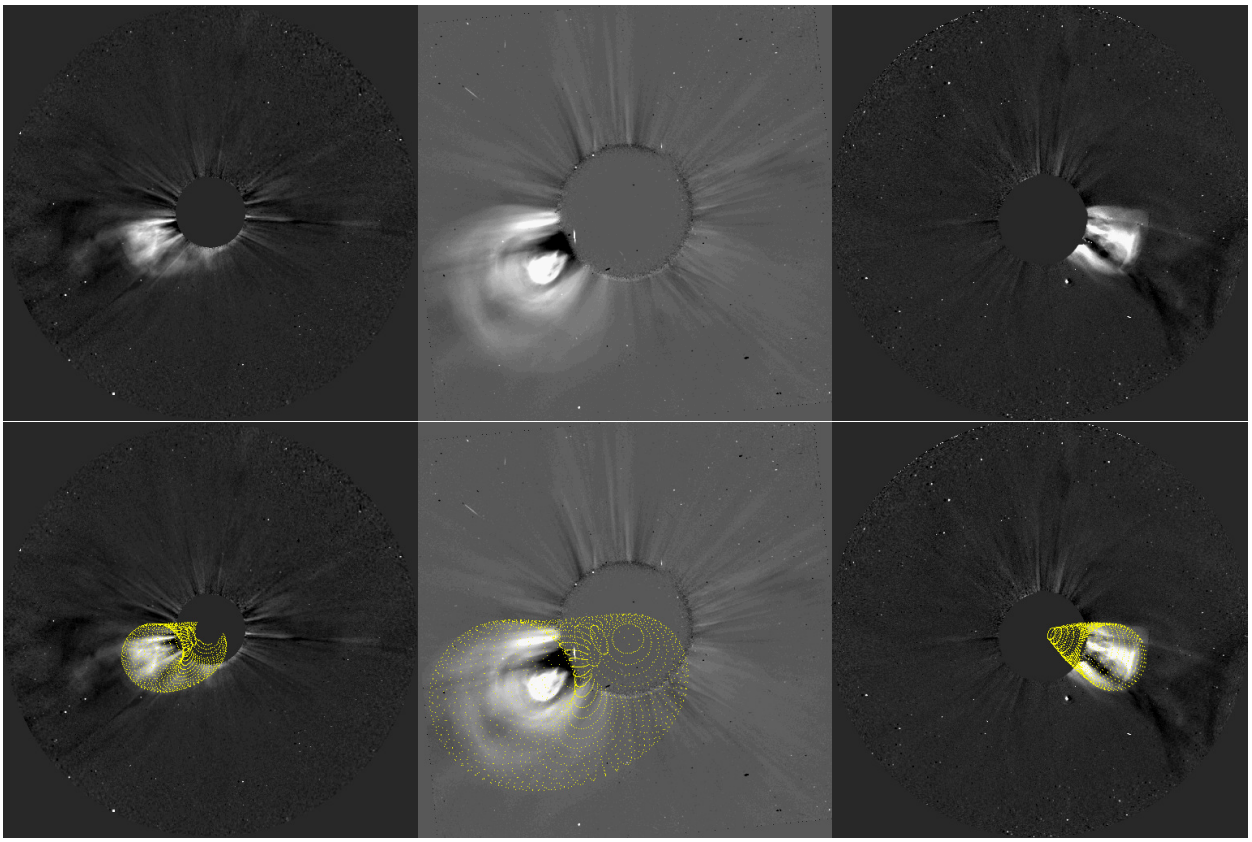


Figure 6.27: GCS fit for CME 25 on April 19, 2012 at 17:24 UT at height $H = 8.4$ $R_\odot$. Table 6.1 lists the GCS parameters for this event.

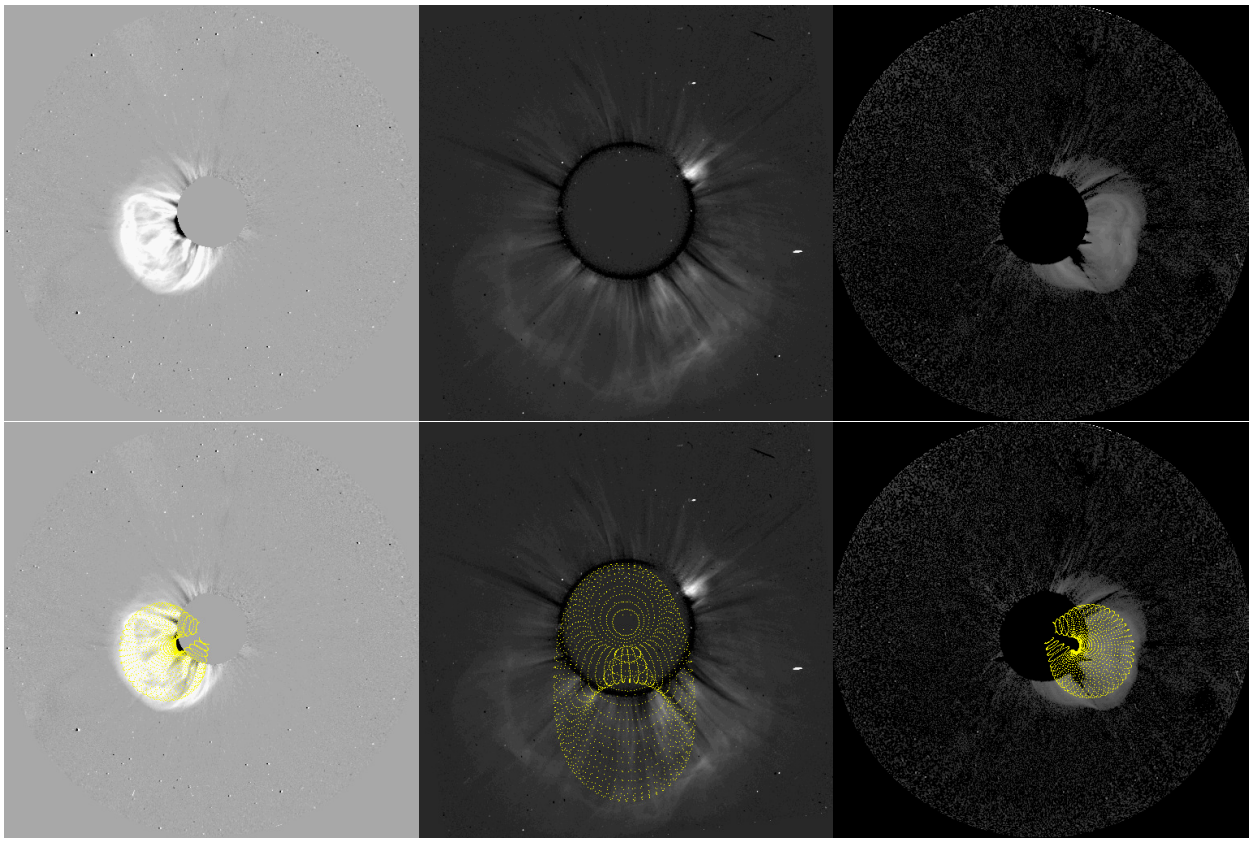


Figure 6.28: GCS fit for CME 26 on June 14, 2012 at 14:39 UT at height $H = 7.8$ $R_\odot$. Table 6.1 lists the GCS parameters for this event.

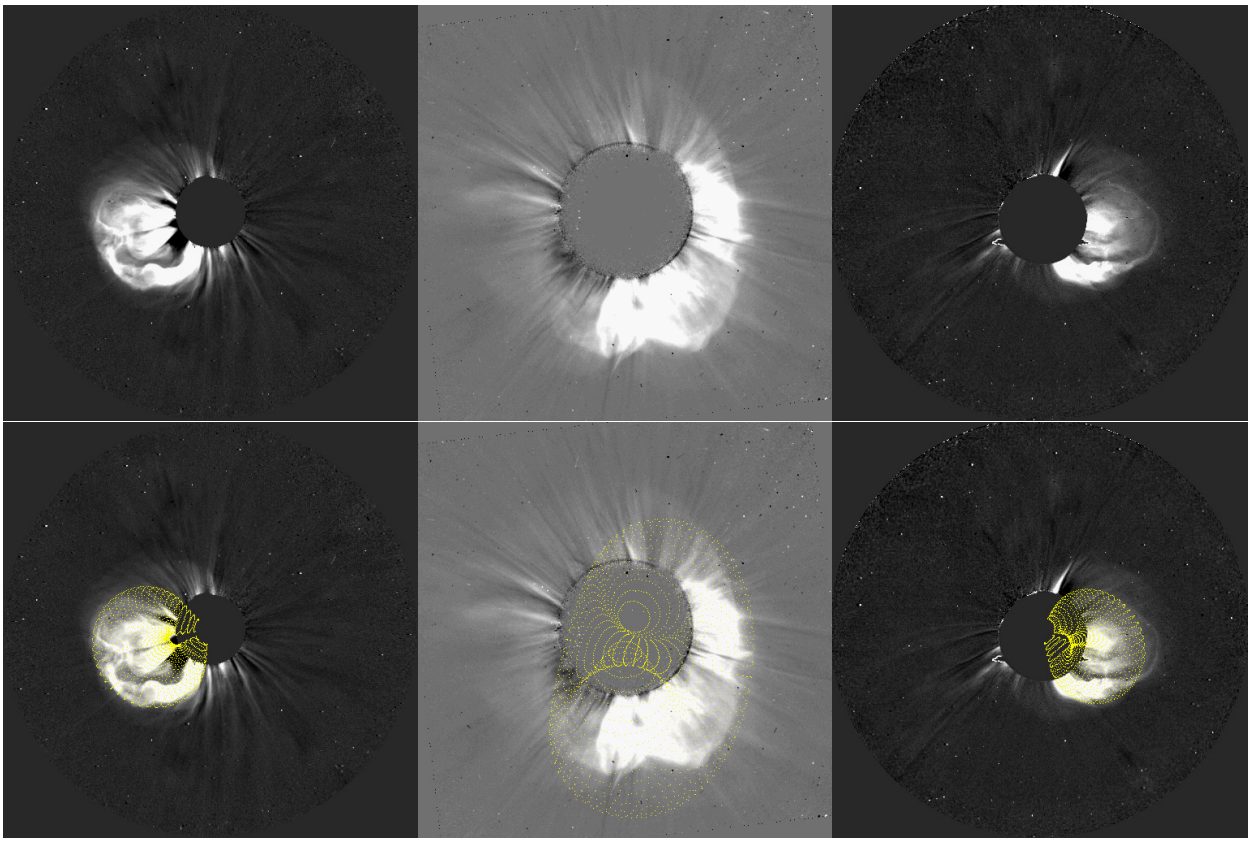


Figure 6.29: GCS fit for CME 27 on July 12, 2012 at 17:39 UT at height $H = 9.2\ \mathrm{R}_{\odot}$. Table 6.1 lists the GCS parameters for this event.

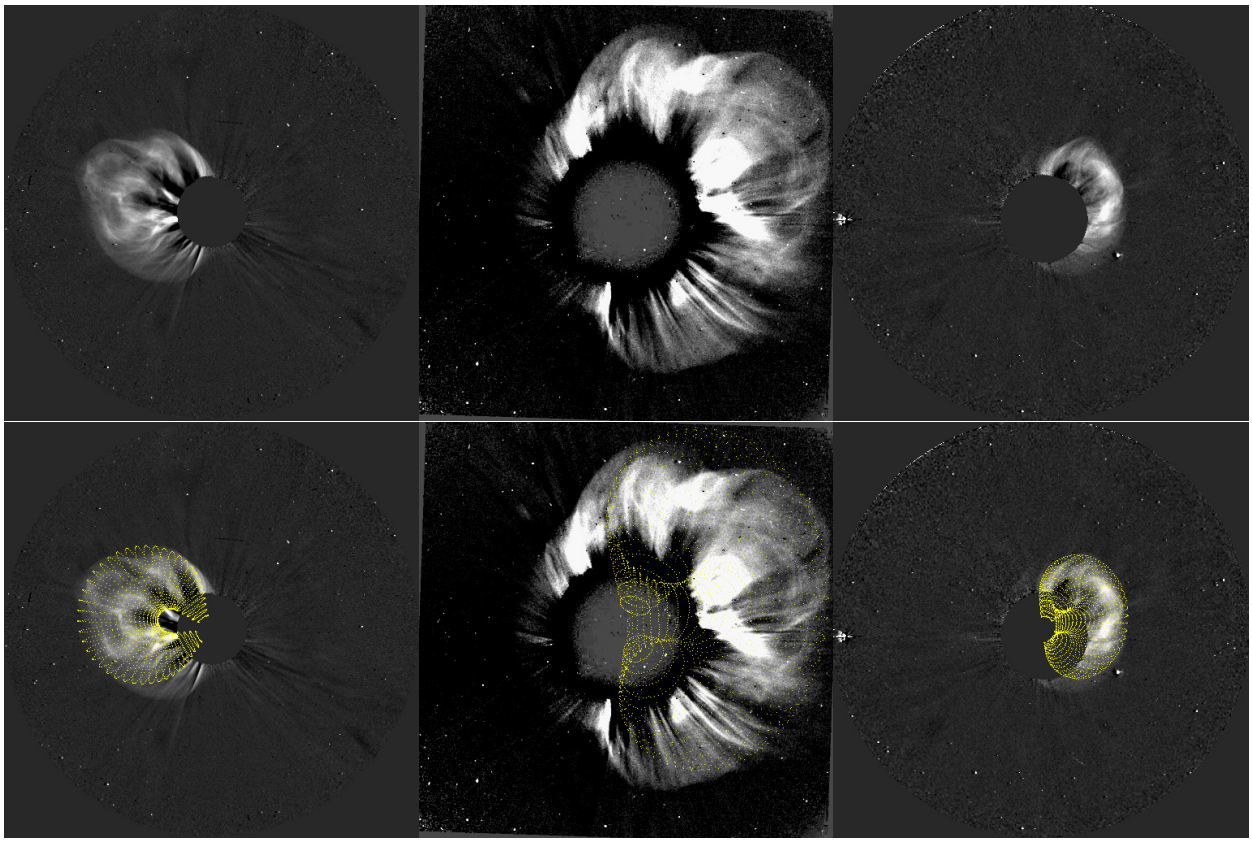


Figure 6.30: GCS fit for CME 28 on September 28, 2012 at 00:54 UT at height $H = 9.9$ $R_\odot$. Table 6.1 lists the GCS parameters for this event.

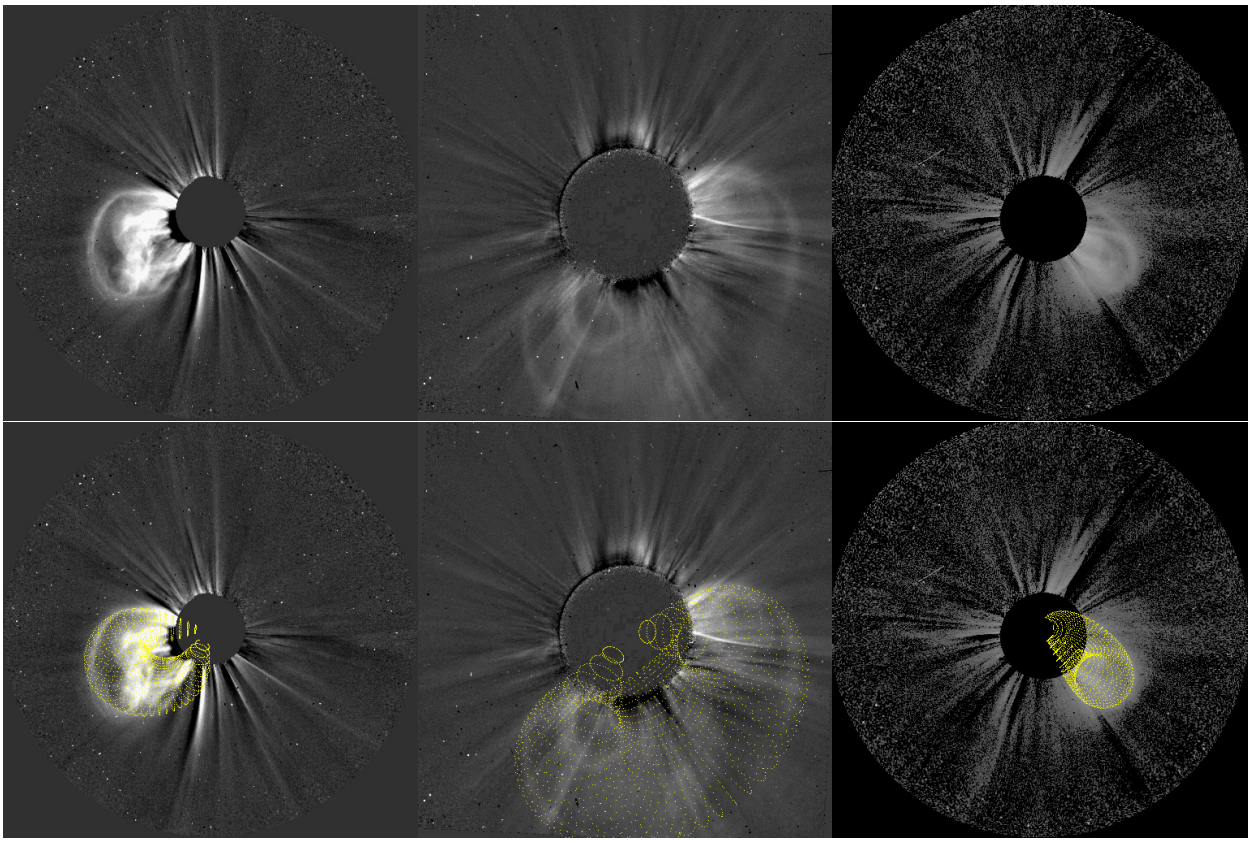


Figure 6.31: GCS fit for CME 29 on October 05, 2012 at 05:54 UT at height $H = 10.0$ $R_{\odot}$. Table 6.1 lists the GCS parameters for this event.

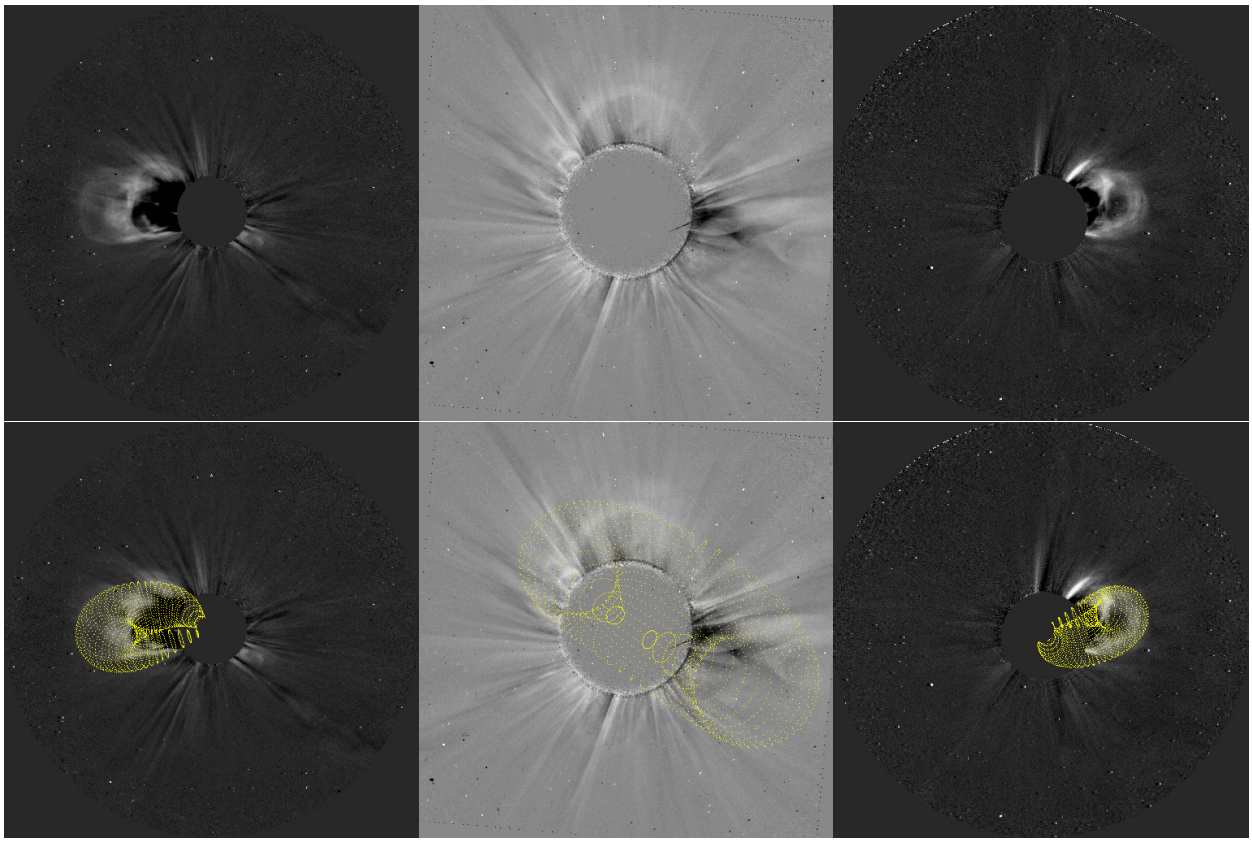


Figure 6.32: GCS fit for CME 30 on October 27, 2012 at 18:54 UT at height $H = 10.5\ \mathrm{R}_{\odot}$. Table 6.1 lists the GCS parameters for this event.

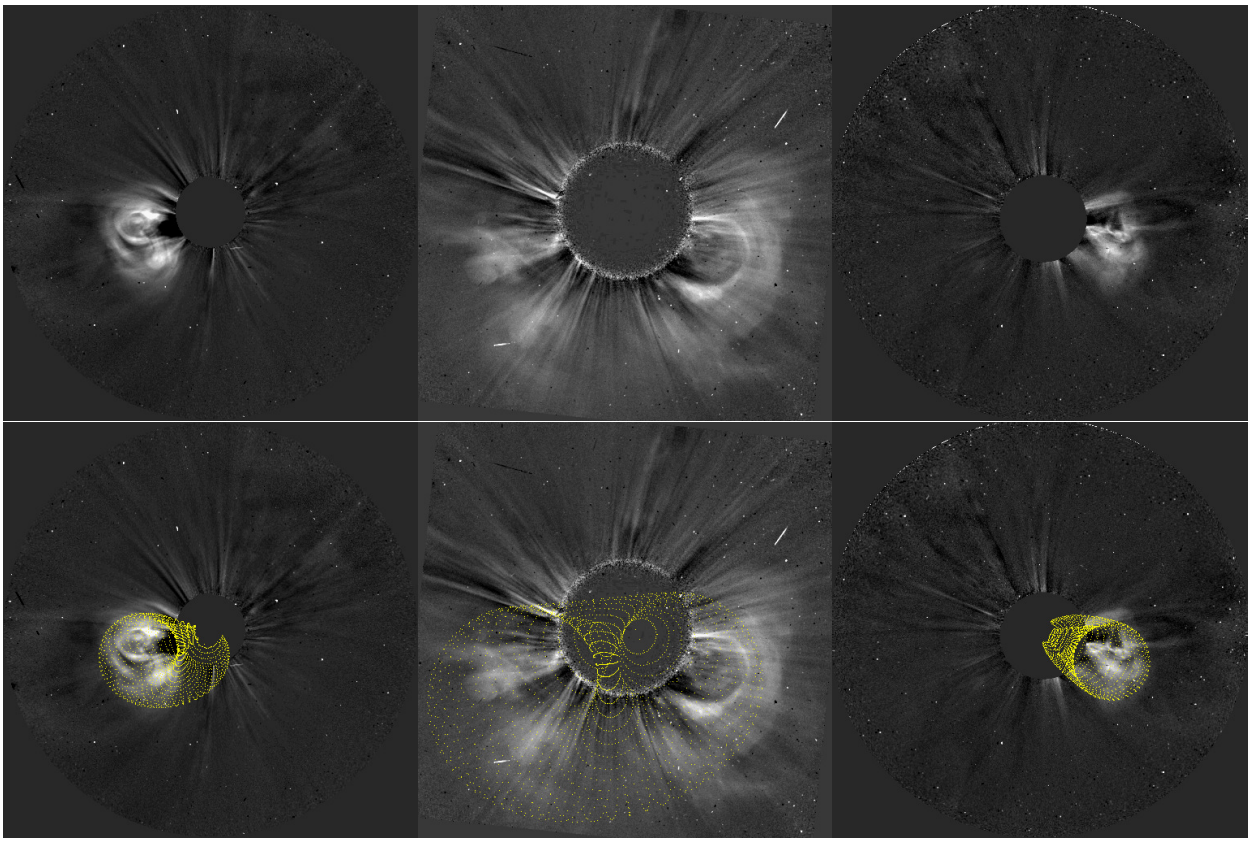


Figure 6.33: GCS fit for CME 31 on November 09, 2012 at 16:54 UT at height $H = 9.9$ $R_\odot$. Table 6.1 lists the GCS parameters for this event.

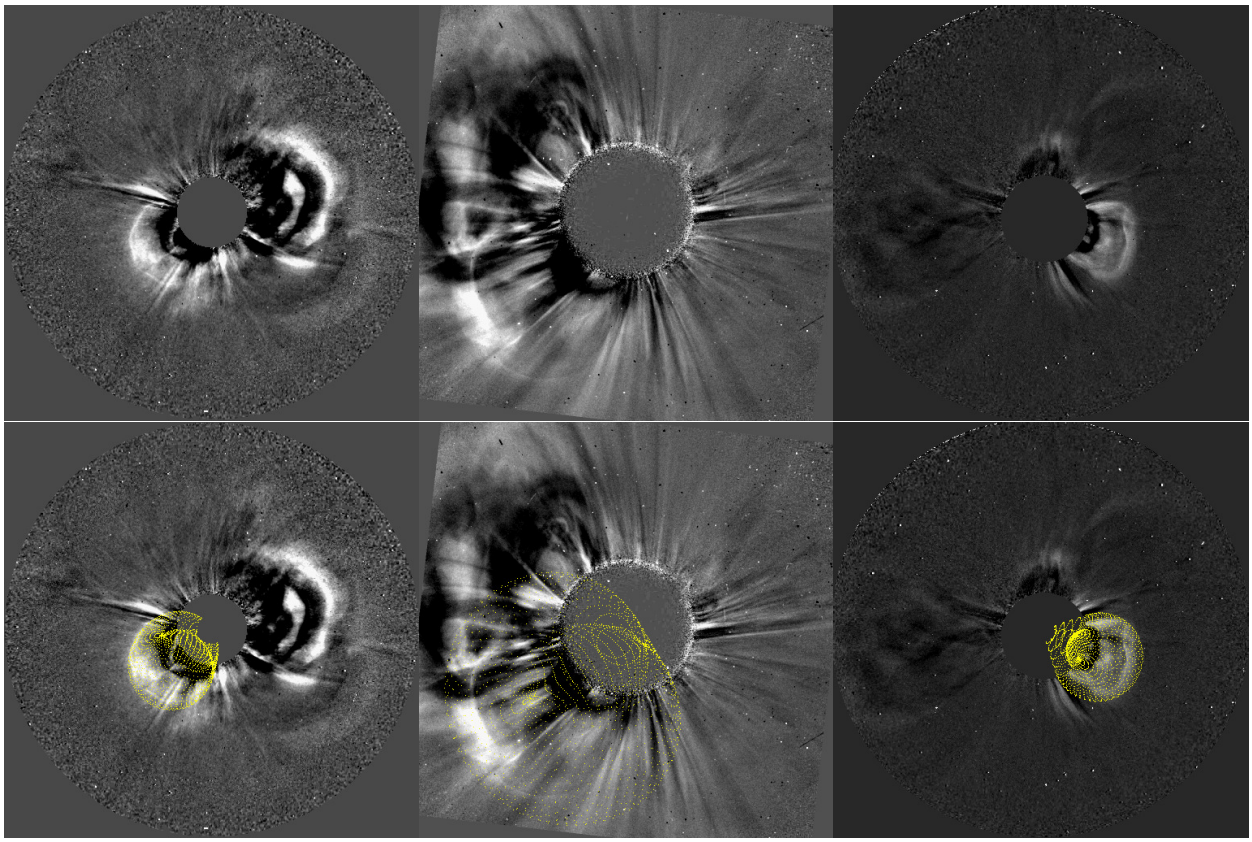


Figure 6.34: GCS fit for CME 32 on November 23, 2012 at 15:24 UT at height $H = 8.9$ $R_\odot$. Table 6.1 lists the GCS parameters for this event.

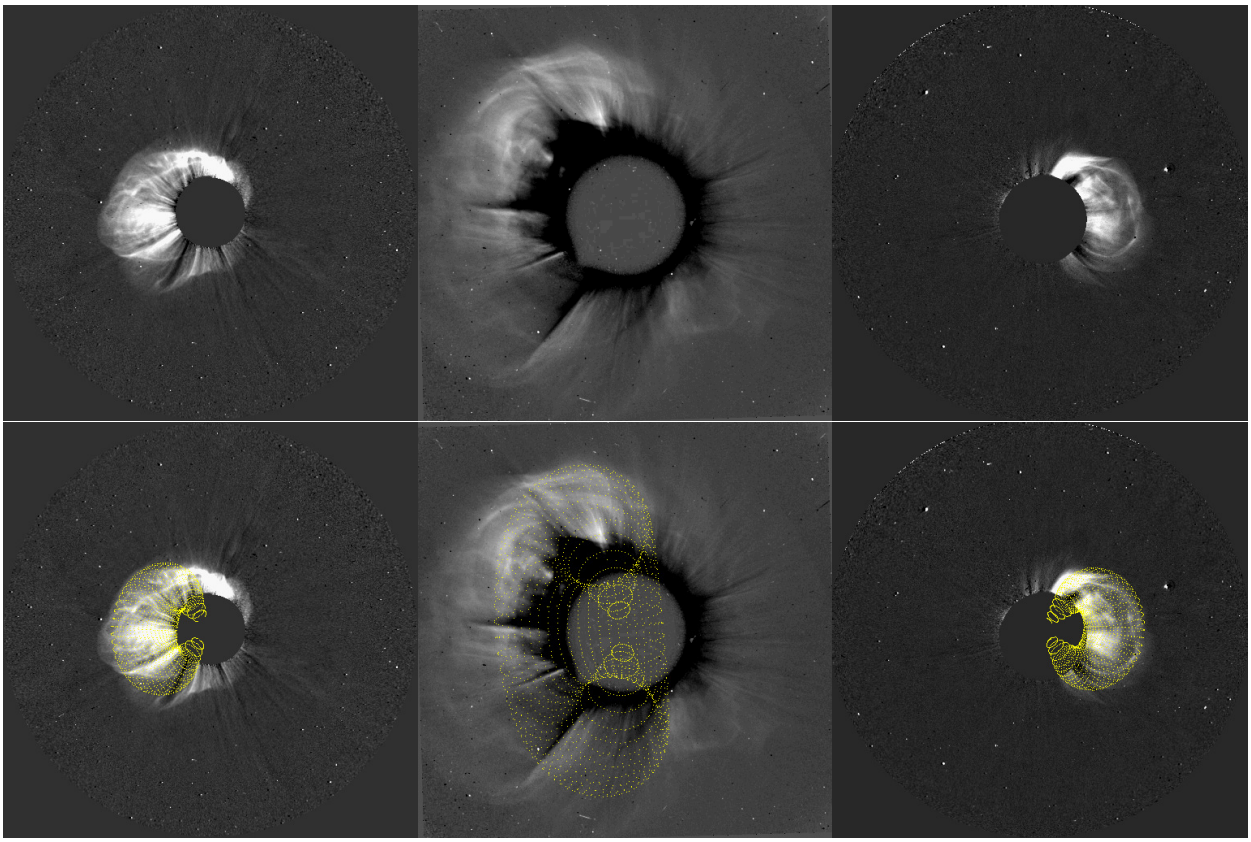


Figure 6.35: GCS fit for CME 33 on March 15, 2013 at 07:39 UT at height $H = 10.2$ $R_{\odot}$. Table 6.1 lists the GCS parameters for this event.

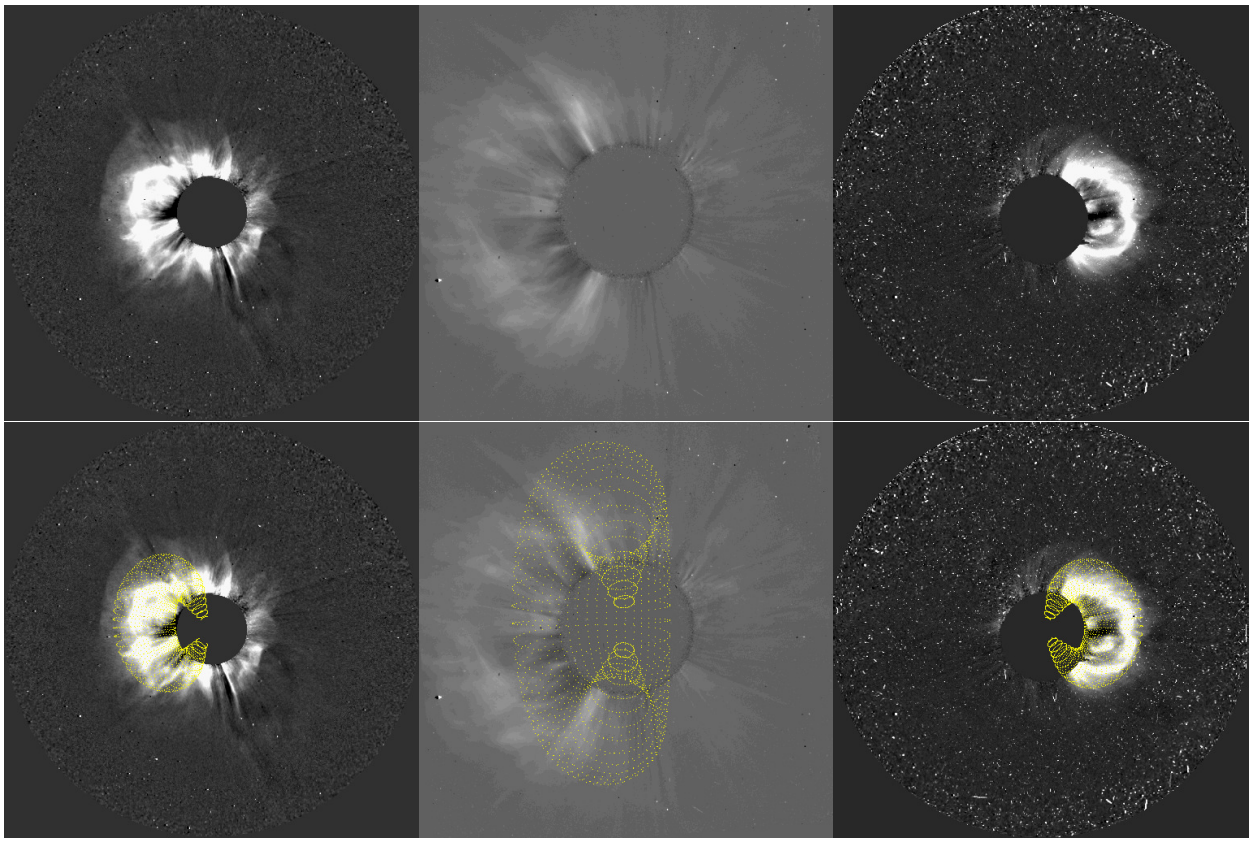


Figure 6.36: GCS fit for CME 34 on April 11, 2013 at 08:24 UT at height $H = 10.2\ \mathrm{R}_{\odot}$. Table 6.1 lists the GCS parameters for this event.

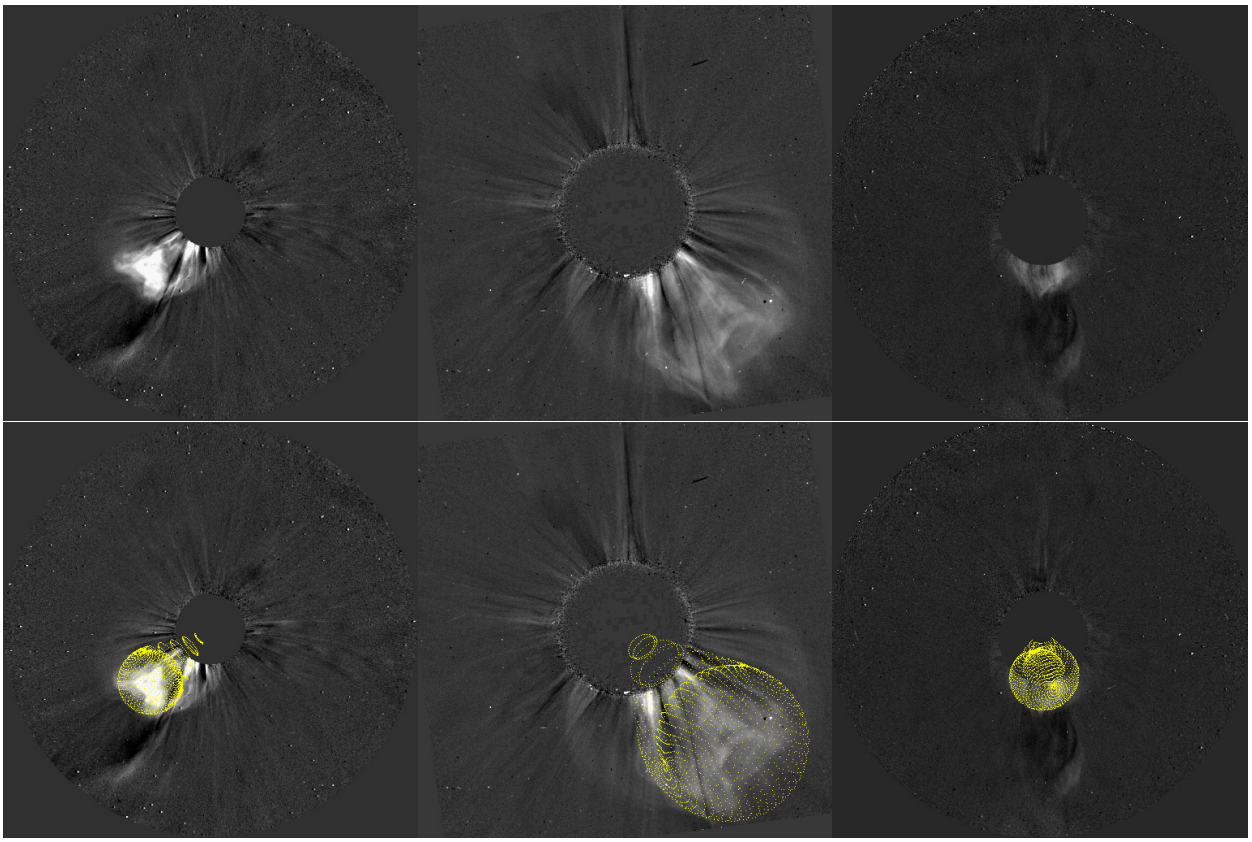


Figure 6.37: GCS fit for CME 35 on June 28, 2013 at 02:39 UT at height $H = 8.2\ \mathrm{R}_{\odot}$. Table 6.1 lists the GCS parameters for this event.

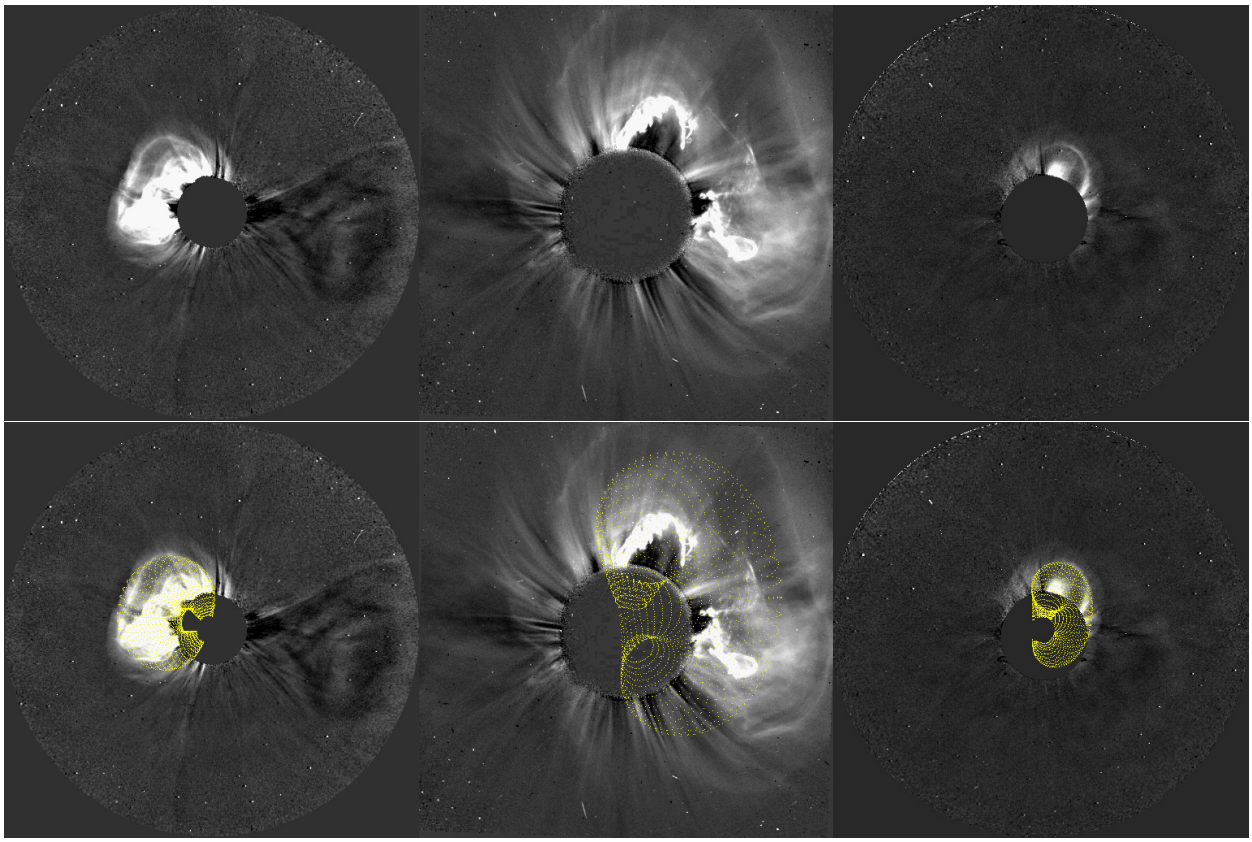


Figure 6.38: GCS fit for CME 36 on September 29, 2013 at 22:54 UT at height $H = 8.1$ $R_\odot$. Table 6.1 lists the GCS parameters for this event.

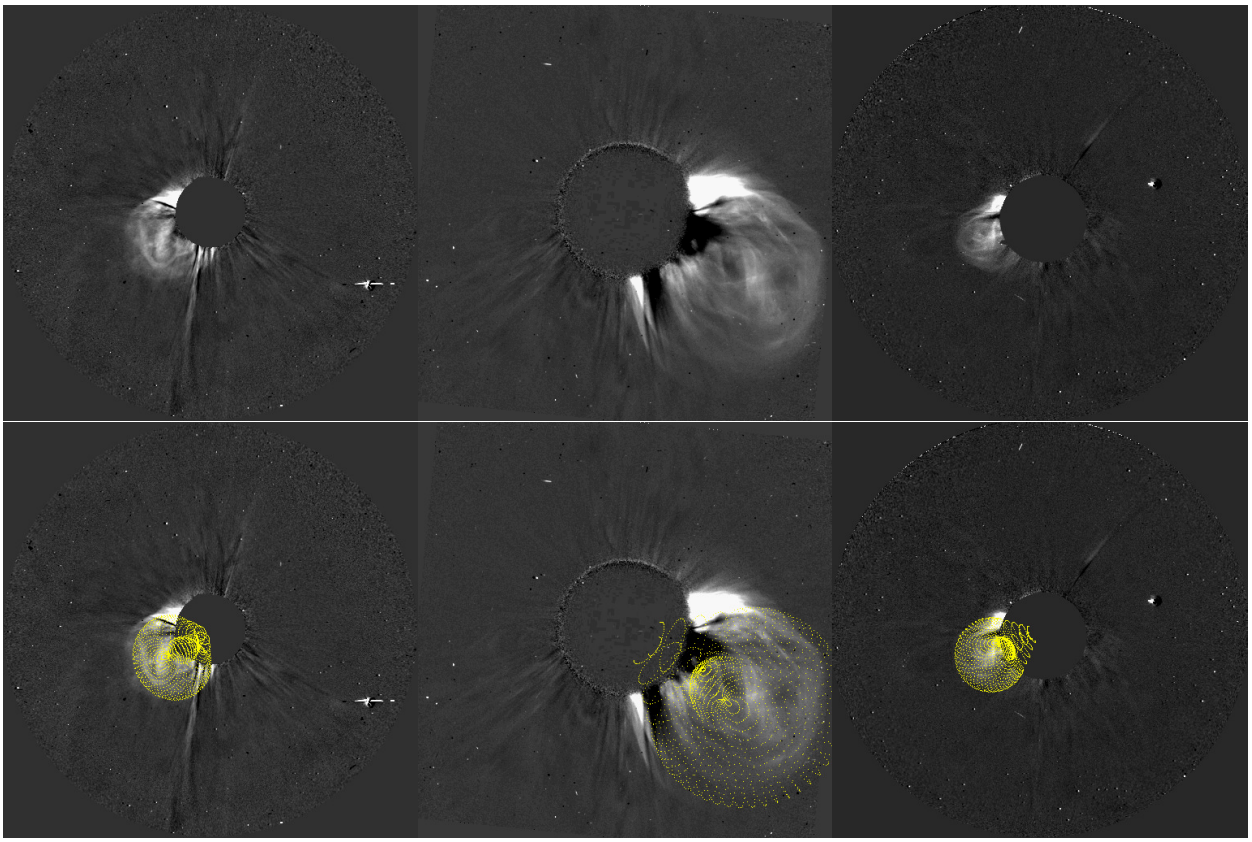


Figure 6.39: GCS fit for CME 37 on November 07, 2013 at 00:39 UT at height $H = 7.7\ \mathrm{R}_{\odot}$. Table 6.1 lists the GCS parameters for this event.

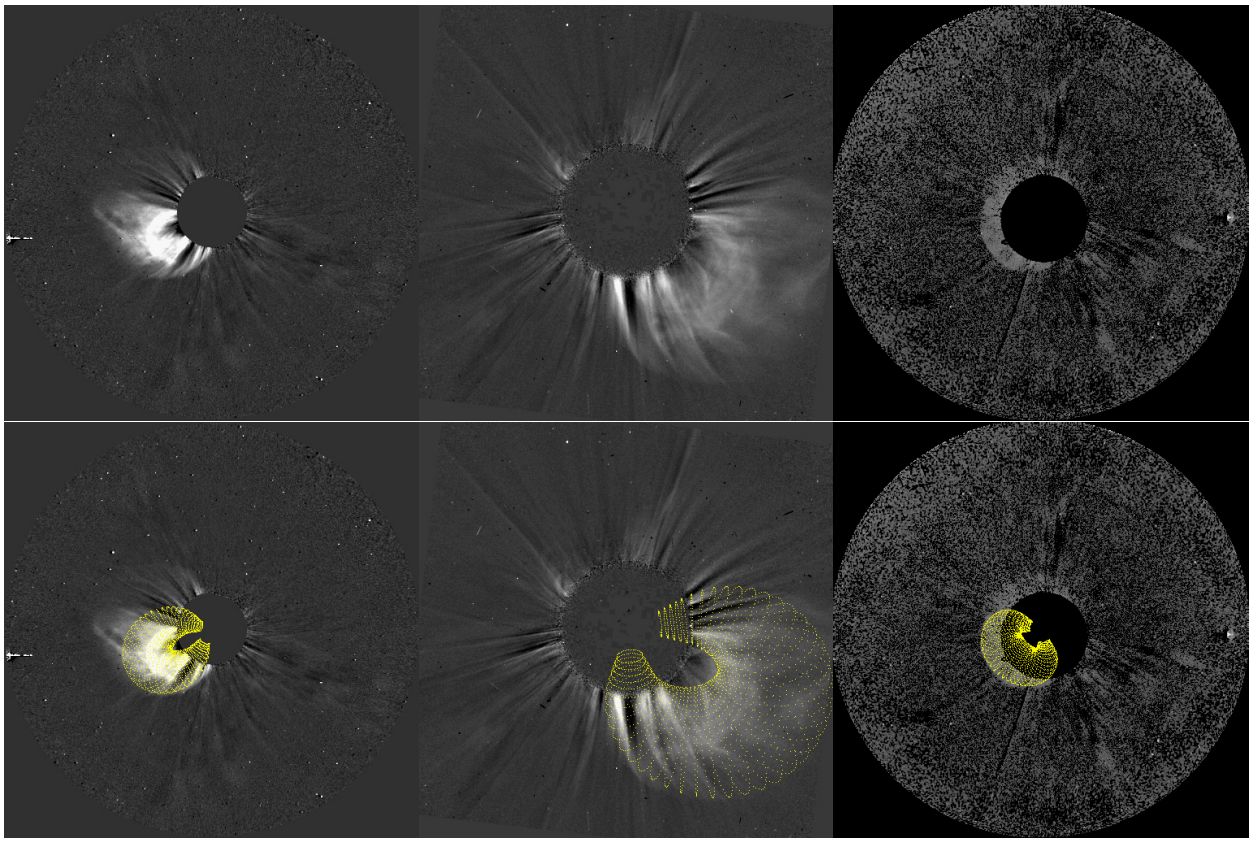


Figure 6.40: GCS fit for CME 38 on December 07, 2013 at 08:24 UT at height $H = 6.8$ $R_\odot$. Table 6.1 lists the GCS parameters for this event.

Table 6.1: GCS parameters corresponding to the fittings in Figures 6.3-6.40 are given. CME no. indicates the serial number of the CME as referenced in Table 2.1. Date and Time are the date of CME event and the timestamp at which the GCS fit for the CME at height H is shown in the corresponding figure. GCS parameters at H are given by Carrington longitude (ϕ), latitude (θ), tilt (γ), aspect ratio (κ) and half angle (α). Fast CMEs are indicated by a superscript (f) and events from Sachdeva et al. (2015) are indicated by a superscript($*$) in their corresponding serial number.

No.	Date	Time (U.T.)	H ($R_\odot$)	ϕ (°)	θ (°)	γ (°)	κ	α (°)
1^*	2010 Mar. 19	17:54	10.07	116.5	-11.7	-35.2	0.28	10.9
2^{*f}	2010 Apr. 03	11:24	9.64	261.6	-24.6	12.3	0.37	25.1
3^*	2010 Apr. 08	06:54	10.2	189.3	-8.9	-29.1	0.19	32.7
4^*	2010 Jun. 16	18:54	9.9	334.8	3.3	-32.9	0.26	9.5
5^*	2010 Sep. 11	05:39	10.3	276.1	20.7	-43.0	0.41	18.1
6^*	2010 Oct. 26	11:54	10.0	70.3	-25.2	-55.3	0.26	29.6
7	2010 Dec. 23	10:24	9.5	29.1	-19.6	-15.6	0.45	18.2
8	2011 Jan. 24	06:39	8.9	336.5	-13.4	-15.1	0.30	22.1
9^*	2011 Feb. 15	03:39	10.9	23.7	-8.9	26.8	0.47	40.8
10	2011 Mar. 03	08:53	10.0	175.5	-22.9	8.4	0.35	21.5
11^*	2011 Mar. 25	15:39	10.0	206.8	-3.9	-11.7	0.31	40.8
12	2011 Apr. 09	02:54	10.2	41.4	5.6	-6.2	0.24	35.2
13	2011 Jun. 14	09:54	9.4	202.4	-1.1	41.4	0.28	57.0
14^f	2011 Jun. 21	04:24	11.3	128.6	5.0	-8.4	0.46	13.7
15^f	2011 Jul. 09	02:24	10.0	264.9	-14.5	15.6	0.37	18.5
16^f	2011 Aug. 04	04:39	9.4	324.2	19.6	65.4	0.68	29.6
17	2011 Sep. 14	02:24	10.5	134.2	19.0	-38.0	0.43	41.4
18^f	2011 Oct. 22	11:24	6.2	54.8	44.7	16.2	0.59	45.0
19	2011 Oct. 26	13:54	10.2	302.9	7.3	-1.1	0.46	9.5
20	2011 Oct. 27	13:39	7.8	223.6	29.1	16.8	0.36	16.5
21^f	2012 Jan. 19	15:54	7.2	212.4	44.2	90.0	0.47	58.1
22^f	2012 Jan. 23	04:24	8.9	206.8	28.5	57.6	0.48	41.1
23^f	2012 Jan. 27	18:39	5.3	188.9	29.6	68.7	0.38	41.4
24^f	2012 Mar. 13	18:24	11.5	301.9	20.7	-39.7	0.74	73.2
25	2012 Apr. 19	17:24	8.4	81.6	-27.9	0.0	0.43	30.5
26^f	2012 Jun. 14	14:39	7.8	91.7	-21.8	-87.2	0.37	31.9
27^f	2012 Jul. 12	17:39	9.2	88.3	-10.6	77.7	0.45	34.9
28^f	2012 Sep. 28	00:54	9.9	165.5	17.3	86.1	0.42	41.6
29	2012 Oct. 05	05:54	10.0	55.9	-20.1	36.9	0.32	38.8
30	2012 Oct. 27	18:54	10.5	118.5	5.6	-35.8	0.28	39.9
31	2012 Nov. 09	16:54	9.9	285.1	-17.9	6.1	0.48	34.6
32	2012 Nov. 23	15:24	8.9	90.6	-21.2	-65.9	0.56	10.3
33^f	2013 Mar. 15	07:39	10.2	71.5	-6.7	-86.1	0.31	39.7
34^f	2013 Apr. 11	08:24	10.2	77.1	-1.1	90.0	0.29	47.2
35^f	2013 Jun. 28	02:39	8.2	176.6	-34.6	-19.6	0.41	5.3
36^f	2013 Sep. 29	22:54	8.1	360.0	22.9	90.0	0.43	47.2
37^f	2013 Nov. 07	00:39	7.7	304.1	-32.4	-74.9	0.48	12.3
38^f	2013 Dec. 07	08:24	6.8	221.4	-31.8	51.4	0.36	46.9

Bibliography

Achenbach, E. (1972). Experiments on the flow past spheres at very high Reynolds numbers. *Journal of Fluid Mechanics*, 54:565–575.

Antiochos, S. K., DeVore, C. R., and Klimchuk, J. A. (1999). A Model for Solar Coronal Mass Ejections. *Astrophys. J.*, 510:485–493.

Arunbabu, K. P., Antia, H. M., Dugad, S. R., Gupta, S. K., Hayashi, Y., Kawakami, S., Mohanty, P. K., Nonaka, T., Oshima, A., and Subramanian, P. (2013). High-rigidity Forbush decreases: due to CMEs or shocks? *Astron. Astrophys.*, 555:A139.

Aschwanden, M. J. (2005). *Physics of the Solar Corona. An Introduction with Problems and Solutions (2nd edition)*.

Baker, D. N. (2000). The occurrence of operational anomalies in spacecraft and their relationship to space weather. *IEEE Transactions on Plasma Science*, 28:2007–2016.

Bein, B. M., Berkebile-Stoiser, S., Veronig, A. M., Temmer, M., Muhr, N., Kienreich, I., and et al. (2011). Impulsive Acceleration of Coronal Mass Ejections. I. Statistics and Coronal Mass Ejection Source Region Characteristics. *Astrophys. J.*, 738:191.

Billings, D. E. (1966). *A guide to the solar corona*.

Bisoi, S. K., Janardhan, P., Ingale, M., Subramanian, P., Ananthakrishnan, S., Tokumaru, M., and Fujiki, K. (2014). A Study of Density Modulation Index in the Inner Heliospheric Solar Wind during Solar Cycle 23. *Astrophys. J.*, 795:69.

Borgazzi, A., Lara, A., Echer, E., and Alves, M. V. (2009). Dynamics of coronal mass ejections in the interplanetary medium. *Astron. Astrophys.*, 498:885–889.

Bothmer, V. and Daglis, I. A. (2007). *Space Weather – Physics and Effects*. Praxis Publishing.

Brueckner, G. E., Howard, R. A., Koomen, M. J., Korendyke, C. M., Michels, D. J., Moses, J. D., and et al. (1995). The Large Angle Spectroscopic Coronagraph (LASCO). *Solar Phys.*, 162:357–402.

Bruno, R. and Trenchi, L. (2014). Radial Dependence of the Frequency Break between Fluid and Kinetic Scales in the Solar Wind Fluctuations. *Astrophys. J. Lett.*, 787:L24.

Burlaga, L., Sittler, E., Mariani, F., and Schwenn, R. (1981). Magnetic loop behind an interplanetary shock - Voyager, Helios, and IMP 8 observations. *J. Geophys. Res.*, 86:6673–6684.

Byrne, J. P., Maloney, S. A., McAteer, R. T. J., Refojo, J. M., and Gallagher, P. T. (2010). Propagation of an Earth-directed coronal mass ejection in three dimensions. *Nature Communications*, 1:74.

Cargill, P. J. (2004). On the Aerodynamic Drag Force Acting on Interplanetary Coronal Mass Ejections. *Solar Phys.*, 221:135–149.

Cargill, P. J., Chen, J., Spicer, D. S., and Zalesak, S. T. (1996). Magnetohydrodynamic simulations of the motion of magnetic flux tubes through a magnetized plasma. *J. Geophys. Res.*, 101:4855–4870.

Carley, E. P., McAteer, R. T. J., and Gallagher, P. T. (2012). Coronal Mass Ejection Mass, Energy, and Force Estimates Using STEREO. *Astrophys. J.*, 752:36.

Chen, J. (1989). Effects of toroidal forces in current loops embedded in a background plasma. *Astrophys. J.*, 338:453–470.

Chen, J. (1996). Theory of prominence eruption and propagation: Interplanetary consequences. *J. Geophys. Res.*, 101:27499–27520.

Chen, J. and Garren, D. A. (1993). Interplanetary magnetic clouds: Topology and driving mechanism. *Geophys. Res. Lett.*, 20:2319–2322.

Chen, J., Howard, R. A., Brueckner, G. E., Santoro, R., Krall, J., Paswaters, S. E., and et. al. (1997). Evidence of an Erupting Magnetic Flux Rope: LASCO Coronal Mass Ejection of 1997 April 13. *Astrophys. J. Lett.*, 490:L191–L194.

Chen, J. and Krall, J. (2003). Acceleration of coronal mass ejections. *Journal of Geophysical Research (Space Physics)*, 108:1410.

Chen, J. and Kunkel, V. (2010). Temporal and Physical Connection Between Coronal Mass Ejections and Flares. *Astrophys. J.*, 717:1105–1122.

Chen, P. F. (2011). Coronal Mass Ejections: Models and Their Observational Basis. *Living Reviews in Solar Physics*, 8:1.

Colaninno, R. C. (2012). *Investigation of the Forces that Govern the Three-Dimensional Propagation and Expansion of Coronal Mass Ejections from Sun to Earth*. PhD thesis, George Mason University.

Colaninno, R. C. and Vourlidas, A. (2009). First Determination of the True Mass of Coronal Mass Ejections: A Novel Approach to Using the Two STEREO Viewpoints. *Astrophys. J.*, 698:852–858.

Coles, W. A. and Harmon, J. K. (1989). Propagation observations of the solar wind near the sun. *Astrophys. J.*, 337:1023–1034.

Constantinescu, G. and Squires, K. (2004). Numerical investigations of flow over a sphere in the subcritical and supercritical regimes. *Physics of Fluids*, 16:1449–1466.

Cremades, H. and Bothmer, V. (2004). On the three-dimensional configuration of coronal mass ejections. *Astron. Astrophys.*, 422:307–322.

Domingo, V., Fleck, B., and Poland, A. I. (1995). The SOHO Mission: an Overview. *Solar Phys.*, 162:1–37.

Dryer, M. and Smart, D. F. (1984). Dynamical models of coronal transients and interplanetary disturbances. *Advances in Space Research*, 4:291–301.

Duan, L., Beekman, I., and Martín, M. P. (2011). Direct numerical simulation of hypersonic turbulent boundary layers. Part 3. Effect of Mach number. *Journal of Fluid Mechanics*, 672:245–267.

Emslie, A. G., Dennis, B. R., Shih, A. Y., Chamberlin, P. C., Mewaldt, R. A., Moore, C. S., and et al. (2012). Global Energetics of Thirty-eight Large Solar Eruptive Events. *Astrophys. J.*, 759:71.

Eyles, C. J., Simnett, G. M., Cooke, M. P., Jackson, B. V., Buffington, A., Hick, P. P., Waltham, N. R., King, J. M., Anderson, P. A., and Holladay, P. E. (2003). The Solar Mass Ejection Imager (Smei). *Solar Phys.*, 217:319–347.

Forbes, T. G. and Isenberg, P. A. (1991). A catastrophe mechanism for coronal mass ejections. *Astrophys. J.*, 373:294–307.

Fry, C. D., Dryer, M., Smith, Z., Sun, W., Deehr, C. S., and Akasofu, S.-I. (2003). Forecasting solar wind structures and shock arrival times using an ensemble of models. *Journal of Geophysical Research (Space Physics)*, 108:1070.

Gabriel, A. H. and Mason, H. E. (1982). Solar physics. In Massey, H. S. W. and Bates, D. R., editors, *Applied Atomic Collision Physics, Volume 1: Atmospheric Physics and Chemistry*, volume 1, pages 345–397.

Garren, D. A. and Chen, J. (1994). Lorentz self-forces on curved current loops. *Physics of Plasmas*, 1:3425–3436.

Gopalswamy, N. (2013). STEREO and SOHO contributions to coronal mass ejection studies: Some recent results. In *Astronomical Society of India Conference Series*, volume 10 of *Astronomical Society of India Conference Series*.

Gosling, J. T. (1993). The solar flare myth. *J. Geophys. Res.*, 98:18937–18950.

Gosling, J. T., Hildner, E., MacQueen, R. M., Munro, R. H., Poland, A. I., and Ross, C. L. (1976). The speeds of coronal mass ejection events. *Solar Phys.*, 48:389–397.

Hansen, R. T., Garcia, C. J., Grognard, R. J.-M., and Sheridan, K. V. (1971). A coronal disturbance observed simultaneously with a white-light coronameter and the 80 MHz Culgoora radioheliograph. *Proceedings of the Astronomical Society of Australia*, 2:57.

Hewish, A., Scott, P. F., and Wills, D. (1964). Interplanetary Scintillation of Small Diameter Radio Sources. *Nature*, 203:1214–1217.

Hood, A. W. and Priest, E. R. (1981). Critical conditions for magnetic instabilities in force-free coronal loops. *Geophysical and Astrophysical Fluid Dynamics*, 17:297–318.

Houminer, Z. and Hewish, A. (1974). Correlation of interplanetary scintillation and spacecraft plasma density measurements. *Planetary and Space Science*, 22:1041–1042.

Howard, R. A., Michels, D. J., Sheeley, Jr., N. R., and Koomen, M. J. (1982). The observation of a coronal transient directed at earth. *Astrophys. J. Lett.*, 263:L101–L104.

Howard, R. A., Moses, J. D., Vourlidas, A., Newmark, J. S., Socker, D. G., Plunkett, S. P., and et al. (2008). Sun Earth Connection Coronal and Heliospheric Investigation (SECCHI). *Space Sci. Rev.*, 136:67–115.

Howard, R. A., Sheeley, Jr., N. R., Michels, D. J., and Koomen, M. J. (1985). Coronal mass ejections - 1979-1981. *J. Geophys. Res.*, 90:8173–8191.

Howard, T. (2011). *Coronal Mass Ejections - An Introduction*. Springer-Verlag New York.

Hundhausen, A. (1999). Coronal Mass Ejections. In Strong, K. T., Saba, J. L. R., Haisch, B. M., and Schmelz, J. T., editors, *The many faces of the sun: a summary of the results from NASA's Solar Maximum Mission.*, page 143.

Iju, T., Tokumaru, M., and Fujiki, K. (2014). Kinematic Properties of Slow ICMEs and an Interpretation of a Modified Drag Equation for Fast and Moderate ICMEs. *Solar Phys.*, 289:2157–2175.

Illing, R. M. E. and Hundhausen, A. J. (1985). Observation of a coronal transient from 1.2 to 6 solar radii. *J. Geophys. Res.*, 90:275–282.

Isenberg, P. A. and Forbes, T. G. (2007). A Three-dimensional Line-tied Magnetic Field Model for Solar Eruptions. *Astrophys. J.*, 670:1453–1466.

Isenberg, P. A., Forbes, T. G., and Demoulin, P. (1993). Catastrophic Evolution of a Force-free Flux Rope: A Model for Eruptive Flares. *Astrophys. J.*, 417:368.

Jackman, C. H., Deland, M. T., Labow, G. J., Fleming, E. L., Weisenstein, D. K., Ko, M. K. W., Sinnhuber, M., and Russell, J. M. (2005). Neutral atmospheric influences of the solar proton events in October-November 2003. *Journal of Geophysical Research (Space Physics)*, 110:A09S27.

Jackson, B. V. (1985). Imaging of coronal mass ejections by the HELIOS spacecraft. *Solar Phys.*, 100:563–574.

Jian, L., Russell, C. T., Luhmann, J. G., and Skoug, R. M. (2006). Properties of Interplanetary Coronal Mass Ejections at One AU During 1995 2004. *Solar Phys.*, 239:393–436.

Jin, M., Manchester, W. B., van der Holst, B., Sokolov, I., Tóth, G., Mullinix, R. E., Taktakishvili, A., Chulaki, A., and Gombosi, T. I. (2017). Data-constrained Coronal Mass Ejections in a Global Magnetohydrodynamics Model. *Astrophys. J.*, 834:173.

Kahler, S. W. (1992). Solar flares and coronal mass ejections. *Annual review of astronomy and astrophysics*, 30:113–141.

Kahler, S. W. and Webb, D. F. (2007). V arc interplanetary coronal mass ejections observed with the Solar Mass Ejection Imager. *Journal of Geophysical Research (Space Physics)*, 112:A09103.

Kaiser, M. L., Kucera, T. A., Davila, J. M., St. Cyr, O. C., Guhathakurta, M., and Christian, E. (2008). The STEREO Mission: An Introduction. *Space Sci. Rev.*, 136:5–16.

Karpen, J. T., Antiochos, S. K., and DeVore, C. R. (2012). The Mechanisms for the Onset and Explosive Eruption of Coronal Mass Ejections and Eruptive Flares. *Astrophys. J.*, 760:81.

Klein, L. W. and Burlaga, L. F. (1982). Interplanetary magnetic clouds at 1 AU. *J. Geophys. Res.*, 87:613–624.

Kliem, B., Lin, J., Forbes, T. G., Priest, E. R., and Török, T. (2014). Catastrophe versus Instability for the Eruption of a Toroidal Solar Magnetic Flux Rope. *Astrophys. J.*, 789:46.

Kliem, B. and Török, T. (2006). Torus Instability. *Physical Review Letters*, 96(25):255002.

Krall, J., St. Cyr, O. C., and Chen, J. (2005). Flux-Rope CME Geometry and its Relation to Observed CME Morphology. *AGU Spring Meeting Abstracts*.

Kumar, A. and Rust, D. M. (1996). Interplanetary magnetic clouds, helicity conservation, and current-core flux-ropes. *J. Geophys. Res.*, 101:15667–15684.

Kunkel, V. and Chen, J. (2010). Evolution of a Coronal Mass Ejection and its Magnetic Field in Interplanetary Space. *Astrophys. J. Lett.*, 715:L80–L83.

Landau, L. D. and Lifshitz, E. M. (1959). *Fluid mechanics*.

Leamon, R. J., Matthaeus, W. H., Smith, C. W., Zank, G. P., Mullan, D. J., and Oughton, S. (2000). MHD-driven Kinetic Dissipation in the Solar Wind and Corona. *Astrophys. J.*, 537:1054–1062.

Leblanc, Y., Dulk, G. A., and Bougeret, J.-L. (1998). Tracing the Electron Density from the Corona to 1au. *Solar Phys.*, 183:165–180.

Lee, C. O., Arge, C. N., Odstrčil, D., Millward, G., Pizzo, V., Quinn, J. M., and et al. (2013). Ensemble Modeling of CME Propagation. *Solar Phys.*, 285:349–368.

Lewis, D. J. and Simnett, G. M. (2002). Bulk flow velocities in the solar corona at solar maximum. *Mon. Not. Roy. Astron. Soc.*, 333:969–976.

Longcope, D., Beveridge, C., Qiu, J., Ravindra, B., Barnes, G., and Dasso, S. (2007). Modeling and Measuring the Flux Reconnected and Ejected by the Two-Ribbon Flare/CME Event on 7 November 2004. *Solar Phys.*, 244:45–73.

Low, B. C. (1996). Solar Activity and the Corona. *Solar Phys.*, 167:217–265.

Lugaz, N., Manchester, IV, W. B., Roussev, I. I., Tóth, G., and Gombosi, T. I. (2007). Numerical Investigation of the Homologous Coronal Mass Ejection Events from Active Region 9236. *Astrophys. J.*, 659:788–800.

Lynch, B. J., Antiochos, S. K., DeVore, C. R., Luhmann, J. G., and Zurbuchen, T. H. (2008). Topological Evolution of a Fast Magnetic Breakout CME in Three Dimensions. *Astrophys. J.*, 683:1192–1206.

MacQueen, R. M., Csoeke-Poeckh, A., Hildner, E., House, L., Reynolds, R., Stanger, A., Tepoel, H., and Wagner, W. (1980). The High Altitude Observatory Coronagraph/Polarimeter on the Solar Maximum Mission. *Solar Phys.*, 65:91–107.

MacQueen, R. M., Eddy, J. A., Gosling, J. T., Hildner, E., Munro, R. H., Newkirk, Jr., G. A., Poland, A. I., and Ross, C. L. (1974). The Outer Solar Corona as Observed from Skylab: Preliminary Results. *Astrophys. J. Lett.*, 187:L85.

Maloney, S. A., Gallagher, P. T., and McAteer, R. T. J. (2009). Reconstructing the 3-D Trajectories of CMEs in the Inner Heliosphere. *Solar Phys.*, 256:149–166.

Manchester, W., Kilpua, E. K. J., Liu, Y. D., Lugaz, N., Riley, P., Török, T., and Vršnak, B. (2017). The Physical Processes of CME/ICME Evolution. *Space Sci. Rev.*, 212:1159–1219.

Manoharan, P. K. (2006). Evolution of Coronal Mass Ejections in the Inner Heliosphere: A Study Using White-Light and Scintillation Images. *Solar Phys.*, 235:345–368.

Manoharan, P. K. (2010). Ooty Interplanetary Scintillation - Remote-Sensing Observations and Analysis of Coronal Mass Ejections in the Heliosphere. *Solar Phys.*, 265:137–157.

Manoharan, P. K., Gopalswamy, N., Yashiro, S., Lara, A., Michalek, G., and Howard, R. A. (2004). Influence of coronal mass ejection interaction on propagation of interplanetary shocks. *Journal of Geophysical Research (Space Physics)*, 109:A06109.

Matamoros, C. S., Klein, K. L., and Trottet, G. (2017). Microwave radio emissions as a proxy for coronal mass ejection speed in arrival predictions of interplanetary coronal mass ejections at 1 AU. *Journal of Space Weather and Space Climate*, 7(27):A2.

Mays, M. L., Taktakishvili, A., Pulkkinen, A., MacNeice, P. J., Rastätter, L., Odstrcil, D., Jian, L. K., Richardson, I. G., LaSota, J. A., Zheng, Y., and Kuznetsova, M. M. (2015). Ensemble Modeling of CMEs Using the WSA-ENLIL+Cone Model. *Solar Phys.*, 290:1775–1814.

McKenna-Lawlor, S. M. P., Dryer, M., Kartalev, M. D., Smith, Z., Fry, C. D., Sun, W., and et al. (2006). Near real-time predictions of the arrival at Earth of flare-related shocks during Solar Cycle 23. *Journal of Geophysical Research (Space Physics)*, 111:A11103.

Michalek, G., Gopalswamy, N., Yashiro, S., and Bronarska, K. (2015). Dynamics of CMEs in the LASCO Field of View. *Solar Phys.*, 290:903–917.

Michels, D. J., Howard, R. A., Koomen, M. J., and Sheeley, Jr., N. R. (1980). Satellite observations of the outer corona near sunspot maximum. In Kundu, M. R. and Gergely, T. E., editors, *Radio Physics of the Sun*, volume 86 of *IAU Symposium*, pages 439–442.

Mishra, W. and Srivastava, N. (2013). Estimating the Arrival Time of Earth-directed Coronal Mass Ejections at in Situ Spacecraft Using COR and HI Observations from STEREO. *Astrophys. J.*, 772:70.

Moore, R. L., Sterling, A. C., Hudson, H. S., and Lemen, J. R. (2001). Onset of the Magnetic Explosion in Solar Flares and Coronal Mass Ejections. *Astrophys. J.*, 552:833–848.

Nature Journal (1871). Observations Upon Magnetic Storms in Higher Latitudes. *Nature*, 4:441–442.

Odstrcil, D., Riley, P., and Zhao, X. P. (2004). Numerical simulation of the 12 May 1997 interplanetary CME event. *Journal of Geophysical Research (Space Physics)*, 109:A02116.

Odstrčil, D. and Pizzo, V. J. (1999). Three-dimensional propagation of CMEs in a structured solar wind flow: 1. CME launched within the streamer belt. *J. Geophys. Res.*, 104:483–492.

Olmedo, O., Zhang, J., and Kunkel, V. (2013). Lorentz Self-force of an Ellipse Current Loop Model. *Astrophys. J.*, 771:125.

Parker, E. N. (1965). Dynamical Theory of the Solar Wind. *Space Sci. Rev.*, 4:666–708.

Pulkkinen, T. (2007). Space Weather: Terrestrial Perspective. *Living Reviews in Solar Physics*, 4:1.

Richter, I., Leinert, C., and Planck, B. (1982). Search for short term variations of zodical light and optical detection of interplanetary plasma clouds. *Astron. Astrophys.*, 110:115–120.

Rollett, T., Möstl, C., Isavnin, A., Davies, J. A., Kubicka, M., Amerstorfer, U. V., and et al. (2016). ElEvoHI: A Novel CME Prediction Tool for Heliospheric Imaging Combining an Elliptical Front with Drag-based Model Fitting. *Astrophys. J.*, 824:131.

Russell, C. T., Shinde, A. A., and Jian, L. (2005). A new parameter to define interplanetary coronal mass ejections. *Advances in Space Research*, 35:2178–2184.

Sachdeva, N., Subramanian, P., Colaninno, R., and Vourlidas, A. (2015). CME Propagation: Where does Aerodynamic Drag 'Take Over'? *Astrophys. J.*, 809:158.

Sachdeva, N., Subramanian, P., Vourlidas, A., and Bothmer, V. (2017). CME Dynamics Using STEREO and LASCO Observations: The Relative Importance of Lorentz Forces and Solar Wind Drag. *Solar Phys.*, 292:118.

Sasikumar Raja, K., Ingale, M., Ramesh, R., Subramanian, P., Manoharan, P. K., and Janardhan, P. (2016). Amplitude of solar wind density turbulence from 10 to 45 Rs. *Journal of Geophysical Research (Space Physics)*, 121:11.

Savani, N. P., Vourlidas, A., Szabo, A., Mays, M. L., Richardson, I. G., Thompson, B. J., Pulkkinen, A., Evans, R., and Nieves-Chinchilla, T. (2015). Predicting the magnetic vectors within coronal mass ejections arriving at Earth: 1. Initial architecture. *Space Weather*, 13:374–385.

Schwenn, R. (2006). Space Weather: The Solar Perspective. *Living Reviews in Solar Physics*, 3:2.

Shafranov, V. D. (1966). Plasma Equilibrium in a Magnetic Field. *Reviews of Plasma Physics*, 2:103.

Shaikh, D. and Zank, G. P. (2010). The turbulent density spectrum in the solar wind plasma. *Mon. Not. Roy. Astron. Soc.*, 402:362–370.

Sheeley, N. R., Walters, J. H., Wang, Y.-M., and Howard, R. A. (1999). Continuous tracking of coronal outflows: Two kinds of coronal mass ejections. *J. Geophys. Res.*, 104:24739–24768.

Sheeley, N. R., Wang, Y.-M., Hawley, S. H., Brueckner, G. E., Dere, K. P., Howard, R. A., Koomen, M. J., Korendyke, C. M., Michels, D. J., Paswaters, S. E., Socker, D. G., St. Cyr, O. C., Wang, D., Lamy, P. L., Llebaria, A., Schwenn, R., Simnett, G. M., Plunkett, S., and Biesecker, D. A. (1997). Measurements of Flow Speeds in the Corona Between 2 and 30 Rs. *Astrophys. J.*, 484:472–478.

Shen, F., Wu, S. T., Feng, X., and Wu, C.-C. (2012). Acceleration and deceleration of coronal mass ejections during propagation and interaction. *Journal of Geophysical Research (Space Physics)*, 117:A11101.

Shi, T., Wang, Y., Wan, L., Cheng, X., Ding, M., and Zhang, J. (2015). Predicting the Arrival Time of Coronal Mass Ejections with the Graduated Cylindrical Shell and Drag Force Model. *Astrophys. J.*, 806:271.

Smith, C. W., Mullan, D. J., Ness, N. F., Skoug, R. M., and Steinberg, J. (2001). Day the solar wind almost disappeared: Magnetic field fluctuations, wave refraction and dissipation. *J. Geophys. Res.*, 106:18625–18634.

Smith, Z. and Dryer, M. (1990). MHD study of temporal and spatial evolution of simulated interplanetary shocks in the ecliptic plane within 1 AU. *Solar Phys.*, 129:387–405.

Spangler, S. R. (2002). The Amplitude of Magnetohydrodynamic Turbulence in the Inner Solar Wind. *Astrophys. J.*, 576:997–1004.

St. Cyr, O. C., Plunkett, S. P., Michels, D. J., Paswaters, S. E., Koomen, M. J., Simnett, G. M., Thompson, B. J., Gurman, J. B., Schwenn, R., Webb, D. F., Hildner, E., and Lamy, P. L. (2000). Properties of coronal mass ejections: SOHO LASCO observations from January 1996 to June 1998. *J. Geophys. Res.*, 105:18169–18186.

Sturrock, P. A. (1989). The role of eruption in solar flares. *Solar Phys.*, 121:387–397.

Subramanian, P., Arunbabu, K. P., Vourlidas, A., and Mauriya, A. (2014). Self-similar Expansion of Solar Coronal Mass Ejections: Implications for Lorentz Self-force Driving. *Astrophys. J.*, 790:125.

Subramanian, P., Lara, A., and Borgazzi, A. (2012). Can solar wind viscous drag account for coronal mass ejection deceleration? *Geophys. Res. Lett.*, 39:L19107.

Subramanian, P. and Vourlidas, A. (2007). Energetics of solar coronal mass ejections. *Astron. Astrophys.*, 467:685–693.

Taktakishvili, A., Kuznetsova, M., MacNeice, P., Hesse, M., Rastätter, L., Pulkkinen, A., and et al. (2009). Validation of the coronal mass ejection predictions at the Earth orbit estimated by ENLIL heliosphere cone model. *Space Weather*, 7:S03004.

Temmer, M. and Nitta, N. V. (2015). Interplanetary Propagation Behavior of the Fast Coronal Mass Ejection on 23 July 2012. *Solar Phys.*, 290:919–932.

Temmer, M., Rollett, T., Möstl, C., Veronig, A. M., Vršnak, B., and Odstrčil, D. (2011). Influence of the Ambient Solar Wind Flow on the Propagation Behavior of Interplanetary Coronal Mass Ejections. *Astrophys. J.*, 743:101.

Temmer, M., Vršnak, B., Rollett, T., Bein, B., de Koning, C. A., Liu, Y., Bosman, E., Davies, J. A. and̃Möstl, C., Žic, T., Veronig, A. M., Bothmer, V., Harrison, R., Nitta, N., Bisi, M., Flor, O., Eastwood, J., Odstrcil, D., and Forsyth, R. (2012). Characteristics of Kinematics of a Coronal Mass Ejection during the 2010 August 1 CME-CME Interaction Event. *Astrophys. J.*, 749:57.

Thernisien, A. (2011). Implementation of the Graduated Cylindrical Shell Model for the Three-dimensional Reconstruction of Coronal Mass Ejections. *Astrophys. J. Supp.*, 194:33.

Thernisien, A., Vourlidas, A., and Howard, R. A. (2009). Forward Modeling of Coronal Mass Ejections Using STEREO/SECCHI Data. *Solar Phys.*, 256:111–130.

Thernisien, A. F. R., Howard, R. A., and Vourlidas, A. (2006). Modeling of Flux Rope Coronal Mass Ejections. *Astrophys. J.*, 652:763–773.

Török, T. and Kliem, B. (2003). The evolution of twisting coronal magnetic flux tubes. *Astron. Astrophys.*, 406:1043–1059.

Török, T., Kliem, B., and Titov, V. S. (2004). Ideal kink instability of a magnetic loop equilibrium. *Astron. Astrophys.*, 413:L27–L30.

Tóth, G., de Zeeuw, D. L., Gombosi, T. I., Manchester, W. B., Ridley, A. J., Sokolov, I. V., and et al. (2007). Sun-to-thermosphere simulation of the 28-30 October 2003 storm with the Space Weather Modeling Framework. *Space Weather*, 5:06003.

Tousey, R. (1973). The solar corona. In Rycroft, M. J. and Runcorn, S. K., editors, *Space Research Conference*, volume 2 of *Space Research Conference*, pages 713–730.

Žic, T., Vršnak, B., and Temmer, M. (2015). Heliospheric Propagation of Coronal Mass Ejections: Drag-based Model Fitting. *Astrophys. J. Supp.*, 218:32.

Venkata, S. N., Prasad, B. R., Nalla, R. K., and Singh, J. (2017). Scatter studies for visible emission line coronagraph on board ADITYA-L1 mission. *Journal of Astronomical Telescopes, Instruments, and Systems*, 3(1):014002.

Verma, M. K. (1996). Nonclassical viscosity and resistivity of the solar wind plasma. *J. Geophys. Res.*, 101:27543–27548.

Vourlidas, A., Balmaceda, L. A., Stenborg, G., and Dal Lago, A. (2017). Multi-viewpoint Coronal Mass Ejection Catalog Based on STEREO COR2 Observations. *Astrophys. J.*, 838:141.

Vourlidas, A., Howard, R. A., Esfandiari, E., Patsourakos, S., Yashiro, S., and Michalek, G. (2010). Comprehensive Analysis of Coronal Mass Ejection Mass and Energy Properties Over a Full Solar Cycle. *Astrophys. J.*, 722:1522–1538.

Vourlidas, A., Subramanian, P., Dere, K. P., and Howard, R. A. (2000). Large-Angle Spectrometric Coronagraph Measurements of the Energetics of Coronal Mass Ejections. *Astrophys. J.*, 534:456–467.

Vršnak, B. (2006). Forces governing coronal mass ejections. *Advances in Space Research*, 38:431–440.

Vršnak, B. (2016). Solar eruptions: The CME-flare relationship. *Astronomische Nachrichten*, 337:1002.

Vršnak, B., Maričić, D., Stanger, A. L., and Veronig, A. (2004). Coronal Mass Ejection of 15 May 2001: II. Coupling of the Cme Acceleration and the Flare Energy Release. *Solar Phys.*, 225:355–378.

Vršnak, B., Temmer, M., Žic, T., Taktakishvili, A., Dumbović, M., Möstl, C., and et al. (2014). Heliospheric Propagation of Coronal Mass Ejections: Comparison of Numerical WSA-ENLIL+Cone Model and Analytical Drag-based Model. *Astrophys. J. Supp.*, 213:21.

Vršnak, B., Žic, T., Falkenberg, T. V., Möstl, C., Vennerstrom, S., and Vrbanec, D. (2010). The role of aerodynamic drag in propagation of interplanetary coronal mass ejections. *Astron. Astrophys.*, 512:A43.

Vršnak, B., Žic, T., Vrbanec, D., Temmer, M., Rollett, T., Möstl, C., Veronig, A., Čalogović, J., Dumbović, M., Lulić, S., Moon, Y.-J., and Shanmugaraju, A. (2013). Propagation of Interplanetary Coronal Mass Ejections: The Drag-Based Model. *Solar Phys.*, 285:295–315.

Wang, Y., Zhang, J., and Shen, C. (2009). An analytical model probing the internal state of coronal mass ejections based on observations of their expansions and propagations. *Journal of Geophysical Research (Space Physics)*, 114:A10104.

Wang, Y.-M. and Sheeley, Jr., N. R. (1990). Solar wind speed and coronal flux-tube expansion. *Astrophys. J.*, 355:726–732.

Webb, D. F. and Howard, T. A. (2012). Coronal Mass Ejections: Observations. *Living Reviews in Solar Physics*, 9:3.

Webb, D. F., Mizuno, D. R., Buffington, A., Cooke, M. P., Eyles, C. J., Fry, C. D., Gentile, L. C., Hick, P. P., Holladay, P. E., Howard, T. A., Hewitt, J. G., Jackson, B. V., Johnston, J. C., Kuchar, T. A., Mozer, J. B., Price, S., Radick, R. R., Simnett, G. M., and Tappin, S. J. (2006). Solar Mass Ejection Imager (SMEI) observations of coronal mass ejections (CMEs) in the heliosphere. *Journal of Geophysical Research (Space Physics)*, 111:A12101.

Welsch, B. (2017). Flux Accretion and Coronal Mass Ejection Dynamics. In *AAS/Solar Physics Division Meeting*, volume 48 of *AAS/Solar Physics Division Meeting*, page 206.07.

Wu, C.-C., Fry, C. D., Wu, S. T., Dryer, M., and Liou, K. (2007). Three-dimensional global simulation of interplanetary coronal mass ejection propagation from the Sun to the heliosphere: Solar event of 12 May 1997. *Journal of Geophysical Research (Space Physics)*, 112:A09104.

Yashiro, S., Gopalswamy, N., Michalek, G., St. Cyr, O. C., Plunkett, S. P., Rich, N. B., and Howard, R. A. (2004). A catalog of white light coronal mass ejections observed by the SOHO spacecraft. *Journal of Geophysical Research (Space Physics)*, 109:A07105.

Zhang, J. and Dere, K. P. (2006). A Statistical Study of Main and Residual Accelerations of Coronal Mass Ejections. *Astrophys. J.*, 649:1100–1109.

Zhang, J., Dere, K. P., Howard, R. A., Kundu, M. R., and White, S. M. (2001). On the Temporal Relationship between Coronal Mass Ejections and Flares. *Astrophys. J.*, 559:452–462.

Zhang, J., Dere, K. P., Howard, R. A., and Vourlidas, A. (2004). A Study of the Kinematic Evolution of Coronal Mass Ejections. *Astrophys. J.*, 604:420–432.

Zhao, X. (2004). Identification of Earth-directed partial halo coronal mass ejections. In Stepanov, A. V., Benevolenskaya, E. E., and Kosovichev, A. G., editors, *Multi-Wavelength Investigations of Solar Activity*, volume 223 of *IAU Symposium*, pages 569–572.

Zhao, X. and Dryer, M. (2014). Current status of CME/shock arrival time prediction. *Space Weather*, 12:448–469.

Zhou, X. and Tsurutani, B. T. (2001). Interplanetary shock triggering of nightside geomagnetic activity: Substorms, pseudobreakups, and quiescent events. *J. Geophys. Res.*, 106:18957–18968.

Publications in international refereed journals

1. CME propagation – where does aerodynamic drag "take over"?
   Sachdeva, N., Subramanian, P., Colaninno, R., Vourlidas, A. 2015, The Astropysical Journal, 809, 158

2. CME dynamics using STEREO and LASCO observations: The relative importance of Lorentz Forces and Solar wind drag.
   Sachdeva, N., Subramanian, P., Vourlidas, A., Bothmer, V. 2017, Solar Physics, 292, 118

The Astrophysical Journal, 809:158 (8pp), 2015 August 20 doi:10.1088/0004-637X/809/2/158
© 2015. The American Astronomical Society. All rights reserved.

CME PROPAGATION: WHERE DOES AERODYNAMIC DRAG "TAKE OVER"?

Nishtha Sachdeva[1], Prasad Subramanian[1,4], Robin Colaninno[2], and Angelos Vourlidas[3]
[1] Indian Institute of Science Education and Research, Dr. Homi Bhabha Road, Pashan, Pune-411008, India; nishtha.sachdeva@students.iiserpune.ac.in
[2] Space Science Division, Naval Reseach Laboratory, Washington, DC 20375, USA
[3] The Johns Hopkins University, Applied Physics Laboratory, Laurel, MD 20723, USA
Received 2015 January 27; accepted 2015 July 18; published 2015 August 20

ABSTRACT

We investigate the Sun–Earth dynamics of a set of eight well observed solar coronal mass ejections (CMEs) using data from the *Solar Terrestrial Relations Observatory* spacecraft. We seek to quantify the extent to which momentum coupling between these CMEs and the ambient solar wind (i.e., the aerodynamic drag) influences their dynamics. To this end, we use results from a 3D flux rope model fit to the CME data. We find that solar wind aerodynamic drag adequately accounts for the dynamics of the fastest CME in our sample. For the relatively slower CMEs, we find that drag-based models initiated below heliocentric distances ranging from 15 to 50 $R_\odot$ cannot account for the observed CME trajectories. This is at variance with the general perception that the dynamics of slow CMEs are influenced primarily by solar wind drag from a few $R_\odot$ onwards. Several slow CMEs propagate at roughly constant speeds above 15–50 $R_\odot$. Drag-based models initiated above these heights therefore require negligible aerodynamic drag to explain their observed trajectories.

Key words: solar–terrestrial relations – solar wind – Sun: coronal mass ejections (CMEs) – Sun: heliosphere

1. INTRODUCTION

Coronal Mass Ejections (CMEs) are hot blobs of plasma and magnetic field that occasionally erupt from the solar corona. Some CMEs are directed toward the Earth and are primary drivers of the majority of so-called "space weather" disturbances that have profound consequences on a variety of technologies that we use in everyday life. Space weather predictions are therefore crucially dependent on accurate estimates of the Sun–Earth travel time of Earth-directed CMEs and their speed upon arrival at the Earth. Although we have some understanding of the factors influencing CME propagation through the inner heliosphere, several crucial aspects such as the origin of the driving and drag forces are still somewhat unclear. Needless to say, a thorough understanding of the physical bases of CME propagation is crucial to enable reliable space weather predictions.

Research on CMEs is often divided into "initiation" and "propagation" issues. Initiation issues deal with the initial eruption stages of a CME, while propagation issues concern forces at work during its subsequent propagation through the solar corona and the heliosphere. The division is somewhat artificial, but one can think of propagation issues as the ones that deal with the post-initiation, "residual" acceleration stage of CMEs (e.g., Zhang & Dere 2006; Subramanian & Vourlidas 2007; Gopalswamy 2013). Based on the temporal evolution of the kinetic and potential energies of a sample of well observed, plane-of-sky CMEs, Subramanian & Vourlidas (2007) showed that they are acted upon by a driving force throughout the Large Angle and Spectrometric Coronagaph (LASCO; Brueckner et al. 1995) field of view (FOV). Around 17% of CMEs in the extensive LASCO dataset are observed to accelerate out to 30 $R_\odot$ (St. Cyr et al. 2000). We will concern ourselves here with the propagation stage of CMEs. During the propagation stage, CMEs are thought to be subject to Lorentz self-forces close to the Sun (which may be a continuation of the initiation phase) and to aerodynamic drag due to momentum coupling with the ambient solar wind farther out. The interplay between these forces determines the dynamics of a CME as it propagates outwards from the Sun. It is generally accepted that:

1. very fast CMEs (generally defined as ones with speeds in excess of 1000 km s^{-1} near the Sun) experience all their acceleration (due to Lorentz self-forces) very close to the Sun, and are subsequently subjected mostly to deceleration due to aerodynamic drag from the ambient solar wind; i.e., they are dragged *down* by the solar wind via aerodynamic drag.
2. the dynamics of slow CMEs (generally defined as CMEs with speeds comparable to the solar wind speed near the Sun, of the order of a few 100 km s^{-1}) are governed primarily by solar wind aerodynamic drag. While Lorentz self-forces are expected to play some role, it is often thought that slow CMEs are primarily dragged *up* by the solar wind.

Our understanding of how Lorentz self-forces operate within CMEs is not very robust, although we know that they can accelerate, as well as decelerate a CME. While Lorentz self-forces must involve misaligned currents and magnetic fields, it has only recently been demonstrated that flux rope CMEs need to be substantially non force-free in order to account for Lorentz self-force driving (Subramanian et al. 2014). There is observational evidence to argue that the magnetic energy contained in flux rope CMEs is adequate to account for the mechanical energy required to propagate them from the Sun to the Earth (e.g., Manoharan et al. 2004; Manoharan 2006; Subramanian & Vourlidas 2007). However, the actual nature of Lorentz self-forces has not yet been well understood; some authors incorporate it in the eruption process (Isenberg & Forbes 2007; Kliem et al. 2014), while some treatments (e.g., Chen 1996) appeal to poloidal flux injection as a proxy for Lorentz self-forces, and use soft X-ray flare profiles as guides

[4] Also Centre for Excellence in Space Sciences, India, http://www.cessi.in

Table 1
Observed CME and Solar Wind Parameters

No.	Date	h_0 ($R_\odot$)	h_f ($R_\odot$)	v_0 (km s^{-1})	n_{wind} (cm^{-3})	v_{wind} (km s^{-1})	$\log(m_0)$	h_{occ} ($R_\odot$)	$\log(\Delta m)$
1	2010 Mar 19–23	3.5	155.5	162	3.60	380	14.7	3.65	14.3
2	2010 Apr 03–05	5.5	210.0	916	7.15	470	15.1	3.46	14.6
3	2010 Apr 08–11	2.9	195.1	468	3.60	440	15.4	3.55	14.7
4	2010 Jun 16–20	5.7	163.3	193	3.50	500	14.9	4.37	14.1
5	2010 Sep 11–14	4.0	150.3	444	4.00	320	15.2	3.84	14.7
6	2010 Oct 26–31	5.3	131.5	215	3.80	350	15.2	5.66	14.7
7	2011 Feb 15–18	4.4	188.6	832	2.50	440	15.6	3.85	13.9
8	2011 Mar 25–29	4.8	211.0	47	3.00	360	15.4	4.43	14.3

Note. Column 1: serial number; Column 2: observed date range for the event; Column 3: initial observed height; Column 4: final measured height; Column 5: initial CME speed; Column 6: observed proton number density at 1 AU; Column 7: observed solar wind speed at 1 AU; Column 8: log of the "true" CME mass at the first measurement; Column 9: occulation height; Column 10: log of mass increase per height.

to tailor the time profile of poloidal flux injection (Chen & Kunkel 2010).

On the other hand, the idea of momentum coupling with the ambient solar wind was motivated by the findings of Gopalswamy et al. (2000), Manoharan (2006), Maloney et al. (2009) and others who found that CMEs launched with speeds exceeding that of the solar wind were decelerated in the interplanetary medium, while those launched with speeds slower than the solar wind were sped up, so that all CMEs tend to equilibrate to the speed of the solar wind. Using a novel method of identifying an "average" CME from LASCO data over a one year period during the approach to solar maximum, Lewis & Simnett (2002) arrived at similar conclusions based on the similarities between the velocity profile of the CME and the ambient solar wind. Such observations have spurred considerable research on drag-based models (e.g., Cargill 2004; Vršnak 2006; Howard et al. 2007; Borgazzi et al. 2009; Byrne et al. 2010; Maloney & Gallagher 2010; Vršnak et al. 2010, 2013; Temmer et al. 2011; Lugaz & Kitner 2013; Mishra & Srivastava 2013; Dolei et al. 2014; Iju et al. 2014; Temmer & Nitta 2015). Most of these investigations employ an empirical drag coefficient C_D in order to characterize the interaction between the CME and the solar wind. An exception is Cargill (2004) where C_D is motivated from the results of 2.5D MHD simulations. Subramanian et al. (2012; SLB2012 hereafter) have obtained a physical prescription for C_D from a calculation of collisionless viscosity in the solar wind. The Sun–Earth travel time and near-Earth CME speed predicted by a model using this prescription is found to agree very well with observations of fast CMEs (SLB2012).

Using a large sample of CMEs observed in LASCO on board the *Solar and Heliospheric Observatory mission* (*SOHO*; Domingo et al. 1995), Michalek et al. (2015) recently characterized three phases of propagation. The first phase is the initial acceleration phase (presumably) due to Lorentz self-forces, followed by the second phase where a balance between the Lorentz and drag forces acting on the CMEs is achieved. The third phase is when the CME primarily decelerates due to aerodynamic drag at the outer edge of LASCO FOV. Our approach is similar, but we only seek to differentiate when CMEs are drag-dominated and when they are not. We note that the solar wind drag can serve to decelerate, as well as accelerate CMEs.

2. DATA AND MODELS

2.1. CME Event Sample

We use a set of eight extensively studied, Earth-impacting CMEs during the rising phase of solar cycle 24 between 2010 March and 2011 June (Colaninno 2012). These CMEs are observed by the *SOHO* LASCO, Sun–Earth Connection Coronal and Heliospheric Investigation (SECCHI; Howard et al. 2008) coronagraphs and the Heliospheric Imagers on board the *Solar Terrestrial Relations Observatory mission* (*STEREO*; Kaiser et al. 2008). Near-Earth parameters for these CMEs are obtained via in situ measurements from the *WIND* spacecraft (http://omniweb.gsfc.nasa.gov). The data set is described comprehensively in Colaninno (2012) and Colaninno et al. (2013), who have used the Graduated Cylindrical Shell Model (GCS; Thernisien et al. 2006, 2009) to obtain a 3D reconstruction of the Sun–Earth trajectory for each of these CMEs. This represents one of the best samples of CMEs for which detailed 3D information is available from the Sun to near the Earth. The ninth CME in the data set of Colaninno (2012) involves CME–CME interactions, which cannot be accommodated by the simple, drag-based model we employ. We therefore omit that event and study only eight CMEs from the sample.

Table 1 contains salient details for each of these CMEs. The CMEs are hereafter referred to using the serial number assigned in this table. For each CME, Colaninno (2012) gives the detailed 3D height–time trajectory and flux rope morphology from the Sun to near the Earth. In addition, we use some other parameters which we describe herein. The quantity h_0 denotes the height at the first measurement and h_f denotes the height at the final measurement. The quantity v_0 is the initial speed of the CME. We note that CMEs 1, 4, 6, and 8 start out fairly slow, with initial speeds <220 km s^{-1}, while CME 3, 5, and 7 start out relatively faster (>400 km s^{-1}). CME 7 was preceded by another CME, thus the solar wind characteristics are expected to be different from the quiescent state. CME 2 starts out with an initial speed of 916 km s^{-1} and is the fastest event in this sample.

2.2. Drag Model

Momentum coupling between the CME and ambient solar wind is typically addressed using the following equation:

$$F_{\rm drag} = m_{\rm cme}\frac{dV_{\rm cme}}{dt} = -\frac{1}{2}\,C_{\rm D}\,A_{\rm cme}\,n\,m_{\rm p}\big(V_{\rm cme}-V_{\rm sw}\big)\big|V_{\rm cme}-V_{\rm sw}\big|, \quad (1)$$

where $F_{\rm drag}$ is the drag force due to momentum coupling between the CME and solar wind, $m_{\rm cme}$ is CME mass, $V_{\rm cme}$ is CME speed, $C_{\rm D}$ is the drag coefficient, $A_{\rm cme}$ is CME area, n is the solar wind density, $m_{\rm p}$ denotes the proton mass, and $V_{\rm sw}$ is the ambient solar wind speed. The dimensionless drag parameter ($C_{\rm D}$) expresses the strength of the momentum coupling between the CME and the solar wind. In fluid dynamics texts (e.g., Landau & Lifshitz 1987), an equation of motion like Equation (1) is used to describe high Reynolds number flows past a solid body, where the bulk of the flow (which can be regarded as a largely potential flow) is separated from the body by a turbulent boundary layer. The solid body boundary conditions require that the entire velocity (both the tangential, as well as the normal component) vanish at the boundary. The turbulence in the boundary layer (which is rather thin, owing to the large Reynolds number) is set up because the velocity needs to transition from its bulk value to zero on the boundary over a very short distance; nonlinear terms in the Navier–Stokes equation assume importance and give rise to turbulence.

We note that Equation (1) is also often expressed in the following form (e.g., Cargill 2004; Vršnak et al. 2010):

$$\frac{F_{\rm drag}}{m_{\rm cme}} \equiv a_d = -\gamma\,\big(V_{\rm cme}-V_{\rm sw}\big)\big|V_{\rm cme}-V_{\rm sw}\big|, \quad (2)$$

where, γ ($\rm cm^{-1}$) is given by

$$\gamma = C_{\rm D}\frac{n m_{\rm p} A_{\rm cme}}{m_{\rm cme}}. \quad (3)$$

The cross-sectional area of CME is calculated using $A_{\rm cme}(R_{\rm cme}) = \pi\,R_{\rm cme}\,W_{\rm cme}$, where $R_{\rm cme}$ is the minor radius and $W_{\rm cme}$ is the major radius of the elliptical cross-section in the x–z plane of a flux-rope CME (Thernisien 2011). For each CME in our sample, the GCS fitting yields the major radius, the ratio of the minor to major radius and the half angle which can be used to calculate $R_{\rm cme}$ and $W_{\rm cme}$ using Equations (27)–(29) of Thernisien (2011).

In this paper we will use the SLB2012 prescription for $C_{\rm D}$, as well as prescriptions where the value of $C_{\rm D}$ is maintained at a constant value. For the sake of completeness, we briefly recapitulate the essentials of the SLB2012 viscosity and $C_{\rm D}$ prescription. The viscosity ($\nu_{\rm sw}$) in the ambient collisionless solar wind is due to resonant scattering of solar wind protons with an Alfvén wave spectrum, and can be expressed in analogy with a fluid expression for turbulent viscosity (Verma 1996):

$$\nu_{\rm sw} = \sqrt{6}\,\frac{2}{15}\,v_{\rm rms}\,\lambda, \quad (4)$$

where $v_{\rm rms}$ is the rms speed of solar wind protons and λ is the mean free path, which we take to be the ion inertial length, (Leamon et al. 1999, 2000; Smith et al. 2001; Bruno & Trenchi 2014) and is given by

$$\lambda = \frac{v_{\rm a}}{\Omega_i} = \frac{c}{\omega_{\rm p}} \sim 228\,n^{-1/2}\ {\rm km}. \quad (5)$$

In Equation (5), $v_{\rm a}$ is the Alfvén speed, Ω_i is the ion cyclotron frequency, $\omega_{\rm p}$ is the ion plasma frequency, and n is the ambient solar wind density. We note that this prescription is similar to that used by Coles & Harmon (1989); but their prescription is a factor of 3 larger. The treatement of SLB2012 uses the Coles & Harmon (1989) prescription for λ, whereas we take it to be the ion inertial length. The CME Reynolds number is defined as

$${\rm Re} \equiv \frac{\big(V_{\rm CME}-V_{\rm sw}\big)R_{\rm CME}}{\nu_{\rm sw}}, \quad (6)$$

where the quantity $\nu_{\rm sw}$ ($\rm cm^2\,s^{-1}$) is the solar wind viscosity calculated using the prescription given in SLB2012. The drag parameter $C_{\rm D}$ is related to Reynolds number using a fit to the data from Achenbach (1972) for the drag on a sphere at high Reynolds numbers:

$$C_{\rm D} = 0.148 - 4.3\times10^{4}\,{\rm Re}^{-1} + 9.8\times10^{-9}\,{\rm Re}. \quad (7)$$

The $C_{\rm D}$ prescription given by Equation (7) was experimentally determined for subsonic, high Reynolds number flow past a solid metal sphere (Achenbach 1972). It is worth commenting on its applicability to our situation. First, as noted earlier, the basic drag force law (Equation (1)) that is used extensively in this field is really a high Reynolds number, solid body law—two of the assumptions inherent in Equation (7) are thus consistent with it. Furthermore, it has been shown that the total (magnetic + particle) pressure exhibits a substantial jump across a typical magnetic cloud boundary, suggesting that they are over-pressured structures (Russell et al. 2005; Jian et al. 2006) that will not deform in response to tangential stresses, much like a solid body. Achenbach's drag formula has also been verified by modern detached-eddy simulations of high Reynolds number flows in the super-critical regime (e.g., Constantinescu & Squires 2004), which is the regime we are interested in. Another aspect to address is the fact that Equation (7) is derived from experimental results for subsonic flow, whereas the motion of CMEs through the solar wind is certainly supersonic. According to the Morokovin hypothesis, which has been verified extensively via numerical simulations (e.g., Duan et al. 2011) a subsonic turbulent drag law is valid even for supersonic flows as long as the fluctuations in the turbulent boundary layer are incompressible, or subsonic. The turbulent fluctuations in the ambient solar wind are certainly incompressible to a very good approximation (e.g., Shaikh & Zank 2010). This is also evident from the small values of the density fluctuation $\Delta n/n$ in the ambient solar wind (e.g., Bisoi et al. 2014). The values for the fluctuations in the magnetic field $\Delta B/B$ in the turbulent sheath between the shock and the CME are also as small as 10% (Arunbabu et al. 2013). Since $\Delta B/B$ is generally representative of $\Delta n/n$ (e.g., Spangler 2002), it follows that the turbulent density fluctuations in the sheath region are also fairly incompressible. In summary, the SLB2012 $C_{\rm D}$ prescription, as described by Equations (4)–(7), is quite appropriate to our situation.

However, as mentioned earlier, we use the SLB2012 $C_{\rm D}$ prescription as well as constant values for $C_{\rm D}$ in the results described below.

2.3. Models for Solar Wind Density, Speed, and CME Mass

We next describe the data-based models we use for computing the CME mass ($m_{\rm cme}$), solar wind speed ($V_{\rm sw}$) and solar wind density (n) in Equation (1). The quantity $n_{\rm wind}$ in Table 1 denotes the proton number density at the Earth, approximately one to two days in advance of the CME and the shock arrival. Assuming that the proton and electron number densities are equal, we use a version of the model given by Leblanc et al. (1998) in order to extrapolate the proton number density Sunwards from the Earth. The electron number density at a given heliocentric distance is given by

$$n(R) = \left(\frac{n_{\rm wind}}{7.2}\right)\left[3.3 \times 10^5 R^{-2} + 4.1 \times 10^6 R^{-4} + 8 \times 10^7 R^{-6}\right]\ {\rm cm}^{-3}, \quad (8)$$

where R is the heliocentric distance in solar radii. The original model of Leblanc et al. (1998) assumes that the number density at 1 AU is $7.2\,{\rm cm}^{-3}$. The factor $n_{\rm wind}/7.2$ ensures that the number density given by Equation (8) matches the proton number density ($n_{\rm wind}$) measured in situ by the *WIND* spacecraft near the Earth. The quantity $n(R)$ thus represents the number density of the ambient solar wind into which a given CME propagates.

It is well known that the ambient solar wind speed is an important factor influencing CME propagation (eg., Temmer et al. 2011). The quantity $v_{\rm wind}$ in Table 1 denotes the near-Earth solar wind speed observed in situ by the *WIND* spacecraft, in advance of the CME. In order to obtain the solar wind speed $V_{\rm sw}(R)$ as a function of heliocentric distance (R) along the Sun–Earth line, we use the solar wind model of Sheeley et al. (1997, 1999):

$$V_{\rm sw}^2(R) = v_{\rm wind}^2\left[1 - e^{-\frac{(R - r_0)}{r_{\rm a}}}\right]. \quad (9)$$

The quantity r_0, which denotes the heliocentric distance where the solar wind speed is zero, is taken to be 1.5 $R_\odot$. The quantity $r_{\rm a}$, which is the e-folding distance over which the asymptotic speed $v_{\rm wind}$ is reached, is taken to be 50 $R_\odot$. We have verified that our results are not very sensitive to the precise value of $r_{\rm a}$; this will be described later in this paper.

To calculate the CME mass, we used the Thomson scattering geometry from Billings (1966), which relates the observed brightness to coronal electron density. We calculated the mass in the COR2 FOV assuming that all the mass of the CME is concentrated in a plane at the longitude derived from the GCS model. This assumption is a first order estimate of the 3D mass consistent with the method of Colaninno & Vourlidas (2009). To correct for the effects of the occulter on the observed 3D mass, we used the prescription of Bein et al. (2013) who suggest the following functional form in the coronagraphic FOV:

$$m_{\rm cme}(R) = m_0 + \Delta m\left(R - h_{\rm occ}\right). \quad (10)$$

In this equation, m_0 is the "true" mass of the CME when it is first visible above the occulter. The quantity Δm is the real mass increase with height and $h_{\rm occ}$ is the size (radius) of the occulter in projection (Table 1). These terms in Equation (10) are derived from fitting the observed mass increase as the CME emerges from behind the occulter. Thus we can estimate the un-occulted 3D mass of the CME in the COR2 FOV with Equation (10). This mass formulation is valid only within the COR2 FOV, therefore, we assume the mass to be constant beyond 15 $R_\odot$.

We have also added the virtual mass (e.g., Cargill et al. 1996; Cargill 2004) to $m_{\rm cme}$ in our calculations. We note that the addition of the virtual mass does not change the results in any significant manner.

3. MODEL PREDICTIONS VERSUS DATA

To recapitulate, Equation (1) is a simplified, one-dimensional equation of motion describing the dynamics of a CME that is governed solely by aerodynamic drag due to momentum coupling with the ambient solar wind. Other effects such as Lorentz self-force driving are not included in this treatment. Due to momentum coupling between the CME and the solar wind, CMEs that travel slower than the solar wind would thus be accelerated, while those travelling faster than the solar wind would be decelerated. As described above, we have used realistic observational values for all parameters. The CME speed supplied to the model as an initial condition is estimated from the observed height–time data using either a multi-polynomial fit as in Colaninno (2012) or via numerical differentiation. We compare the prediction of the CME trajectory from Equation (1) with the observed height–time trajectory obtained via 3D GCS flux rope fitting for each of the CMEs in Table 1. Equation (1) yields the speed of a CME ($V_{\rm cme}$) as a function of time from the start of the event. The output of Equation (1) is integrated to obtain a height–time trajectory predicted by the model. We compare the predicted height–time trajectory with the observed height–time data for each CME in the next subsection. Other relevant parameters dealing with the comparison between the observations and corresponding models are discussed in Section 3.1.

3.1. Comparision of Height–Time Profiles

The observed height–time data together with the model predictions are shown in Figures 1 and 2. The results for CMEs 1, 2, 3, and 4 of Table 1 in Figure 1 and those for CMEs 5, 6, 7, and 8 are shown in Figure 2. Observed height–time data points are denoted by diamonds, while the lines show the model predictions. The dash–dotted line (red) shows the prediction of the model (Equation (1)) when it is initiated with quantities corresponding to the first data point. The solid (blue) line, on the other hand, shows the model prediction when it is initiated with these quantities corresponding to a later time; in other words, the model CME is initiated from a height larger than the first observation. Other details about the model predictions for each CME are discussed in the following sections.

3.1.1. CME 2

We note that the dash–dotted line which is computed using the SLB2012 $C_{\rm D}$ prescription agrees reasonably with the data points for the fastest CME in our sample, CME 2, which has a starting speed of $916\,{\rm km\,s}^{-1}$. This is expected, since fast CMEs, which are primarily decelerating, are dominated by solar wind aerodynamic drag, which is the only force that is included in Equation (1).

Although the height–time plot (Figure 1) looks roughly like a straight line, and might suggest that the CME speed is nearly

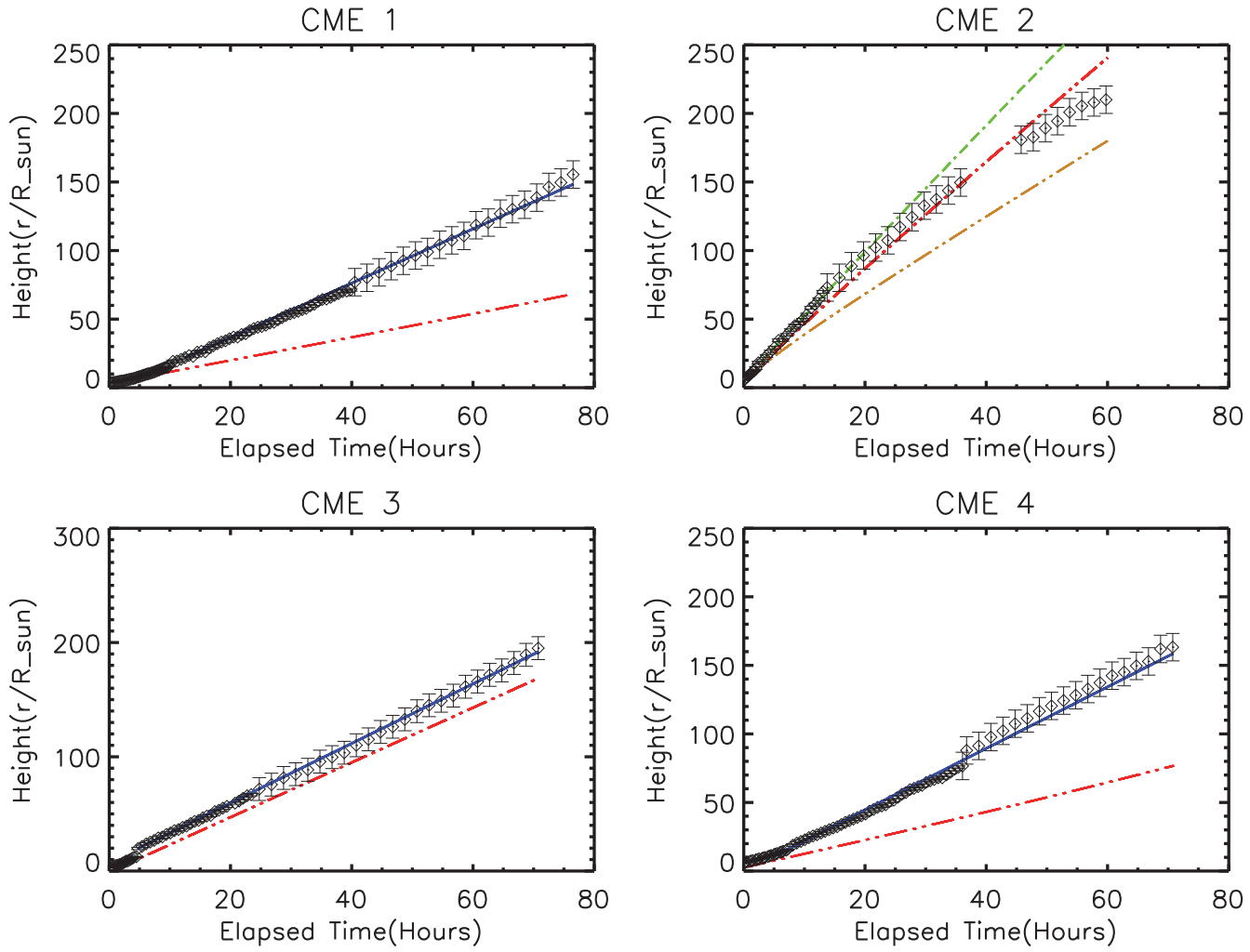


Figure 1. Height–time observations and model predictions for CMEs 1, 2, 3, and 4. The height–time data points are denoted by diamond symbols along with error bars for COR2 and HI data. The red dash–dotted line denotes the predictions of the model when it is initiated from the first observed data point, while the blue solid line denotes the model predictions when it is initiated from $\tilde{h}_0$. In the case of CME 2, the green dash–dotted line indicates the model solutions when initiated from the start with a constant C_D of 0.1 while the brown dash–dotted line represents the model predictions using a constant C_D of 5.0.

constant, we note that this is not so; CME 2 decelerates from ∼916 to ∼715 km s^{-1}.

The modeled CME is somewhat faster than the observed one; the observed Sun–Earth travel time for CME 2 was ≈60 hr and the model predicts that the CME arrives at the Earth around 8 hr earlier. This represents an error of 14%. $\Delta\tilde{h}$ which is the difference between the last measured height from observations and the final modeled height, was $-31.1\ R_\odot$ for this CME.

Our time of arrival (ToA) errors are comparable to the values of ≈10–12 hr obtained from MHD models (Mays et al. 2015) and drag-based models (Shi et al. 2015). Although we have used observational data as much as possible for the model fitting, there is some room for uncertainty in the quantity r_a. We find that a decrease (increase) in r_a of 50% results in a 3.7% decrease (increase) in the predicted CME travel time. It is also possible that errors in the GCS flux rope fitting procedure can lead to errors in the measured cross-sectional area of the CME. We find that a 50% decrease in the CME area results in a 6% decrease in the CME travel time.

The range of C_D values predicted by SLB2012 C_D prescription for CME 2 is 0.6–1.4. Model predictions using a constant $0.6 < C_D < 2.0$ are reasonably similar to the dash–dotted (red) line of CME 2 in Figure 1 which uses the SLB2012 C_D. On the other hand, constant C_D models with values for C_D that lie substantially outside of $0.6 < C_D < 2.0$ perform poorly. This is evident from the examples shown in Figure 1; model solutions with constant C_Ds of 0.1 (green dash–dotted line) and 5 (brown dash dotted line) disagree considerably with the observed height–time data for CME 2. For the $C_D = 0.1$ model, the difference between the predicted and the observed ToA at 180 $R_\odot$ is ≈ −8 hr. For $C_D = 5.0$, it is ≈14 hr, and only −1.8 hr for the SLB2012 C_D prescription.

3.1.2. Slower CMEs

Next, we turn our attention to the somewhat slower CMEs in our sample (Table 1): CMEs 1, 3, 4, 5, 6, 7, and 8. For such CMEs, it is generally believed that Lorentz self-forces are dominant for the initial part of its trajectory, while aerodynamic drag takes over at larger heights (e.g., Michalek et al. 2015). Some authors (e.g., Lewis & Simnett 2002) claim that representative slow CMEs are exclusively dragged *up* by the solar wind. Some authors (e.g., Mishra & Srivastava 2013) apply the drag-based model to explain observations of slow CMEs over its entire trajectory while some authors (e.g., Byrne

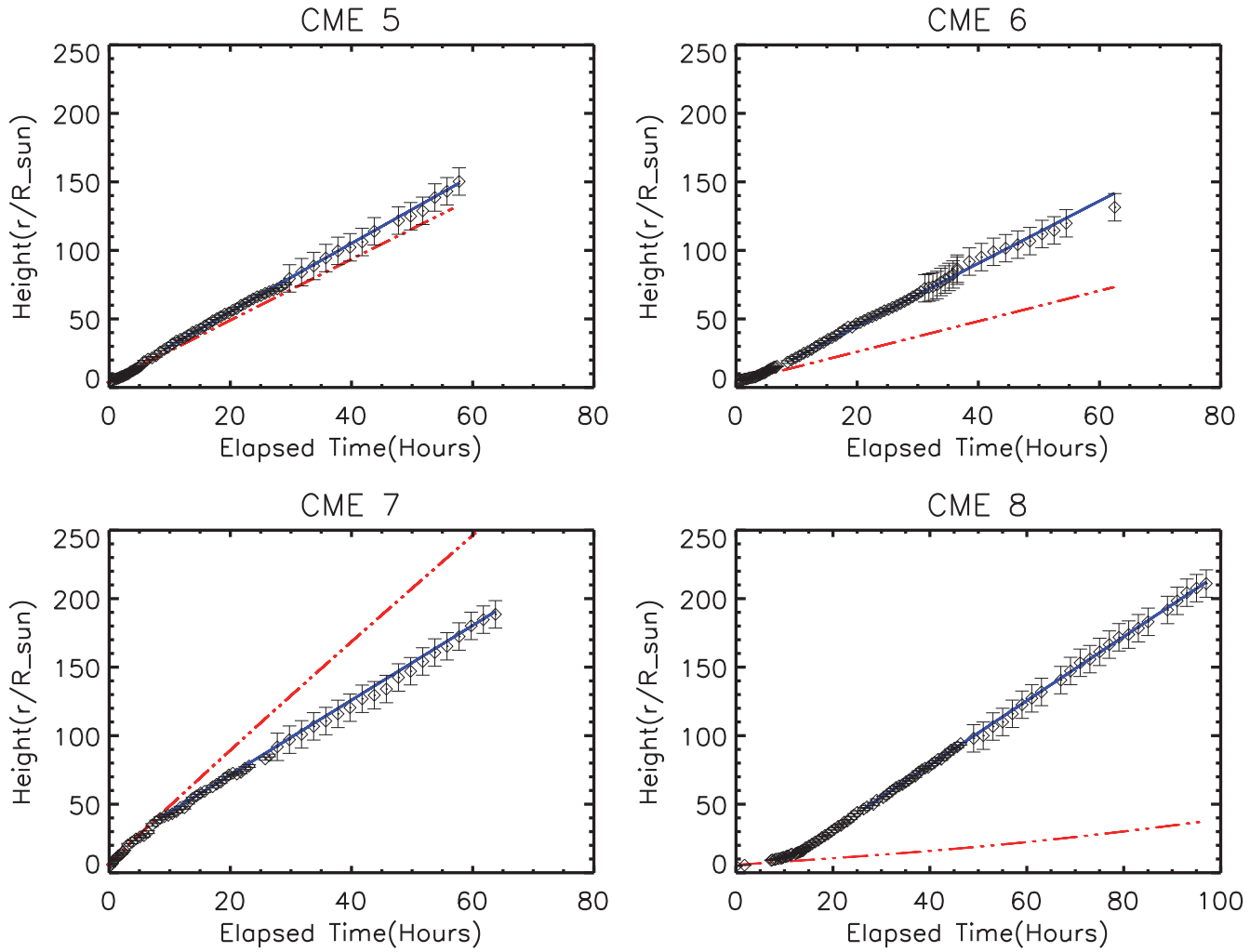


Figure 2. Height–time plot for data and derived heights from the drag-only model for CMEs 5, 6, 7, and 8. The height–time data points are denoted by diamond symbols along with error bars for COR2 and HI data. The dash–dotted lines denoted the predictions of the model when it is initiated from the first observed data point, while the solid line denotes the model predictions when it is initiated from $\widetilde{h}_0$.

et al. 2010; Carley et al. 2012; Gopalswamy 2013) think that solar wind aerodynamic drag becomes dominant for slow CMEs beyond a few solar radii. It is evident from Figures 1 and 2 that the dash–dotted line disagrees considerably with the data (denoted by diamonds) for all events except CME 2. The maximum height (at the last timestamp) predicted by the model (when initiated from the start) falls short of the final observed height (h_f) for each CME (except CME 7, in which case it is much larger than h_f). We find that the difference between the final height predicted by the model and the observed final height is large, ranging between 17 and 175 $R_\odot$ for CMEs 1, 3, 4, 5, 6, 7, and 8. This suggests that there is a large discrepancy in the predicted and observed trajectory when the model is initiated from low heights. In other words, momentum coupling with the ambient solar wind alone does not satisfactorily explain the dynamics of the CMEs other than CME 2.

While the dash–dotted (red) lines use the SLB2012 C_D prescription, we also find that constant C_D models with $0.1 < C_D < 5$ cannot account for the data when initiated from the first observation. This points to the conclusion that CMEs 1, 3, 4, 5, 6, 7, and 8 cannot be considered to be drag-dominated (either drag-accelerated or decelerated) from the start. This conclusion is independent of the specific C_D model used (the SLB2012 C_D or a constant C_D). In order to find the height where the solar wind drag "takes over" for the relatively slower CMEs we adopt the following strategy—we initiate the model at a larger height. The initial conditions supplied to the differential equation (Equation (1)), such as the CME initial speed, mass, cross-sectional area, solar wind speed, and background density are those appropriate to this height, which is larger than that at the first observed data point. We repeat this exercise with increasing initiation heights until there is a reasonable agreement between the modeled (solid line) and observed height–time data. We carry out this exercise using the SLB2012 C_D model as well as constant C_D models. As with CME 2, we find that the values for C_D predicted by the SLB2012 prescription are a good guide for the constant C_D model. In other words, only those constant C_D models with C_D values that are close to those predicted by SLB2012 prescription (last column in Table 2) agree reasonably well with the data. The initiation height beyond which the solid line agrees reasonably with the data is denoted by $\widetilde{h}_0$ in Table 2, and the CME speed at $\widetilde{h}_0$ is denoted by $\widetilde{v}_0$. At heights below $\widetilde{h}_0$, no drag model yields good agreement with observations. We have verified this by initiating the model at different heights ranging

Table 2
CME Model Parameters and SLB2012 C_D

No.	$\tilde{h}_0$ ($R_\odot$)	$\tilde{v}_0$ (km s^{-1})	$\tilde{h}_f$ ($R_\odot$)	$\Delta\tilde{h}$ ($R_\odot$)	SLB2012 C_D
1	21.9	383	148.3	7.1	0.1–0.3
2	5.5	916	241.1	−31.1	0.6–1.4
3	19.7	506	191.8	3.3	0.2–0.4
4	15.2	437	158.4	4.8	0.2–0.3
5	27.7	490	149.1	1.2	0.4–0.6
6	20.1	445	141.7	−10.3	0.25–0.5
7	39.7	530	190.7	−2.1	0.25–0.4
8	46.5	456	212.0	−1.0	0.25–0.35

Note. Column 1: CME number corresponding to Table 1; Column 2: height at which model is initiated; Column 3: CME speed at height $\tilde{h}_0$; Column 4: final height at last observed timestamp when the model is initiated from $\tilde{h}_0$; Column 5: difference between h_f and $\tilde{h}_f$; Column 6: range of C_D values predicted by SLB2012 C_D prescription.

from the first observed height (h_0) to $\tilde{h}_0$, using the SLB2012 C_D prescription, as well as the constant C_D prescription. Since we do not include any forces other than solar wind drag, the only definitive statement we can make about CMEs 1, 3, 4, 5, 6, 7, and 8 is that they are not drag dominated when the model is initiated at *any height below* $\tilde{h}_0$.

Table 2 also lists for each CME the quantity $\tilde{h}_f$ which is the final height predicted by the model when it is initiated from $\tilde{h}_0$ (corresponding to the solid lines in Figures 1 and 2 and dash–dotted line for CME 2). $\Delta\tilde{h}$ is the difference between h_f and $\tilde{h}_f$.

For CMEs 1, 3, 4, 5, and 6, we have reconstructed 3D data only up to ∼160 $R_\odot$. In order to avoid empirical extrapolation, we therefore compare the model velocity predictions with the observed quantities at the last timestamp for all CMEs. Table 3 lists the quantities V_{ldp}, which is the velocity observed at the last timestamp (at h_f) for each event and V_{pred}, which is the predicted velocity at the same instant. ΔV is the difference between V_{pred} and V_{ldp}. A positive ΔV means that the predicted CME velocity at last data point is larger than the observed one, while a negative ΔV means the converse. The ratio of ΔV to the observed velocity V_{ldp} (at heliocentric height h_f) is also given in Table 3. $\Delta V/V_{ldp}$ ranges between 0.3% and 31%, which indicates that the model performs well. Depending on how the ambient solar wind speed compares with $\tilde{v}_0$, the solar wind drag decelerates/accelerates the CMEs.

As with the velocity comparisons, in order to avoid empirical extrapolation, we compare the ToA for each event at two heights: 130 $R_\odot$ and 180 $R_\odot$. Only CMEs 2, 3, 7, and 8 attain heights > 180 $R_\odot$; therefore ToA comparisions at 180 $R_\odot$ are made for only these four events. For the remaining events we make ToA comparisons at 130 $R_\odot$. Table 3 describes the quantity ΔT which is the difference between the predicted and observed ToA at these heights, when the model is initiated at $\tilde{h}_0$ (except for CME2, where the model is initiated at h_0). A positive ΔT means that the arrival time of the model CME is delayed with respect to the observed one, while a negative ΔT denotes its converse. The quantity $\Delta T/T$ denotes the ratio of ΔT to the observed CME transit time up to each height. It ranges between 1% and 5% for 130 $R_\odot$ and for 180 $R_\odot$ it ranges between 0.1% and 4%.

An important point to be noted is that that most of the slow CMEs show little evolution in their speeds beyond $\tilde{h}_0$. While CME 5 decelerates moderately (∼13 km s^{-1}) between 28 $R_\odot$ and 150 $R_\odot$, CME 1 hardly decelerates. As before, constant C_D models with values of C_D that are close to the SLB2012 C_D predictions yield similar results. Since the deceleration is so small, even constant C_D models with $C_D \approx 0$ yield good results. Initiating drag-based models above $\tilde{h}_0$ thus does not constrain the drag-based models to any appreciable extent, and only reinforces the fact that most slow CMEs do not accelerate or decelerate much beyond $\tilde{h}_0$.

4. DISCUSSION AND CONCLUSIONS

We worked with a dataset of eight well observed CMEs that were tracked by the *SOHO* LASCO and SECCHI coronagraphs and the HI imagers aboard the *STEREO* spacecraft (Colaninno 2012). These events were fitted with the GCS model, which yields the 3D height–time profile of the CME as it propagates through the heliosphere (Table 1). Despite the relatively small number of events, our sample covers a wide range of speeds: some events start out fairly slow (around a few 100 km s^{-1}), some have intermediate speeds and one is relatively fast (starting speed of 916 km s^{-1}), although it is certainly not among the fastest CMEs observed. We focused here on the effect of solar wind aerodynamic drag on CMEs using a simple, widely used 1D model (Equation (1)) that allows one to obtain

Table 3
CME Arrival Time and Speeds: Observations vs. Predictions

No.	V_{ldp} (km s^{-1})	V_{pred} (km s^{-1})	ΔV (km s^{-1})	$\Delta V/V_{ldp}$ (%)	130 $R_\odot$		180 $R_\odot$	
					ΔT (hr)	$\Delta T/T$ (%)	ΔT (hr)	$\Delta T/T$ (%)
1	439	382	−57	13	0.85	1	⋯	⋯
2	639	731	92	14	⋯	⋯	−1.8	4
3	501	503	2	0.3	⋯	⋯	0.07	0.09
4	501	483	−18	3	2.5	4.5	⋯	⋯
5	564	477	−87	15	−1.98	3.8	⋯	⋯
6	457	439	−18	4	−0.75	1.27	⋯	⋯
7	595	526	−69	12	⋯	⋯	0.12	0.2
8	342	451	109	31	⋯	⋯	−0.39	0.46

Note. Column 1: CME number correspoing to Table 1; Column 2: observed CME velocity at last observed timestamp; Column 3: predicted model velocity at the last timestamp when the model is initiated from $\tilde{h}_0$ (except CME 2 in which case model starts from h_0); Column 4: ΔV is the difference between V_{pred} and V_{ldp}; Column 5: Ratio of ΔV and V_{ldp}; Column 6: difference between the Predicted and Observed ToA at 130 $R_\odot$; Column 7: ratio of ΔT and the observed ToA at 130 $R_\odot$; Column 8: difference between the Predicted and Observed ToA at 180 $R_\odot$; Column 9: ratio of ΔT and the observed ToA at 180 $R_\odot$.

the predicted height–time trajectory of a CME that is subject only to this drag (Lorentz self-forces are not included). It may be noted that solar wind drag can serve to decelerate, as well as accelerate a CME. We used two prescriptions for the drag parameter C_D: the SLB2012 prescription, and a prescription where the value of C_D is maintained at a constant value. For a given CME, we use observationally determined values for the CME cross-sectional area, mass, initial speed, ambient solar wind density and speed to solve Equation (1) and obtain the predicted height–time trajectory, which we compare with the observed one. In general, such a model is expected to work best for very fast CMEs, for which (accelerating) Lorentz self-forces are expected to cease very soon after initiation (e.g., Chen & Kunkel 2010), and the only operating force from then onwards is the (decelerating) solar wind aerodynamic drag. In keeping with this expectation, we find that the drag-based model performs well in describing the dynamics of the fastest CME in our sample, CME 2.

Its generally thought that slow CMEs are "picked up by the solar wind" (i.e., accelerated by aerodynamic drag) from as early as a few $R_\odot$. Results from drag-based models reported in the most of the existing literature refer to initiation from the first observed timestamp, which typically correspond to only a few $R_\odot$. For the slow CMEs in our sample, we find that the predictions of drag-based models do not agree with the observations when initiated at any heliocentric height below $\widetilde{h}_0$ ($\widetilde{h}_0$ for slow CMEs ranges from 15 to 50 $R_\odot$). When initiated at heights $<\widetilde{h}_0$, the errors in predicting the final height for slow CMEs range from 12% to 80%. Our results thus suggest that solar wind drag is not the dominant influence on CME trajectories until 15–50 $R_\odot$. It might be important to include other forces such as Lorentz forces, at least as far as 15 to 50 $R_\odot$. Recent work by Žic et al. (2015) also assumes that solar wind drag is effective only above 15 $R_\odot$.

The speeds of several slow CMEs in our sample stay roughly constant for heights $>\widetilde{h}_0$. Although drag-based models initiated above $\widetilde{h}_0$ seem to generally perform well, solar wind drag in fact "does not have much to do" for these CMEs (since the CME speed evolution at heights $>\widetilde{h}_0$ is negligible) and the drag parameter C_D is not well constrained.

N.S. acknowledges support from a PhD studentship at IISER Pune. P.S. acknowledges support from the Asian Office of Aerospace Research and Development. R.C. and A.V. are supported by NASA contract S-136361-Y to NRL. The SECCHI data are produced by an international consortium of the NRL, LMSAL and NASA GSFC (USA), RAL and Univ. Bham (UK), MPS (Germany), CSL (Belgium), IOTA and IAS (France). We acknowledge a very thorough review by the referee, which helped us considerably in improving this paper.

REFERENCES

Achenbach, E. 1972, JFM, 54, 565
Arunbabu, K. P., Antia, H. M., Dugad, S. R., et al. 2013, A&A, 555, A139
Bein, B. M., Temmer, M., Vourlidas, A., et al. 2013, ApJ, 768, 31
Billings, D. E. 1966, A Guide to the Solar Corona (New York: Academic)
Bisoi, S. K., Janardhan, P., Ingale, M., et al. 2014, ApJ, 795, 69
Borgazzi, A., Lara, A., Echer, E., et al. 2009, A&A, 498, 885
Brueckner, G. E., Howard, R. A., Koomen, M. J., et al. 1995, SoPh, 162, 357
Bruno, R., & Trenchi, L. 2014, ApJL, 787, L24
Byrne, J. P., Maloney, S. A., McAteer, R. T. J., et al. 2010, NatCo, 1, 74
Cargill, P. J. 2004, SoPh, 221, 135
Cargill, P. J., Chen, J., Spicer, D. S., & Zalesak, S. T. 1996, JGR, 101, 4855
Carley, E. P., McAteer, R. T. J., & Gallagher, P. T. 2012, ApJ, 752, 36
Chen, J. 1996, JGR, 101, 27499
Chen, J., & Kunkel, V. 2010, ApJ, 717, 1105
Colaninno, R. C. 2012, PhD thesis, George Mason Univ., (arXiv:1206.4290)
Colaninno, R. C., & Vourlidas, A. 2009, ApJ, 652, 1747
Colaninno, R. C., Vourlidas, A., & Wu, C. C. 2013, JGR, 118, 6866
Coles, W. A., & Harmon, J. K. 1989, ApJ, 337, 1023
Constantinescu, G., & Squires, K. 2004, PhFl, 16, 1449
Dolei, S., Bemporad, A., & Spadaro, D. 2014, A&A, 562, A74
Domingo, V., Fleck, B., & Poland, A. I. 1995, SoPh, 162, 1
Duan, L., Beekman, I., & Martin, M. P. 2011, JFM, 672, 245
Gopalswamy, N. 2013, in ASI Conf. Ser. 10, STEREO and SOHO Contributions to Coronal Mass Ejection Studies: Some Recent Results, ed. N. Gopalswamy et al. (Pune, India: ASI), 11
Gopalswamy, N., Lara, A., Lepping, R. P., et al. 2000, GeoRL, 27, 145
Howard, R. A., Moses, J. D., Vourlidas, A., et al. 2008, SSRv, 136, 67
Howard, T. A., Fry, C. D., Johnston, J. C., et al. 2007, ApJ, 667, 610
Iju, T., Tokumaru, M., & Fujiki, K. 2014, SoPh, 289, 2157
Isenberg, P. A., & Forbes, T. G. 2007, ApJ, 670, 1453
Jian, L., Russell, C. T., Luhmann, J. G., & Skoug, R. M. 2006, SoPh, 239, 393
Kaiser, M. L., Kucera, T. A., Davilla, J. M., et al. 2008, SSRv, 136, 5
Kliem, B., Lin, J., Forbes, T. G., et al. 2014, ApJ, 789, 46
Landau, L. D., & Lifshitz, E. M. 1987, Fluid Mechanics (2nd ed.; Oxford: Pergamon)
Leamon, R. J., Matthaeus, W. H., Smith, C. W., et al. 2000, ApJ, 537, 1054
Leamon, R. J., Smith, C. W., Ness, N. F., et al. 1999, JGR, 104, 22331
Leblanc, Y., Dulk, G. A., & Bourgeret, J.-L. 1998, SoPh, 183, 165
Lewis, D. J., & Simnett, G. M. 2002, MNRAS, 333, 969
Lugaz, N., & Kitner, P. 2013, SoPh, 285, 281
Maloney, S. A., & Gallagher, P. T. 2010, ApJL, 724, L127
Maloney, S. A., Gallagher, P. T., & McAteer, R. T. J. 2009, SoPh, 256, 149
Manoharan, P. K. 2006, SoPh, 235, 345
Manoharan, P. K., Gopalswamy, N., Yashiro, S., et al. 2004, JGR, 109, A06109
Mays, M. L., Taktakishvili, A., Pulkkinen, A., et al. 2015, arXiv:1504.04402
Michalek, G., Gopalswamy, N., & Yashiro, S. 2015, SoPh, 290, 903
Mishra, W., & Srivastava, N. 2013, ApJ, 772, 70
NASA's Space Phsyics Data Facility (SPDF), Greenbelt, MD U.S.A., NASA's Goddard Space Flight Center, http://omniweb.gsfc.nasa.gov/
Russell, C. T., Shinde, A. A., & Jian, L. 2005, AdSpR, 35, 2178
Shaikh, D., & Zank, G. P. 2010, MNRAS, 402, 362
Sheeley, N. R., Jr., Walters, J. H., Wang, Y.-M., et al. 1999, JGR, 104, 24,739
Sheeley, N. R., Wang, Y.-M., Hawley, S. H., et al. 1997, ApJ, 484, 472
Shi, T., Wang, Y., Wan, L., et al. 2015, arXiv.1505.00884
Smith, C. W., Mullan, D. J., Ness, N. F., et al. 2001, JGR, 106, 18625
Spangler, S. R. 2002, ApJ, 576, 997
St. Cyr, O. C., Plunkett, S. P., Michels, D. J., et al. 2000, JGR, 105, 18169
Subramanian, P., Arunbabu, K. P., Vourlidas, A., et al. 2014, ApJ, 790, 125
Subramanian, P., Lara, A., & Borgazzi, A. 2012, GeoRL, 39, L19107
Subramanian, P., & Vourlidas, A. 2007, A&A, 467, 685
Verma, M. K. 1996, JGR, 101, 27543
Vršnak, B. 2006, AdSpR, 38, 431
Vršnak, B., Žic, T., Falkenberg, T. V., et al. 2010, A&A, 512, A43
Vršnak, B., Žic, T., Temmer, M., et al. 2013, SoPh, 285, 295
Temmer, M., & Nitta, N. 2015, SoPh, 290, 919
Temmer, M., Rollett, T., Mästl, C., et al. 2011, ApJ, 743, 101
Thernisien, A. 2011, ApJS, 194, 33
Thernisien, A. F. R., Howard, R. A., & Vourlidas, A. 2006, ApJ, 652, 763
Thernisien, A. F. R., Vourlidas, A., & Howard, R. A. 2009, SoPh, 256, 111
Zhang, J., & Dere, K. P. 2006, ApJ, 649, 1100
Žic, T., Vršnak, B., & Temmer, M. 2015, ApJS, 218, 32

Solar Phys (2017) 292:118
DOI 10.1007/s11207-017-1137-9

CME Dynamics Using STEREO and LASCO Observations: The Relative Importance of Lorentz Forces and Solar Wind Drag

Nishtha Sachdeva[1] · Prasad Subramanian[1,2] · Angelos Vourlidas[3,4] · Volker Bothmer[5]

Received: 8 February 2017 / Accepted: 5 July 2017
© Springer Science+Business Media B.V. 2017

Abstract We seek to quantify the relative contributions of Lorentz forces and aerodynamic drag on the propagation of solar coronal mass ejections (CMEs). We use Graduated Cylindrical Shell (GCS) model fits to a representative set of 38 CMEs observed with the *Solar and Heliospheric Observatory* (SOHO) and the *Solar and Terrestrial Relations Observatory* (STEREO) spacecraft. We find that the Lorentz forces generally peak between 1.65 and 2.45 $R_\odot$ for all CMEs. For fast CMEs, Lorentz forces become negligible in comparison to aerodynamic drag as early as 3.5 – 4 $R_\odot$. For slow CMEs, however, they become negligible only by 12 – 50 $R_\odot$. For these slow events, our results suggest that some of the magnetic flux might be expended in CME expansion or heating. In other words, not all of it contributes to the propagation. Our results are expected to be important in building a physical model for understanding the Sun–Earth dynamics of CMEs.

Keywords Coronal mass ejections · Initiation · Propagation

1. Introduction

Coronal mass ejections (CMEs) from the Sun are generally acknowledged as the main cause of disturbances in the near-Earth space environment. Due to the considerable technological

Earth-affecting Solar Transients
Guest Editors: Jie Zhang, Xochitl Blanco-Cano, Nariaki Nitta, and Nandita Srivastava

✉ N. Sachdeva
nishtha.sachdeva@students.iiserpune.ac.in

1 Indian Institute of Science Education and Research, Dr. Homi Bhabha Road, Pashan, Pune 411008, India

2 Centre for Excellence in Space Sciences, Kolkata, India

3 Applied Physics Laboratory, The Johns Hopkins University, Laurel, MD 20723, USA

4 IAASARS, National Observatory of Athens, 15236 Penteli, Greece

5 Institute of Astrophysics, University of Göttingen, Friedrich-Hund-Platz 1, 37077 Göttingen, Germany

Published online: 16 August 2017

impacts caused by such disturbances, it has become increasingly important to study and understand various aspects related to CME impacts on the Earth's magnetosphere (Gosling *et al.*, 1991; Bothmer and Daglis, 2007). One of the most basic quantities in this regard concerns the time it takes for a CME to reach the Earth after it has been detected leaving the Sun using space-based coronagraphs. This quantity is called the Sun–Earth travel time. Among the factors that affect the travel time are the CME size, mass, initial velocity and the ambient solar wind speed (Bosman *et al.*, 2012). An accurate and reliable forecast of the Sun–Earth travel time is obviously important to a space weather mitigation framework, as is a good estimate of the expected speed of the CME near the Earth. These quantities are typically computed from a dynamical model for CME propagation that uses near-Sun coronagraph observations as input.

The basic outlines of such dynamical CME propagation models have been well established for a while. One-dimensional (1D) models that incorporate Lorentz-force driving, aerodynamic drag, and other effects have been in vogue since 1996 (*e.g.* Chen, 1996; Kumar and Rust, 1996). So-called drag-based models (DBM), which consider only aerodynamic drag, have been very popular lately (*e.g.* Cargill, 2004; Vršnak *et al.*, 2010; Mishra and Srivastava, 2013; Temmer and Nitta, 2015). More sophisticated three-dimensional (3D) MHD models such as ENLIL (*e.g.* Taktakishvili *et al.*, 2009; Lee *et al.*, 2013; Vršnak *et al.*, 2014; Mays *et al.*, 2015), the global MHD model using the data-driven Eruptive Event Generator of Gibson-Low (EEGGL) (*e.g.* Jin *et al.*, 2017), CME and shock propagation models like the Shock Time of Arrival model (STOA), the Interplanetary Shock Propagation Model (ISPM) and the Hakamada–Akasofu–Fry version 2 model (*e.g.* Fry *et al.*, 2003; McKenna-Lawlor *et al.*, 2006), other hybrid models (Wu *et al.*, 2007) and the Space Weather Modeling Framework (SWMF; Lugaz *et al.*, 2007; Tóth *et al.*, 2007) are also often used in modeling CME propagation.

Despite considerable progress, our ability to successfully model the Sun–Earth travel time and the near-Earth speed of Earth-directed CMEs is still limited (Zhao and Dryer, 2014), even for relatively simple events that do not involve interacting CMEs (*e.g.* Temmer *et al.*, 2012). Part of the reason for this is that the models are still largely empirical. For instance, most drag-based models use the dimensionless drag coefficient C_{D} and/or the parameter γ (ratio of drag acceleration and square of the difference between the CME and solar wind speeds) as a fitting parameter. The physical basis of the aerodynamic drag experienced by CMEs is only starting to be understood (Subramanian, Lara, and Borgazzi, 2012; Sachdeva *et al.*, 2015). As far as Lorentz forces go, it is also generally thought that they are dominant only in the initial phases of CME propagation, when they are relatively near the Sun. However, for a given CME, its not clear where Lorentz forces peak and when they cease to be important. Some 1D models (*e.g.* Chen and Kunkel, 2010; Zhang *et al.*, 2001) assume that the Lorentz force follows the temporal profile of the soft X-ray flare that often accompanies the CMEs.

In this article we adopt the physical definition for CME aerodynamic drag outlined in Sachdeva *et al.* (2015), referred to as Paper 1 from now on, together with a specific model (Kliem and Török, 2006) for Lorentz forces to address some of these questions: What is the heliocentric distance range where Lorentz forces dominate? Beyond what heliocentric distance is a drag-only model justified?

The rest of the article is organized as follows. In Section 2 we discuss the forces affecting the CME propagation. Section 3 provides details of the CME event sample and data obtained from Graduated Cylindrical Shell (GCS) fittings. The analysis and main results are outlined in Section 4, followed by discussion and conclusions in Section 5.

2. Forces Acting on CMEs

Descriptions of CME evolution usually consider an initiation phase comprising the initial CME eruption, which is followed by the propagation phase. There is an interplay between Lorentz forces, gravity and solar wind aerodynamic drag in the propagation phase; this provides the residual acceleration (*e.g.* Zhang and Dere, 2006; Subramanian and Vourlidas, 2007; Gopalswamy, 2013). Gravitational forces and plasma pressure are generally taken to be negligible for flux-rope models of CMEs (Forbes, 2000; Isenberg and Forbes, 2007). Lorentz forces are thought to accelerate CMEs up to a few solar radii in the low corona (*e.g.* Vršnak, 2006; Bein *et al.*, 2011; Carley, McAteer, and Gallagher, 2012), beyond which the solar wind aerodynamic drag takes over. Paper 1 shows that aerodynamic drag accounts for the observed CME trajectory only beyond $15-50$ $R_\odot$ for the slow (near-Sun speeds < 900 km s^{-1}) CMEs; for fast CMEs (near-Sun speed > 900 km s^{-1}), aerodynamic drag can account for their dynamics from 5 $R_\odot$ onwards. Rollett *et al.* (2016) also show that their drag-based model (DBM) is applicable only beyond a heliocentric distance of 21 ± 10 $R_\odot$.

The forces acting on a CME are often represented in the following form (in cgs units):

$$\begin{aligned} F &= m_{\rm cme}\frac{{\rm d}^2R}{{\rm d}t^2} \\ &= F_{\rm Lorentz} + F_{\rm drag} \\ &= \left\{\left[\frac{\pi I^2}{c^2}\left(\ln\left(\frac{8R}{b}\right) - \frac{3}{2} + \frac{l_{\rm i}}{2}\right)\right] - \frac{(\pi R) I B_{\rm ext}(R)}{c}\right\} \\ &\quad - \frac{1}{2}C_{\rm D}A_{\rm cme}n_{\rm sw}m_{\rm p}(V_{\rm cme} - V_{\rm sw})|V_{\rm cme} - V_{\rm sw}| \end{aligned} \tag{1}$$

where F is the total force, $m_{\rm cme}$ is the CME mass, R is the heliocentric distance of the leading edge of the CME, and t represents time. $F_{\rm Lorentz}$ is the net Lorentz force acting on the CME in the major radial direction which is given by the term in the curly brackets (see *e.g.* Shafranov, 1966; Kliem and Török, 2006). The first term (within the square brakets) represents the Lorentz self-forces ($(1/c)J \times B$, where J is the current density and B the magnetic field) acting on the expanding CME current loop (*e.g.* Chen, 1989) that accelerate the CME, while the second term is the force due to the external poloidal field, $B_{\rm ext}$, that tends to hold down the expanding CME. In the equation, I is the CME current, c is the speed of light, b is CME minor radius, and $l_{\rm i}$ is the internal inductance. The axial current, I, is determined by the conservation of total (*i.e.* flux-rope + external) magnetic flux.

The term in Equation 1 involving $C_{\rm D}$ represents the aerodynamic drag experienced by the CME as it propagates through the solar wind. The strength of the momentum coupling between the CME and the solar wind is represented by the dimensionless drag coefficient, $C_{\rm D}$. We use a non-constant $C_{\rm D}$ given by Equation 7 of Paper 1. For completeness, we include the $C_{\rm D}$ definition here:

$$C_{\rm D} = 0.148 - 4.3\times10^4 Re^{-1} + 9.8\times10^{-9}Re, \tag{2}$$

where Re is the Reynolds number calculated using the solar wind viscosity expression as described in Paper 1. The quantity $A_{\rm cme}$ is the cross-sectional area of the CME, $n_{\rm sw}$ is the solar wind density, and $m_{\rm p}$ is the proton mass. $V_{\rm cme}$ and $V_{\rm sw}$ denote the CME and solar wind velocities, respectively. Depending on how fast or slow a CME is traveling (relative to the solar wind), the solar wind can either "drag down" the CME or "pick it up". Paper 1 finds that fast CMEs (initial velocity ~ 916 km s^{-1}) are governed primarily by aerodynamic drag from as early as ~ 5.5 $R_\odot$. On the other hand, slower CMEs are governed by solar wind aerodynamic drag only above $15-50$ $R_\odot$.

In this article we analyze a diverse sample of 38 well observed CMEs. Using measurements with the Graduated Cylindrical Shell (GCS) method for each CME, we determine the heliocentric distance, $\tilde{h}_0$, above which the CME dynamics is dominated by aerodynamic drag. Using the torus instability (TI) model to describe the Lorentz forces (Kliem and Török, 2006), we address questions such as: Where does the Lorentz force peak? How does the Lorentz force compare with the aerodynamic drag force at and beyond $\tilde{h}_0$?

3. CME Data Sample

3.1. Event Selection

We investigate CMEs observed during the rising phase of Solar Cycle 24 between 2010 and 2013. The primary data we use is from the *Large Angle and Spectrometric Coronagaph* (LASCO: Brueckner *et al.*, 1995) onboard the *Solar and Heliospheric Observatory* mission (SOHO) and the *Sun–Earth Connection Coronal and Heliospheric Investigation* (SECCHI: Howard *et al.*, 2008) coronagraphs and the *Heliospheric Imagers* (HI) onboard the *Solar Terrestrial Relations Observatory* mission (STEREO; Kaiser *et al.*, 2008). *In-situ* measurements are obtained from the *Wind* spacecraft,[1] which gives the near-Earth parameters for these CMEs. The 38 CMEs we identify for this work have near-Sun speeds ranging from 50 $\mathrm{km\,s^{-1}}$ to 2400 $\mathrm{km\,s^{-1}}$. Of these, 13 events are partial halo (PH) CMEs and 21 are full halo (FH) CMEs as indicated in the SOHO/LASCO CME Catalog.[2] The remaining four events have angular width $< 120°$. All the CMEs in our sample are Earth-directed. The respective separations of the STEREO B and A spacecraft from the Earth vary from 71° and 66° in March 2010 to about 149° and 150° by the end of 2013. Along with the LASCO C2 coronagraph, the three-point view provides a favorable set up for observing Earth-directed CMEs. We only include CMEs that have continuous observations in LASCO C2, STEREO-A and -B COR 2, HI1 and HI2. We require that the images from all the instruments must include the CMEs as clear, bright structures. Events with major distortions and CME–CME interactions were excluded.

3.2. GCS Fitting

Needless to say, precise information as regards the three-dimensional (3D) evolution of CMEs is central to building a good model. Early efforts in this direction include those of Chen *et al.* (1997) and Wood *et al.* (1997). The advent of SECCHI/STEREO data facilitated this task greatly. We use the Graduated Cylindrical Shell (GCS: Thernisien, Howard, and Vourlidas, 2006; Thernisien, Vourlidas, and Howard, 2009; Thernisien, 2011) model to fit the visible CME structure. Table 1 lists the GCS fitting parameters for all the CMEs. The serial number of each CME in Table 1 will be used as a reference to the corresponding event hereafter. The eight events from Paper 1 (marked with an asterisk $*$) have observations up to the HI2 field of view (FOV), while the remaining events have been fitted up to the HI1 FOV. The second and third columns in Table 1 indicate the CME event date and time of the first observation in the LASCO C2 FOV. The quantity h_0 is the height of the leading edge of the CME from the GCS fitting technique, at the time of first observation. The CME initial

[1] http://omniweb.gsfc.nasa.gov/.

[2] http://cdaw.gsfc.nasa.gov/CME_list/.

Table 1 Details of all the CMEs in the sample. Near-Earth and observational GCS parameters. The first column is the serial number of each event with which it is referenced in the article. For each event the observation date and time when it is first fitted the C2 FOV is shown in the second and third columns. h_0 is the observed GCS height at the first observation and v_0 is the derived velocity at h_0. $n_{\rm wind}$ and $v_{\rm wind}$ are the observed proton number density and solar wind speed at 1 AU respectively. GCS parameters at h_0 are given by the Carrington longitude, ϕ, heliographic latitude, θ, tilt, γ, aspect ratio, κ, and half angle, α. All the fast CMEs are indicated by a superscript (f) in their serial number. The events from Paper 1 are indicated by a superscript ($*$) by their corresponding serial number.

No.	Date	Time	h_0	v_0	$n_{\rm wind}$	$v_{\rm wind}$	GCS parameters at h_0				
							ϕ	θ	γ	κ	α
		[UT]	[$R_\odot$]	[km s^{-1}]	[cm^{-3}]	[km s^{-1}]	[°]	[°]	[°]		[°]
1*	2010 Mar. 19	11:39	3.5	162	3.6	380	119	−10	−35	0.28	10
2*^{f}	2010 Apr. 03	10:24	5.5	916	7.1	470	267	−25	33	0.34	25
3*	2010 Apr. 08	03:24	2.9	468	3.60	440	180	17	−18	0.20	22
4*	2010 Jun. 16	15:24	5.7	193	3.50	500	336	0.5	−15	0.23	9.5
5*	2010 Sep. 11	02:24	4.0	444	4.00	320	260	23	−49	0.41	18
6*	2010 Oct. 26	07:39	5.3	215	3.80	350	74	−31	−55	0.25	22
7	2010 Dec. 23	05:54	3.7	147	6.10	321	29	−28	−15	0.40	18
8	2011 Jan. 24	03:54	4.4	276	9.00	320	336	−15	−15	0.30	22
9*	2011 Feb. 15	02:24	4.4	832	2.50	440	30	−6	30	0.47	27
10	2011 Mar. 03	05:54	4.9	349	2.25	550	175	−22	8	0.35	21
11*	2011 Mar. 25	07:00	4.8	47	3.00	360	207	1	9	0.21	37
12	2011 Apr. 08	23:39	4.7	300	5.00	375	41	6	−6	0.30	35
13	2011 Jun. 14	07:24	3.6	562	3.70	455	202	1	36	0.26	57
14^f	2011 Jun. 21	03:54	8.4	1168	8.00	470	129	5	−8	0.45	14
15^f	2011 Jul. 09	00:54	4.1	903	7.50	445	264	17	15	0.35	18
16^f	2011 Aug. 04	04:24	7.3	1638	2.00	355	324	19	65	0.69	29
17	2011 Sep. 13	23:39	3.8	493	2.13	468	134	19	−38	0.43	41
18^f	2011 Oct. 22	10:54	4.0	1276	8.00	300	54	44	16	0.60	45
19	2011 Oct. 26	12:39	7.8	889	3.00	260	302	7	−1	0.46	9
20	2011 Oct. 27	12:39	5.3	882	8.42	411	223	29	16	0.36	16
21^f	2012 Jan. 19	15:24	4.6	1823	7.00	310	212	44	90	0.47	58
22^f	2012 Jan. 23	03:24	4.0	1910	6.00	416	206	28	58	0.48	41
23^f	2012 Jan. 27	17:54	3.5	2397	4.00	420	193	30	69	0.38	41
24^f	2012 Mar. 13	17:39	3.9	1837	1.00	533	302	21	−40	0.74	73
25	2012 Apr. 19	15:39	4.1	648	10.00	325	82	−28	0.0	0.27	30
26^f	2012 Jun. 14	14:24	6.2	1152	3.23	324	92	−22	−87	0.38	20
27^f	2012 Jul. 12	16:54	4.4	1248	3.20	355	88	−10	78	0.45	35
28^f	2012 Sep. 28	00:24	6.7	1305	7.00	320	165	17	86	0.42	42
29	2012 Oct. 05	03:39	4.4	461	6.00	320	56	−24	37	0.30	31
30	2012 Oct. 27	17:24	7.3	380	5.00	280	118	8	−36	0.20	40
31	2012 Nov. 09	14:54	3.8	602	13.00	290	285	−18	7	0.48	35
32	2012 Nov. 23	14:39	6.3	492	7.00	370	91	−21	−66	0.52	10
33^f	2013 Mar. 15	06:54	4.7	1504	4.50	470	76	−7	−86	0.31	40
34^f	2013 Apr. 11	07:39	5.9	1115	3.30	445	77	−1	90	0.14	47
35^f	2013 Jun. 28	02:24	6.6	1637	10.00	420	177	−35	−20	0.41	5
36^f	2013 Sep. 29	22:24	4.9	1217	11.00	260	360	21	90	0.38	47
37^f	2013 Nov. 07	00:24	5.9	975	5.50	381	304	−30	−75	0.34	12
38^f	2013 Dec. 07	08:24	6.8	1039	15.00	367	221	32	51	0.36	47

speed v_0 at h_0 is calculated by fitting a third-degree polynomial to the height–time observations. The quantities $n_{\rm wind}$ and $v_{\rm wind}$ are the proton number density and solar wind velocity at 1 AU as observed *in situ* by the *Wind* spacecraft. These observed values are extrapolated sunward for use in $F_{\rm drag}$ for calculating $n_{\rm sw}$ and $V_{\rm sw}$ in Equation 1. We follow the detailed description given in Paper 1 to calculate the various parameters, such as $A_{\rm cme}$, $n_{\rm sw}$, $V_{\rm sw}$, and $C_{\rm D}$, required in evaluating $F_{\rm drag}$.

GCS parameters like Carrington longitude, ϕ, and heliographic latitude, θ, along with the tilt, γ, provide details of the position of the source region (SR) and the orientation of the propagating CME. The quantity κ is the aspect ratio and α is half of the angle between the axes and the legs of the flux rope. Using the GCS fitted height of the leading edge (R), κ, and α at each time instant, other geometrical parameters like CME minor radius, b, ratio, R/b, elliptical cross-sectional width, and CME area, $A_{\rm cme}$, are calculated (Thernisien, 2011) to be used in Equation 1. The observed height–time data for each CME in our sample is thus derived from the GCS fitting of images at each timestamp.

Our sample includes 38 CMEs with an initial velocity range $47 < v_0 < 2400\,{\rm km\,s^{-1}}$. There are 18 CMEs with initial velocities $v_0 > 900\,{\rm km\,s^{-1}}$. We call these events "fast" and indicate them by a superscript (f) in Tables 1 and 2. The fastest event is CME 23 on 27 January 2012, with $v_0 \sim 2400\,{\rm km\,s^{-1}}$. The remaining 20 CMEs in the sample having $v_0 < 900\,{\rm km\,s^{-1}}$ are called "slower" CMEs.

4. Analysis and Results

Our main aim in this article is to determine the heliocentric distance range(s) where the Lorentz-force terms and the aerodynamic drag terms (Equation 1) are respectively dominant.

4.1. Aerodynamic Drag

We first try to reconcile the observed CME dynamics with a solar wind aerodynamic drag-only model following the procedure described in Paper 1. In other words, we consider only the $F_{\rm drag}$ term in Equation 1 using observationally derived parameters and compare the model solutions with the observed height–time data. We find that the drag-only model solutions agree reasonably well with the observed CME profile right from the first data point (h_0) for the fast CMEs (initial velocity $> 900\,{\rm km\,s^{-1}}$). Figure 1 shows the height–time plot for CME 18 ($v_0 \sim 1276\,{\rm km\,s^{-1}}$) and CME 36 ($v_0 \sim 1217\,{\rm km\,s^{-1}}$), to compare the model results (red dash-dotted line) and data (diamonds). It is clear that, for both these CMEs, solar wind drag explains the observed trajectory quite well from 4 and 4.9 $R_\odot$ onwards, respectively. This result is representative of all the 18 fast CMEs in our sample. However, this is not true for slower CMEs. Figure 2 shows the results for two representative slower CMEs (CME 8, $v_0 \sim 276\,{\rm km\,s^{-1}}$ and CME 29, $v_0 \sim 461\,{\rm km\,s^{-1}}$) with the drag-only model initiated from the first observation point. The disagreement between the data (diamond symbols) and predicted solution (red dash-dotted line) is obvious, and indicates that the drag-only model, when initiated from the first data point, provides a poor explanation for the observed CME dynamics for slower CMEs. As in Paper 1, we then initiate the drag-only model at progressively later heights (using observational inputs appropriate to the initiation height). The initiation height at which the drag solution matches the observations is denoted by $\tilde{h}_0$ in Table 2. The model predicted solution (denoted by a solid blue line) shown in Figure 2 indicates that the drag-only model initiated above $\tilde{h}_0$ ($\sim$ 21 and 31 $R_\odot$ for CME 8 and 29 respectively) provides a good description of the dynamics of these relatively slower CMEs. We follow this procedure

Table 2 Parameters for the solar wind drag and Lorentz-force analysis are shown here. The first column indicates the serial number of the CME from Table 1. $\tilde{h}_0$ is the height at which drag force takes over the CME dynamics and $\tilde{v}_0$ is the corresponding speed at this height. Lorentz-force parameters include the decay index, n, height at which the Lorentz force peaks, $h_{\rm peak}$, equilibrium current, $I_{\rm eq}$, at $h_{\rm eq}$, equilibrium field, $B_{\rm ext}$, also evaluated at $R = h_{\rm eq}$, and *Fall%*, which gives the amount by which the Lorentz force decreases from its maximum value (at $h_{\rm peak}$) to its value at $\tilde{h}_0$. In the last column, $F_{\rm diff}$ denotes the quantity $\frac{F_{\rm drag}-F_{\rm Lorentz}}{F_{\rm drag}} \times 100\%$ at 40 $R_\odot$ for all events (except CME 11, for which it is evaluated at 50 $R_\odot$).

CME No.	Drag parameters		Lorentz force parameters					
	$\tilde{h}_0$ [$R_\odot$]	$\tilde{v}_0$ [km s^{-1}]	n	$h_{\rm peak}$ [$R_\odot$]	$I_{\rm eq}$ [10^{10} A]	$B_{\rm ext}(h_{\rm eq})$ [10^{-1} G]	*Fall%* [%]	$F_{\rm diff}$ [%]
1*	21.9	383	2.5	1.75	0.41	0.13	96	18.6
2*[f]	5.5	916	1.6	2.35	3.13	0.94	30	43.2
3*	19.7	506	1.9	2.05	0.55	0.19	86	16.3
4*	15.2	437	2.5	1.75	0.31	0.11	93	−41.3
5*	27.7	490	1.6	2.35	1.77	0.33	79	6.6
6*	20.1	445	1.7	2.25	0.66	0.22	73	5.9
7	27.1	583	1.6	2.35	2.30	0.65	81	4.2
8	20.8	454	1.6	2.35	1.21	0.38	77	19.7
9*	39.7	530	2.1	1.95	1.10	0.29	97	0.2
10	18.2	511	2.5	1.75	0.50	0.15	95	−33.3
11*	46.5	456	1.9	2.05	0.71	0.25	94	0.9
12	12.1	373	2.5	1.75	0.47	0.15	91	24.3
13	24.4	767	1.6	2.35	1.72	0.56	80	30.7
14[f]	8.4	1168	1.6	2.35	6.26	1.71	48	21.6
15[f]	4.1	903	1.9	2.05	2.66	0.79	29	52.4
16[f]	7.3	1638	1.6	2.45	5.90	1.39	41	61.3
17	38.8	636	1.7	2.25	1.06	0.29	91	0.3
18[f]	4.0	1276	2.1	1.95	8.40	2.09	35	80.0
19	30.5	313	2.1	1.95	0.47	0.13	96	2.1
20	39.4	491	2.2	1.95	1.67	0.49	98	0.3
21[f]	4.6	1823	3.0	1.65	11.60	3.11	66	80.9
22[f]	4.0	1910	3.0	1.65	10.30	2.74	58	93.7
23[f]	3.5	2397	3.0	1.65	8.51	2.47	49	94.6
24[f]	3.9	1837	1.9	2.05	3.92	0.91	25	83.2
25	23.1	684	1.6	2.35	3.68	1.19	71	3.3
26[f]	6.2	1152	1.6	2.35	2.89	0.84	35	70.5
27[f]	4.4	1248	1.6	2.35	4.07	1.11	18	64.9
28[f]	6.7	1305	1.6	2.35	8.53	2.37	39	59.2
29	31.1	790	1.6	2.35	4.05	1.28	79	7.8
30	36.9	570	1.6	2.35	1.56	0.56	84	29.2
31	26.5	597	2.9	1.75	11.07	2.96	98	4.4
32	27.7	668	1.7	2.25	3.41	0.89	86	10.4
33[f]	4.7	1504	1.8	2.15	4.29	1.32	32	56.0
34[f]	5.9	1115	1.6	2.35	1.29	0.52	34	83.5
35[f]	6.6	1637	2.5	1.85	9.55	2.69	26	60.3
36[f]	4.9	1217	2.1	1.95	7.06	2.04	48	80.7
37[f]	5.9	975	1.7	2.25	2.50	0.75	60	68.3
38[f]	6.8	1039	1.9	2.05	6.91	2.04	57	8.9

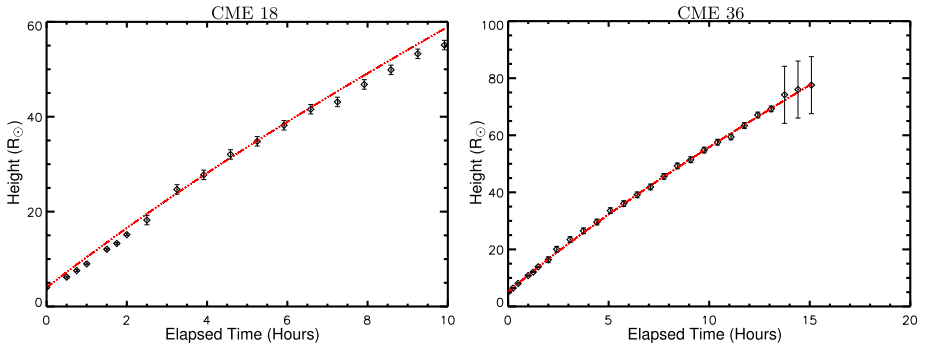


Figure 1 The observed height–time data is shown with diamonds. The *red dash-dotted line* is the drag model solution when it is initiated from the first observed height, h_0. CME 18 refers to the event on 22 October 2011, with an initial speed $\sim 1276\ \mathrm{km\,s^{-1}}$, and CME 36 represents an event on 29 September 2013, with an initial speed $\sim 1217\ \mathrm{km\,s^{-1}}$. Both these events are fast CMEs.

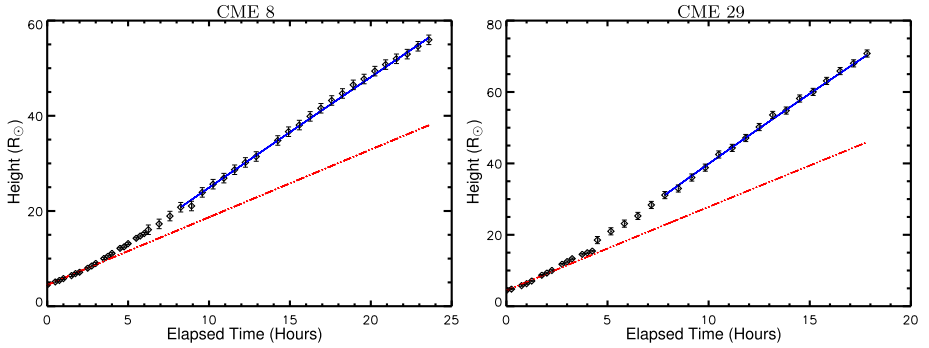


Figure 2 The observed height–time data is shown with diamonds. The *red dash-dotted line* is the drag model solution when it is initiated from the first observed height h_0. The *blue solid line* shows the predicted height–time trajectory when the drag model is initiated from height $\tilde{h}_0$. CME 8 refers to the event on 24 January 2011, with an initial speed $\sim 276\ \mathrm{km\,s^{-1}}$. CME 29 represents an event on 05 October 2012, with an initial speed $\sim 461\ \mathrm{km\,s^{-1}}$. Both CMEs 8 and 29 are slow CMEs.

for each event in our sample. The quantities $\tilde{h}_0$ and corresponding velocity $\tilde{v}_0$ are listed for each event in Table 2. We use the coefficient of determination (often called R squared) to determine how well the predicted model solutions fit the data. Model solutions with $R^2 > 98\%$ are considered acceptable. The CME dynamics can be considered to be dominated by solar wind aerodynamic drag above the height $\tilde{h}_0$. The left panel of Figure 3 shows a plot of $\tilde{h}_0$ (Table 2) *versus* the CME initial velocity (v_0). We see that, for CMEs with $v_0 < 900\ \mathrm{km\,s^{-1}}$, $\tilde{h}_0$ lies between $12-50\ \mathrm{R_\odot}$, while for CMEs with $v_0 > 900\ \mathrm{km\,s^{-1}}$, $\tilde{h}_0$ is the same as the initial observed height for the event (h_0 in Table 1, which ranges from $3.9-8.4\ \mathrm{R_\odot}$ for the fast CMEs in our sample). In other words, Figure 3 shows that fast CMEs are drag dominated from $3.9-8.4\ \mathrm{R_\odot}$ onwards, while slower CMEs are drag dominated only beyond $12-50\ \mathrm{R_\odot}$.

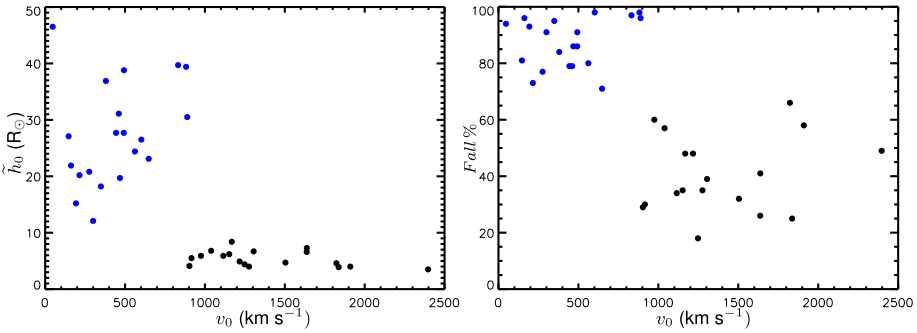


Figure 3 Plot of initiation height ($\tilde{h}_0$) and *Fall% versus* the CME initial speed. *Left panel* shows the quantity $\tilde{h}_0$ (from where solar wind drag dominates) as a function of CME initial velocity, v_0. The *right panel* depicts the percentage fall in the Lorentz force from its peak value to its value at $\tilde{h}_0$ (%) as a function of CME initial velocity, v_0. *Symbols in blue* represent slow CMEs (*i.e.* $v_0 < 900$ km s^{-1}) and *symbols in black* represent fast CMEs ($v_0 > 900$ km s^{-1}). See Table 2 for the values in the figure.

4.2. Lorentz Forces

If the aerodynamic drag dominates for heliocentric distances $R > \tilde{h}_0$ (*i.e.* it is not necessary to invoke Lorentz forces to explain their dynamics), it is natural to investigate the behavior of Lorentz forces for $R < \tilde{h}_0$. The first two terms in Equation 1 are a feature of most Lorentz-force models that deal with CME initiation. All such models predict that the (total) Lorentz force increases until it peaks at a certain heliocentric distance, beyond which it decreases and becomes negligible. Some models tailor the injected poloidal flux (or equivalently, the driving current) so as to achieve this Lorentz-force profile (Chen and Kunkel, 2010). Others, such as the torus instability model (Kliem and Török, 2006), rely on the fact that the external Lorentz forces need to decrease (with heliocentric distance) faster than a certain rate in order to "launch" the CME. This also results in a Lorentz-force profile that increases initially and achieves a peak before decreasing. Kliem *et al.* (2014) have also shown the equivalence of TI and the catastrophe mechanism for CME eruption (Forbes and Isenberg, 1991).

In this description, the equilibrium position of the flux rope, $h_{\rm eq}$, is defined by a balance between the Lorentz self force and the external force. For the sake of concreteness, we adopt $h_{\rm eq} = 1.05$ R$_\odot$ in our work. The equilibrium position is also defined by an equilibrium current, $I_{\rm eq}$. The current carried by the flux rope at a given R is defined by (Kliem and Török, 2006):

$$I = \frac{c'_{\rm eq} I_{\rm eq} h_{\rm eq}}{c' R}\left(1 + \frac{(c'_{\rm eq} + \frac{1}{2})}{2c'_{\rm eq}(2-n)}\left[\left(\frac{R}{h_{\rm eq}}\right)^{2-n} - 1\right]\right), \tag{3}$$

where $c'(R) = [\ln(8R/b) - 2 + l_{\rm i}/2]$ and $c'_{\rm eq} = c'(R = h_{\rm eq}) = [\ln(8h_{\rm eq}/b_{\rm eq}) - 2 + l_{\rm i}/2]$. The quantity b is the flux-rope minor radius. The external (ambient) magnetic field is $\propto R^{-n}$, and n needs to be greater than a certain critical value for the torus instability to be operative, causing the flux rope to erupt. The quantity $l_{\rm i}$ is the internal inductance of the flux rope, and we use $l_{\rm i} = 1/2$. The equilibrium current, $I_{\rm eq}$, carried by the flux rope is related to the external field, $B_{\rm ext}(h_{\rm eq})$, at the equilibrium position via

$$I_{\rm eq} = \frac{B_{\rm ext}(h_{\rm eq}) h_{\rm eq} c}{c'_{\rm eq} + \frac{1}{2}}. \tag{4}$$

For a given value of n, the value of I_{eq} (and equivalently $B_{ext}(h_{eq})$) is determined by the condition $F_{drag}(\tilde{h}_0) = F_{Lorentz}(\tilde{h}_0)$. It constrains the equilibrium current I_{eq} and n. For a given event, n is chosen to be the minimum value that will ensure that $|F_{drag}| > F_{Lorentz}$ for $R > \tilde{h}_0$.

Table 2 gives the values of the equilibrium current I_{eq} and $B_{ext}(h_{eq})$ for all CMEs for the corresponding value of the decay index n. The GCS fits to our observations yield values for the flux-rope aspect ratio R/b. For heliocentric distances below the first observed point h_0 (which is typically around 3 $R_\odot$), we assume that R/b is the same as the observed value at the first observed point (h_0). In other words, we assume that the flux rope expands in a self-similar manner from h_{eq} to h_0; beyond h_0, we do not have to rely on any such assumption, since we have access to the observed values of R/b.

4.3. Lorentz Force *versus* Aerodynamic Drag

As an example, we show a plot of the Lorentz force *versus* heliocentric distance for CMEs 18 and 36 in Figure 4 and CMEs 8 and 29 in Figure 5. The red solid line indicates the points between h_{eq} and h_0 where we do not have data for R/b (in this region we assume that R/b is the same as its value at h_0) and black diamonds indicate points for which we have observationally determined values for R/b. Clearly, the Lorentz force on the flux rope increases from its value at h_{eq} to reach a peak at h_{peak}, after which it decreases. For each CME, the position at which the Lorentz force peaks (h_{peak}) is given in Table 2. The peak is generally between 1.65 and 2.45 $R_\odot$ for the CMEs in our sample. The green circles in Figures 4 and 5 indicate the absolute value of solar wind drag force with height above $\tilde{h}_0$. The location of $\tilde{h}_0$ is indicated by a blue dashed vertical line. The quantity marked *Fall%* in Table 2 quantifies the amount by which the Lorentz force at $\tilde{h}_0$ has fallen from its peak value at h_{peak}. For both the fast CMEs, CME 18 (left panel) and CME 36 (right panel) in Figure 4, the Lorentz force peaks at 1.95 $R_\odot$ with $n = 2.1$. The Lorentz force falls by 35% for CME 18 and by 48% for CME 36 from h_{peak} up to $\tilde{h}_0$; for these fast CMEs, $\tilde{h}_0$ happens to be the same as h_0. For the slower CMEs (CME 8 and CME 29, shown in Figure 5), $n = 1.6$ and the Lorentz force peaks at 2.35 $R_\odot$ for both CMEs. The Lorentz force decreases by as

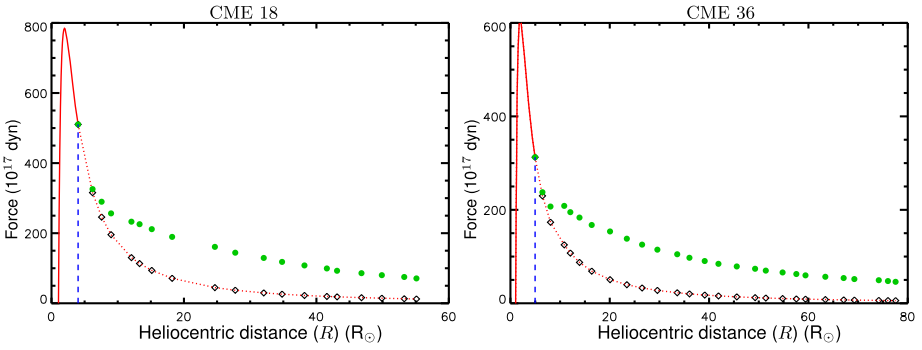


Figure 4 Comparison of Lorentz and drag forces for fast CMEs. The *open diamond symbols* represent the Lorentz-force values derived observationally starting from h_0. The *red solid line* indicates the Lorentz-force values for heights between h_{eq} and h_0. The *filled green circles* represent the absolute value of the solar wind drag force. The *dashed vertical line* (*blue*) indicates the height $\tilde{h}_0$ at which the solar wind drag force takes over. This height is the first observation point for both CMEs 18 and 36. For CME 18 $\tilde{h}_0 \sim 4$ $R_\odot$, while for CME 36 $\tilde{h}_0 \sim 4.9$ $R_\odot$.

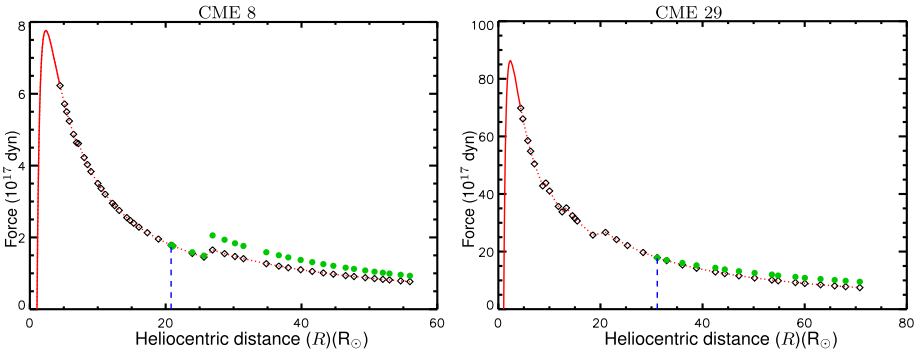


Figure 5 Comparison of Lorentz and drag forces for the slow CMEs (8 and 29). The *symbols* and *line* styles are the same as in Figure 4.

much as 77% from its value at $h_{\rm peak}$ up to $\tilde{h}_0 = 20.8$ R$_\odot$, beyond which the solar wind drag takes over for CME 8. Similarly, for CME 29, the Lorentz force decreases by 79% from $h_{\rm peak}$ up to $\tilde{h}_0 = 31$ R$_\odot$. This is typical of slower CMEs; for all the slower CMEs in Table 2, the Lorentz force at $\tilde{h}_0$ (which is 12 – 50 R$_\odot$) has fallen by around 70 – 98 % from its peak value. The Lorentz force peaks fairly early on ($h_{\rm peak} \approx 1.65 - 2.45$ R$_\odot$) for slow(er) CMEs, this means that they become negligible only as far out as 12 – 50 R$_\odot$.

For all the CMEs in our sample, the right panel of Figure 3 shows the percentage by which the Lorentz force has fallen at $\tilde{h}_0$ (relative to its peak value) as a function of the CME initial speed. Slower CMEs are denoted by blue circles and fast ones by black circles. The *Fall%* is clearly larger for the slower CMEs. Since the fast CMEs are drag dominated from relatively early on (left panel of Figure 3), the *Fall%* is relatively lower.

Reiterating the results summarized in Table 2. Column 1 indicates the CME serial number corresponding to the events listed in Table 1. Column 2 lists the height $\tilde{h}_0$ above which the solar wind drag dominates the CME dynamics. For slow CMEs, this height lies in the range 12 – 50 R$_\odot$, while for faster events it is the same as h_0 in Table 1. $\tilde{v}_0$ is the CME speed at height $\tilde{h}_0$. The values of n in column 4 represent the decay index for each CME and lie between 1.6 and 3. We note that the fastest CMEs typically have the highest values for n. The quantity $h_{\rm peak}$ quoted in column 5 gives the position where the Lorentz force peaks; it ranges between 1.65 and 2.45 R$_\odot$. The equilibrium current, $I_{\rm eq}$, in column 6 is in units of 10^{10} A. The $I_{\rm eq}$ estimates are in agreement with the average axial current calculated by Subramanian and Vourlidas (2007). The quantity $B_{\rm ext}(h_{\rm eq})$ in column 7 is the equilibrium magnetic field at $h_{\rm eq} = 1.05$ R$_\odot$ in units of G. *Fall%* in column 8 describes the amount by which the Lorentz force at $\tilde{h}_0$ has decreased relative to its peak value. For slow CMEs, the percentage fall is between 70 – 98%, while for faster CMEs, it is between 20 – 60 %. The last column indicates the quantity $F_{\rm diff} = ((F_{\rm drag} - F_{\rm Lorentz})/F_{\rm drag}) \times 100\%$ evaluated at 40 R$_\odot$ (except for CME 11, where it is evaluated at 50 R$_\odot$).

5. Discussion and Conclusions

5.1. Discussion

Our main aim in this paper is to quantify the relative contributions of Lorentz forces and solar wind aerodynamic drag on CMEs as a function of heliocentric distance. Since these

are the two main forces thought to be responsible for CME dynamics, it is essential to know their relative importance to build reliable models for CME Earth arrival time and speed. It is well known that aerodynamic drag dominates CME dynamics only beyond distances as large as 15 – 50 $R_\odot$ for all but the fastest CMEs (Paper 1). This trend has also been confirmed by independent studies using an empirical fitting parameter for aerodynamic drag (*e.g.* Temmer and Nitta, 2015). One would assume that Lorentz forces are dominant below these heliocentric distances (and negligible above it), but this has not been explicitly confirmed so far. To the best of our knowledge, this is the first systematic study in this regard using a diverse CME sample.

We use a sample of 38 CMEs that are well observed by the SECCHI coronagraphs and the heliospheric imagers onboard STEREO and the LASCO coronagraphs onboard SOHO. We use detailed geometrical parameters from GCS fitting to the CMEs. Our prototypical models for aerodynamic drag and Lorentz forces are shown in Equation 1. The model for aerodynamic drag follows the physical definition outlined in Paper 1, and the model for Lorentz forces follows the TI model of Kliem and Török (2006). Using only the aerodynamic drag term, we compute the heliocentric distance $\tilde{h}_0$ beyond which solar wind drag can be considered to be the only force influencing the CME dynamics. This calculation makes use of several observational inputs for each CME: the ambient solar wind density and velocity, GCS fitted height, velocity and area for each CME. Subsequently, we use only the Lorentz-force term. Using observational data for the aspect ratio of the CME flux rope, we determine the heliocentric distance $h_{\rm peak}$ at which the Lorentz force attains its peak value. We also determine the percentage by which the Lorentz force decreases from its peak value at $h_{\rm peak}$ up to $\tilde{h}_0$ (beyond which aerodynamic drag becomes the dominant force). Table 2 summarizes all our results.

Some of the trends revealed by our results are depicted graphically in Figures 3, 6, and 7. Blue circles indicate slow CMEs, while the black circles represent fast events. As discussed earlier, Figure 3 shows that aerodynamic drag dominates the dynamics of fast CMEs from a few solar radii onwards, whereas it is dominant for slow CMEs only beyond 12 – 50 $R_\odot$.

Figure 6a shows the first observed height, h_0, of each CME as a function of its initial speed v_0. There does not seem to be a definite distinction between fast and slow CMEs in this regard. It is possible, however, that the limited time cadence of the LASCO C2 coronagraphs affects the values of h_0 for fast CMEs. We note that the first observed height for about 60% of the CMEs lies between 2.9 and 5.0 $R_\odot$.

As depicted in Figures 4 and 5, the Lorentz-force profile shows a steep increase from $h_{\rm eq}$ until it peaks at $h_{\rm peak}$, beyond which it decreases. Figure 6b is a scatterplot of the position of the Lorenz force peak ($h_{\rm peak}$; see Table 2) as a function of the CME initial speed, v_0. The value of $h_{\rm peak}$ is between 1.65 and 2.45 $R_\odot$ for all CMEs, with no noticeable trend distinguishing slow and fast ones.

As shown in the right panel of Figure 3, the percentage decrease, *Fall%*, of the Lorentz force at $\tilde{h}_0$ (relative to its value at $h_{\rm peak}$) is considerably higher for slow CMEs than it is for fast ones. Figure 6c shows a different way of visualising this data - the quantity *Fall%* is plotted as a function of $\tilde{h}_0$. It shows that the percentage decrease is larger for CMEs with larger $\tilde{h}_0$ (the slow ones) than it is for those with relatively smaller values of $\tilde{h}_0$ (the fast ones).

The drag-only model accounts well for the CME trajectory when initiated at $\tilde{h}_0$ (or beyond). This implies that other forces (such as Lorentz forces) are not important beyond this height. We find this to be true for 36 of the 38 CMEs in our sample. CMEs 4 and 10 (which are slow) are the only exceptions. However, we find that the difference between the drag force and the Lorentz force beyond $\tilde{h}_0$ is much more pronounced for fast CMEs than

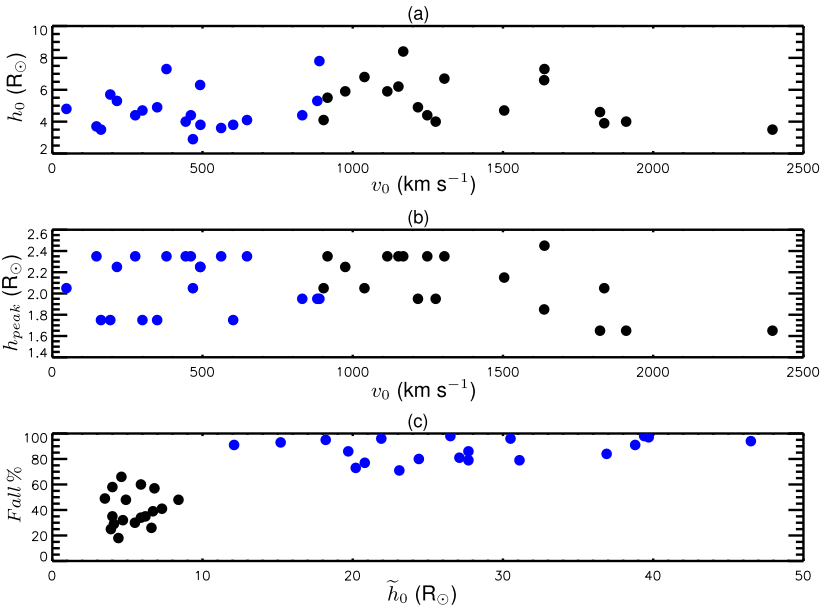


Figure 6 Summary of some of the results in Table 2. *Blue circles* represent quantities for slow CMEs and *black circles* represent fast CMEs. Panels **a** and **b** plot the quantities h_0 and $h_{\rm peak}$ respectively as a function of CME initial velocity, v_0. Panel **c** shows the percentage decrease, *Fall%*, in Lorentz force (between its peak and $\tilde{h}_0$) as a function of $\tilde{h}_0$ for both slow (*blue circles*) and fast (*black circles*) CMEs.

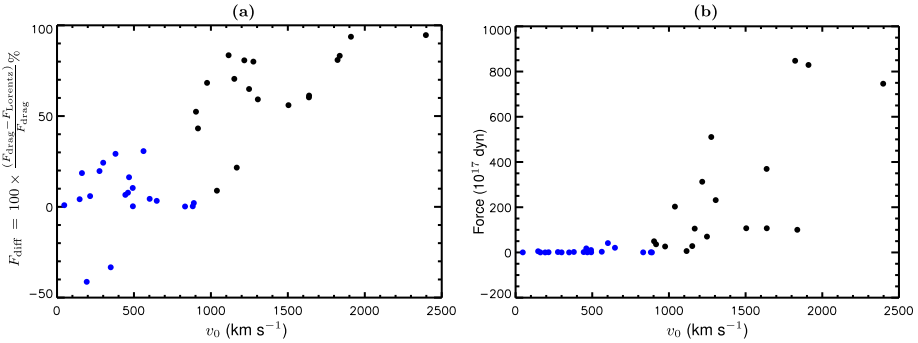


Figure 7 Plot of the relative difference between the two forces and variation of the drag force magnitude at $\tilde{h}_0$ *versus* CME initial velocity, v_0. Panel **a** shows the percentage difference between drag and Lorentz forces as a function of CME initial velocity, v_0. $F_{\rm diff}$ is calculated at 40 R$_\odot$ for all CMEs except CME 11, for which it is evaluated at 50 R$_\odot$. Panel **b** shows the absolute value of drag force at $\tilde{h}_0$ for all CMEs with respect to the CME initial velocity, v_0. Details are described in the text. The *blue circles* represent slow CMEs and the black ones represent fast CMEs.

for slow ones (*e.g.* Figures 4 and 5). In order to quantify this, we compute the quantity $F_{\rm diff} = 100 \times (F_{\rm drag} - F_{\rm Lorentz})/F_{\rm drag}$ for all the CMEs in our list. This quantity is plotted in Figure 7a as a function of the CME initial velocity, v_0; as before, blue circles represent slow CMEs, while black ones represent fast ones. We show the relative percentage difference for all events at 40 R$_\odot$ except for CME 11. Since $\tilde{h}_0 \sim 46$ R$_\odot$ for CME 11, $F_{\rm diff}$ is evaluated

at 50 $R_\odot$ for this event. The drag force is 50 – 90% larger at 40 $R_\odot$ than the Lorentz force for most of the fast events. This justifies the success of the drag-only model for fast events. On the other hand, this number ranges from 0.2% and 30% for the slower events. Evidently, for some of the slower CMEs, the computed Lorentz force is only slightly smaller than the drag force, even well beyond $\tilde{h}_0$. For the slow CMEs 4 and 10, the Lorentz force is in fact larger than the solar wind drag force in magnitude. Figure 7b shows a plot of the absolute magnitude of the solar wind drag force (in units of 10^{17} dyn) for all CMEs at $\tilde{h}_0$ *versus* the CME initial velocity, v_0. Since a drag-only model describes the data well for all the events in our list, it follows that the Lorentz force we compute for some of the slower CMEs is an overestimate. Our Lorentz-force computations assume that the total magnetic flux is frozen in. The time evolution of the enclosed current, I, follows from this assumption. However, this assumption might not be accurate – some of the magnetic energy might be expended in CME expansion and/or heating of the CME plasma. Our results suggest that such effects might be especially important for slower CMEs.

5.2. Conclusions

Our main conclusions are:

- Our analysis shows that a model that includes only the solar wind aerodynamic drag accurately describes the trajectory of fast CMEs from very early on. The converse is true for slower CMEs. The distance $\tilde{h}_0$ beyond which the solar wind aerodynamic drag dominates over the Lorentz force can be as small as 3.5 – 4 $R_\odot$ for fast (> 900 km s^{-1}) CMEs, and as large as 12 – 50 $R_\odot$ for slower ones (47 – 890 km s^{-1}).
- The distance $h_{\rm peak}$ at which the Lorentz force peaks is between 1.65 and 2.45 $R_\odot$ for all CMEs.
- At $\tilde{h}_0$, the Lorentz force has typically fallen by 20 – 60 % (relative to its peak value) for fast CMEs. For slower CMEs, the decrease ranges between 70 – 98%.
- Well beyond $\tilde{h}_0$, the drag force exceeds the Lorentz driving force by a significant amount for fast CMEs (50% – 90%). However, for some slow CMEs the dominance of the drag force is not as pronounced, suggesting that part of the CME magnetic flux may be dissipated in aiding its expansion or heating.

In calculating the Lorentz force, the initial equilibrium position for the CME flux rope is taken to be $h_{\rm eq} = 1.05$ $R_\odot$ for all events. The overlying field is taken to decrease as $B_{\rm ex} \propto R^{-n}$. The quantity n needs to be greater than a critical value $n_{\rm cr}$ ($n_{\rm cr} = 3/2 - 1/(4c'_{\rm eq})$) for the torus instability to be operative, ensuring CME eruption. For each CME, we choose a value of n that is $> n_{\rm cr}$. We demand that the Lorentz force equals the aerodynamic drag force at $\tilde{h}_0$. The value for n is chosen such that the Lorentz force remains lower than the aerodynamic drag force beyond $\tilde{h}_0$. For the CMEs in our sample, the critical decay index $n_{\rm cr}$ ranges from 1.29 to 1.39.

For a fixed value of n, we note that an increase in $h_{\rm eq}$ by 14 % increases the peak force position value by $\sim 15\%$. It decreases the $Fall\,\%$ of the Lorentz force at $\tilde{h}_0$ (relative to its peak value) by 5 %. For a fixed value of $h_{\rm eq}(-1.05$ $R_\odot)$, an increase in n by 31% decreases the peak position by 17%. It also increases the *Fall*% of the Lorentz force at $\tilde{h}_0$ (relative to its peak value) by 19.5%.

Although we have considered only Lorentz forces and solar wind aerodynamic drag in order to explain CME dynamics, we note that there can be other important contributors to the overall energetics. For instance, the work involved in CME expansion and the energy expended in possibly heating the CME plasma (see, *e.g.*, Kumar and Rust, 1996; Wang, Zhang,

and Shen, 2009; Emslie *et al.*, 2012) are not considered here. These could well be important, in addition to the energy dissipated due to aerodynamic drag. An understanding of these quantities can be achieved via observations of CME expansion, as well as measurements of thermodynamic quantities inside the CME as it progresses through the heliosphere. The latter can possibly be done with the upcoming *Solar Probe Plus* and *Solar Orbiter* missions or via an off-limb spectroscopy mission.

Acknowledgements NS acknowledges support from a PhD studentship at IISER Pune, from NAMASTE India-EU scholarship, and from the Infosys Foundation Travel Award. NS is thankful to A. Pluta and N. Mrotzek for their help and useful discussions as regards data selection and fitting procedures. PS acknowledges support from the Indian Space Research Organization via a RESPOND grant. AV is supported by NNX16AH70G. VB acknowledges support of the CGAUSS (Coronagraphic German and US *Solar Probe Plus* Survey) project for WISPR by the German Space Agency DLR under grant 50 OL 1601. The SECCHI data are produced by an international consortium of the NRL, LMSAL and NASA/GSFC (USA), RAL and Univ. Bham (UK), MPS (Germany), CSL (Belgium), IOTA and IAS (France).

Disclosure of Potential Conflicts of Interest The authors declare that they have no conflicts of interest.

References

Bein, B.M., Berkebile-Stoiser, S., Veronig, A.M., Temmer, M., Muhr, N., Kienreich, I., *et al.*: 2011, Impulsive acceleration of coronal mass ejections, I: Statistics and coronal mass ejection source region characteristics. *Astrophys. J.* **738**, 191. DOI. ADS.

Bosman, E., Bothmer, V., Nisticò, G., Vourlidas, A., Howard, R.A., Davies, J.A.: 2012, Three-dimensional properties of coronal mass ejections from STEREO/SECCHI observations. *Solar Phys.* **281**, 167. DOI. ADS.

Bothmer, V., Daglis, I.A.: 2007, *Space Weather – Physics and Effects*. *Praxis Pub*. DOI. ADS.

Brueckner, G.E., Howard, R.A., Koomen, M.J., Korendyke, C.M., Michels, D.J., Moses, J.D., *et al.*: 1995, The large angle spectroscopic coronagraph (LASCO). *Solar Phys.* **162**, 357. DOI. ADS.

Cargill, P.J.: 2004, On the aerodynamic drag force acting on interplanetary coronal mass ejections. *Solar Phys.* **221**, 135. DOI. ADS.

Carley, E.P., McAteer, R.T.J., Gallagher, P.T.: 2012, Coronal mass ejection mass, energy, and force estimates using STEREO. *Astrophys. J.* **752**, 36. DOI. ADS.

Chen, J.: 1989, Effects of toroidal forces in current loops embedded in a background plasma. *Astrophys. J.* **338**, 453. DOI. ADS.

Chen, J.: 1996, Theory of prominence eruption and propagation: Interplanetary consequences. *J. Geophys. Res.* **101**, 27499. DOI. ADS.

Chen, J., Kunkel, V.: 2010, Temporal and physical connection between coronal mass ejections and flares. *Astrophys. J.* **717**, 1105. DOI. ADS.

Chen, J., Howard, R.A., Brueckner, G.E., Santoro, R., Krall, J., Paswaters, S.E., *et al.*: 1997, Evidence of an erupting magnetic flux rope: LASCO coronal mass ejection of 1997 April 13. *Astrophys. J. Lett.* **490**, L191. DOI. ADS.

Emslie, A.G., Dennis, B.R., Shih, A.Y., Chamberlin, P.C., Mewaldt, R.A., Moore, C.S., *et al.*: 2012, Global energetics of thirty-eight large solar eruptive events. *Astrophys. J.* **759**, 71. DOI. ADS.

Forbes, T.G.: 2000, A review on the genesis of coronal mass ejections. *J. Geophys. Res.* **105**, 23153. DOI. ADS.

Forbes, T.G., Isenberg, P.A.: 1991, A catastrophe mechanism for coronal mass ejections. *Astrophys. J.* **373**, 294. DOI. ADS.

Fry, C.D., Dryer, M., Smith, Z., Sun, W., Deehr, C.S., Akasofu, S.-I.: 2003, Forecasting solar wind structures and shock arrival times using an ensemble of models. *J. Geophys. Res.* **108**, 1070. DOI. ADS.

Gopalswamy, N.: 2013, STEREO and SOHO contributions to coronal mass ejection studies: Some recent results. *Astron. Soc. India C.S.* **10**. ADS.

Gosling, J.T., McComas, D.J., Phillips, J.L., Bame, S.J.: 1991, Geomagnetic activity associated with earth passage of interplanetary shock disturbances and coronal mass ejections. *J. Geophys. Res.* **96**, 7831. DOI. ADS.

Howard, R.A., Moses, J.D., Vourlidas, A., Newmark, J.S., Socker, D.G., Plunkett, S.P., *et al.*: 2008, Sun Earth connection coronal and heliospheric investigation (SECCHI). *Space Sci. Rev.* **136**, 67. DOI. ADS.

Isenberg, P.A., Forbes, T.G.: 2007, A three-dimensional line-tied magnetic field model for solar eruptions. *Astrophys. J.* **670**, 1453. DOI. ADS.

Jin, M., Manchester, W.B., van der Holst, B., Sokolov, I., Tóth, G., Mullinix, R.E., Taktakishvili, A., Chulaki, A., Gombosi, T.I.: 2017, Data-constrained coronal mass ejections in a global magnetohydrodynamics model. *Astrophys. J.* **834**, 173. DOI. ADS.

Kaiser, M.L., Kucera, T.A., Davila, J.M., St. Cyr, O.C., Guhathakurta, M., Christian, E.: 2008, The STEREO mission: An introduction. *Space Sci. Rev.* **136**, 5. DOI. ADS.

Kliem, B., Török, T.: 2006, Torus instability. *Phys. Rev. Lett.* **96**(25), 255002. DOI. ADS.

Kliem, B., Lin, J., Forbes, T.G., Priest, E.R., Török, T.: 2014, Catastrophe versus instability for the eruption of a toroidal solar magnetic flux rope. *Astrophys. J.* **789**, 46. DOI. ADS.

Kumar, A., Rust, D.M.: 1996, Interplanetary magnetic clouds, helicity conservation, and current-core flux-ropes. *J. Geophys. Res.* **101**, 15667. DOI. ADS.

Lee, C.O., Arge, C.N., Odstrčil, D., Millward, G., Pizzo, V., Quinn, J.M., *et al.*: 2013, Ensemble modeling of CME propagation. *Solar Phys.* **285**, 349. DOI. ADS.

Lugaz, N., Manchester, W.B. IV, Roussev, I.I., Tóth, G., Gombosi, T.I.: 2007, Numerical investigation of the homologous coronal mass ejection events from active region 9236. *Astrophys. J.* **659**, 788. DOI. ADS.

Mays, M.L., Taktakishvili, A., Pulkkinen, A., MacNeice, P.J., Rastätter, L., Odstrcil, D., Jian, L.K., Richardson, I.G., LaSota, J.A., Zheng, Y., Kuznetsova, M.M.: 2015, Ensemble modeling of CMEs using the WSA-ENLIL+cone model. *Solar Phys.* **290**, 1775. DOI. ADS.

McKenna-Lawlor, S.M.P., Dryer, M., Kartalev, M.D., Smith, Z., Fry, C.D., Sun, W., *et al.*: 2006, Near real-time predictions of the arrival at Earth of flare-related shocks during Solar cycle 23. *J. Geophys. Res.* **111**, A11103. DOI. ADS.

Mishra, W., Srivastava, N.: 2013, Estimating the arrival time of Earth-directed coronal mass ejections at in situ spacecraft using COR and HI observations from STEREO. *Astrophys. J.* **772**, 70. DOI. ADS.

Rollett, T., Möstl, C., Isavnin, A., Davies, J.A., Kubicka, M., Amerstorfer, U.V., *et al.*: 2016, ElEvoHI: A novel CME prediction tool for heliospheric imaging combining an elliptical front with drag-based model fitting. *Astrophys. J.* **824**, 131. DOI. ADS.

Sachdeva, N., Subramanian, P., Colaninno, R., Vourlidas, A.: 2015, CME propagation: Where does aerodynamic drag 'take over'? *Astrophys. J.* **809**, 158. DOI. ADS.

Shafranov, V.D.: 1966, Plasma equilibrium in a magnetic field. *Rev. Plasma Phys.* **2**, 103. ADS.

Subramanian, P., Vourlidas, A.: 2007, Energetics of solar coronal mass ejections. *Astron. Astrophys.* **467**, 685. DOI. ADS.

Subramanian, P., Lara, A., Borgazzi, A.: 2012, Can solar wind viscous drag account for coronal mass ejection deceleration? *Geophys. Res. Lett.* **39**, L19107. DOI. ADS.

Taktakishvili, A., Kuznetsova, M., MacNeice, P., Hesse, M., Rastätter, L., Pulkkinen, A., *et al.*: 2009, Validation of the coronal mass ejection predictions at the Earth orbit estimated by ENLIL heliosphere cone model. *Space Weather* **7**, S03004. DOI. ADS.

Temmer, M., Nitta, N.V.: 2015, Interplanetary propagation behavior of the fast coronal mass ejection on 23 July 2012. *Solar Phys.* **290**, 919. DOI. ADS.

Temmer, M., Vršnak, B., Rollett, T., Bein, B., de Koning, C.A., Liu, Y., Bosman, E., Davies, J.A., Möstl, C., Žic, T., Veronig, A.M., Bothmer, V., Harrison, R., Nitta, N., Bisi, M., Flor, O., Eastwood, J., Odstrcil, D., Forsyth, R.: 2012, Characteristics of kinematics of a coronal mass ejection during the 2010 August 1 CME–CME interaction event. *Astrophys. J.* **749**, 57. DOI. ADS.

Thernisien, A.: 2011, Implementation of the graduated cylindrical shell model for the three-dimensional reconstruction of coronal mass ejections. *Astrophys. J. Suppl.* **194**, 33. DOI. ADS.

Thernisien, A., Vourlidas, A., Howard, R.A.: 2009, Forward modeling of coronal mass ejections using STEREO/SECCHI data. *Solar Phys.* **256**, 111. DOI. ADS.

Thernisien, A.F.R., Howard, R.A., Vourlidas, A.: 2006, Modeling of flux rope coronal mass ejections. *Astrophys. J.* **652**, 763. DOI. ADS.

Tóth, G., de Zeeuw, D.L., Gombosi, T.I., Manchester, W.B., Ridley, A.J., Sokolov, I.V., *et al.*: 2007, Sun-to-thermosphere simulation of the 28 – 30 October 2003 storm with the space weather modeling framework. *Space Weather* **5**, 06003. DOI. ADS.

Vršnak, B.: 2006, Forces governing coronal mass ejections. *Adv. Space Res.* **38**, 431. DOI. ADS.

Vršnak, B., Žic, T., Falkenberg, T.V., Möstl, C., Vennerstrom, S., Vrbanec, D.: 2010, The role of aerodynamic drag in propagation of interplanetary coronal mass ejections. *Astron. Astrophys.* **512**, A43. DOI. ADS.

Vršnak, B., Temmer, M., Žic, T., Taktakishvili, A., Dumbović, M., Möstl, C., *et al.*: 2014, Heliospheric propagation of coronal mass ejections: Comparison of numerical WSA-ENLIL+cone model and analytical drag-based model. *Astrophys. J. Suppl.* **213**, 21. DOI. ADS.

Wang, Y., Zhang, J., Shen, C.: 2009, An analytical model probing the internal state of coronal mass ejections based on observations of their expansions and propagations. *J. Geophys. Res.* **114**, A10104. DOI. ADS.

Wood, B.E., Karovska, M., Cook, J.W., Brueckner, G.E., Howard, R.A.: 1997, LASCO observations of variability in the quiescent solar corona. *Bull. Am. Astron. Soc.* **29**, 1321. ADS.

Wu, C.-C., Fry, C.D., Wu, S.T., Dryer, M., Liou, K.: 2007, Three-dimensional global simulation of interplanetary coronal mass ejection propagation from the Sun to the heliosphere: Solar event of 12 May 1997. *J. Geophys. Res.* **112**, A09104. DOI. ADS.

Zhang, J., Dere, K.P.: 2006, A statistical study of main and residual accelerations of coronal mass ejections. *Astrophys. J.* **649**, 1100. DOI. ADS.

Zhang, J., Dere, K.P., Howard, R.A., Kundu, M.R., White, S.M.: 2001, On the temporal relationship between coronal mass ejections and flares. *Astrophys. J.* **559**, 452. DOI. ADS.

Zhao, X., Dryer, M.: 2014, Current status of CME/shock arrival time prediction. *Space Weather* **12**, 448. DOI. ADS.